Large linear sensitivity of CoFe based CIP-GMR magnetic sensor using metastable bcc Cu spacer and auxiliary biquadratic coupling through Rh spacer

A thesis submitted

by

Dolly Taparia

to

Indian Institute of Technology Guwahati

in

Partial fulfillment of the requirement for the award of the degree of

Doctor of Philosophy in Physics

Department of Physics

Indian Institute of Technology Guwahati

Guwahati 781 039, Assam, India

July 2021

Large linear sensitivity of CoFe based CIP-GMR magnetic sensor using metastable bcc Cu spacer and auxiliary biquadratic coupling through Rh spacer

A thesis submitted

by

Dolly Taparia

to

Indian Institute of Technology Guwahati

in

Partial fulfillment of the requirement for the award of the degree of

Doctor of Philosophy in Physics

Department of Physics

Indian Institute of Technology Guwahati

Guwahati 781 039, Assam, India

July 2021

Statement

The work contained in the thesis, entitled "Large linear sensitivity of CoFe based CIP-GMR magnetic sensor using metastable bcc Cu spacer and auxiliary biquadratic coupling through Rh spacer", has been carried out by me under the supervision of Prof. Perumal Alagarsamy and Prof. Ananthakrishnan Srinivasan at the Department of Physics, Indian Institute of Technology Guwahati. This work has not been submitted elsewhere for the award of any degree.

Dolly Taparia

20 July 2021

(Dolly Taparia)
Roll No: 156121031
Department of Physics
Indian Institute of Technology Guwahati
Guwahati – 781039
India.

Certificate

It is certified that the work contained in this thesis, entitled "Large linear sensitivity of CoFe based CIP-GMR magnetic sensor using metastable bcc Cu spacer and auxiliary biquadratic coupling through Rh spacer" submitted by Dolly Taparia, a Ph.D. student of the Department of Physics, Indian Institute of Technology Guwahati for the award of the degree of Doctor of Philosophy, has been carried out under the supervision of Prof. Perumal Alagarsamy and Prof. Ananthakrishnan Srinivasan. This work has not been submitted elsewhere for the award of any degree.

20 July 2021

(Prof. Perumal Alagarsamy)
Department of Physics
Indian Institute of Technology Guwahati
Guwahati – 781039
India.

(Prof. Ananthakrishnan Srinivasan)
Department of Physics
Indian Institute of Technology Guwahati
Guwahati – 781039
India.

Dedicated to

my beloved Maa and Grandmaa

Acknowledgments

"*The road to success in life is never an individual battle but a collective effort*"- Abdulazeez Henry Musa. I have been extremely fortunate to be blessed with some fantastic people who were always ready to make that effort and drive my Ph.D. to its accomplishment. It has been a fabulous five and half years of rich experience, growth, and relationships, both professional and personal, in IIT Guwahati. Although all good things must come to an end, the journey I set out on here as a researcher will go on. It gives me immense pleasure to finally have the opportunity to express my gratitude towards the people who helped steer my research life to this critical milestone.

Firstly, I wish to convey my profound gratitude and respect to my thesis supervisors, Prof(s). Perumal Alagarsamy and Ananthakrishnan Srinivasan, Department of Physics, IIT Guwahati, providing me with the opportunity for my research under their valuable guidance. They have been a constant source of encouragement and inspiration throughout my research life here, helping me through any difficult times that I would ever come across. The fierce sincerity and devotion towards research and the humbleness and care in their nature have shaped my persona as a research scholar, which I would forever cherish. In addition, the knowledge gained from their valuable insights and the immeasurable depth of their experience in this field has created a firm backbone for my research career.

I would like to offer my sincere gratitude to my Doctoral committee members, Prof. S. Ravi, Dr. D. Pamu, and Prof. S. Senthilvelan, for their valuable suggestions/feedback to improve the quality of my thesis work. My profound gratefulness to the present Head of Department (HoD) of Physics, Prof. Perumal Alagarsamy, and former HoD(s), Prof. S. Ghosh and Prof. P. Poulose, for their extensive administrative cooperation. I'm thankful to all the faculty members and other non-teaching staff of the Physics department for their help and support throughout my Ph.D.

I am very much thankful to Dr. Y. Sakuraba, Mr. Kresna B. Fathoni, Dr. Prabhanjan D. Kulkarni, Dr. Varun Kushwaha, Dr. Mamoud Rasly, Dr. T. Sasaki, and Prof. K. Hono, National Institute for Materials Science, Japan, for their support and guidance during my internship work. I am thankful for the financial support received from NIMS, Japan, through the internship program.

I'm earnestly thankful to the Department of Physics, IIT Guwahati, for allowing me to pursue my dreams and providing a nurturing work environment where I could feel safe,

empowered, and learn the traits of professionalism. I convey my gratitude to Dr. S. Sarma, a scientific officer in the Department of Physics, for his guidance in operating various high-precision instruments. I am also grateful to Heads, scientific officers, and technical staff, Central Instruments Facility (CIF), IIT Guwahati for extending their expertise in using various sophisticated instruments during my Ph.D. tenure.

I am thankful to MHRD, Govt. of India, for the financial assistance during the Ph.D. work period. And the infrastructure facilities provided by DST, New Delhi [SR/S2/CMP-19/2006, SR/FST /PII-020/2009] and BRNS [37(3)/14/29/ 2015/BRNS]. The broader administration of IIT, Guwahati, also has a special token of my gratitude for providing a delightful campus that I could call home for a good five and half years of my life. The campus is a treat to the eyes and soul and provides everything that I would require to de-stress from a stressful day at work.

I would like to express my profound appreciation to my seniors Dr. A. Gayen, Dr. P. Ravikumar, Dr. T. R. Gopalarao, Dr. C. Das, and Dr. A. M. Padhan, for helping me in various ways throughout my research work. I would like to acknowledge my lab-mates, Ritupan, Subrata, Manisha, Nitu, Pushpesh, Pushpa, Alok, Didwmsha, Madhav, Dev, Aritra, Dinesh, and Harekrushna, for their support and creating a cordial environment in the lab. I would especially like to convey my heartiest gratitude to my friends Dr. Aakansha and Ankan for always standing by my side, listening to my problems, and cheering me up.

Finally, I would like to express my deep and sincere gratitude to my family for supporting me in all walks of my life and being the most excellent source of strength and motivation to keep chasing my dreams. I am forever indebted to my parents for their unconditional love and encouragement, which was fundamental in achieving whatever I have accomplished in life. Special thanks to Divya, Dipesh, and Arpita for being a fresh breeze of air in my life. I would like to convey my regards to my in-laws for being so supportive and caring. I would like to thank my husband, Mr. Aritra Roy, for being my backbone and trusting me when I doubted myself. His constant motivation and support helped me move forward with my spirits high. I would also like to acknowledge every person who has played a role in my journey, directly or otherwise, some of whom I may have inadvertently not acknowledged. Last but not least, I would like to express my gratitude and regards to the almighty God for blessing me with the strength and courage always to stay focused.

- Dolly Taparia

PREFACE

Magnetism is a fascinating subject inextricably linked with electricity. The rich diversity of magnetic phenomena has revolutionized the world with incredible technological advancements such as biomagnetic sensors, electric motors, hard disk drives, magnetic recording heads, magnetic random access memory, magnetic sensors, non-destructive materials testing, reconfigurable magnetic logic, *etc*. The discovery of giant magnetoresistance (GMR) in magnetic multilayers is a major successful step in the development of spintronics. Recent advances in magnetic sensors demand a linear and reversible magnetoresistance (MR) response to the applied magnetic field. This is achievable by utilizing a non-collinear arrangement of magnetization of adjacent ferromagnetic layers. Moreover, the two main factors required for obtaining a large MR ratio are perfect lattice and electronic band matching of the majority spin electrons between the ferromagnetic and nonmagnetic metal interfaces.

The advances in thin film technology facilitated the tailoring of the magnetic properties of $Co_{50}Fe_{50}$ binary alloys based on their crystal structure. This has promoted the research on linear sensors utilizing non-orthogonal magnetic configuration in the $Co_{50}Fe_{50}$ system owing to their thickness-dependent magnetic anisotropy. For instance, the magnetic spin valve-based linear and reversible MR sensors consisting of CoFe based ferromagnetic layers sandwiched by different spacer layers with face-centered-cubic (*fcc*) structure have yielded the highest sensitivity of ~ 0.0015 %/mT and 0.018 %/mT, respectively. Furthermore, a dramatic enhancement in the MR of the current in-plane (CIP)-GMR device, made of CoFe/ Cu/ CoFe trilayer up to 40.5 %, was achieved by introducing the metastable body-centered-cubic (*bcc*) Cu spacer layer. As the magnetic layers are deposited sequentially with a fine nonmagnetic spacer layer, magnetic interactions between the ferromagnetic layers are noticeably unavoidable. There are three major types of couplings, namely, 0º or ferromagnetic, 180º or antiferromagnetic, and 90º or biquadratic coupling, observed in layered magnetic systems. Among these, the biquadratic coupling is of particular interest as it results in the linear variation of resistance with the applied field. It is anticipated that integrating a *fcc* spacer layer, *e.g*., Rh along with Cu in the CoFe multilayer stacking, may result in a linear variation of the *R-H* curve along with a high MR ratio.

Considering all the above aspects, a detailed investigation of CoFe based CIP-GMR devices is presented in this thesis. This study includes (i) an investigation of the effect of Rh

spacer layer on the structural and magnetotransport properties of CoFe(3 nm)/ wedge-shaped Rh(t_{Rh} = 0 – 7.3 nm)/ CoFe(1.5 nm)/ MgO(2 nm) and CoFe(3 nm)/ wedge-shaped Rh(t_{Rh} = 0 – 2.5 nm)/ CoFe(1.5 nm)/ Cu(1.6 nm)/ CoFe(3 nm)/ MgO(2 nm) thin films, (ii) optimization of the Rh layer thickness in flat samples to obtain linear and reversible MR response, (iii) investigation of the effect of middle and top CoFe layers' thicknesses on the structural, magnetic and magnetotransport properties of CoFe(3 nm)/ Rh(0.84 nm)/ CoFe(1.5 nm)/ MgO(2 nm) and CoFe(3 nm)/ Rh(0.84 nm)/ CoFe(x = 1.0, 1.5, 2.0 nm)/ Cu(1.6 nm)/ CoFe(y = 0, 2, 3, 4 nm)/ MgO(2 nm) multilayer films, (iv) numerical simulation based analysis of the experimentally obtained *M-H* loops to understand the origin of linear *R-H* variation and (v) linear fitting of the experimentally obtained *R-H* curves to evaluate the sensing parameters of the linear magnetic field sensors. Accordingly, the present thesis is organized as follows:

- **Chapter 1** presents a brief introduction to the contents of the thesis along with a detailed literature review on relevant topics.
- **Chapter 2** covers the fundamental aspects and theoretical models related to the contents of the thesis, including the basics of thin film growth, magnetism, intrinsic properties of magnetic materials, magnetic anisotropy, magnetoresistance, interlayer coupling in multilayer films, structural and magnetic properties of Co_xFe_{1-x} alloys, and numerical simulation methods.
- In **Chapter 3**, a brief description of experimental methods and techniques used in this thesis is given. This comprises the fabrication of samples, patterning of the films into CIP-GMR devices, and characterization tools.
- **Chapter 4** discusses Rh spacer layer thickness-dependent structural and magnetotransport properties of CoFe(3 nm)/ wedge-shaped Rh(t_{Rh})/ CoFe(1.5 nm)/ MgO(2 nm) thin films over a wide range of Rh thickness from 0 to 7.3 nm at first and then optimizing the Rh thickness to obtain linear MR response. Numerical simulation analyses of the experimental *M-H* loops carried out to understand the origin of linear *R-H* variation in the optimized flat sample of CoFe(3 nm)/ Rh(0.84 nm)/ CoFe(1.5 nm)/ MgO(2 nm) are also presented here.
- **Chapter 5** focuses on enhancing the linear MR ratio in CIP-GMR magnetic sensors using Rh and metastable *bcc* Cu spacers. Studies on the influence of Rh spacer layer on the nature of MR curve of CIP-GMR films consisting of CoFe(3 nm)/ wedge-shaped Rh(t_{Rh} = 0 – 2.5 nm)/ CoFe(1.5 nm)/ Cu(1.6 nm)/ CoFe(3 nm)/ MgO(2 nm) are elaborated. This is followed by a description of numerical simulation analyses of the optimized flat sample of CoFe(3 nm)/ Rh(0.84 nm)/ CoFe(1.5 nm)/ Cu(1.6 nm)/

CoFe(3 nm)/ MgO(2 nm) thin films carried out to elucidate the origin of enhanced linear MR with the addition of Cu spacer.

- **Chapter 6** deals with a systematic investigation of the effect of top and middle CoFe layer thickness on the sensing characteristics of asymmetric structured fully epitaxial CIP-GMR-based linear magnetic sensors. Structural and magnetotransport properties of all the flat samples of CoFe(3 nm)/ Rh(0.84 nm)/ CoFe(x = 1.0, 1.5, 2.0 nm)/ Cu(1.6 nm)/ CoFe(y = 0, 2, 3, 4 nm)/ MgO(2 nm) thin films are presented in detail. Numerical simulation analyses carried out to correlate the origin of the linear MR response with the nature of magnetic interaction between CoFe layers are also described. CIP-GMR device with the structure of CoFe(3 nm)/ Rh(0.84 nm)/ CoFe(1.5 nm)/ Cu(1.6 nm)/ CoFe(3 nm)/ MgO(2 nm) exhibited the highest linear sensitivity of 0.047 %/mT due to a large MR ratio (21 %) and linear response through a biquadratic coupling and reduced nonlinearity of 0.98 % full scale along with a substantially wider operation field range of 220 mT.
- Conclusions drawn from the thesis work and a brief write-up about the future scope of research in these types of CIP-GMR devices are summarized in **Chapter 7**.
- References and a list of publications originating from this thesis work and other collaborative research works are listed at the end of the thesis.

CONTENTS

1.	Prologue		1
	1.1.	Introduction	2
	1.2.	Motivation behind the work	4
	1.3.	Objectives of the thesis work	8
2.	Fundamental aspects and theoretical models		9
	2.1.	Introduction to thin film technology	10
		2.1.1. A brief history	10
	2.2.	Thin film growth	10
		2.2.1. Nucleation and growth	10
	2.3.	Epitaxial thin films	11
	2.4.	Magnetic ordering	12
		2.4.1. Introduction	12
		2.4.2. Origin of magnetism	12
		2.4.3. Diamagnetism	13
		2.4.4. Paramagnetism	14
		2.4.5. Ferromagnetism	16
		2.4.6. Antiferromagnetism	18
	2.5.	Intrinsic properties of magnetic materials	19
		2.5.1. Exchange interaction	19
	2.6.	Anisotropy	22
		2.6.1. Magnetocrystalline anisotropy	24
		2.6.2. Shape anisotropy	26
		2.6.3. Induced anisotropy	28
		2.6.4. Magnetostrictive anisotropy	29
		2.6.5. Magnetic surface anisotropy	30
	2.7.	Magnetoresistance	31
		2.7.1. Ordinary magnetoresistance	31
		2.7.2. Anisotropic magnetoresistance	31
		2.7.3. Colossal magnetoresistance	32
		2.7.4. Giant magnetoresistance	32
		2.7.5. Tunnel magnetoresistance	35
	2.8.	Interlayer coupling in multilayer thin films	37

2.8.1. Exchange coupling 37
2.8.1.1. Direct exchange coupling 37
2.8.1.2. Indirect exchange coupling 38
2.8.2. Magnetostatic coupling 39
2.8.2.1. Topological coupling 39
2.8.2.2. Stray field coupling 39
2.8.2.3 Domain wall stray field coupling 40
2.8.3. Phenomenological description of interlayer exchange coupling 41
2.9. Structural and magnetic properties of Co_xFe_{100-x} alloys 43
2.10. Numerical simulation methods 45
2.10.1. Trilayer structure 45
2.10.2. Multilayer structure 47
2.10.3. Limitations of the model 48
3. Experimental methods 51
3.1. Introduction 52
3.2. Techniques used for sample preparation 52
3.2.1. Sputtering technique 52
3.2.1.1. DC sputtering technique 54
3.2.1.2. RF sputtering technique 54
3.2.1.3. Magnetron sputtering technique 56
3.2.1.4. Ultra-high vacuum thin film deposition system 58
3.2.2. Calibration of deposition rate 60
3.3. Physical etching technique 61
3.3.1. Photolithography 61
3.4. Structural property characterization 66
3.4.1. X-ray diffraction 66
3.4.2. Transmission electron microscope 67
3.5. Magnetic property characterization 72
3.5.1. Vibrating sample magnetometer 72
3.5.2. Superconducting quantum interference device magnetometer 73
3.6. Magnetotransport property characterization 75
3.6.1. DC four-probe setup 75
3.6.2. Physical property measurement system 76
3.6.2.1. Magnetic measurements 76

3.6.2.2. Magnetotransport measurements 77
3.6.3. Versa lab setup 78
4. Linear magnetoresistance in CIP-GMR magnetic sensor using Rh spacer 81
4.1. Introduction 82
4.2. Experimental details 83
4.3. Numerical simulation methods for trilayer structure 84
4.4. Results and discussion 87
4.4.1. Properties of CoFe(3 nm)/ wedge-shaped Rh(t_{Rh} = 0 – 7.3 nm)/ CoFe(1.5 nm) films 87
4.4.1.1. Structural properties 87
4.4.1.2. Rh thickness dependent magnetotransport properties 87
4.4.2. Properties of flat CoFe(3 nm)/ Rh(0.84 nm)/ CoFe(1.5 nm)/ MgO(2 nm) trilayer film 90
4.4.2.1. Structural properties 90
4.4.2.2. Magnetic and magnetotransport properties: Experiment and numerical simulations 92
4.4.2.3. Sensing properties as a magnetic field sensor 95
4.5. Summary 96
5. Enhancing linear magnetoresistance in CIP-GMR device with metastable bcc-Cu spacer and auxiliary biquadratic coupling through Rh spacer 99
5.1. Introduction 100
5.2. Experimental details 101
5.3. Numerical simulation methods for multilayer structure 102
5.4. Results and discussion 104
5.4.1. Properties of CoFe(3 nm)/ wedge-shaped Rh(t_{Rh} = 0 - 2.5 nm)/ CoFe (1.5 nm)/ Cu(1.6 nm)/ CoFe(3 nm)/ MgO(2 nm) films 104
5.4.1.1. Rh thickness-dependent magnetotransport properties 104
5.4.2. Properties of flat CoFe(3 nm)/ Rh(0.84 nm)/ CoFe(1.5 nm)/ Cu(1.6 nm)/ CoFe(3 nm)/ MgO(2 nm) film 107
5.4.2.1. Structural properties 107
5.4.2.2. Magnetic and magnetotransport properties: Experiment and numerical simulations 109
5.4.2.3. Sensing properties as a magnetic field sensor 114
5.5. Summary 116

6.	Effect of CoFe layer thickness on the sensing characteristics of asymmetric structured fully epitaxial CIP-GMR based linear magnetic sensors		119
	6.1.	Introduction	120
	6.2.	Experimental details	121
	6.3.	Numerical simulation methods for multilayer structure	122
	6.4.	Results and discussion	122
		6.4.1. Properties of flat CoFe(3 nm)/ Rh(0.84 nm)/ CoFe(x = 1.0, 1.5, 2.0 nm)/ Cu(1.6 nm)/ CoFe(y = 0, 2, 3, 4 nm)/ MgO(2 nm) multilayer films	122
		6.4.1.1. Structural properties	122
		6.4.1.2. Magnetic and magnetotransport properties: Experiment and numerical simulations	125
		6.4.1.3. Sensing properties as a magnetic field sensor	130
	6.5.	Summary	133
7.	Summary and scope for future work		135
	7.1.	Summary of the results	136
	7.2.	Scope for future work	139
References			141
Publications			153

Chapter 1

Prologue

1.1. Introduction

"Miniaturization" presumably embodies the revolution spawned by powerful and efficient electronics that were faster and elegantly smaller than their contemporaries. The trend is fueled by extensive research in optimizing materials that can further miniaturize the size and, at the same time, have a wide range of tunable properties. In traditional semiconductor electronics, only the charge degree of electrons is utilized. However, in spintronics, the short form for **spin tr**ansport electr**onics** or **spin** elec**tronics**, *a.k.a.*, magnetoelectronics, the intrinsic spin of the charge carriers is exploited, adding the property of spin to conventional charge based electronics. The discoveries of tunnel magnetoresistance (TMR) in 1975 and giant magnetoresistance (GMR) in 1988 are considered as the beginning of a new era of spin-based electronics [BAIB1988, BINA1989, JULL1975]. The magnetoresistance (MR) effect is observed in the magnetic multilayers thin films composed of alternate ferromagnetic (FM) and nonmagnetic (NM) layers [BENN1994, DECH2012, HADJ2013, HART2000, MELE2015, MORA2013, NALW2002, WEIS2013, WOLF2001]. These artificially structured multilayer thin films can be engineered to offer multipurpose magnetic, electrical, and optical properties, as demonstrated in Figure 1.01. Spintronics phenomena flourish in the overlapping regions, for instance, spin-dependent conduction, such as GMR and TMR effects [ANDO2015].

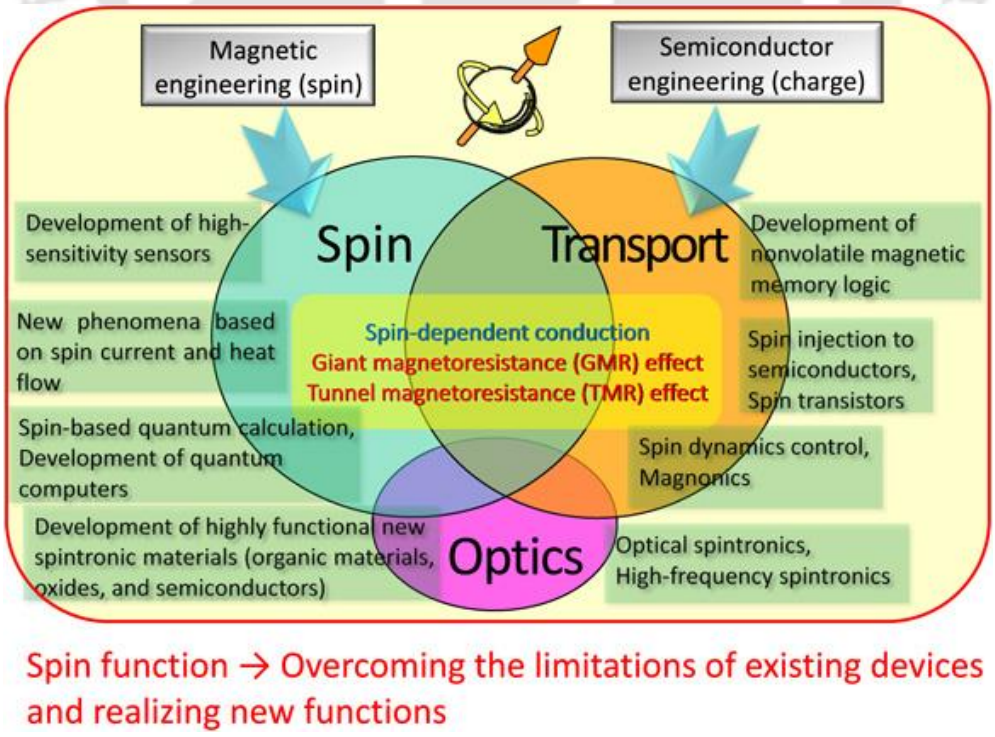

Figure 1.01: Conceptual design of spintronics [ANDO2015].

Since the discovery of the GMR effect in multilayer thin films, the underlying physics and interlayer exchange coupling (IEC) between the FM layers are broadly understood, expanding the spectrum of their successful application in hard disks, magnetic random access memory (MRAM), magnetic field sensors, lab-on-chip, reconfigurable magnetic logic, non-destructive materials testing, *etc*. [DIEN2016, HEDI2013, HIRO2013, IANN2014, KURI2017, LEON2014, MALL2012, PIRA2007, PIRA2011, TANG2010, TSYM2001, WANG2017, WOLF2001]. Another significant achievement is implementing GMR/TMR-based devices in the read-heads with perpendicular recording, increasing the storage density steeply [FREI2016, HIRO2015, SATO2015, TSYM2016, VILL2010, YOUC2017, ZHOU2017]. The recent breakthrough in the field of spin filter magnetic tunnel junctions (sf-MTJ) using bilayer and four-layer CrI_3 antiferromagnet and achievement of 530 % and 19,000 % sf-TMR, respectively, has left the world bewildered. Although the results are obtained at 2 K, the sf-MTJ is a promising candidate for magnetic memory and processing applications [SONG2018].

Driven by technological applications, further development of spintronic devices demands the FM layer to satisfy the following properties: (i) low Gilbert damping constant, $\alpha < 0.001$ (for free layers), (ii) high perpendicular anisotropy (PMA), $K_U > 1$ MJ/m^3, although reducing α while maintaining high K_U is still an immense challenge, (iii) large spin polarization, $P \sim 100\%$ at room temperature, (iv) back end of the line (BEOL) compatibility, demanding low annealing temperature, $T_A < 550$ K to promote interfacial smoothness and atomic ordering, and, (v) small stray field, $H_{SF} \sim 0$ to reduce cross-talk, in turn, minimizing noise in the system [VEDM2020]. The strong influence of interfaces, proximity effects, significant spin-orbit effect inducing out-of-plane anisotropy, and influencing magnetic damping in the system define the physics for novel material development to achieve improved prediction capabilities. Therefore, the controlled growth and tailorable properties of magnetic multilayer films have become a very active field of research for the realization of futuristic magnetic devices.

Recently, the technical committee of the IEEE magnetics society has selected seven research topics: 1) hard disk drives, 2) magnetic random access memories, 3) domain-wall devices, 4) permanent magnets, 5) sensors and actuators, 6) magnetic materials, and 7) organic devices to develop their roadmaps, where major developments should be listed alongside expected timelines [HIRO2015]. Among these, the technological progress of MR

sensors has opened up a variety of sensor applications, products, and services. These application-based areas require MR sensors with diverse properties.

For instance, (a) high sensitivity and easy detectability for biomedical applications, (b) high mechanical flexibility and maximum compactness for flexible electronics, (c) the low power consumption and small physical dimension for position sensing (PS) and human-computer interaction (HCI), and (d) low cost and mass manufacturability for largescale non-destructive evaluation and monitoring (NDEM) systems, with high accuracy and stability for navigation and transportation systems. Hence, the widespread utilization of MR sensors tends to become the backbone for enriching and upgrading the context of intelligent living, such as smart homes, smart healthcare, smart grid, and smart transportation, as illustrated in Figure 1.02 [ZHEN2019].

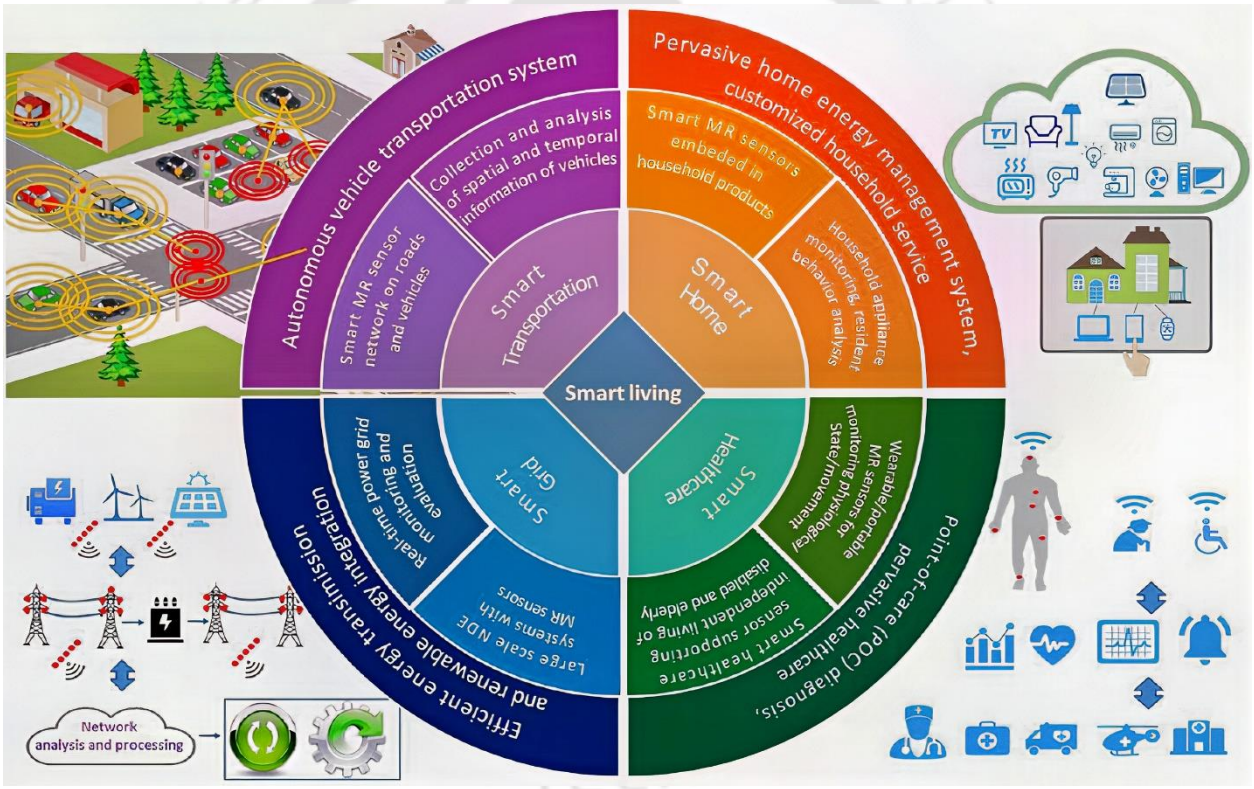

Figure 1.02: Contribution and impact of MR sensor technology in the concept of intelligent living, including smart home, smart healthcare, smart grid, and smart transportation [ZHEN2019].

1.2. Motivation behind the work

In recent years, the study of thin films, interfaces, and interactions in layered magnetic thin films has become one of the most active research areas from both fundamental and applied

research points of view. The phenomenon of the IEC determines the relative orientations of the magnetization in alternate FM layers at equilibrium, giving rise to spin torque, GMR, and TMR effects. Hence, extensive investigations have been performed theoretically and experimentally on the spacer layer and FM layer thickness and temperature dependence of the IEC coupling strength. Mott *et al.* [MOTT1936, MOTT1964] proposed the initial idea of spin-dependent scattering of electrons in a ferromagnetic material, *i.e.*, the electrons with different spins experience different resistivities for the same applied voltage. Later, the discovery of GMR by Peter Grünberg and Albert Fert [NOBE2007] led to enhanced interest in understanding the IEC mechanism in a variety of magnetic multilayers such as Fe/Cr [BAIB1988, PARK1990, BART1990, FERT1992, SCHA1994, SCHA1995, SHIR1987], Fe/Cu [FERT1992, OLIV1999, PETR1991], Fe/Mo [BRUB1991], Fe/Al [FUSS1992, BRAJ2010], Fe/Au [FUSS1992], Fe/Ta [NAOE1996], Fe/Zr [CAST1997], Co/Ru [BLOE19941, PARK1990, OUNA1992], Co/Cr [PARK1990], Co/Cu [FERT1992, PARK19911, PARK19912], Co/Ag [ARAK1993], Ni/Cu [SHIR1987], CoFe/Cu [INOM1993], Fe/ Cr/ Fe(100) [IVES1994, GRUN1986, UNGU1991], Fe/ Cu/ Fe [BENN1990], full body-centered-cubic (*bcc*) Fe/ Cu/ Fe(001) [HEIN1990], Fe/ Au/ Fe [GRUN1986], Fe/ Mo/ Fe [QIU1993], Fe/ Mn/ Fe [PURC1992], Co/ Cu/ Co [BLOE19942, STIL2002, QIU1993], Co/ Cu/ Co(111) [IVES1994], CoFe(*bcc*)/ Mn(body-centered-tetragonal, *bct*)/ CoFe(*bcc*) [FILI1995], CoFe/ Ir/ CoFe [COLI2001], full *bcc* $Co_{50}Fe_{50}$/ Cu/ $Co_{50}Fe_{50}$ [FATH2019], $[Ni_{81}Fe_{19}/Cu]_n$ [PARK1992], *etc.* A detailed literature survey reveals that in a typical GMR device, the FM layer comprises at least one of the 3*d* transition elements, *i.e.*, Fe, Co, Ni and/or their alloys. The NM metal-is selected mainly from the group consisting of Al, Ag, Au, Cr, Cu, Ir, Mo, Mn, Rh, Ru, Ta, and Zr. So far, three major types of couplings, namely, 0º or FM, 180º or antiferromagnetic (AFM), and 90º or biquadratic coupling, have been observed in FM/NM multilayer stacking. GMR devices demonstrating 0º or 180º coupling have been widely studied and find applications in read-heads of hard disk drives, non-volatile memory such as MRAM, magnetic memory chips, *etc*. The highest reported values of the MR ratio are 220 % (42 %) for Fe/Cr [SCHA1994, SCHA1995] and 115 % (65 %) for Co/Cu [PARK19912] multilayers at 4.2 K (300 K). Despite obtaining such high values of MR ratio at room temperature, the nonlinear variation of the resistance with respect to the applied field (*R-H* curve) limits their application as futuristic magnetic field sensors.

The nature of the *R-H* curve is mainly determined by three types of magnetic interactions: IEC, exchange bias, and induced magnetocrystalline anisotropy. For most current sensor applications, the *R-H* curve exhibits a rapid increase in the MR ratio and hysteresis in MR curves. However, for the advancements in sensor technology, the linear and reversible MR response with respect to the applied magnetic field is crucial. This can be achieved when one of the FM layers has a uniaxial anisotropy with the easy axis of magnetization perpendicular to the magnetization of the other FM layer [RIJK1994]. This arrangement of crossed magnetization results in a coherent rotation of the sensing layer, leading to a linear and reversible variation of the *R-H* curve. Such non-collinear arrangement of the magnetization vectors of the adjacent FM layers can be accomplished by utilizing (i) annealing one of the FM layers in the presence of a magnetic field applied orthogonal to the easy axis of the other FM layer, (ii) employing PMA material as one of the FM layers [COLI2001, DIJK2005, LIU2016, MANC2000, NAKA2017, TAGA2000, YILD20092, YILD20093], and (iii) inducing 90º or biquadratic coupling between the adjacent FM layers [BARN1993, CHAP1999, ERIC1993, RUHR1991, SLON1991, VAVA2001].

The performance of a GMR device is governed by the interplay between materials properties, *i.e.*, perfect lattice and electronic band matching at the FM/NM metal interface. Lattice mismatch results in misfit dislocations and other structural defects, leading to roughness and intermixing near the interfaces. These defects give rise to spin-independent scattering in the NM spacer layer, reducing the MR ratio. Similarly, electronic band matching for one spin direction implies higher transmission for that spin, enhancing the MR ratio [ERLE2001, TODO1996, TSYM2001]. In an endeavor to fulfill these conditions using the same material for all the FM layers appeared fairly self-evident, and in fact, it has been backed by many similar studies. One such system for the FM layer is the alloy of Co and Fe. The magnetic anisotropy in Co_xFe_{100-x} films is strongly dependent on the film thickness and composition. A detailed literature survey from both theoretical and experimental points of view reveals that for $Co_{50}Fe_{50}$ films grown on Rh(001) substrate, the magnetic anisotropy changes from out-of-plane to in-plane as thickness increases above 1.5 nm [ANDE2006, ANDE2010, BRUK2004, HYOD2015, KOTA2012, KOTA2013, LUO2007, MAND2018, OOMI2015, SHIK2009, TURE2012, WINK2006, YILD20092]. This promoted research in linear sensors employing the thickness dependence of non-orthogonal magnetic configuration in the CoFe system. For instance, Colis *et al.* [COLI2001] in CoFe(t = 1.5 and 3 nm)/ Ir(0.5 nm)/ CoFe(3 nm) and Dijken *et al.* [DIJK2005] in CoFe(t = 0.7 – 2.5 nm)/

Cu(2.9 nm)/ CoFe(2.5 nm)/ Ru(0.7 nm)/ CoFe(2 nm) reported on magnetic spin valve consisting of CoFe (FM) and different spacer layers made of face-centered-cubic (*fcc*) for obtaining the linear and reversible MR sensors. They achieved rationally the highest sensitivity of ~ 0.0015 %/mT and 0.018 %/mT, respectively. Recently, Fathoni *et al.* [FATH2019] reported a very high MR ratio of 40.5 % in current-in-plane (CIP)-GMR films consisting of antiferromagnetically coupled fully epitaxial all *bcc* $Co_{50}Fe_{50}$/ Cu/ $Co_{50}Fe_{50}$ trilayer at room temperature. The crystal structure and microstructure displayed nearly a perfect lattice matching and a large spin-asymmetry of the interfacial electronic band matching at *bcc* $Co_{50}Fe_{50}$ and the metastable *bcc*-Cu spacer. Such an arrangement provided a giant MR ratio. However, such CIP-GMR devices did not exhibit linear MR responses, limiting their application in advanced magnetic field sensors. It may be noted that the fabrication of multilayer films with more number of layers not only increases the interfaces but also complicates the magnetic coupling between the FM layers [PARK2008, NAVA2014]. This motivated us to integrate another spacer layer regulating the IEC between CoFe layers such that linear MR with a high MR ratio is obtained while still maintaining a simple multilayer structure. Accordingly, the objectives of the thesis are defined as follows:

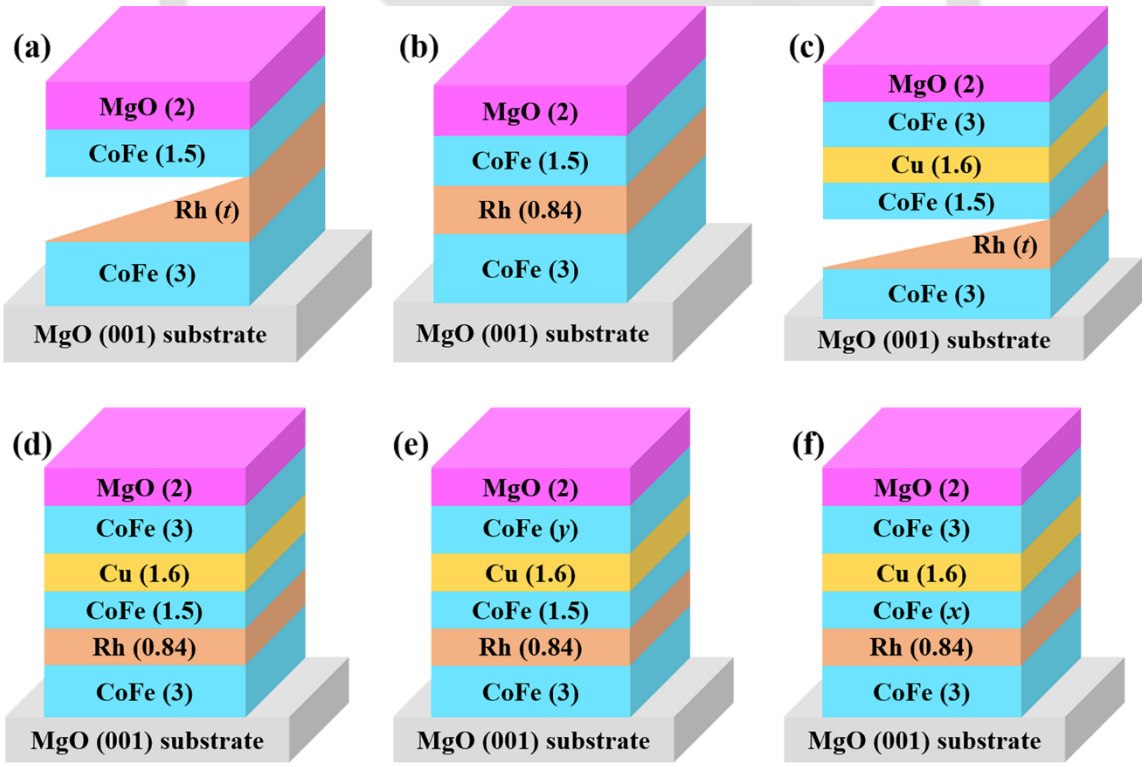

Figure 1.03: Schematic drawing of the film stack investigated in the current study. All values given in the parenthesis are on the nanometer scale.

1.3. Objectives of the thesis work

- To prepare CIP-GMR devices consisting of CoFe(3 nm)/ wedge-shaped Rh(t_{Rh} = 0 – 7.3 nm)/ CoFe(1.5 nm)/ MgO(2 nm) thin films [*c.f.* Figure 1.03(a)] on single-crystal MgO(001) substrate using an ultra-high vacuum (UHV) compatible magnetron sputtering system at ambient temperature and to understand the effect of Rh spacer thickness on the structural, magnetic and magnetotransport properties.
- To prepare a flat sample of CoFe(3 nm)/ Rh(t_{Rh} nm)/ CoFe(1.5 nm)/ MgO(2 nm) thin films [*c.f.* Figure 1.03(b)] on MgO(001) substrate and to optimize the Rh thickness (t_{Rh} = 0.84 nm) for studing the structural, magnetotransport and obtaining the linear MR response and sensing properties.
- To integrate Cu spacer with another CoFe FM layer in the existing stack structure and prepare CIP-GMR devices consisting of CoFe(3 nm)/ wedge-shaped Rh(t_{Rh} = 0 – 2.5 nm)/ CoFe(1.5 nm)/ Cu(1.6 nm)/ CoFe(3 nm)/ MgO(2 nm) thin films [*c.f.* Figure 1.03(c)] deposited on MgO(001) substrate at ambient temperature to understand Rh thickness dependence of magnetotransport properties, the MR ratio and sensitivity.
- To prepare flat sample of CoFe(3 nm)/ Rh(0.84 nm)/ CoFe(1.5 nm)/ Cu(1.6 nm)/ CoFe(3 nm)/ MgO(2 nm) thin films [*c.f.* Figure 1.03(d)] on MgO(001) substrate and to study the structural, magnetotransport and sensing properties.
- To prepare CIP-GMR devices consisting of flat CoFe(3 nm)/ Rh(0.84 nm)/ CoFe(x = 1.0, 1.5, 2.0 nm)/ Cu(1.6 nm)/ CoFe(y = 0, 2, 3, 4 nm)/ MgO(2 nm) thin films [*c.f.* Figure 1.03(e,f)] on MgO(001) substrate and to study the effect of top and middle CoFe layer thickness on the structural, magnetotransport and sensing properties.
- To perform numerical simulation analysis of the experimentally obtained *M-H* loop and investigate the IEC parameters to obtain a linear MR response in (i) CoFe(3 nm)/ Rh(0.84 nm)/ CoFe(1.5 nm)/ MgO(2 nm) and (ii) CoFe(3 nm)/ Rh(0.84 nm)/ CoFe(x = 1.0, 1.5, 2.0 nm)/ Cu(1.6 nm)/ CoFe(y = 0, 2, 3, 4 nm)/ MgO(2 nm).
- To correlate the origin of the linear MR response with respect to the nature of magnetic interaction between CoFe layers and tune the sensing parameters.

Chapter 2

Fundamental aspects and theoretical models

2.1. Introduction to thin film technology

2.1.1. A brief history

Thin film technology is concurrently one of the oldest arts and one of the newest sciences. Dating back to the metal ages of antiquity, thin films have a documented history of more than 5000 years [MILT2002]. The evolution of the modern art of thin film making started with the advances in vacuum technologies in the 1600s and dc power supplies in the 1700s [GREE2017]. The technology of thin film primarily developed for the silicon integrated circuit industry is now unrivaled for applications in the field of solar cells, spintronics, microelectronics, protective coatings, optoelectronics, *etc.* [CHOP1985, SESH2002, THIR2017].

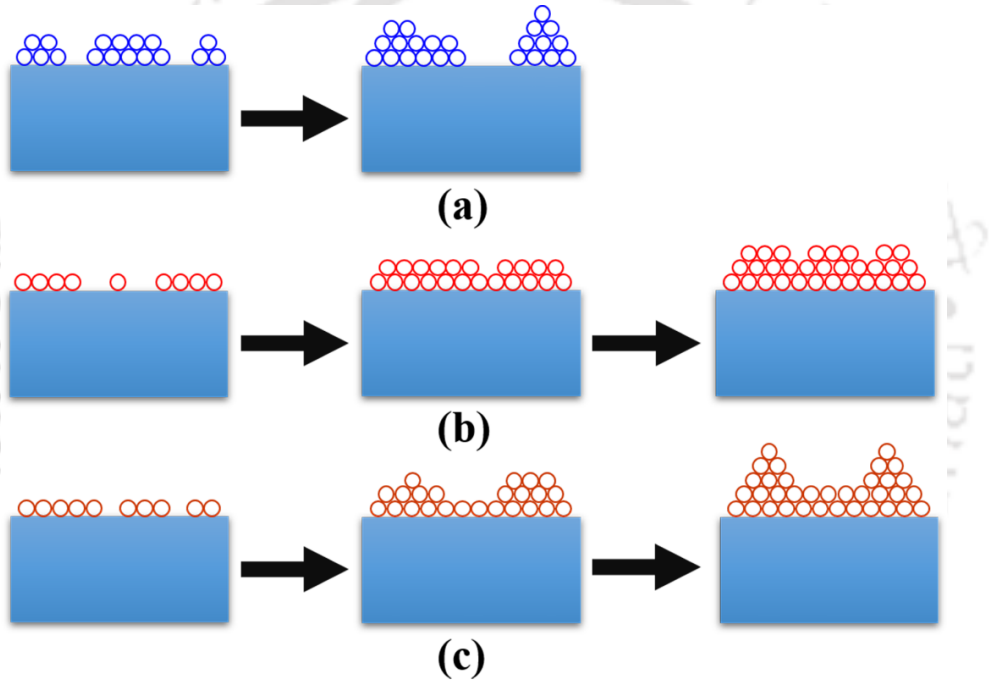

Figure 2.01: Basic thin film growth models: (a) Vollmer - Weber mode or 3D - island growth mechanism, (b) Frank - van der Merve mode or 2D - layer by layer growth mechanism, and (c) Stranski - Krastanov growth mode [MILT2002].

2.2. Thin film growth

2.2.1. Nucleation and growth

Thin films exhibit various properties that can be tuned based on the bonding of neighboring atoms, particle size, defects, crystallographic orientation, and composition. The ability to manipulate these atomic arrangements to harvest the desired features is of fundamental importance.

Three main growth models describing film growth are [MILT2002]:

(a). Vollmer - Weber mode or 3D - island growth mechanism

Three-dimension (3D) island growth occurs when clusters of atoms nucleate on the substrate and start growing in 3D to form islands. As demonstrated in Figure 2.01(a), this 3D growth happens when atoms or molecules to be deposited have more affinity to bind with each other than to the surface of the substrate.

(b). Frank - van der Merve mode or 2D - layer by layer growth mechanism

Two-dimension (2D) layer by layer growth shows exactly the opposite features of the 3D - island growth mechanism. In this case, the stable nucleates on the substrate extend themselves in 2D to create the first monolayer on which the second monolayer is formed. Only after the growth of the current layer is completed, the next layer follows. Here, the atoms or molecules are more bound to the substrate than one another, as shown in Figure 2.01(b). One of the most critical examples is the single-crystal epitaxial growth of thin films.

(c). Stranski - Krastanov growth mode

Stranski - Krastanov growth mode, also known as layer plus island growth mechanism, is quite a common growth mode observed in day-to-day thin film making. As the name suggests, this mode is a combination of the earlier two growth mechanisms, where the film growth starts as 2D - layer growth, forming a few monolayers, and the system becomes energetically unfavorable and continues with 3D - island growth, as displayed in Figure 2.01(c).

2.3. Epitaxial thin films

Epitaxial thin film growth is defined as a highly controllable method by which a deposited film is assembled into a well-defined crystal orientation of the substrate that it is deposited on with atomic-scale precision. Epitaxy arises when the system tends to minimize its interfacial energy to align the lattice of the deposited film with respect to the substrate. The inherent merits of epitaxial thin films to integrate with significant scientific and technological advances make them suitable candidates for next-generation solid state devices. There are mainly two types of epitaxy: (i) homoepitaxy, where the film and substrate are composed of the same material (*e.g.*, Si on Si), and (ii) heteroepitaxy, where the epitaxially deposited film

is of a different material than its substrate (*e.g.*, AlAs on GaAs). In the case of homoepitaxy, there is generally no strain at the interface because of the perfectly matched lattice parameters of the film and the substrate. However, in the case of heteroepitaxy, there is a mismatch of lattice parameters. Besides, the strain is introduced at the interface depending on the degree of the mismatch. If the lattice mismatch is considerably smaller, the interface is almost identical to the homoepitaxial interface [MILT2002].

2.4. Magnetic ordering

2.4.1. Introduction

The history of magnetism dates back to discovering the first-ever magnetic material called magnetite (Fe_3O_4). As a child, we all have played with magnets and been left bewildered by the mysterious, attractive, and repulsive forces between them. The mystery of magnetic compass needles aligning with Earth's north geographic pole has constantly prompted humankind to understand the underlying physics. It is well-known that most of the contemporary technological devices such as magnetic recording heads, hard disk drives, sensors, electric motors, *etc.*, have their roots in magnetism and magnetic materials. This triggered extensive fundamental research for the development of new magnetic materials having diverse applications. The tailoring of magnetic properties by tuning their composition, layer thickness, and layer structure is essential in achieving novel properties to cater to upcoming technological advances. This section provides insight into the origin of magnetism, which includes basics on magnetism, intrinsic properties of the magnetic materials, different types of magnetic anisotropy, various magnetoresistance, and interlayer coupling in multilayer film structures.

2.4.2. Origin of magnetism

The macroscopic magnetic properties of the materials are the consequence of magnetic moments associated with individual electrons in an atom [KITT2004, OHAN2000]. Magnetism in any material arises from its atomic structure. The net magnetic moment is the sum of two contributions: (a) orbital motion of the electron around the nucleus that generates a small magnetic field, which has a magnetic moment along the axis of rotation [see Figure 2.02(a)] and (b) spin of the electron that generates magnetic moment aligned along the spin axis either up or down determined by the direction of rotation [see Figure 2.02(b)]. This implies that each electron could be thought of as a small magnet having permanent orbital

and spin magnetic moments in an atom. Furthermore, the electrons in an atom occupy the energy states according to Pauli's exclusion principle and Hund's rule. As a result, the net magnetic moment of an atom is the addition of the individual magnetic moments of each electron in the atom, including both orbital and spin contributions. This accounts for the moment cancellation in wholly filled orbitals.

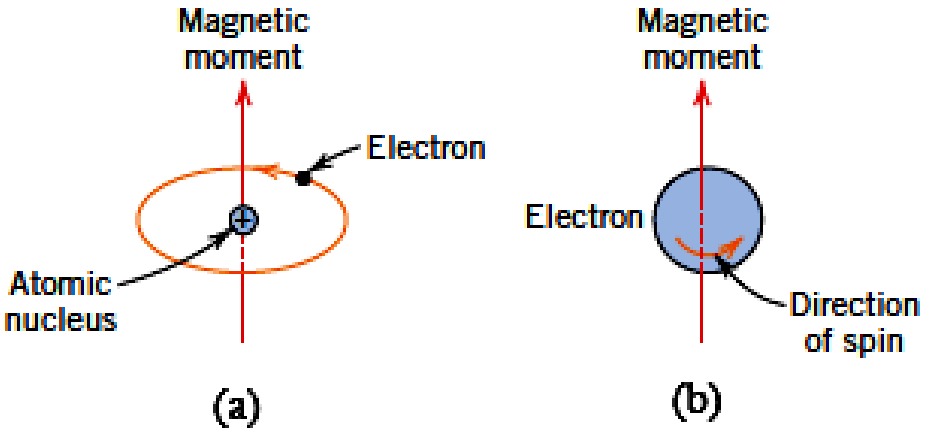

Figure 2.02: Schematic representation of (a) orbital magnetic moment and (b) spin magnetic moment.

For an atom having completely filled orbitals, when all the electrons are taken into account, the total cancellation of both moments occurs. Hence, materials having completely filled orbitals cannot be magnetized permanently. The net magnetic moment will depend on the number of unpaired electrons in an atom, their orientation in the orbitals, and the spin-orbit interaction between the electron orbital angular momentum and spin angular momentum. By taking the response of magnetic materials in the externally applied field condition, they are broadly classified as diamagnetic, paramagnetic, ferromagnetic, antiferromagnetic, and ferrimagnetic [KRON2003].

2.4.3. Diamagnetism

Diamagnetism is one of the inherent properties of all magnetic materials. It is the manifestation of Lenz's law, *i.e.*, if one applies a magnetic field to a system of moving charges, their motions change in such a way that they create a magnetization opposing the original applied magnetic field [OHAN2000]. This effect is observed in all materials but is often concealed by other types of magnetism and hence is observable only those materials which have wholly filled electronic configuration. The atoms and molecules of diamagnetic

substances do not have any net magnetic moment (*i.e.*, all orbital shells are filled, leaving no unpaired electron). However, when a magnetic field is exposed, the electrons orient themselves to oppose the applied magnetic field, and thus they register negative magnetization and negative susceptibility. Most of the semiconductor materials like ZnO, MgO, SnO_2, *etc*., are diamagnetic by nature.

2.4.4. Paramagnetism

Every atom possesses a permanent dipole moment in certain solids because of incomplete cancellation of electron spin and/or orbital magnetic moments. These atomic magnetic moments are randomly oriented in the absence of an external magnetic field, causing no net macroscopic magnetization. However, these atomic dipoles have rotational degrees of freedom, and paramagnetism occurs when they align by rotation with an external magnetic field [KITT2004]. Some of the atoms or ions in this category of materials have a net magnetic moment due to unpaired electrons in the partially filled orbital. However, the distinct magnetic moments are magnetically non-interactive. In the presence of a magnetic field, there is a partial alignment of the magnetic dipoles along the applied field direction, resulting in a net positive magnetization and positive susceptibility. Both paramagnetic and diamagnetic materials are at large considered to be nonmagnetic since they show magnetization only when an external magnetic field is applied. The tendency to align the magnetic moments along the applied field direction is opposed by the thermal energy fluctuations, which try to randomize the spin orientation. Hence, they exhibit temperature (T) dependent susceptibility, χ_{para}, known as the Curie Law,

$$\chi_{para} = \frac{C}{T} \tag{2.01}$$

where C is the Curie constant and T is the absolute temperature in Kelvin [BLUN2003]. In classical theory, each of the atomic moment is considered as magnetic dipoles aligned in a particular direction, making an angle θ with respect to the applied field direction and the average magnetic moment along the field direction, z is expressed as

$$< \mu^z > = \mu L(y) \tag{2.02}$$

where μ is the magnetic moment of each dipole, and $L(y)$ is the Langevin function, $L(y) = Coth(y) - 1/y$, where $y = B\mu/(k_B T)$. This Langevin function represents the magnetization of small particles made up of atomic clusters. In the case of low applied fields or at higher temperatures, y is small. As a result, $L(y)$ tends to $y/3$. So,

$$< \mu^z > = \frac{\mu y}{3} = \frac{\mu^2 B}{3k_B T} \tag{2.03}$$

Or, the magnetization

$$M = N < \mu^z > = \frac{N\mu^2 B}{3k_B T} \tag{2.04}$$

So, the susceptibility

$$\chi_{para} = \frac{M}{H} = \frac{\mu^2 N \mu_0}{3k_B T} = \frac{C}{T} \tag{2.05}$$

where B is the magnetic field, k_B is the Boltzman constant, μ_0 is the permeability of free space, and N is the no. of dipole moment. The above expression is the well-known Curie law, as formulated by the classical theory. Built on the quantum mechanical treatment together with the quantization of total angular momentum for each atom, the average magnetic moment per atom along the direction of the applied field (*i.e.*, z-direction) in any paramagnetic sample can be defined as [BLUN2003, GUIM1998, JILE1997].

$$< \mu_J{}^z > = g\mu_B J B_J(x) \tag{2.06}$$

Here, g is the Landé g-factor that depends on the spin-orbit coupling of each electron in an atom, J is the total angular momentum quantum number, μ_B is the Bohr magneton having the value of 9.27×10^{-24} J/T, and $B_J(x)$ is Brillouin function, expressed as,

$$B_J(x) = \frac{1}{J}\left[\left(J+\frac{1}{2}\right) Coth\left(J+\frac{1}{2}\right)x - \frac{1}{2} Coth\frac{x}{2}\right] \tag{2.07}$$

Here, $x = g\mu_B B/(k_B T)$, where k_B is Boltzmann constant and T is temperature. If N is the number of atoms per unit volume, the volume magnetization, M can be defined as,

$$M = N < \mu_J{}^z > = Ng\mu_B J B_J(x) \tag{2.08}$$

For the selection of the magnetic field B and temperature T such that x is small, $B_J(x) \sim [J(J+1)/3]x$. This assumption holds true for paramagnetic samples over a wide temperature region and at the low applied field. Therefore,

$$< \mu^z > = Ng\mu_B J \frac{(J+1)}{3} x = \frac{Ng^2\mu_B^2 B}{3k_B T} J(J+1) \tag{2.09}$$

Or the susceptibility,

$$\chi_{para} = \frac{\mu_0 N g^2 \mu_B^2}{3k_B T} J(J+1) \tag{2.10}$$

which is in the form of Curie law, C/T. Thus, the magnetic susceptibility built on Brillouin function expression reduces to Curie-law. Examples of paramagnetic materials include W, Ce, Al, Li, Mg, *etc.* with typical χ_{para} values of 6.8×10^{-5}, 5.1×10^{-5}, 2.2×10^{-5}, 1.4×10^{-5} and 1.2×10^{-5}, respectively in SI units [BLUN2003].

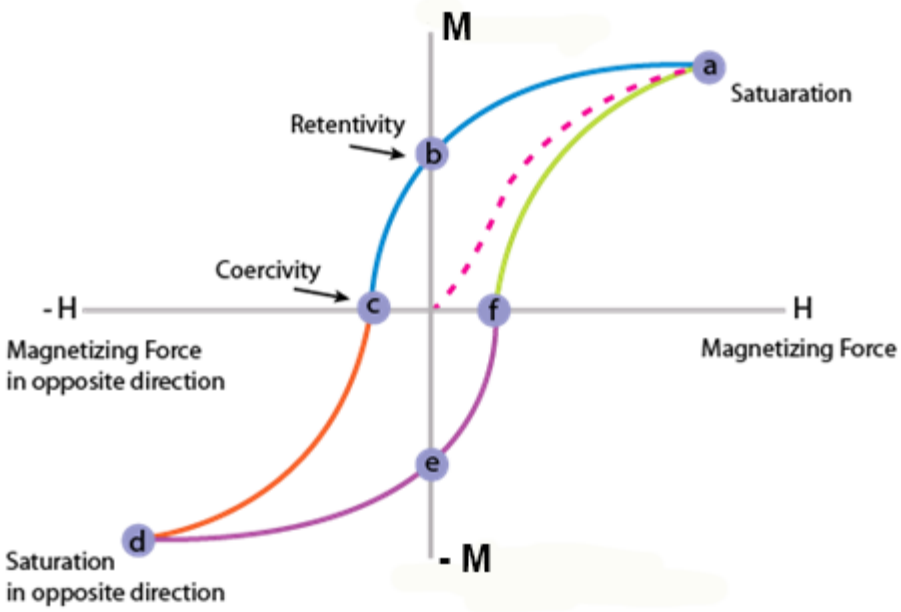

Figure 2.03: Magnetic hysteresis loop of a ferromagnetic material [PERU20131].

2.4.5. Ferromagnetism

Some materials acquire a permanent magnetic moment due to the strong interaction between the magnetic moments of their atoms, even in the absence of an applied magnetic field. This dominates over the thermal energy fluctuations and locks the alignment of magnetic moments in a particular direction. Such behavior is displayed by transition metals Co, Fe, Ni, and some rare earth metals like Gd. Ferromagnetic materials show two distinct properties: (1) spontaneous magnetization and (2) the presence of magnetic ordering temperature. Spontaneous magnetization is the net magnetization occurring inside a uniformly magnetized microscopic volume even without an external magnetic field. The magnitude of this magnetization at a particular temperature depends upon the spin magnetic moments of electrons. In ferromagnetic materials, the atomic moments either align in a parallel or an antiparallel arrangement, revealing robust interactions fashioned by the electronic exchange forces. Consequently, a considerable net magnetization even after removing the external applied magnetic field exists in the ferromagnetic material.

All ferromagnetic materials exhibit a magnetic hysteresis loop (*M-H* loop) in the presence of an applied magnetic field, as demonstrated in Figure 2.03. By studying the hysteresis loop, we can obtain complete information about the magnetic properties of the ferromagnetic material. The loop is generated by quantifying the magnetization of a ferromagnetic material while the magnetizing field is altered continuously. Initially, the ferromagnetic material is in a virgin state 'o', and the magnetic domains are oriented randomly to produce zero magnetization. The ferromagnetic materials follow the dashed line starting from the origin 'o'. As the external field increases and reaches the point 'a', almost all magnetic domains align with the field direction. Further increase in the magnetizing field generates a very little or no more increase in the magnetization. The magnetization value at this point is termed saturation magnetization (M_S). When the magnetizing field is reduced to zero, the curve doesn't trace the path to 'o'; instead goes from point 'a' to 'b'. As a result, certain magnetic flux remains in the material even at zero external fields. This is known as retentivity and denotes the remanence or level of residual magnetization in the ferromagnetic material. On reversing the magnetic field, the curve goes to point 'c', where the magnetization value truly reaches zero. This point is known as coercivity (H_C) or coercive force. Upon further increasing the external field in the negative direction, materials again saturate magnetically, but here the moments align in the opposite direction (point 'd'). On further reducing the field to zero, the curve moves to point 'e'. At this point, the value of residual magnetism is almost equal to that achieved in the positive direction (point 'b'). Now, increasing the field again in the positive direction, the magnetization returns to zero. Consequently, the magnetic curve takes a different path from the point 'f' back to the saturation point 'a', where it completes the loop. The following magnetic parameters can be obtained from the *M-H* loop: (i) Retentivity: the ability of a material to retain some amount of magnetization when the applied field is removed after attaining saturation, (ii) Coercivity: the magnitude of the negative magnetic field needed to make the magnetization zero; (iii) Permeability: the property of the material that expresses the ease with which a magnetic flux is established in the component. These magnetic parameters are inherent properties and depend on several parameters: the grain size, internal stresses, domain state, and temperature. The dependence of magnetic parameters on the grain size makes them useful for magnetic grain sizing of the natural samples. The elements Fe, Co, and Ni and their alloys are typical examples of ferromagnetic materials. Ferromagnetic materials are broadly classified into two categories: (a) soft ferromagnetic materials exhibiting low H_C (< 100 Oe), which are

generally used for the read head, transformer core, magnetic sensor applications, *etc.* and (b) hard ferromagnetic materials with high H_C (> 1000 Oe) are mostly used as permanent magnets, media for data storage, *etc*. With the increase in temperature, ferromagnetic material displays a transition from ferromagnetic state to paramagnetic state at a temperature called the Curie temperature (T_C), where the thermal energy ultimately overcomes the exchange energy, leading to paramagnetism by randomizing the electronic spins.

The phenomenon of ferromagnetism can be described by the Mean-field or Molecular field model. The molecular field model assumes that all the interactions from the neighboring magnetic moments could be expressed in terms of an effective internal field or molecular field B_m, which is proportional to the magnetization, $B_m = \lambda M$, here λ is the Weiss molecular field constant. Hence, the total magnetic field experienced by each of the dipoles is the addition of external magnetic field B and molecular field B_m. Thus, the expression for magnetization, as stated in Eqn. (2.08) may be modified as

$$M = \frac{Ng^2\mu_B^2 J(J+1)}{3k_B T}(B_a + \lambda M) \qquad (2.11)$$

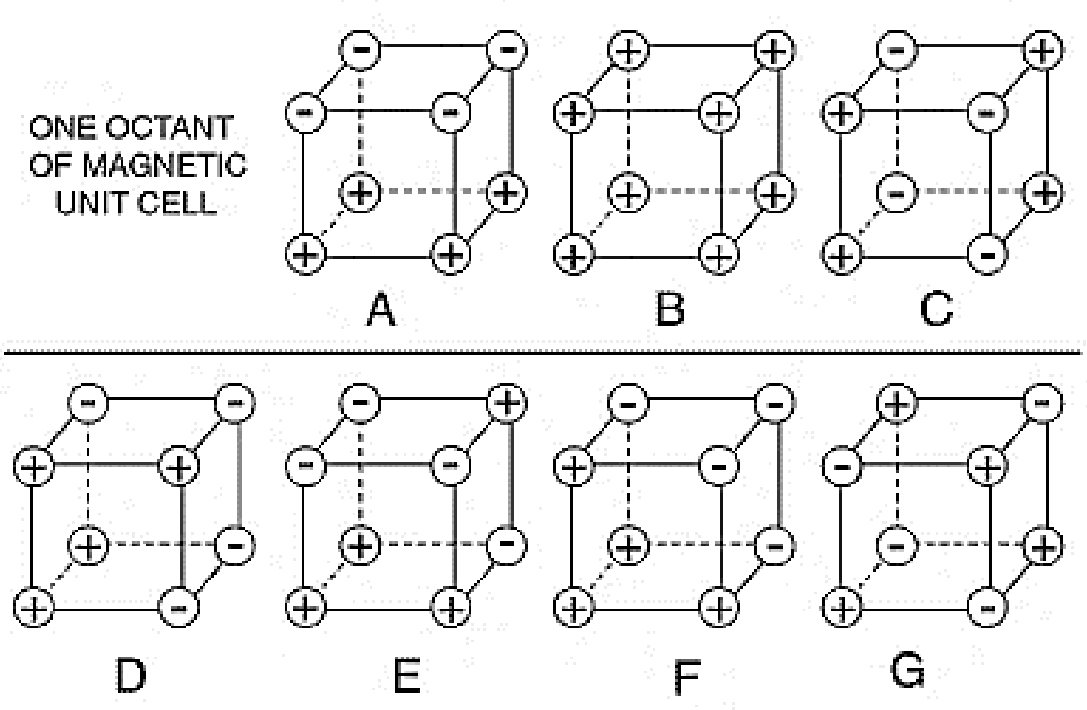

Figure 2.04: Different types of antiferromagnetic arrangement in a unit cell.

2.4.6. Antiferromagnetism

In some materials, the spins of electrons are aligned in a regular pattern with neighboring spins pointing in the opposite directions, below a definite temperature, known as the Néel

temperature (T_N). The substance is antiferromagnetic below T_N and paramagnetic above T_N because of the randomization of magnetic moments. T_N generally lies well below room temperature. Hence, it is necessary to carry out the magnetic susceptibility measurements at low temperatures to realize if the given material is paramagnetic at room temperature and indeed antiferromagnetic at lower temperatures.

The antiferromagnetic ordering in a given material is possible depending on its preferred magnetic unit cell structure, as displayed in Figure 2.04, except for the *B* type, which is ordered ferromagnetically. In the *A*-type structure, magnetic ions are ferromagnetically coupled in each (001) plane, but the alternate planes being aligned in an opposite spin orientation fashion resulting in a net antiferromagnetic interaction. However, the *B*-type structure is ferromagnetic in nature, where all the six nearest neighbor magnetic ions are coupled ferromagnetically. In the case of *C*-type structure, atoms in the (101) and (110) planes are aligned ferromagnetically, with each atom having two ferromagnetic and four antiferromagnetic nearest neighbors resulting in the net antiferromagnetic unit cell. In a *G*-type structure, each ion is antiferromagnetically coupled to all the six nearest neighbors. Some materials tend to follow a structure resulting from the coupling of two types of magnetic structures. The examples of antiferromagnetic materials are MnO, MnF_2, CoO, FeO, Cr_2O_3, α-Fe_2O_3, NiO with T_N of 116 K, 67 K, 292 K, 116 K, 307 K, 950 K, and 525 K, respectively [BLUN2003].

2.5. Intrinsic properties of magnetic materials

The intrinsic properties of ferromagnetic materials are saturation magnetization (M_S), Curie temperature (T_C), and magnetocrystalline anisotropy (MCA). These properties are responsible for the equilibrium characteristics of the material on the atomic scale.

2.5.1. Exchange interaction

In 1907, Weiss reported that in addition to any externally applied magnetic field *H*, there is an internal molecular field or exchange field in a ferromagnetic material proportional to its magnetization, *i.e.*,

$$\overrightarrow{B_E} = \lambda \vec{M} \tag{2.12}$$

where the constant λ is independent of temperature. According to Eqn. (2.12), each spin experiences the average magnetization of all the other spins. This molecular field is not actually a magnetic field and hence does not enter into the Maxwell equations. For instance,

the current density $\vec{j}$ related to $\overrightarrow{B_E}$ by $\vec{\nabla} \times \vec{H} = 4\pi\vec{j}/c$ is zero. The magnitude of this molecular field could be as high as 10^3 Tesla. Now the question is, what is the precise origin of such an enormous internal molecular field? For example, consider the value of the magnetic field at a distance *r* due to a magnetic dipole having dipole moment *m*. It is [KITT2004],

$$\overrightarrow{B_{dip}} = \left(\frac{\mu_0 M}{4\pi r^3}\right)[2cos\theta\overrightarrow{e_r} + sin\theta\overrightarrow{e_\theta}] \tag{2.13}$$

The order of magnitude of the magnetic field, $B_{dip}\left(= \mu_0 H_{dip} = \mu_0 M/4\pi r^3\right)$. For m = 1 μ_B and r = 0.1 nm, $B_{dip} \approx 1$ Tesla (=10 kG) only. This shows that the huge internal molecular field is not due to the magnetic dipole interaction. This mystery remained as a haunting topic until 1928, when the concept of exchange interaction was proposed by Heisenberg [HEIS1928]. The origin of the Heisenberg exchange interaction has its roots in electrostatics but fundamentally involves quantum mechanical explanations. The charge distribution of any system of two spins depends on whether the spins are aligned parallel or antiparallel. Pauli's exclusion principle discards the possibility of any two identical electrons occupying the same quantum state simultaneously. Nevertheless, it does not exclude the same criterion for electrons having an opposite spin. Thus, the electrostatic energy of a system is dependent on the relative orientation of the spins, where the difference in energies defines the exchange energy. The energy of interaction between the atoms *i* and *j* bearing electron spins S_i and S_j is defined from the Heisenberg model as [OHAN2000],

$$E_{exch} = -2\sum_{i<j} J_{ij} S_i . S_j \tag{2.14}$$

where J_{ij}'is the exchange integral and is associated with the overlap of the charge distribution of the atoms *i* and *j*. Expecting that the exchange interaction is the same for all nearest-neighbor pairs, eqn. (2.14) can be written as

$$E_{exch} = -2J\sum_{i<j}^{nn} S_i . S_j \tag{2.15}$$

J must be positive for the parallel alignment of spins (ferromagnet), and for the antiparallel orientation of magnetizations, *J* must be negative. The dependence of *J* on the ratio of inter-atomic distance to the radius of 3*d* orbital is expressed as the 'Bethe-Slater curve', which is illustrated in Figure 2.05. It is well understood from Figure 2.05 that the value of *J* and consequently the short-range exchange interaction depends largely on the inter-atomic distance.

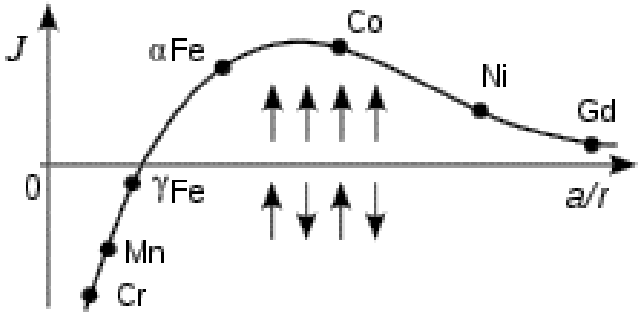

Figure 2.05: Bethe-slater curve: Elements above (below) the horizontal axis are ferromagnetic (antiferromagnetic).

Eqn. (2.15) can be further simplified by taking into account the energy of the i^{th} atom interacting with its j^{th} nearest neighbor, *i.e.*,

$$E_{exch}^{i} = -2JS_i \sum_j S_j \tag{2.16}$$

while for the whole material,

$$E_{exch} = -\frac{1}{2}\sum_j E_{exch}^{i} \tag{2.17}$$

Hence, the discrete pairwise interaction may be replaced by supposing that the magnetic moment $\mu_m^i = g\mu_B S_i$ at the i^{th} site interact with the molecular field. H_{eff} is then given by the net effect of z nearest-neighbor spins as

$$E_{exch}^{i} = -\mu_0 \mu_m^i H_{eff} = -g\mu_0\mu_B S_i H_{eff} \tag{2.18}$$

Here, g is the Landé g-factor, μ_0 is the permeability of free space (= $4\pi\times10^{-7}$ H/m) and μ_B is the Bohr magneton. As we compare eqn. (2.18) with eqn. (2.16), the effective field can be expressed as,

$$H_{eff} = \frac{2J}{g\mu_0\mu_B}\sum_j S_j \cong \frac{2zJ}{g\mu_0\mu_B}\langle S_j\rangle \tag{2.19}$$

Here, the sum over the z neighboring spins has been replaced by z times the value of the average spin $\langle S_j\rangle$. Using $M = N_v g\mu_B\langle S_j\rangle$, eqn. (2.19) becomes,

$$H_{eff} \cong \frac{2zJ}{N_v g^2 {\mu_B}^2 \mu_0} M \tag{2.20}$$

Eqn. (2.20) reveals that H_{eff} is the Weiss molecular field expressed as, $H_{mol} = \lambda M$ provided

$$\lambda = \frac{2zJ}{N_v g^2 {\mu_B}^2 \mu_0} \tag{2.21}$$

Taking the value of the molecular field coefficient λ as 10^3, J is estimated to be 2×10^{-21} J or 0.01 eV/atom. Exchange interactions are stronger than spin-orbit interactions but weaker than Coulomb interactions which distinguish levels of different principal and orbital quantum numbers. Following the treatment of Weiss molecular field where $T_C = \lambda C$ with $C = N_v {\mu_m}^2 \mu_0 / 3k_B$, the expression for T_C could be obtained from Eqn. (2.21) as

$$T_C = \frac{2zJ{\mu_m}^2}{g^2 {\mu_B}^2 3k_B} = \frac{2zJs(s+1)}{3k_B} \tag{2.22}$$

where $\mu_m = \sqrt{g\mu_B s(s+1)}$. Another key relation between exchange energy and magnetization is expressed as,

$$\frac{E_{exch}^{ij}}{V} = \frac{s^2 a^2 J N_v'}{2}\left(\frac{\nabla M}{M}\right)^2 = A\left(\frac{\nabla M}{M}\right)^2 \tag{2.23}$$

where a is the distance between the spins, A is the exchange stiffness constant with a value of 5×10^{-12} J/m to 30×10^{-12} J/m for most of the ferromagnets, and N_v is the number of nearest-neighboring atoms per unit volume. Hence, it is clear from the above equations that the exchange energy or the Heisenberg exchange interaction is strongly dependent on temperature because of the dependence of interatomic distance on temperature. Specifically, the disordered ferromagnetic system is the subject of low T_C value because of the low value of J.

2.6. Anisotropy

When a physical property relies on the direction in a given material, the material is said to exhibit anisotropy. In magnetism, the tendency of magnetization orientations in a particular direction of materials is known as magnetic anisotropy. As magnetic anisotropy has a substantial contribution in determining the nature of the *M-H* loop, it is essential to understand the possible sources of its origin and its influence on the magnetic properties. The anisotropy in a material can be intrinsic owing to its crystal chemistry or shape or induced by using a suitable processing technique. Figure 2.06 demonstrates a typical situation where the magnetization points along the easy axis (α = 0) under no external magnetic field. When an external field is applied, the magnetization is pulled towards the field's direction and inclines closer to the field direction with increasing magnitude of the external field. For any

intermediate values of α, the magnetization gets pulled along two opposite directions, *i.e.*, upward by the field and downward by the anisotropy.

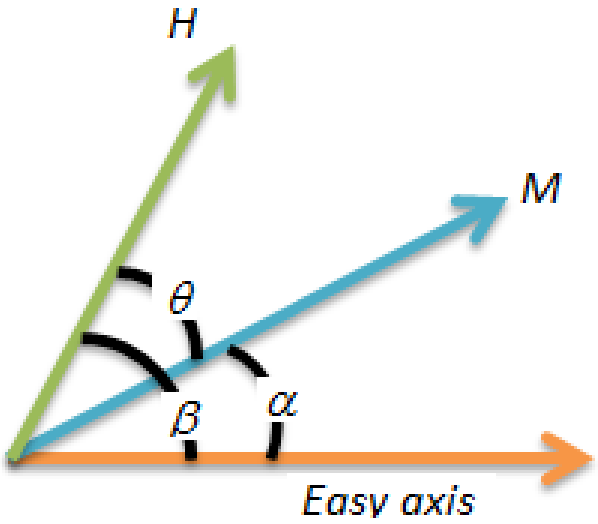

Figure 2.06: Schematic diagram of magnetization, external field, and easy axis for a given material [PERU20131].

Let us assume that all the magnetization is pointing in the same direction in a given magnetic material. This confirms that the material exhibits an easy magnetization direction. In such a situation, the energy per unit volume of the magnetization is given as,

$$E = K\ sin^2\alpha \tag{2.24}$$

where K is the anisotropy constant having unit of energy per unit volume (SI - J/m^3 or CGS - erg/cc). Generally, the magnitude of uniaxial magnetic anisotropy is expressed in terms of anisotropy field, which is described as the field necessary to saturate the magnetization of a uniaxial crystal along the hard axis direction, and defined as,

$$H_k = \frac{2K}{\mu_0 M} \tag{2.25}$$

In general, the energy of magnetization is expressed as,

$$E = K\ sin^2\alpha - \mu_0 MH\ cos(\beta - \alpha) \tag{2.26}$$

where the first term is the anisotropy energy, and the second term is because of the magnetic field. The difference in the angle (β - α) is the angle between H and M. To attain equilibrium, the first derivative of E should be zero, *i.e.*,

$$\frac{dE}{d\alpha} = 2K \sin\alpha \cos\alpha - \mu_0 MH \sin(\beta - \alpha) = 0 \qquad (2.27)$$

Assuming the value of β as 90° for equilibrium angle for the magnetization relative to the easy axis and considering Eqn. (2.25), we have

$$\sin\alpha = \frac{H}{H_k} \qquad (2.28)$$

The above equation indicates that if $H = 0$, the magnetization points in the easy axis direction, and when $H = H_K$, the magnetization points along the field direction. For intermediate values of the field, the magnetization points along a value of angle governed by Eqn. (2.28) rotating smoothly between the easy axis and the external field.

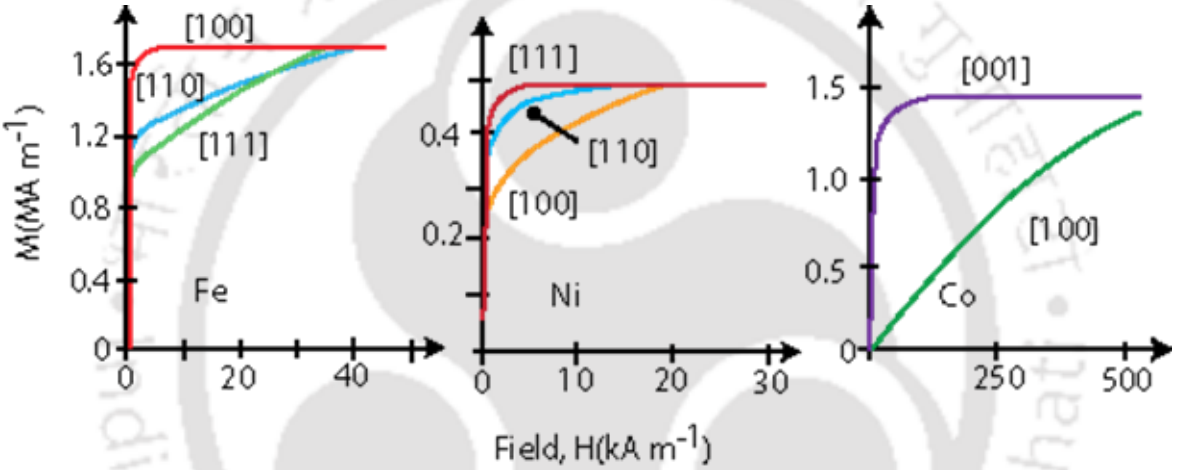

Figure 2.07: Magnetization of single crystals of Iron, Nickel and Cobalt [PERU20131].

2.6.1. Magnetocrystalline anisotropy

The tendency of the magnetization orienting along a preferred crystallographic axis is known as the magnetocrystalline anisotropy. This is an intrinsic property of a magnetic material. The favored crystallographic direction is known as the 'easy axis' since it is easiest to magnetize a material to saturation if the external field is applied along this direction. On the other hand, the direction along which a much larger field is needed to attain saturation is called the 'hard axis'. Thus, the crystal is in a higher energy state when the magnetization direction points along the hard axis compared to the easy direction. The energy difference per unit volume between the material magnetized along the easy and hard axis is known as the magnetocrystalline anisotropy energy (MAE). It is calculated through the area between the easy and hard magnetization curves. The initial magnetization (*IM*) curves of single crystals of different 3*d* ferromagnetic materials are depicted in Figure 2.07. It can be noted that

materials approach saturation magnetization in different ways depending on the magnetization directions. For instance, Iron (Fe) with body-centered-cubic (*bcc*) crystal structure exhibits (100) as the easy direction and (111) as the hard axis, whereas nickel having face-centered-cubic (*fcc*) crystal structure has (111) as the easy direction and (100) as the hard axis. This behavior can be well understood by examining the development of anisotropy energy in different symmetries as explained below,

For hexagonal:

$$E_a = K_1 \sin^2\theta + K_2 \sin^4\theta + K_3 \sin^6\theta + K_3' \sin^6\theta \sin 6\phi \tag{2.29}$$

For tetragonal:

$$E_a = K_1 \sin^2\theta + K_2 \sin^4\theta + K_2' \sin^4\theta \cos 4\phi + K_3 \sin^6\theta + K_3' \sin^6\theta \sin 6\phi \tag{2.30}$$

For cubic:

$$E_a = K_{1c}(\alpha_1^2\alpha_2^2 + \alpha_2^2\alpha_3^2 + \alpha_3^2\alpha_1^2) + K_{2c}(\alpha_1^2\alpha_2^2\alpha_3^2) \tag{2.31}$$

where α_i are the direction cosines of the magnetization and K_{1c} is equivalent to $K_{1c}(\sin^2\theta\, cos^2\,\phi \sin^2\phi + \cos^2\theta \sin^2\theta)$. When, $\theta = 0$, $\phi = 0$, the K_{1c} term reduces to Eqn. (2.24) [COEY2010].

Origin of magnetocrystalline anisotropy: There are two different sources of magnetocrystalline anisotropy: (i) single-ion contributions and (ii) two-ion contributions. The single-ion contribution is because of the electrostatic interaction of the orbitals having the magnetic electrons with the potential being created at the atomic site by the rest of the crystal. The crystal field interaction stabilizes a specific orbital, and then by spin-orbit interaction, the magnetic moment gets oriented along a particular crystallographic direction. For example, a uniaxial crystal with 2×10^{28} ions/m^3 expressed by a spin Hamiltonian DS^2 where $D/k_B = 1$ K and $S = 2$ will have the anisotropy constant as $K_1 = nDS^2 = 1.1\times10^6$ J/m^3. Single-ion contribution is one of the major anisotropic components in hard magnetic materials, which have the tendency for the magnetization to orient along a specific crystallographic direction turns the magnetic susceptibility into a tensor rather than a scalar quantity. On the other hand, the two-ion contribution imitates the anisotropy of the dipole-dipole interaction.

Figure 2.08: Schematic drawing of broadside and head-to-tail configurations for a pair of ferromagnetically coupled magnetic moments [PERU20131].

Considering the broadside and head-to-tail configurations of the two dipoles, each with moment m, as depicted in Figure 2.08, the energy of the head-to-tail configuration is smaller by $3\mu_0 m^2/(4\pi r^3)$. This makes the magnets to tend to orient head-to-tail. In non-cubic lattices, the dipole interaction is the primary source of ferromagnetic anisotropy.

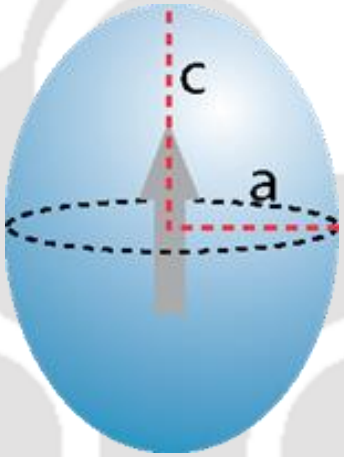

Figure 2.09: Magnetization of a prolate ellipsoid of revolution with $c > a$ and no magnetocrystalline anisotropy. c-axis is the easy direction of magnetization [PERU20131].

2.6.2. Shape anisotropy

Although most magnetic materials exhibit magnetocrystalline anisotropy, a polycrystalline sample with no favored orientation of its grains doesn't possess an overall crystalline anisotropy. Nevertheless, if the sample is completely spherical, then the same field is needed to magnetize the material in every direction. On the other hand, if it is non-spherical, it is easier to magnetize it along a relatively longer axis. This phenomenon due to asymmetric shapes is known as shape anisotropy [SPAL2010]. Shape anisotropy is of crucial importance in thin films where one of the dimensions is very short compared to other dimensions. The demagnetization field within the material or the stray field outside the material is dependent on the magnetization and shape of the material [BLUN2003, JILE1997, OHAN2000]. The

magnetostatic energy of a ferromagnetic ellipsoid (Figure 2.09) with magnetization M_S is stated as

$$E_m = \frac{1}{2}\mu_0 V N M_S^2 \tag{2.32}$$

The shape anisotropy energy is related to the difference in energy ΔE when the ellipsoid is magnetized along its hard and easy axis. N is the demagnetization factor tensor along the easy direction. $N' = (1/2)\,(1 - N)$ is the demagnetization factor tensor along the hard directions. Thus,

$$\Delta E_m = \frac{1}{2}\mu_0 V M_S^2 \left[\frac{1}{2}(1-N) - N\right]$$

$$\Delta E_m = \frac{1}{4}\mu_0 V M_S^2 [1 - 3N]$$

$$K_{sh} = \frac{1}{4}\mu_0 M_S^2 [1 - 3N] \tag{2.33}$$

Furthermore, the demagnetization factor tensor relating the demagnetization field with the material magnetization as a function of the position is expressed by [NEAL1994],

$$N(r) = -\frac{1}{4\pi}\iiint d^3r' \nabla' \left(\nabla' \left(\frac{1}{r - r'}\right)\right) \tag{2.34}$$

Table 2.01: Demagnetization factors (in Gaussian units) of selected shapes.

Shape	N_1	N_2	N_3
*Sphere	4π/3	4π/3	4π/3
Long Cylinder along the z-axis	2π	2π	0
Infinite plate normal to the *z*-axis	0	0	4π
Strip film normal to the *z*-axis (with t – thickness, W – Width, L – Length; $t \le W \le L$)	0	$8t/W$	4π

*The shape anisotropy is zero for a sphere since N = 1/3. Shape anisotropy is fully effective in materials that are so small that they do not break up into domains [COEY2010].

This tensor is given by the integral over the object volume and is evaluated either inside or exterior to the body. The value of tensor N depends mostly on the specimen shape, which is difficult to obtain in closed-form and can only be calculated for an ellipsoidal shape

precisely. In many symmetrical materials, for example, any ellipsoids of revolution, there are only three principal components of the demagnetization factor tensor, *i.e.*,

$$\begin{pmatrix} H_1 \\ H_2 \\ H_3 \end{pmatrix} = -\begin{pmatrix} N_1 & 0 & 0 \\ 0 & N_2 & 0 \\ 0 & 0 & N_3 \end{pmatrix}\begin{pmatrix} M_1 \\ M_2 \\ M_3 \end{pmatrix} \tag{2.35}$$

where $N_1 + N_2 + N_3 = 1$ (in SI) or $N_1 + N_2 + N_3 = 4\pi$ (Gaussian). The demagnetization factors for the selected shapes are summarized in Table 2.01. A complete calculation of the demagnetization factor for various objects can be found in [NEAL1994].

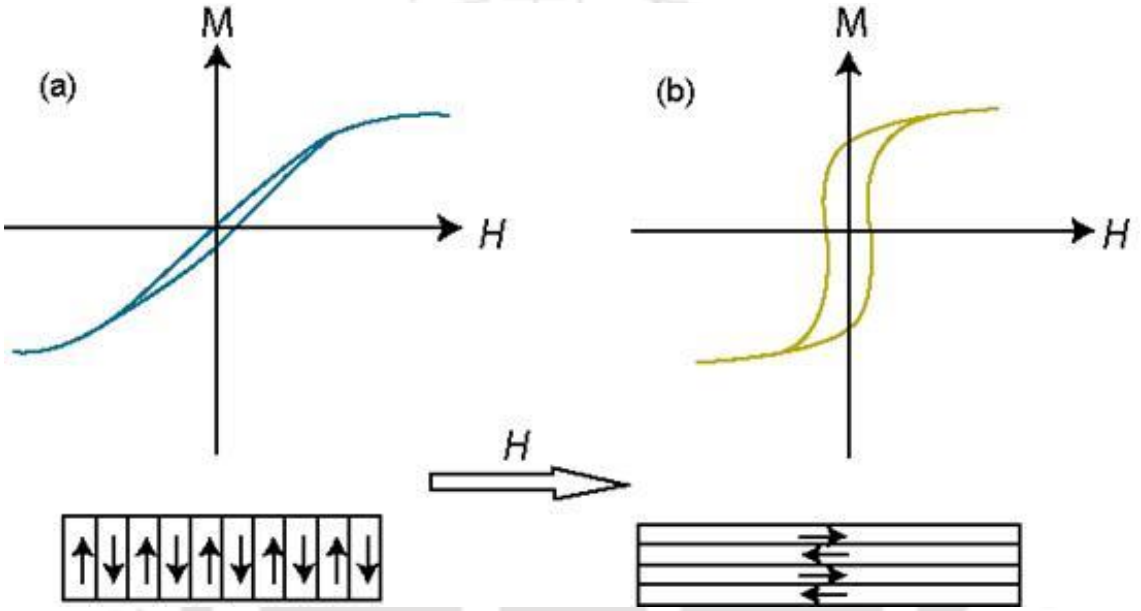

Figure 2.10: Magnetization of a thin film with induced anisotropy created by annealing in a magnetic field. The sheared (open) loop and the corresponding schematic representation of their magnetic domains in Fig. 2.10 a (b) is observed when the measuring field *H* is applied perpendicular (parallel) to the annealing field direction [PERU20131].

2.6.3. Induced anisotropy

For some magnetic materials, the magnetic anisotropy can be extrinsically induced in many ways, such as (i) fabricating a film in the presence of a magnetic field, (ii) post-annealing the film in an external magnetic field, and (iii) applying uniaxial stress. The presence of a magnetic field in the first two cases may align the easy axis of magnetization of the sample along the direction of the magnetic field. This induced anisotropy is independent of any crystalline anisotropy or any other type of anisotropy that might be present. Figure 2.10 depicts the typical example of inducing the anisotropy in ferromagnetic samples by annealing in the presence of an external field.

In the last case, the uniaxial anisotropy is induced by applying uniaxial stress (σ) inside a ferromagnetic solid [KRON2003]. The magnitude of this stress-induced anisotropy is

$$K_{u\sigma} = \frac{3}{2}\sigma\lambda_S \tag{2.36}$$

where λ_S is the saturation magnetostriction.

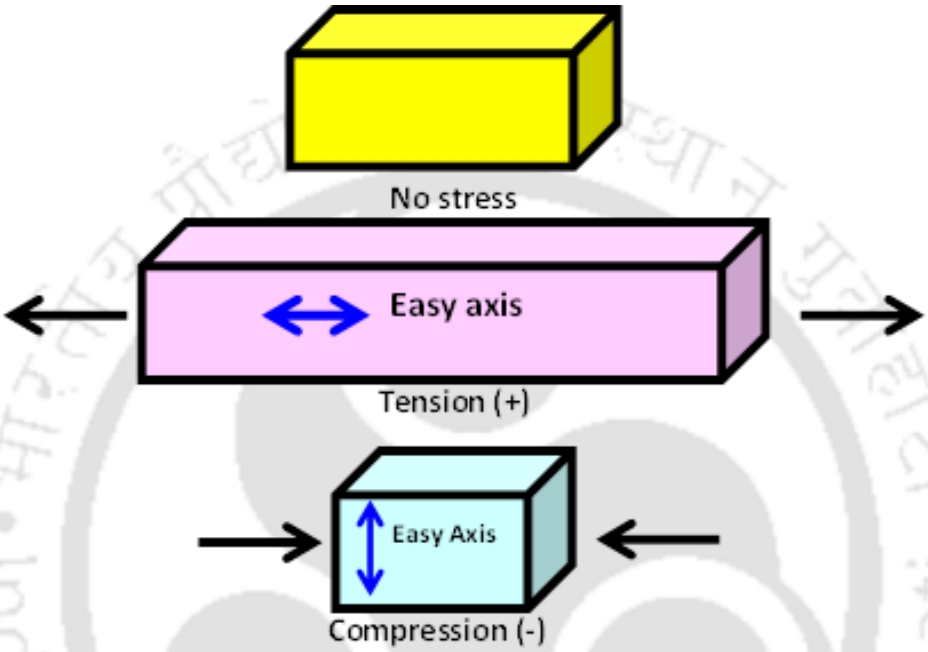

Figure 2.11: Schematic drawing of bars to demonstrate inducing an easy-axis in a material with the positive magnetostriction [PERU20131].

Both the single-ion and two-ion anisotropy contribute to stress-induced anisotropy. The highest values of uniaxial anisotropy are observed in hexagonal and other uniaxial crystals. On the contrary, the smallest values are found in cubic alloys and amorphous ferromagnetic materials.

2.6.4. Magnetostrictive anisotropy

Another crucial form of anisotropy in ferromagnetic materials is magnetostriction, a change in magnetization due to the lattice's mechanical strain, creating a unique easy axis of magnetization. Magnetostriction relates the stress in a magnetic material to an anisotropy resulting from that stress. Figure 2.11 displays schematic views of bars with different applied stress situations. If λ_S is positive in Eqn. (2.36), then applying tensile stress to the bar will

create an easy axis along the direction of the applied stress. However, if compressive stress is applied, the easy axis will be created perpendicular to the stress direction. On the other hand, if the λ_S for the material is negative, then the above phenomena will be reversed: tensile stress will create an easy axis perpendicular to the direction of the stress, and compressive stress will create an easy axis along the direction of the applied stress.

2.6.5. Magnetic surface anisotropy

The orientation of magnetic moments in ultrathin films significantly affects the magnetic properties and therefore attracts enormous interest in magnetic-based random access memory and recording industry since past decades [IKHT2018, PAND2016]. In ultrathin films, magnetic moments align along a perpendicular direction to the film plane up to a certain critical thickness as a result of the magnetic surface anisotropy, which has the following origins: (i) reduced symmetry at the interface due to the lack of neighboring atoms gives rise to magnetocrystalline surface anisotropy [NEEL1954], (ii) strain at the interface due to lattice mismatch between substrate and the film, and (iii) the interface roughness. The orientation of magnetization in ultrathin films is defined by the competition between shape (or dipolar anisotropy) and magnetic surface anisotropy, *i.e.*, when the thickness of the film is below its critical thickness, the surface anisotropy is dominant over the shape anisotropy. On the contrary, the shape anisotropy is dominant over the surface anisotropy above the critical thickness, providing an in-plane orientation of the magnetization [GARR2005, HIND2011, PESC1987, YILD20091, YILD20092]. Critical thickness and the easy axis of uniaxial surface anisotropy strongly depend on the type of substrates, deposition conditions, temperature, materials composition, and microstructure of the film [BRUN1989]. For instance, the magnetization of Ni(111) ultrathin films grown on Au/Ni/Au-(111) multilayers always lie within the film plane [BRUN1989]. On the contrary, the easy axis of magnetic surface anisotropy of *bcc*-Fe(100) deposited on Ag(100) is perpendicular to the film plane [HEIN1987, KOON1987]. Hexagonal-closed-packed (*hcp*) Co grown at room temperature on atomically flat polycrystalline Au(111) and capped by Au exhibits perpendicular magnetization for thicknesses less than 12 Å (6 ML) [CHAP1988]. Recently, CoFeB films are reported to show strong thickness dependent magnetic properties due to various anisotropic contributions, including surface and interfacial anisotropies [LIUT2012, NAIK2012].

2.7. Magnetoresistance

Magnetoresistance (MR) is defined as the property of a material to change the value of its electrical conductivity or electrical resistivity under the application of an external magnetic field. William Thomson, well-known as Lord Kelvin, first discovered this effect while examining the resistance of iron and nickel pieces in 1856 [THOM1857]. Depending on the MR effect observed in different materials, MR is mainly classified into (i) ordinary magnetoresistance (OMR), (ii) anisotropic magnetoresistance (AMR), (iii) colossal magnetoresistance (CMR), (iv) giant magnetoresistance (GMR), and (v) tunnel magnetoresistance (TMR).

2.7.1. Ordinary magnetoresistance

For a particle having charge q, moving with a velocity $\vec{v}$ under an applied field $\vec{B}$, the Lorentz force ($\vec{F}$) experienced can be expressed as

$$\vec{F} = q\left(\vec{E} + \frac{\vec{v}}{c} \times \vec{B}\right) \tag{2.37}$$

where $\vec{E}$ is the electric field and *c* is the speed of light in a vacuum. The Lorentz force is always directed perpendicular to the motion and deflects the path of the charged particle. This results in an increased path length, developing a change in the material resistivity. This is generally known as ordinary magnetoresistance (OMR). The OMR effect is directly proportional to the magnitude and is independent of the direction of the applied field. Unlike other types of MR effects, the OMR doesn't saturate even at the large applied magnetic field and is generally very small in metals (< 1% for an applied field of 1 T) and is demonstrated by all conducting materials (both magnetic and nonmagnetic) [TSYM2001, TUMA2001].

2.7.2. Anisotropic magnetoresistance

In some ferromagnetic materials, the measured magnetoresistance depends on the relative angle between the magnetization direction and the electric current direction. This phenomenon is known as anisotropic magnetoresistance (AMR). Its origin can be explained based on the spin-orbit interaction, which results in a lower probability of *s-d* scattering when electrons move perpendicular to the magnetization and a higher scattering probability when they move parallel to it. As a result, longitudinal resistivity is more significant than transverse resistivity. The highest reported value of AMR in ferromagnetic materials is of the order of

2-3%. Despite being low in magnitude, the AMR effect in 3*d* transition metals is several orders higher in magnitude than its OMR counterpart [BLUN2001, TUMA2001].

2.7.3. Colossal magnetoresistance

Colossal magnetoresistance (CMR) is the property of certain materials in which the change in electrical resistance with respect to the applied field is dependent on the presence of metal-insulator transition in the vicinity of the Curie temperature. Manganese perovskites are one of the most common oxide materials exhibiting CMR. Such materials show a huge magnetoresistive effect, which has been called CMR, to differentiate it from the GMR effect. However, since CMR results from metal-insulator transition near the material's Curie temperature and requires very high magnetic fields of several orders of Tesla, this limits the industrial applicability of CMR materials [BLUN2001].

2.7.4. Giant magnetoresistance

Giant magnetoresistance (GMR) is one of the fascinating advances in condensed matter physics that combines tremendous technological potential and profound fundamental physics. Since the discovery of GMR by Grünberg and Fert in 1988 [BAIB1988, BINA1989], commercial devices based on this phenomenon, such as hard-disk read-heads, magnetic memory chips, and magnetic field sensors, became available in the market. The MR effects discussed above are mainly bulk phenomena. On the other hand, GMR is achieved by stacking metallic multilayers consisting of alternate ferromagnetic layers separated by nonmagnetic spacer layers, as shown in Figure 2.12.

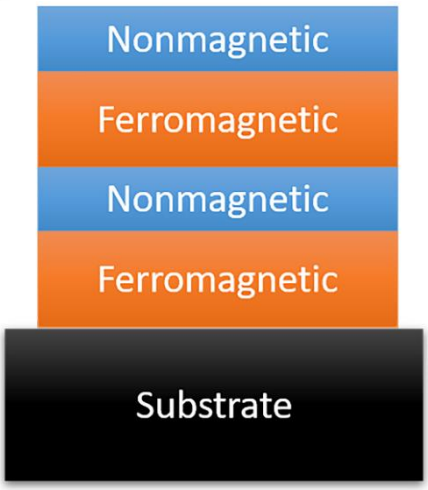

Figure 2.12: The schematic diagram of simple GMR multilayer film.

Hence, the discovery of GMR was, to a great extent, due to the substantial progress in thin-film deposition techniques. It was first observed in a Fe/Cr multilayer, which displayed a considerable reduction of the electrical resistance on the application of a magnetic field. This effect was found to be much greater than any other MR effect and hence called GMR.

In metallic multilayer films, the magnetization of the adjacent ferromagnetic layers separated by a nonmagnetic spacer layer spontaneously aligns either parallel or antiparallel, depending on the thickness of the space layer. The relative magnetization orientation in each ferromagnetic layer dramatically influences the electrical resistance. A parallel orientation (ferromagnetic coupling) showcases low electrical resistance, while an antiparallel orientation (antiferromagnetic coupling) is a state of high resistance. The fact that spacer layer thickness determines the original magnetization configuration, an initial antiparallel orientation can be realized, which is then forced into parallel orientation by an external field, thereby significantly reducing the electrical resistance of the system.

If the electrical resistance at zero fields is denoted by $R(0)$ and at the saturation magnetic field, H_S by $R(H_S)$, the GMR ratio can be expressed as

$$GMR\ ratio\ (\%) = \frac{R(0) - R(H_S)}{R(H_S)} \times 100\ \% \qquad (2.38)$$

The GMR effect can be qualitatively described using the Mott model introduced in early 1936. The Mott model is based on the fact that the electrical conductivity in metals can be explained in terms of two completely independent conducting channels, determined by the up-spin and down-spin electrons, which are distinguishable depending on the projection of their spins along the quantization axis. The possibility of spin-flip scattering processes in metals is negligible, indicating that up-spin and the down-spin electrons do not mix over long distances. Hence, the electrical conduction happens in parallel for both the spin channels.

Using Mott's approach, it is pretty straightforward to explain GMR in magnetic multilayers. Considering collinear magnetic configurations, as is depicted in Figure 2.13, and assuming that the scattering is stronger for electrons having spins antiparallel to the magnetization direction and weaker for the electrons with spins parallel to the magnetization direction. For the parallelly aligned magnetic layers [Figure 2.13(a)], the up spin electrons suffer almost no scattering from either of the ferromagnetic layers. This is because the spins are parallel to the magnetization direction of the layers. On the other hand, the down spin electrons are scattered strongly by both ferromagnetic layers since their spin is antiparallel to the magnetization direction of the layers. As conduction happens in parallel for both the spin

channels, the total resistivity of the system is governed mainly by the highly conductive up spin electrons and happens to be very low. In the case of antiparallel aligned multilayer [Figure 2.13(b)], both up and down spin electrons are scattered strongly by one of the ferromagnetic layers. Hence, in this case, the total resistivity of the multilayer goes very high.

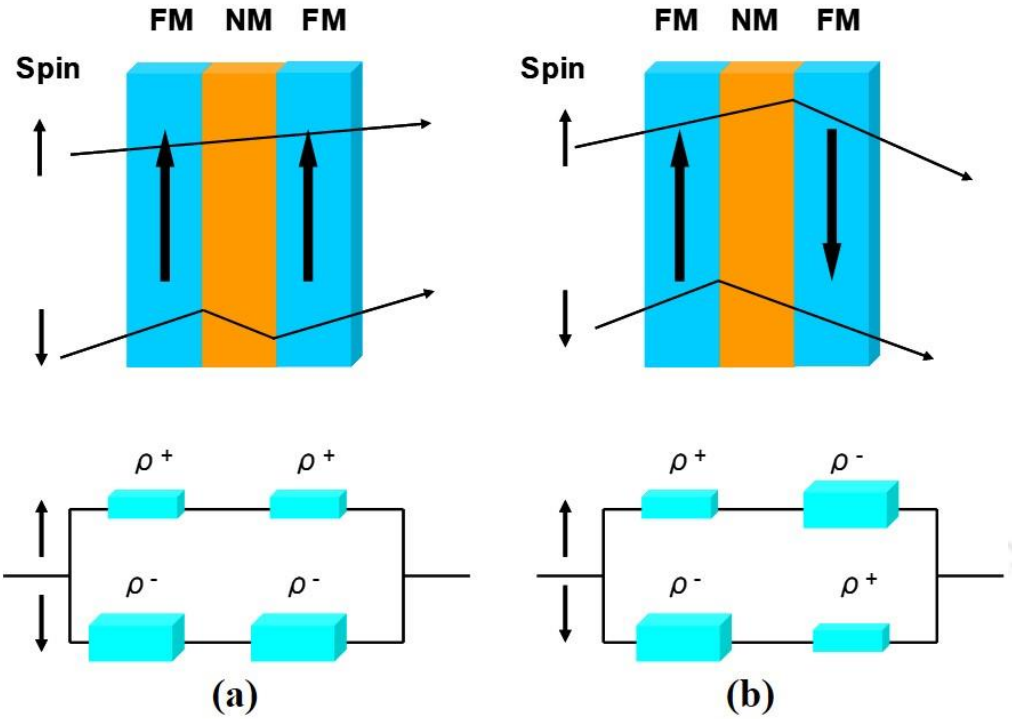

Figure 2.13: Schematic illustration of the Mott model for two spin channels: (a) parallel and (b) antiparallel magnetizations.

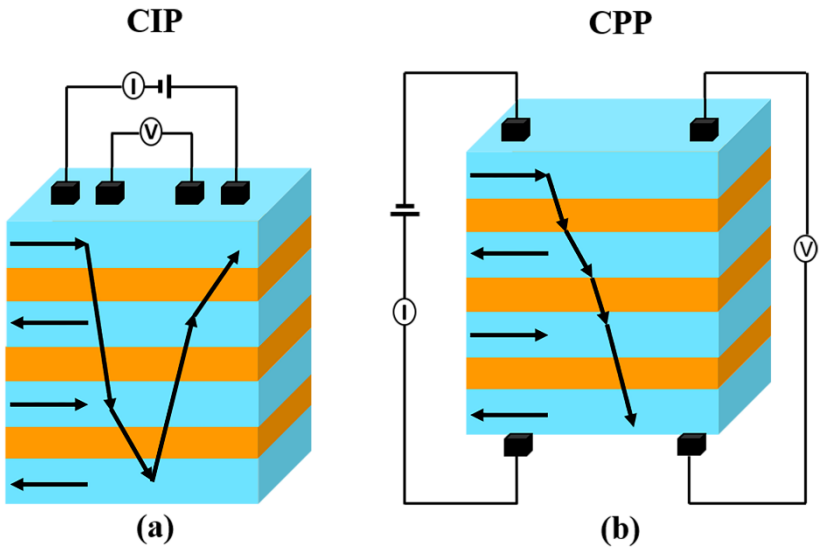

Figure 2.14: Schematic illustration of the (a) CIP and (b) CPP configurations of a GMR device.

The Mott model shown in Figure 2.14 holds true for both the current-in-plane (CIP) and current-perpendicular-to-plane (CPP) configurations. However, since the current distribution is different among the electron wave vectors for CIP and CPP configurations, they can result in different GMR ratios. For the CIP configuration, the current and the magnetic field can be uniform along the transport direction, which is the plane of the multilayer. But in the case of CPP configuration, the situation becomes more complex, where the net transport happens perpendicular to the plane of multilayers along which the structure is non-uniform. Also, the scaling length is different for CIP and CPP configurations. The scaling length in the CIP configuration is determined by the electron's mean free path, whereas the spin diffusion length defines the scaling length for the CPP configuration. When the scaling length is smaller than the layer thickness, it limits the use of the simple Mott model, and more complicated physics needs to be taken into account [TSYM2001].

GMR is not unique to magnetic multilayers. It has been readily observed in magnetic granular films, *e.g.*, CoAg, CoCu, FeAg, *etc*. [MAED1994, MALK1999, SANG1995]. The diversity of GMR in different granular films strongly depends on ferromagnetic element concentration, granular size, and fabrication conditions. Considering the importance of thin film-based GMR, a granular film-based GMR concept is not discussed in detail.

2.7.5. Tunnel magnetoresistance

Tunnel magnetoresistance (TMR, *a.k.a*. junction magnetoresistance) was discovered by Jullière in 1975 while studying the conductance of FeGeCo junctions at temperatures less than 4.2 K [JULL1975]. Later, the advent of room temperature TMR in 1994 aroused considerable interest due to its possible applications in the magnetic sensor and non-volatile storage industry. The phenomenon of TMR is observed in magnetic tunnel junctions (MTJ), where a thin insulating spacer layer separates the ferromagnetic metallic layers. Analogous to GMR, TMR is also determined by the relative orientation of magnetic moments of the alternating ferromagnetic layers. Despite having similar applications, both these phenomena are fundamentally very distinct in terms of the physics involved. GMR is observed in metallic multilayer structures due to the classical electron transport mechanism. On the contrary, TMR is realized in multilayer systems where an insulating spacer layer separates the ferromagnetic layers. This insulating spacer layer hinders classical electron transport. However, if the insulating spacer layer is thin enough (~ few monolayers), the spin-polarized electrons may

tunnel through the insulating barrier. The probability of tunneling is dependent on the thickness of the barrier.

The tunneling process is also largely dependent on the available electronic states at the ferromagnetic interfaces and the available channels in the insulator. Furthermore, the tunneling electron on one side of the insulating barrier must be in the same energy state in the band structure where there is an empty energy state on the other side of the barrier.

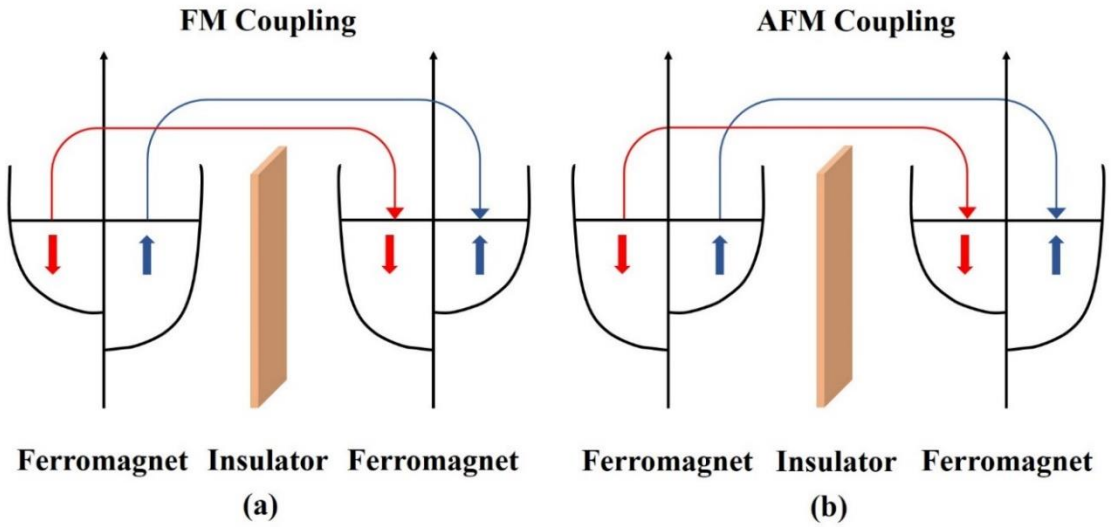

Figure 2.15: Schematic demonstration of DOS and spin-dependent tunneling process for (a) ferromagnetic and (b) antiferromagnetic coupling in a TMR device.

If P_1 and P_2 represent the spin polarization of electrons in two ferromagnetic layers on both sides of barriers, the magnitude of TMR can be expressed as

$$TMR\ ratio\ (\%) = \frac{2P_1P_2}{1 - P_1P_2}\ \text{x}\ 100\ \% \tag{2.39}$$

Here, the TMR value tends to infinity if P_1 and $P_2 \rightarrow 1$. Such class of materials is called half metals, which include several Heusler alloys and oxides [TAKA2010]. The polarization P is defined as

$$P = \frac{D_\uparrow(E_F) - D_\downarrow(E_F)}{D_\uparrow(E_F) + D_\downarrow(E_F)} \tag{2.40}$$

where $D_\uparrow$ and $D_\downarrow$ are the density of states (DOS) for the electrons having up spin and down spin respectively at the Fermi energy. A schematic demonstration of the DOS and spin dependent tunneling process for parallel and antiparallel alignments of magnetization is depicted in Figure 2.15.

2.8. Interlayer coupling in multilayer thin films

The study of magnetic properties of multilayer thin films has attracted considerable attention, owing to various fascinating properties resulting from the interplay of electron transport and magnetic behavior [IKHT2018, INOU2014, REIG2013, TSYM2016, ZHOU2017]. These artificial structures are promising candidates for memory elements, magnetic field sensors, magnetic tunneling junctions, *etc*. To harvest the full potential of these structures, it is important to understand and control the interlayer coupling between the magnetic layers through the nonmagnetic spacer layer. It has been reported that two different effects, such as the magnetostatic coupling arising due to uncompensated poles near the edges and magnetostatic coupling among the stray fields of domain walls, and Néel coupling due to the interface roughness tend to yield extraneous magnetic fields along the plane of the free layer. In addition, the interlayer coupling originates from two types of interactions: (i) short-range exchange interaction and (ii) long-range exchange interaction.

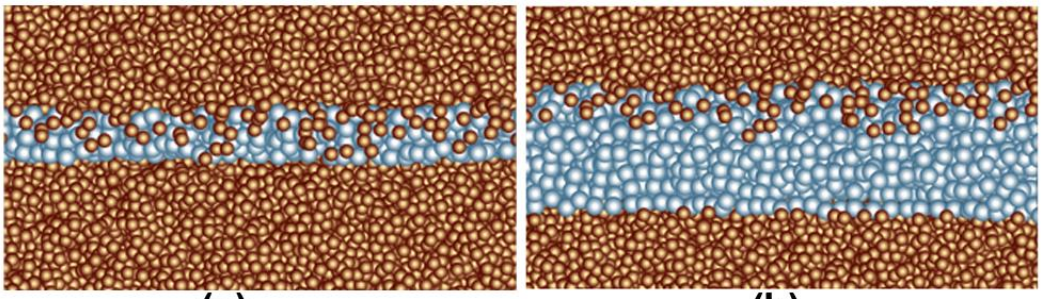

Figure 2.16: Schematic representation of multilayer films with thin and thick interlayers.

2.8.1. Exchange coupling

2.8.1.1. Direct exchange coupling

Magnetic layers separated by a thin nonmagnetic insulating or metallic spacer layer are coupled directly through the pinholes present in the thin spacer layer, as illustrated in Figure 2.16(a). Since the pinhole exists mainly due to the formation of a noncontinuous spacer layer at low spacer layer thickness, the number of pinholes, which determine the strength of the coupling, depends strongly on the thickness of the spacer layer, growth conditions, and the atomic size of elements present in the spacer and magnetic layers [PONG2008, SAIT2002, SING2015, STIL2005]. Multilayer films exhibiting direct exchange coupling through the pinholes have strong temperature-dependent magnetic properties because of strong temperature-dependent magnetic properties of the diffused magnetic atoms in the nonmagnetic spacer layer [OLIV1999, SING2013].

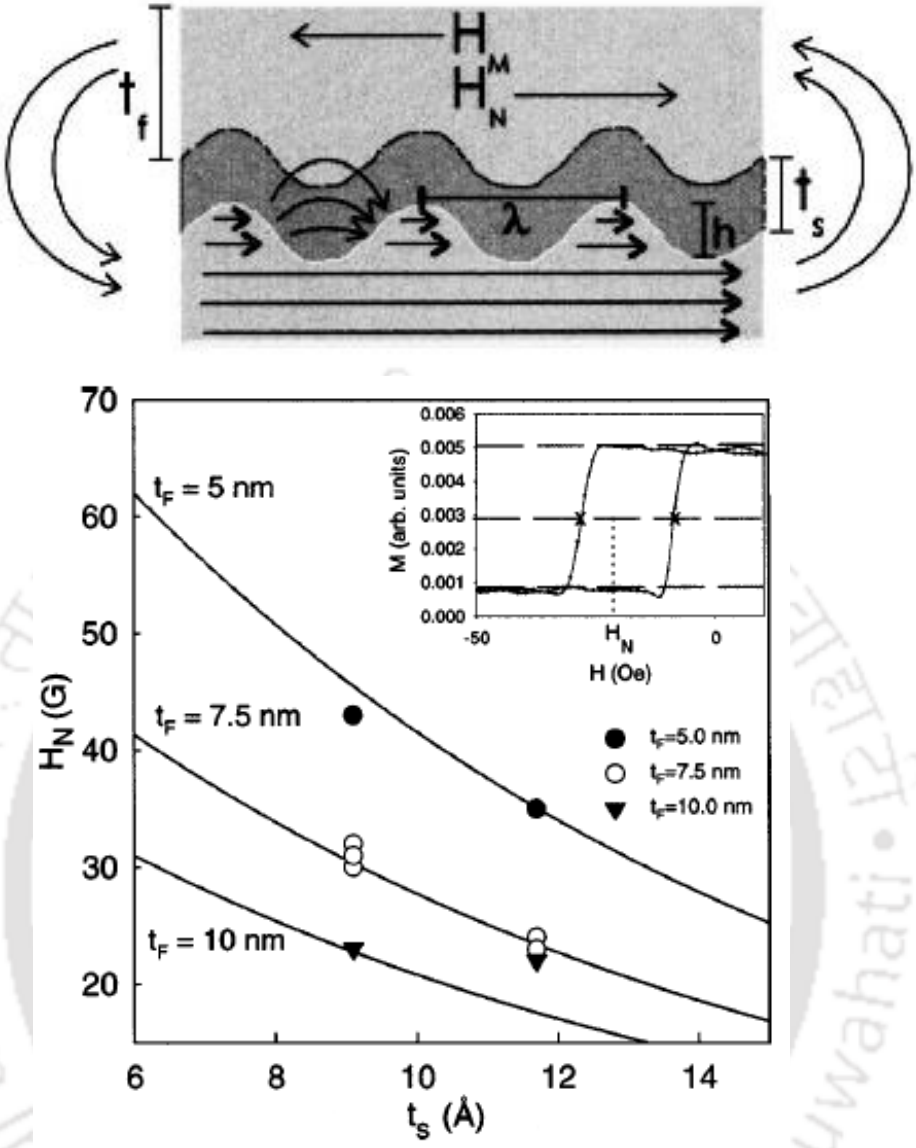

Figure 2.17: (Top) Schematic illustration of two dominant interlayer coupling mechanisms, and (Bottom) variations of Néel coupling with spacer layer thickness for different multilayer films [SCHR2000].

2.8.1.2. Indirect exchange coupling

Increasing spacer layer thickness between the magnetic layers results in interlayer coupling between the ferromagnetic layers through the conduction electrons of the nonmagnetic metallic spacer layer [see Figure 2.16(b)]. This is known as indirect exchange interaction or the Ruderman-Kittel-Kasuya-Yosida (RKKY) interaction. The theory of indirect exchange interaction was first developed by Ruderman and Kittel [RUDE1954] and later on extended by Tadao Kasuya [KASU1956] and Kei Yosida [YOSI1957]. RKKY interaction was applied to multilayer thin film structures to understand the magnetization orientation and the GMR

properties. It has been observed that RKKY coupling aligns the magnetization of adjacent ferromagnetic layers into either ferromagnetic (parallel) or antiferromagnetic (antiparallel) alignment. As a result, the magnetoresistance of the multilayer films has a strong dependence on the spacer layer thickness and exhibits an oscillating nature with the spacer layer thickness. The amplitude of oscillation decreases with increasing spacer layer thickness [BAIB1988, BRUN1991, BRUN1992, PARK1990]. Nevertheless, the coupling strength also depends on the roughness at the interfaces.

2.8.2. Magnetostatic coupling

2.8.2.1. Topological coupling

The topological coupling, also known as Néel's orange peel coupling or dipolar coupling, is the magnetostatic interaction induced by the magnetic poles present at the interface. These magnetic poles are formed due to the interface roughness. Néel carried out the first calculation for topological coupling of semi-infinite magnetic layers exhibiting a correlated sinusoidal interface roughness [NEEL1962]. Subsequently, other researchers extended the model to calculate the roughness of arbitrary phase and finite magnetic layer thickness [KOOL1999, ZHAN19961, ZHAN19962]. The coupling strength is a function of the thickness of each of the magnetic layers and spacer layers, magnetization of the magnetic layers, roughness amplitude at the interface, and the wavelength of the roughness profile. Néel coupling between two ferromagnetic layers is expressed as [SCHR2000],

$$H_N = \frac{\pi^2}{\sqrt{2}}\left(\frac{h^2}{\lambda t_F}\right) M_S exp\left(-\frac{2\pi\sqrt{2}t_s}{\lambda}\right) \qquad (2.41)$$

where t_F and t_s are the thickness of the magnetic layers and spacer layers, respectively, h and λ are respectively, the amplitude and wavelength of the roughness, as demonstrated in Figure 2.17 (top). The coupling field strength strongly depends on the spacer layer thickness and on the ferromagnetic layer thickness [see Figure 2.17 (bottom)].

2.8.2.2. Stray field coupling

Another type of magnetostatic coupling is due to the presence of magnetic poles at the edges of the film, commonly known as stray field coupling. The stray field originating from the edge of one of the magnetic layers magnetostatically couples to the other layers is shown in Figure 2.17 (top).

As the coupling is magnetostatic in nature, it strongly depends on the films' dimensions and provides a substantial interlayer coupling for thicker films [ANGU2000]. The dependence of stray field coupling on the films' dimension can be expressed as [ANGU2000],

$$H_M = A\frac{W^{\alpha}}{L} \tag{2.42}$$

where W and L are the width and length of the sample (in micrometers), respectively, A and α (= 0.22) are constants. The value of α varies with sample dimension, *i.e.*, when the separation between the free layers and the pinned layer is much larger than its width, α tends to be one, whereas in the opposite limit, α should be nearly zero [ANGU2000].

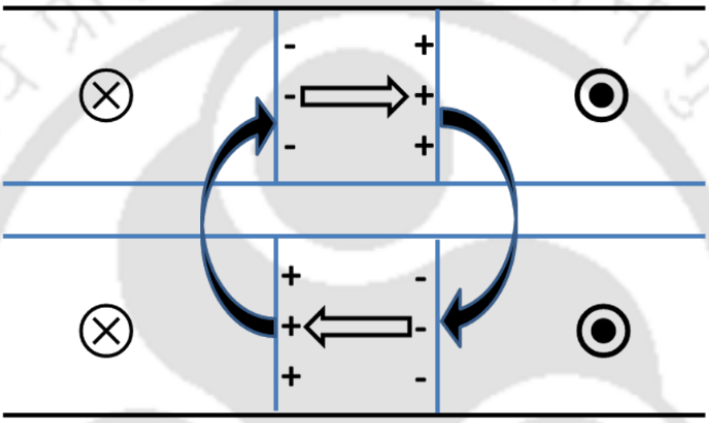

Figure 2.18: Schematic illustration of Néel wall pair separating parallel domains. Superimposed Néel walls are energetically favorable entities because of the complete flux closure associated with them [CHOP2000].

2.8.2.3. Domain wall stray field coupling

Stray fields originating from domain walls of a given ferromagnetic layer magnetostatically lock in with the stray fields from walls of adjacent layers, as shown in Figure 2.18 [CHOP2000, CHOP2005]. The double arrows illustrate the magnetization rotation within a Néel wall. The stray field originating out of the Néel walls, denoted by curved arrows, ensure magnetization fluctuation in the adjacent layers above and below it, leading to the formation of quasi-Néel walls. This stray field originating from each domain wall closes its flux by magnetostatic locking-in with stray fields from the domain wall in the adjacent layers. This results in an overall reduction of the wall energy and thus the coercivity. Magnetic thin films demonstrate substantial thickness dependent magnetic properties. In general, ultrathin films having in-plane magnetic anisotropy exhibits in-plane magnetization with large-sized domains and Néel wall [OHAN2000]. Likewise, the multilayer thin films with thin

ferromagnetic layers also show in-plane magnetization with large-sized domains and Néel wall, resulting in a minimum or zero stray field coupling. On the contrary, the existence of multidomain patterns above the critical thickness depends on the net magnetization of the ferromagnetic layers, anisotropy of the films, the microstructure of the film, substrate nature, and the growth conditions of the thin films [ALLE1994, FELD1971, OEPE1990]. Hence, at larger thicknesses, the multidomain pattern with the Bloch wall is energetically more favorable. This indicates that the domain wall stray field provides a substantial coupling among the ferromagnetic layers causing a strong variation in the magnetic properties of the multilayer structured films measured at different temperatures.

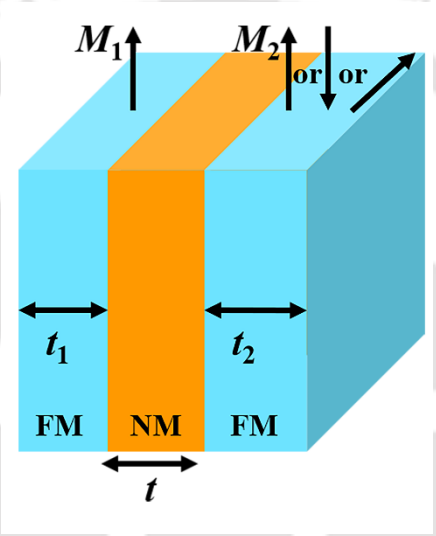

Figure 2.19: Illustration of different possible orientations of two FM films due to IEC across NM spacer layers [GRUN2001].

2.8.3 Phenomenological description of interlayer exchange coupling

Interlayer exchange coupling (IEC) is an indirect exchange interaction, where the magnetizations of two ferromagnetic layers separated by a nonmagnetic (NM) spacer layer are controlled by the electrons in the spacer layer. In magnetic multilayers, three types of coupling have been identified so far: (i) ferromagnetic (FM), (ii) antiferromagnetic (AFM), and (iii) biquadratic (BQ) or 90° type coupling [GRUN2001]. However, in most practical cases, the FM and AFM coupling can coexist with biquadratic coupling, resulting in canted angular distributions of magnetization vectors at some intermediate values.

Let us consider a system of two FM films separated by an NM spacer layer, as shown in Figure 2.19. The interlayer coupling areal energy density E_I describes the three basic

coupling mechanisms, namely, FM, AFM, and BQ coupling utilizing energy minima of E_I and can be expressed as

$$E_I = -J_1 \frac{\vec{M}_1.\vec{M}_2}{|\vec{M}_1|.|\vec{M}_2|} - J_2 \left(\frac{\vec{M}_1.\vec{M}_2}{|\vec{M}_1|.|\vec{M}_2|}\right)^2 = -J_1 \cos\theta - J_2 \cos^2\theta \qquad (2.43)$$

where θ is the angle between magnetization vectors $\vec{M}_1$ and $\vec{M}_2$ of the ferromagnetic films with respect to the applied field, J_1 and J_2 are bilinear and BQ coupling parameters. Positive J_1 corresponds to FM coupling, while negative J_1 implies AFM coupling between the adjacent FM layers. Likewise, negative J_2 represents 90º alignment of the FM layers in the film plane. However, positive J_2 is not assigned to any physical meaning. In the literature, various definitions of the bilinear and BQ coupling parameters exist. J_2 has been used with the opposite sign compared to Eqn. (2.43) [HEIN1993, SLON1993]. Bruno has finally replaced both plus signs in Eqn. (2.43) in place of the minus signs [BRUN1995].

The coupling energy is expressed in several theoretical works in terms of the energy difference (E_{FM} - E_{AFM}) between the FM and AFM alignments, corresponding to $\Delta\theta = 0$ and $\Delta\theta = \pi$ in Eqn. (2.43). Both E_{FM} and E_{AFM} are generally understood as energy per lateral unit cell. Assuming E ($\Delta\theta = 0$) = E_{FM}/A, where A is the area occupied by 2D interface unit cell, and neglecting the J_2 term, Eqn. (2.43) becomes

$$J_1 = -\frac{(E_{FM} - E_{AFM})}{2A} \qquad (2.44)$$

If $E_{FM} - E_{AF} > 0$, the AFM alignment is more favorable, and J_1 is negative in agreement with the sign convention used in Eqn.(2.43). Also, the consideration of energy terms due to the presence of an external field, H, and magnetic anisotropy, K is required to evaluate the experiments. For instance, in a four-fold cubic magnetic anisotropy, the total energy can be expressed as:

$$E = E_I - \mu_0 H(M_1 t_1 \cos\theta_1 + M_2 t_2 \cos\theta_2) + \frac{K_1}{4}(t_1 \sin^2(2\theta_1) + t_2 \sin^2(2\theta_2)) \qquad (2.45)$$

where t_1 and t_2 are the thicknesses of the two ferromagnetic layers, H is the externally applied field along one of the easy axes, and K_1 is the first-order cubic anisotropy constant. θ_1 and θ_2 are the angles between the magnetizations of the two films and the external field H, also $\theta = \theta_1 - \theta_2$. In CGS units $\mu_0 = 1$. The minima of Eqn. (2.45) can be obtained by numerical methods.

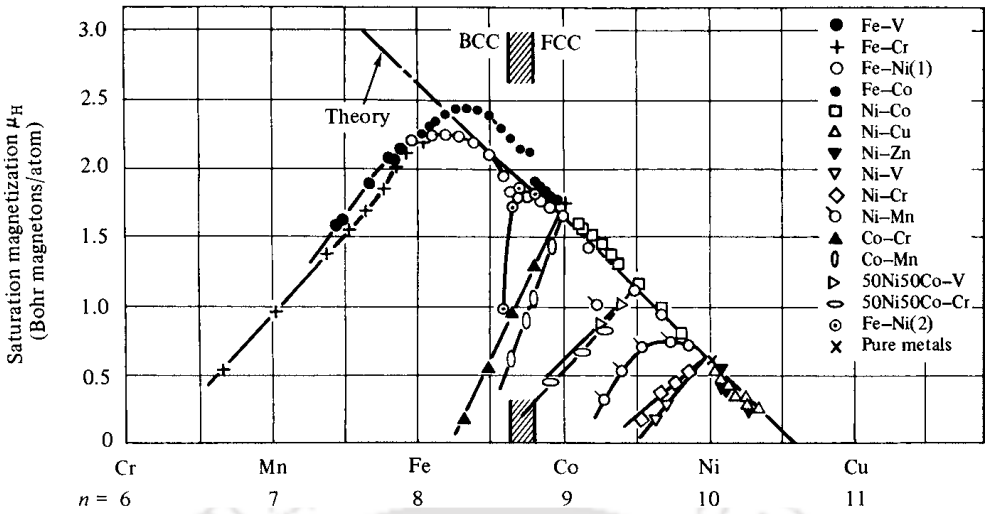

Figure 2.20: Slater–Pauling curve: dependence of saturation magnetization of alloys on the number of (3d + 4s) electrons per atom [CULL2009].

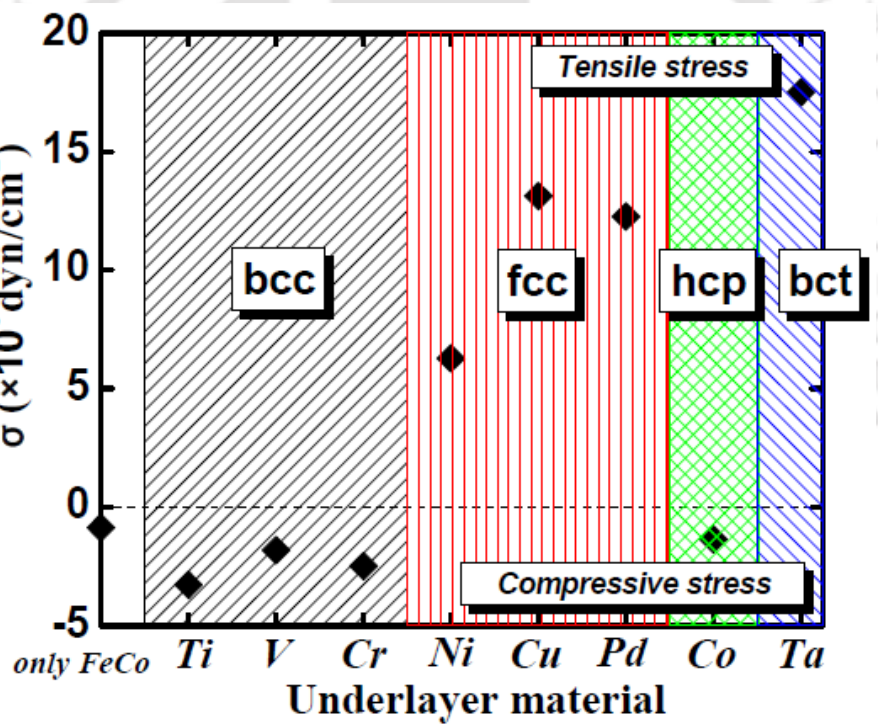

Figure 2.21: Internal stress CoFe films deposited onto various underlayers [LIU2011].

2.9. Structural and magnetic properties of Co_xFe_{100-x} alloys

Cobalt (Co), Iron (Fe), and their various alloys are typically soft magnetic materials with high M_S, which find widespread applications, especially in high-temperature applications owing to their high Curie temperature. These 3*d* transition metals are at the peak of the Slater-Pauling curve (Figure 2.20). Iron-rich alloys have been observed to exhibit increased

magnetization when combined with Cobalt, which is less magnetic than Iron. A 30% Co alloy ($Co_{30}Fe_{70}$) is characterized with a value of M_s much higher than any other known material at room temperature [CULL2009]. In more recent times, research interest has been triggered in Co_xFe_{100-x} alloys due to the advances in thin film technology, enabling tailoring of the magnetic properties of this binary alloy on the basis of their crystal structure. The internal and interfacial stress can alter ultra-thin CoFe films' microstructure and define their magnetic and electric properties. The underlayers play a significant role in engineering the overall microstructure, magnetic anisotropy, magnetostriction, and electrical resistivity of the film in various ways.

To develop Co_xFe_{100-x} based alloys for industrial applications, it is important to understand the effect of different underlayers on the film properties. Liu *et al.* [LIU2011] reported on the effect of various underlayers ranging from group 4 to group 11 metals (Ti, V, Cr, Co, Ni, Cu, Ta, and Pd) on $Co_{35}Fe_{65}$ film. Figure 2.21 shows the dependence of internal stress in the CoFe film on the underlayers. It can be clearly seen that the crystal structure of CoFe film changes with the nature of the underlayer used. For instance, $Co_{35}Fe_{65}$ film deposited on Ni, Cu, and Ta underlayer displays large tensile stress. This leads to a higher magnetocrystalline anisotropy. It is important to note that underlayers having an *fcc* structure display comparatively low internal stresses than underlayers with a *bcc* structure. The body-centered-tetragonal (*bct*) structure is a tetragonally strained *bcc* structure, inducing perpendicular magnetic anisotropy (PMA) in the CoFe system. Most literature studies reveal that PMA materials consist of rare earth elements [COEY1991, COEY1999, COEY2011, CUI2014, KRAM2012, MITC2012]. In 3*d* transition metals, the magnetic ordering is governed by lattice strain owing to the close correlation between the electronic structure and the magnetic properties, *i.e.*, anisotropy and exchange coupling [ANDE2010]. The preferred magnetization directions can be tuned by choosing materials composition, suitable spacers, and underlayers that create desirable changes in the electronic structure. Yildiz *et al.* investigated the tetragonal distortion of Co_xFe_{100-x} films grown epitaxially on Pd(001), Ir(001), and Rh(001) substrates. The strongest PMA is achieved for $Co_{50}Fe_{50}$ films grown on Rh(001) with lattice constant ratio, c/a = 1.24. PMA systematically decreases for Ir(001) with c/a = 1.18 and Pd(001) with c/a = 1.13 [YILD20092]. On the other hand, Shikada *et al.* [SHIK2009] observed an in-plane easy axis of magnetization in $Co_{50}Fe_{50}$ films prepared on MgO(100), MgO(110), and MgO(111) substrates. Burkert *et al.* [BRUK2004] calculated the uniaxial anisotropy energy (K_u) achievable for tetragonally strained Co_xFe_{100-x} to be about 10

MJ/m^3 in alloys with $50 \leqslant x \leqslant 70$ and a tetragonal strain of $1.2 \leqslant c/a \leqslant 1.25$. Kota *et al.* [KOTA2012, KOTA2013], Hyodo *et al.* [HYOD2015] and Turek *et al.* [TURE2012] also estimated the K_u of CoFe alloys, considering both the tetragonal distortion using first-principles calculations considering coherent potential approximation and the *B*2 type chemical ordering (with ordering parameter *S*). They predicted anisotropy energy of around 5 MJ/m^3 for $S = 1.0$ and $c/a = 1.25$. To achieve such a high value of anisotropy energy, several efforts have been made [ANDE2006, ANDE2010, LUO2007, MAND2018, OOMI2015, WINK2006, YILD20092]. Oomiya *et al.* [OOMI2015] studied the thickness and composition dependence of K_u of tetragonally distorted Co_xFe_{100-x} epitaxial films prepared using Rh buffer on a MgO substrate. They predicted K_u of approximately 5 MJ/m^3 for $S = 1.0$ and $c/a = 1.25$. They reported the highest K_u of 1.6 MJ/m^3 when the c/a ratio was 1.15 – 1.25 for $Co_{50}Fe_{50}$ films with 1.5 nm thickness [OOMI2015]. Mandal *et al.* [MAND2018] reported a K_u value of 0.573 MJ/m^3 for the $Co_{50}Fe_{50}$ on Rh film, where PMA strongly depends on the lattice distortion, which originates from the epitaxial growth in the large lattice misfit system of $Co_{50}Fe_{50}$ and Rh. The above results indicate that the underlayer plays an important role in inducing desirable strain on the CoFe lattice and preferably reorienting the magnetization direction. In addition to a proper tetragonal distortion, an appropriate adjustment of the Fermi level generates a strong uniaxial anisotropy in $Co_{50}Fe_{50}$ films grown on Rh(001) substrate [LUO2007, YILD20091].

2.10. Numerical simulation methods

2.10.1. Trilayer structure

The *M-H* loop is simulated using a numerical simulation model to study the nature of magnetic couplings between CoFe layers through Rh and Cu spacers. We consider three major energy expressions as shown in Eqn. (2.46) [BOSU2010], such as the magnetic anisotropy energy (E_{MA}), the Zeeman energy (E_Z), and the exchange coupling energy (E_{EX}), for the total energy (E_{Total}), which is expressed as follows:

$$E_{Total} = E_{MA} + E_Z + E_{EX} \tag{2.46}$$

where

$$\begin{aligned} E_{MA} &= K_a t_a sin^2\alpha\, cos^2\alpha + K_b t_b sin^2\beta\, cos^2\beta \\ E_Z &= -M_a t_a H cos\alpha - M_b t_b H cos\beta \\ E_{EX} &= -J_1 cos(\alpha - \beta) - J_2 cos^2(\alpha - \beta) \end{aligned} \tag{2.47}$$

Here, *M*, *K* and *t* are the saturation magnetization, the first-order cubic magnetocrystalline anisotropy constant, and ferromagnetic layers' thickness, respectively. Subscripts *a* and *b* represent the bottom and top ferromagnetic layers in FM/ NM /FM film, as shown in Figure 2.22.

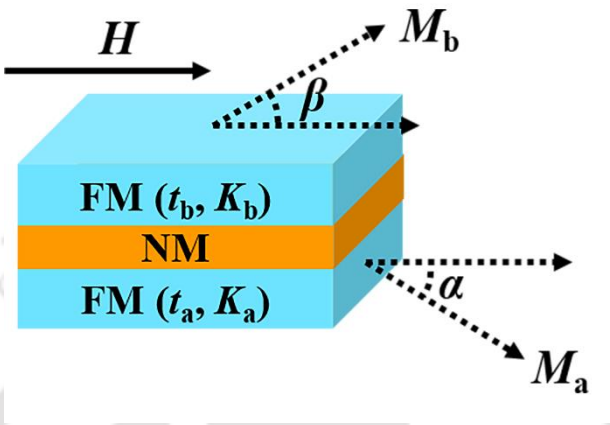

Figure 2.22: Schematic illustration of the numerical simulation parameters in FM/ NM/ FM trilayer structure. All the arrows represent in-plane directions.

The value of *K* is determined from *M-H* loops measured along with the easy and hard axes directions of single-layer ferromagnetic film. J_1 and J_2 are the bilinear and biquadratic coupling energies, respectively. The positive value of J_1 represents FM coupling, while the negative values of J_1 and J_2 correspond to 180° and 90° magnetic configurations, respectively. *H* is the applied magnetic field. The angle $\alpha(\beta)$ is the angle between the direction of *H* and *M* in the bottom (top) ferromagnetic layer. Therefore, α-β represents the relative orientation between two magnetization vectors of the bottom and top ferromagnetic layers. The saturation magnetization value for top and bottom ferromagnetic layers, *M* is determined from the easy axis measurement of single and trilayer samples. The first-order cubic anisotropy constant, *K* is measured by applying the magnetic field along easy (100) and hard (110) directions of single layer CoFe.

For simulating *M-H* loops, the minimum energy of the system is searched as a function of α and β for each respective value of *H* and thereby α and β are determined for the lowest possible local energy condition by varying the value of α and β from 0 to 180º. The values of different coupling parameters, J_1 and J_2, are evaluated by comparing the simulated *M-H* loop with the experimental one.

For the simulation of *M-H* loops along the hard axis, the Zeeman energy term in Eqn. (2.47) has been replaced by follows

$$E_Z = -M_a t_a H cos(\alpha - {}^{\pi}/_{4}) - M_b t_b H cos(\beta - {}^{\pi}/_{4}) \qquad (2.48)$$

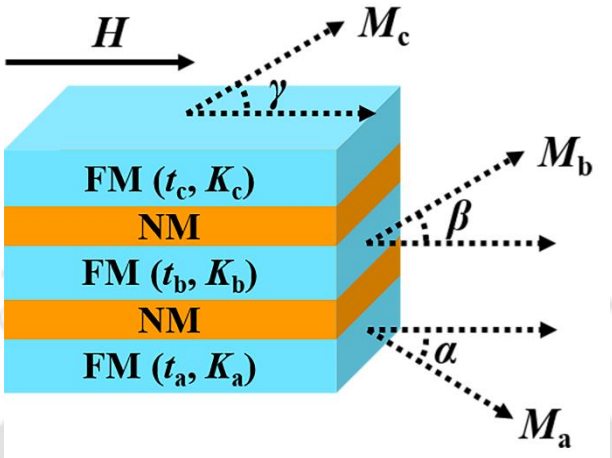

Figure 2.23: Schematic illustration of numerical simulation parameters in FM/ NM/ FM/ NM/ FM multilayer structure. All the arrows point in-plane directions.

2.10.2. Multilayer structure

Similarly, for FM/ NM/ FM/ NM/ FM multilayer film, E_{MA}, E_Z, and E_{EX} can be expressed as

$$\begin{aligned} E_{MA} &= K_a t_a sin^2\alpha\, cos^2\alpha + K_b t_b sin^2\beta\, cos^2\beta + K_c t_c sin^2\gamma\, cos^2\gamma \\ E_Z &= -M_a t_a H cos\alpha - M_b t_b H cos\beta - M_c t_c H cos\gamma \\ E_{EX} &= -J_1' cos(\alpha - \beta) - J_2' cos^2(\alpha - \beta) - J_1'' cos(\beta - \gamma) \\ &\quad - J_2'' cos^2(\beta - \gamma) \end{aligned} \qquad (2.49)$$

Subscripts *a*, *b*, and *c* represent the bottom, middle, and top ferromagnetic layers, respectively [FULL1996, GORI2011]. The terms J_1' (J_1'') and J_2' (J_2'') are the bilinear (biquadratic) coupling energies, respectively, across the bottom (top) spacer. The positive value of J_1 represents FM coupling, while the negative values of J_1 and J_2 correspond to 180° and 90° magnetic configurations, respectively. α, β, and γ represent angles between *H* and *M* in the bottom, middle, and top FM layers, respectively, as shown in Figure 2.23. Therefore, α-β, γ-β and α-γ present the relative orientation between the magnetization direction of bottom and middle, top and middle, and bottom and top CoFe layers, respectively. The *M-H* loop is simulated by minimizing the total energy expressed by Eqn. (2.49). For the simulation of *M-H* loops along the hard axis, the Zeeman energy term in Eqn. (2.49) has been replaced by

$$E_Z = -M_a t_a H cos(\alpha - {}^{\pi}/_{4}) - M_b t_b H cos(\beta - {}^{\pi}/_{4}) - M_c t_c H cos(\gamma - {}^{\pi}/_{4}) \quad (2.50)$$

2.10.3. Limitations of the model

- The strength of the FM coupling (+J_1) alone can't be determined based on this model since there is no torque when the two FM layers are aligned parallel to each other. Therefore, the consideration of any value of $J_1 > 0$ in simulation for FM coupling does not have any physical meaning (see Figure 2.24). However, the strength of the FM coupling can be determined when both +J_1 and –J_2 contribute.

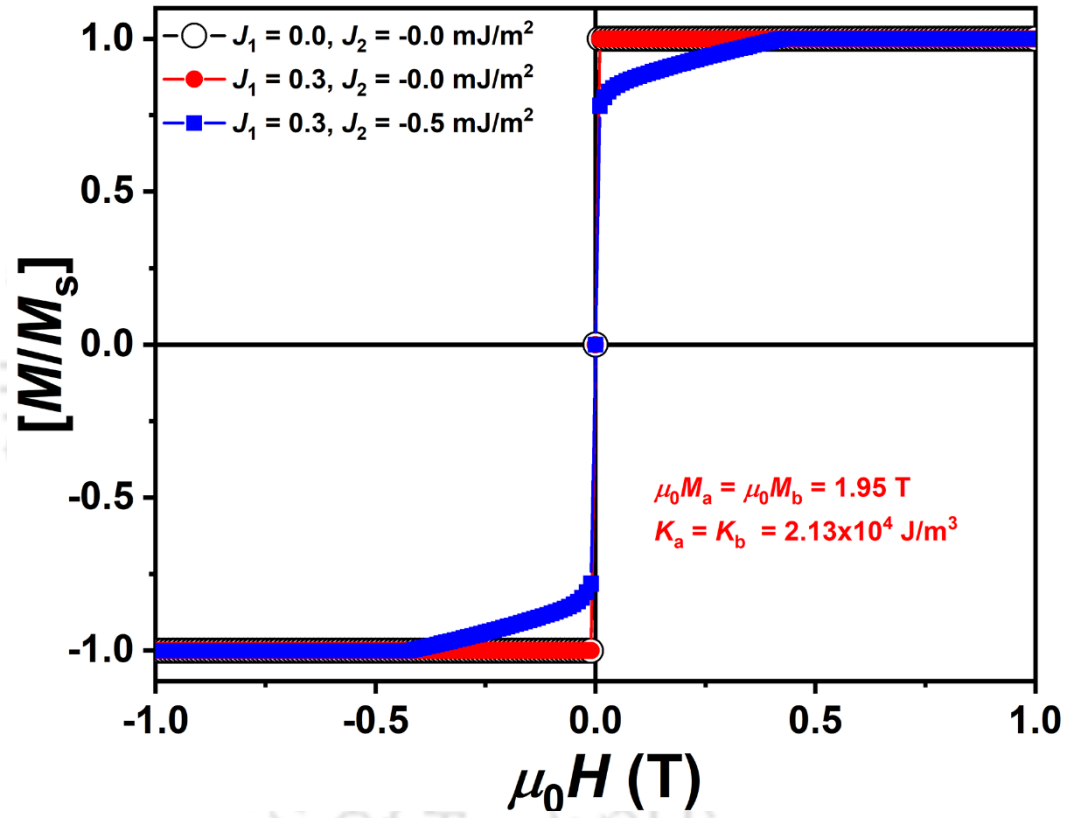

Figure 2.24: Numerically simulated *M-H* loops for a flat sample of CoFe(3 nm)/ Rh(0.84 nm)/ CoFe(3 nm)/ MgO(2 nm) considering FM coupling.

- The simulated *M-H* loops are compared with experimental *M-H* loops and judged by the natural view to determine the coupling parameters. Therefore, there might be uncertainty in the value of coupling strength that usually varies about ±5% for J_1' [Figure 2.25(a)], ~ ±6.5 % for J_2' [Figure 2.25(b)] and ~ ± 5% for J_1'' [Figure 2.25(c)].

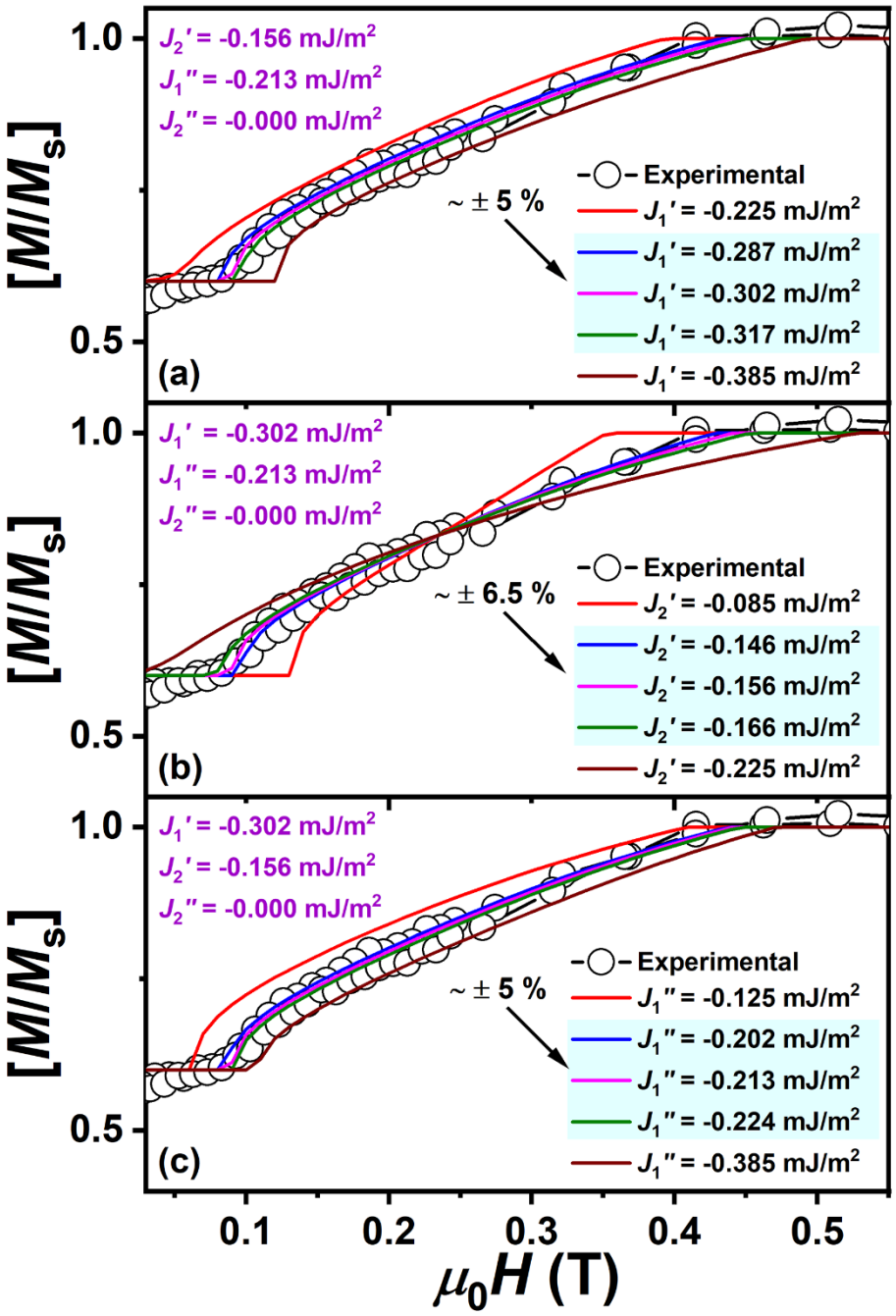

Figure 2.25: Possible error in the estimation of coupling parameters from the numerically simulated *M-H* loops for a flat sample of CoFe(3 nm)/ Rh(0.84 nm)/ CoFe(3 nm)/ Cu(1.6 nm)/ CoFe(3 nm)/ MgO(2 nm).

- This model doesn't take coercivity into account. As a result, the simulation of experimental *M-H* loops with high coercivity value doesn't fit well through the whole loop. In such situations, the best fitting is considered only for the first quarter of the *M-H* loop.

Chapter 3

Experimental methods

3.1. Introduction

In the course of the present investigations, various experimental techniques were used for fabricating and characterizing the single layer and multilayer thin films. This chapter provides a concise description of those experimental techniques.

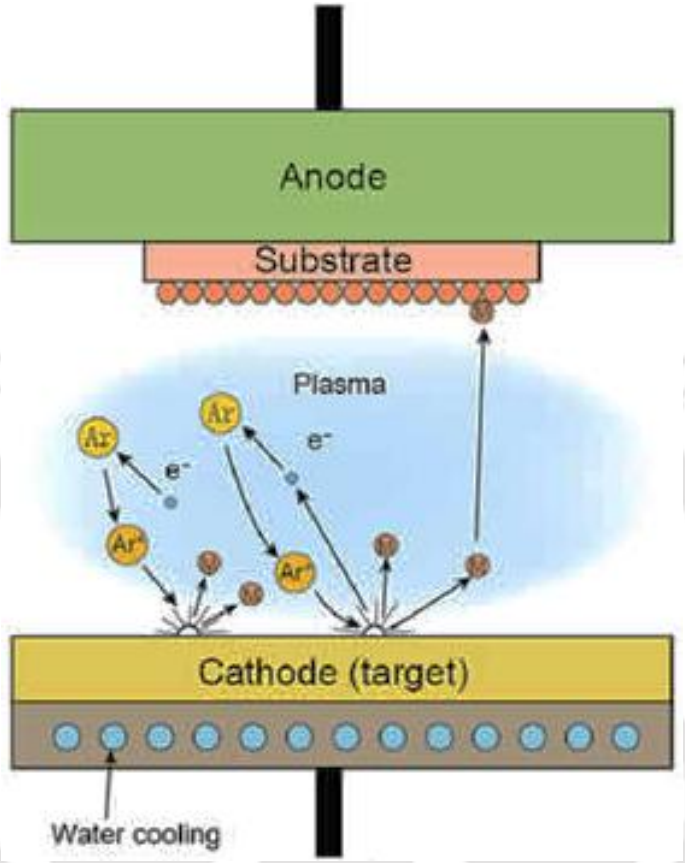

Figure 3.01: Schematic diagram of the sputtering process [PERU20132].

3.2. Techniques used for sample preparation

3.2.1. Sputtering technique

Sputtering is one of the most versatile techniques that is tremendously used for the synthesis of thin films. The ejection of atoms from the surface of the cathode by the bombardment of energetic positive ions of noble gases like helium, argon, neon, and krypton, at a reduced gas pressure in the presence of high direct current (DC) voltage [OHRI1992, SESH2002, WAGE1994] is commonly known as sputtering. In 1852, Sir W. R. Grove coincidentally discovered surface coatings developed in the valve under a glow discharge. Sir W. Thomson termed the phenomenon as spluttering, which later espoused as sputtering. The sputtering process involves a momentum transfer between the bombarding positive noble gas ions and

the surface atoms of the cathode, as displayed in Figure 3.01, resulting in the physical removal of atoms from the cathode's surface.

Sputtering yield is described as the ratio between average numbers of emitted atoms to the number of incident ions on the surface of the cathode.

- The sputtering yield increases with a) energy, b) mass of the bombarding ions, and c) decrease of the angle of incidence to the cathode.
- A minimum threshold of energy is required to kick start the sputtering process.
- The sputter atoms are evicted along with the crystallographic directions of the cathode metal lattices.
- Sputtering yield decreases with a significant increase in ion energy because of the deeper penetration of ions inside the cathode lattice.
- Sputtering is unavoidably accompanied by the emission of secondary electrons from the cathode surface.
- Sputtering yield is independent of the cathode temperature.
- If the sputtering process does not involve any of the chemical reactions between the bombarding gas ions and the cathode material, it is known as physical sputtering.
- If any chemical reactions are involved, it is termed reactive sputtering.

The physical deposition process consists of three steps, viz.,

1. Emission of the atoms from the target source.
2. Their transport to the substrate.
3. Condensation on the substrate.

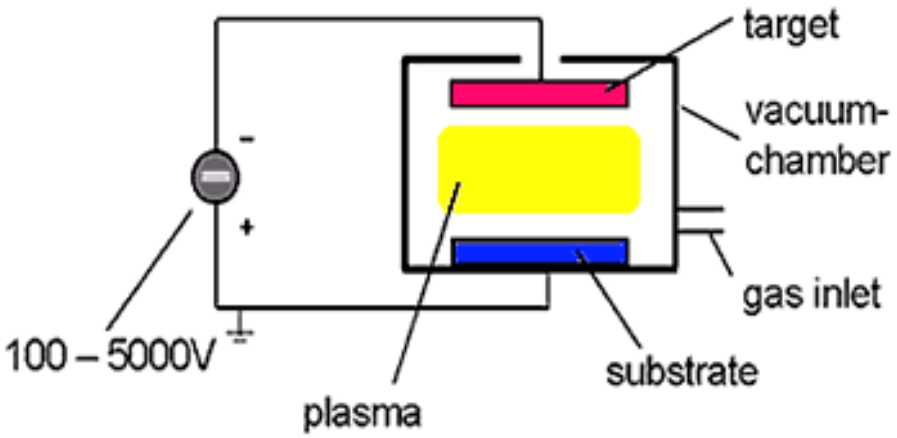

Figure 3.02: Schematic arrangement of DC sputtering technique [PERU20132].

Four different types of sputtering processes, viz., Direct-Current (DC), Radio-Frequency (RF), Magnetron, and Reactive sputtering, are used for thin-film fabrication. We have used DC and RF magnetron sputtering for fabricating the films in the current investigation.

3.2.1.1. DC sputtering technique

Figure 3.02 demonstrates a typical arrangement used for DC sputtering. The target and substrate face opposite to each other in a vacuum chamber with a distance of a few centimeters to a few tens of centimeters. The target is connected to the negative output of a DC power supply and thus acts as the cathode. On the other hand, the substrate and the chamber walls act as the anode. After creating the necessary Argon gas atmosphere in the pressure range of about 0.13 Pa – 1.33 Pa, the gas discharge is ignited by applying a DC voltage. The electric field ionizes the Argon gas. The created Ar^+ ions accelerate towards the target, ejecting atoms from the target surface. These atoms subsequently get deposited on the substrate. At lower pressures, the mean free path is large, hence the ionization efficiency is low and self-sustained discharges can't be maintained below 0.13 Pa. As the Ar pressure increases at a fixed voltage, the electron mean-free-path decreases, leading to the generation of more ions and hence large current flow. However, if the pressure is too high, the sputtered atoms undergo increased collisional scattering resulting in a lower deposition rate. The deposition rate is proportional to (a) power consumed, (b) square of the current density, and (c) reciprocal of electrode spacing. DC sputtering works with all types of target materials that are electrically conductive in nature.

However, DC sputtering is subject to two major limitations compared to conventional evaporation: (i) lower deposition rate and (ii) higher thermal load on the substrate due to the impingement of secondary electrons. To raise the deposition rate and tune the thermal load, magnetron sputtering is deployed to deposit thin films.

3.2.1.2. RF sputtering technique

Figure 3.03 demonstrates a typical arrangement for RF sputtering. For instance, materials such as oxides, nitrides, or ceramics have incredibly high DC impedance and require very high voltages to ignite and sustain a plasma. This inhibits the neutralization of the positive charges accumulated on the cathode surface during ion bombardment. Hence, the deposition of such electrically insulating materials can't be carried out feasibly by DC sputtering. Nevertheless, the impedance of such materials varies with the frequency of the applied

power. Thus, it can be overcome by applying a very high-frequency potential to the metal electrode behind the insulator. Using the power delivered at radio frequencies (~ 13.56 MHz) and an automatic impedance matching network, the overall impedance of the circuit can be regulated to 50 Ω, which is ideal for plasma ignition in typical sputtering environments. Since the insulator can now be alternately bombarded by ion and electron, the positive charge accumulated on the surface during the negative or the sputter portion of each cycle will be neutralized by the electrons during the positive part of the cycle [DAVI1967]. Wehnerl, in his review article on sputtering by ion bombardment, proposed the principle of RF sputtering [WEHN1955]. Consequently, Davidse and Maissel further developed RF sputtering to fabricate insulator films at high rates [DAVI1966]. In the present thesis, the sputtering of the MgO target is carried out by RF magnetron sputtering.

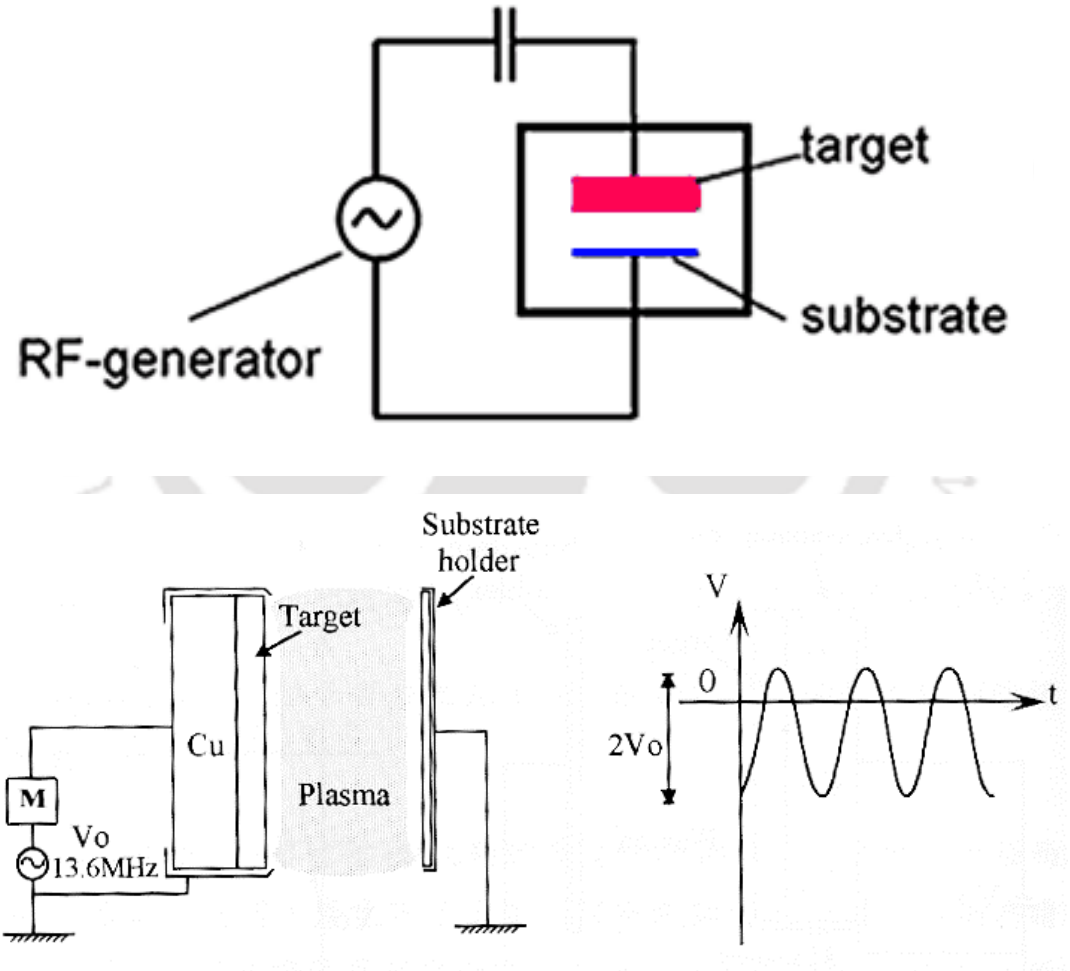

Figure 3.03: Schematic presentation of RF magnetron sputtering assembly [PERU20132].

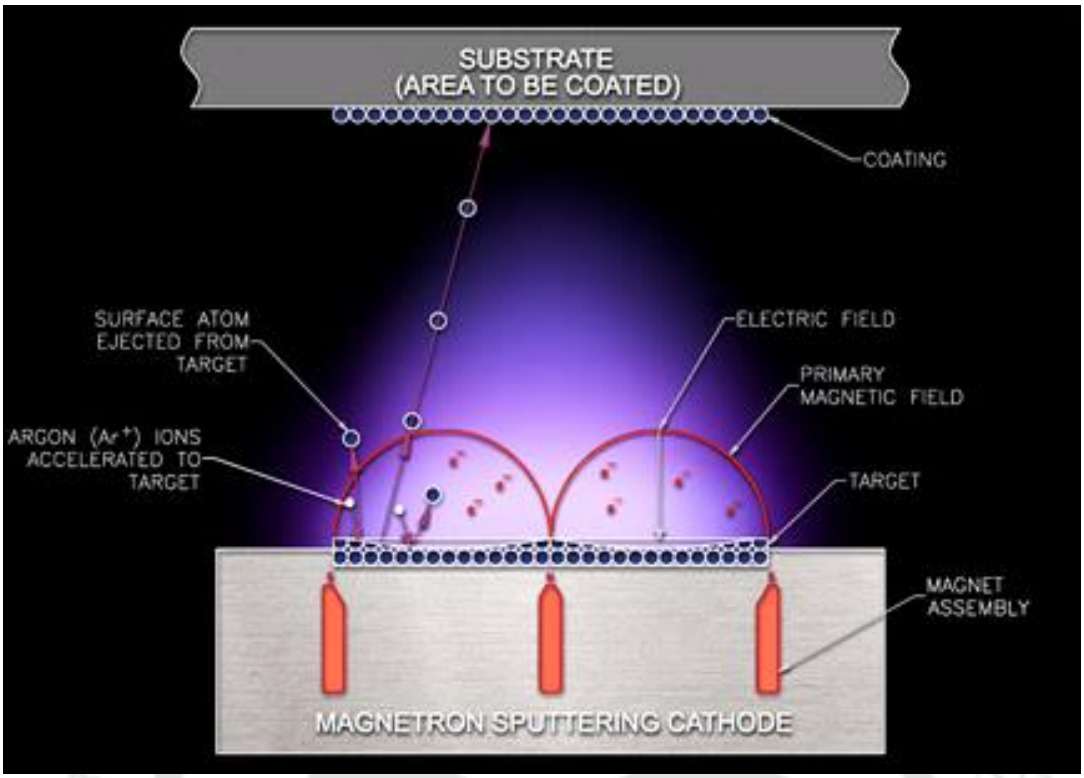

Figure 3.04: Schematic presentation of magnetron sputtering gun assembly [PERU20132].

3.2.1.3. Magnetron sputtering technique

In magnetron sputtering, electrons ideally don't reach the anode but are confined near the target material by the magnetic field and thereby augmenting the ionization efficiency. This is accomplished by applying a magnetic field parallel to the target and perpendicular to the electric field. Practically, this can be achieved by placing bar magnets behind the target material, as shown in Figure 3.04. The magnetic field lines originate first normal to the target, bend with a component parallel to the target surface, and finally return to the magnet, completing the magnetic circuit. Electrons emitted from the cathode are initially accelerated toward the anode but undergo a helical motion when they encounter the region of parallel magnetic field lines. As a result, they are bent in orbit back to the cathode. The primary reasons for its success are (1) high sputtering rates (~ 5 - 10 times) due to increased plasma density around the cathode, (2) low discharge voltages of 300 to 1000 V because of the reduced plasma impendence resulting from high plasma density, and (3) lower thermal load of the substrate due to deflection of the secondary electrons by the magnetic field.

(a)

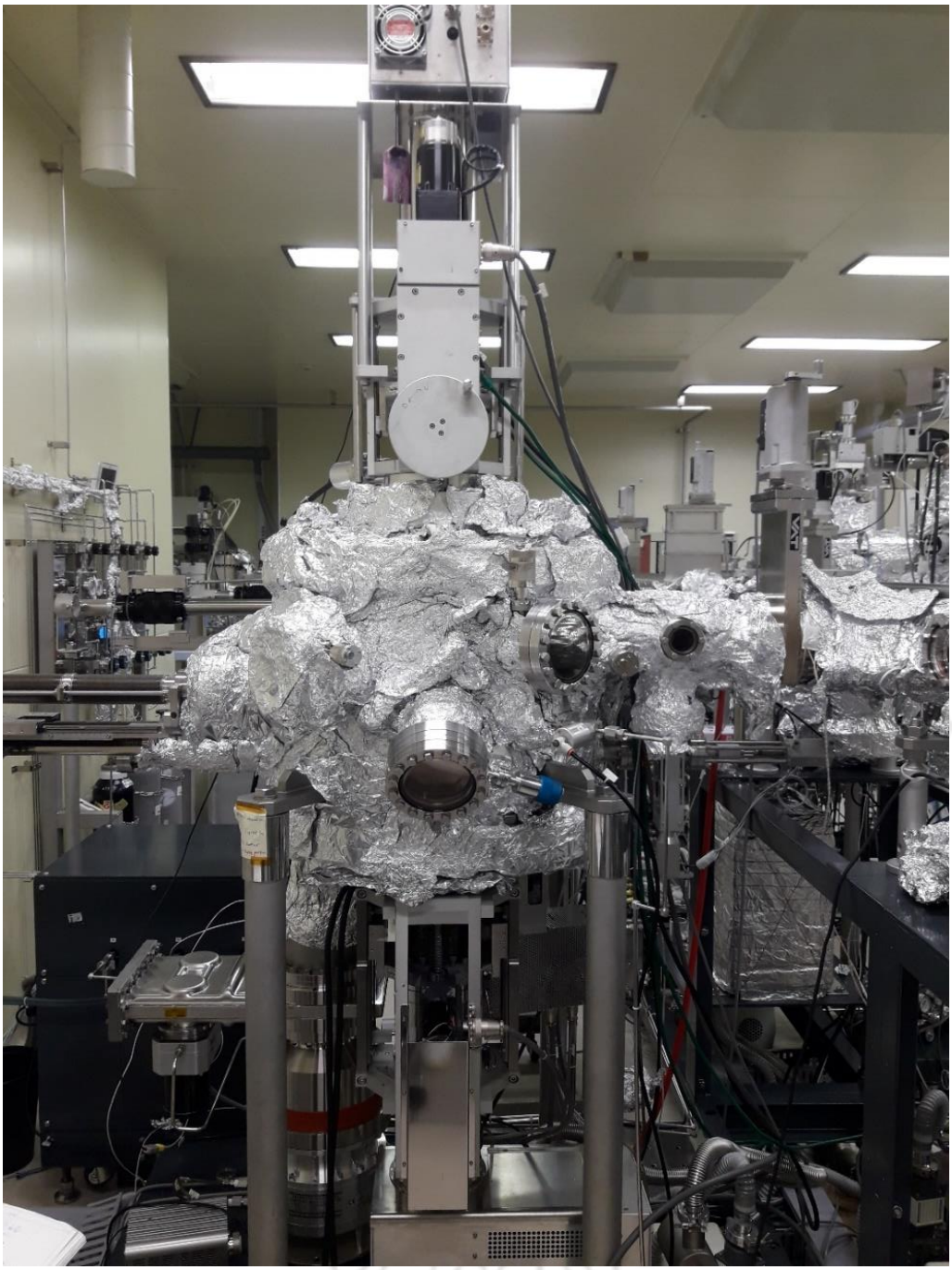

(b)

Figure 3.05: Photographic views (a,b) of the ultra-high vacuum magnetron sputtering system used in the present work [NIMS2019].

3.2.1.4. Ultra-high vacuum thin film deposition system

Figure 3.05 depicts the ultra-high vacuum (UHV) thin film deposition system equipped with multiple DC/RF magnetron sputtering guns used in the present thesis work for fabricating single and multilayer structured thin films. The base pressure of the chamber was maintained

to be better than 1×10^{-7} Pa. The sputtering chambers are interconnected through transfer chambers and equipped with 18 different sputtering guns to deposit multilayer thin films in a single go without any exposure to the open-air atmosphere. The presence of the load-lock chamber allows changing samples without breaking the ultra-high vacuum condition. The UHV condition is reached/maintained using the combination of the turbo-molecular pump (TMP) and a rotary pump (RP). Ion vacuum gauges monitor the pressure at the UHV condition, and a Pirani vacuum gauge measures the chamber Ar pressure. In the sputtering chamber, the surface of the MgO substrate was etched by Argon ion milling before depositing the films to obtain (001)-oriented epitaxial growth. The Ar gas of optimum pressure was allowed into the chamber using a mass flow controller (MFC). The working pressure of the Ar gas inside the chamber was maintained by adjusting the MFC and processing valve. The optimized working Ar gas pressure for the deposition of CoFe, Rh, Cu, and MgO films was fixed at 3, 3, 5, and 10 mTorr, respectively. After stabilizing the constant Ar gas pressure inside the chamber, a constant DC power was applied to commence the sputtering process.

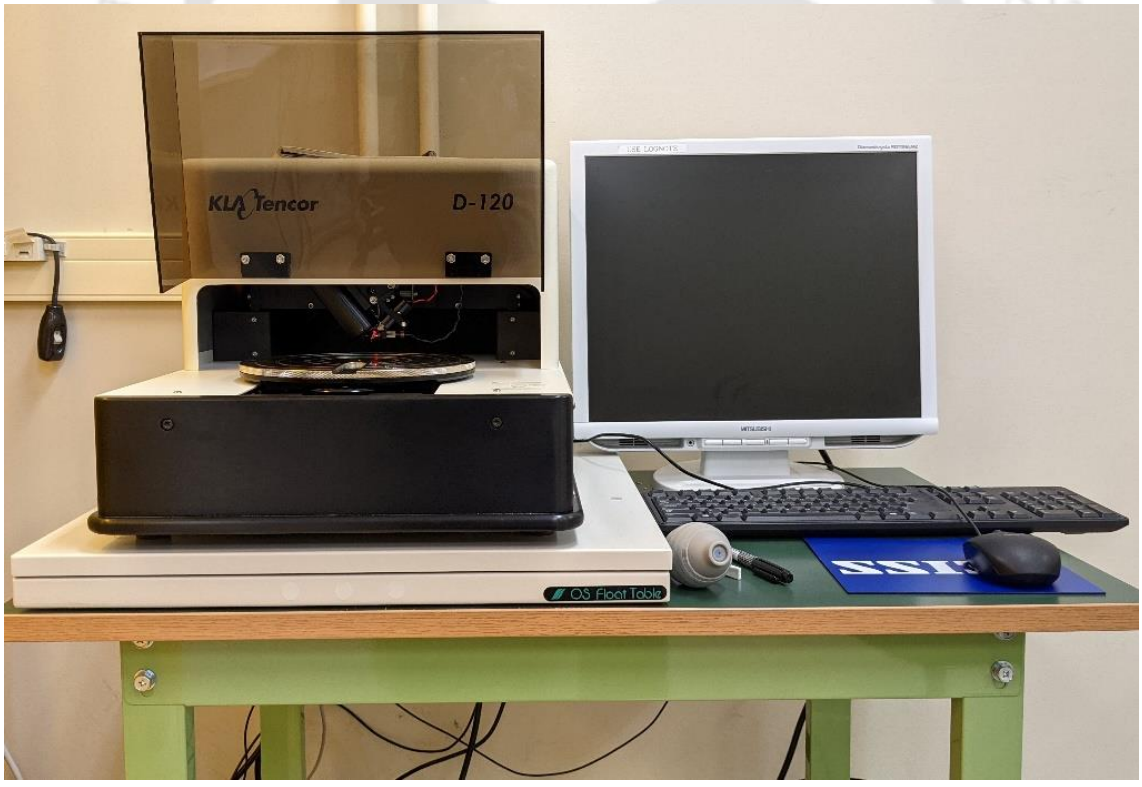

Figure 3.06: Photographic view of KLA-Tencor D-120 stylus profilometer used in the present investigation [NIMS2019].

The deposition of the films was carried out after stabilizing the Ar^+ plasma and completing the pre-sputtering process. The deposition rate of all the films was calibrated utilizing an *ex-*

situ stylus profilometer (KLA-Tencor D-120), as illustrated in the following section. There are shutters placed separately in front of each sputtering target and a main shutter before the sample holder. Hence, by optimizing the deposition rate of each target material and by utilizing shutters, multilayer films with different thicknesses were successfully prepared.

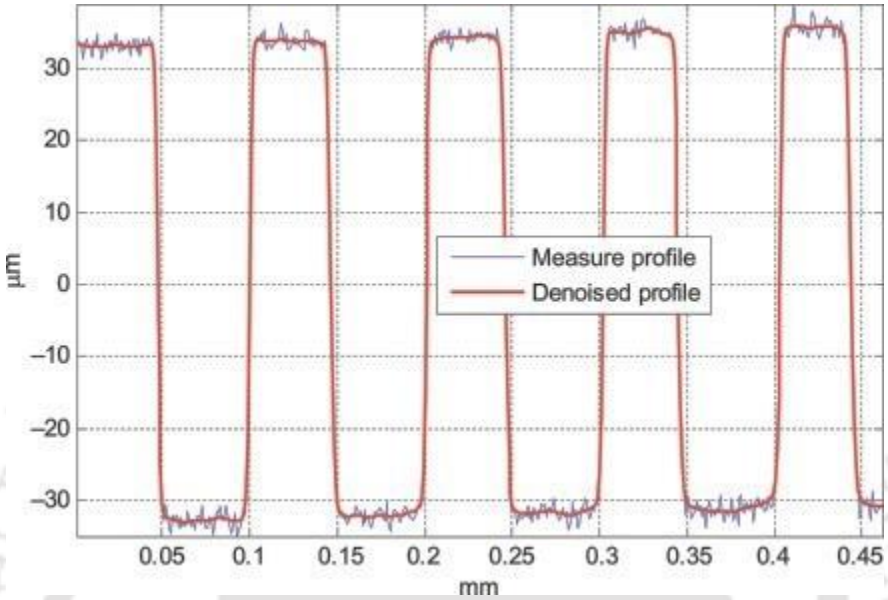

Figure 3.07: A typical scan profile of a standard sample using the stylus profilometer.

3.2.2. Calibration of deposition rate

As the properties of thin films are strongly dependent on their thickness, the pre-calibration of thickness under the optimized sputtering condition becomes crucial. To optimize the properties of the films at different thicknesses, it is vital to control the thickness of the film deposited under a controlled environment. The deposition rate of the thin films fabricated in the present study was calibrated with a surface profilometer (KLA-Tencor D-120), as illustrated in Figure 3.06. Stylus profilometer is one of the most versatile measurement tools for examining surface topography. The primary function is to measure film thickness by scanning step heights and trench depths. The stylus profilometer typically relies on a small-diameter stylus moving along the surface either by the stylus movement or by the movement of the surface of interest. An ideal stylus profilometer moves linearly to acquire the measurement. As the stylus encounters any surface features, the stylus moves vertically to measure the nature of the surface feature, such as the deposited film, surface irregularities, *etc*. To estimate the thickness of the prepared films, first, neat markings were made using a permanent marker on top of the cleaned substrate. Subsequently, the deposition was carried out under a controlled sputtering environment (constant working Ar gas pressure, DC power,

and substrate to target distance, *etc*.) for a constant time at ambient temperature. After completing the deposition, the film was cleaned in ethanol, followed by sonication in acetone. As a result, the film deposited on the substrate developed an explicit step.

The step height was estimated using the surface profilometer, as displayed in Figure 3.07 for the standard sample. The mean deposition rate was calculated by dividing the mean thickness measured at various locations on the substrate with deposition time. Several films were subsequently made under the exactly same sputtering conditions and examined using the surface profilometer to confirm the reproducibility. Similar procedures were followed for all the films deposited under different sputtering conditions.

3.3. Physical etching technique

3.3.1. Photolithography

Lithography-based microfabrication is a set of techniques that allow complex 3D structures in the micrometer or sub-micrometer scale. Advantages of lithography include (i) designing of complex geometries that are otherwise impossible, (ii) integration of multiple devices and miniaturization of the chip area, and (iii) improving the circuit performance and higher degree of control in preparing the electrodes. The method of micro fabricating devices comprises of the following basic steps: 1) cleaning and preparation of the thin film surface, 2) resist coating, 3) exposure and development of the pattern, and 4) etching and removal of resist [MACK2007, RASS2011]. The entire process is summarized in Figure 3.08 and explained in more detail below.

1) Cleaning and preparation

Organic or inorganic contaminants present on the surface of films were removed by sonicating the sample for 10 minutes in butanone. The sample was then sonicated in isopropyl alcohol for 10 minutes. Later, the surface of the films was flushed using an N_2 air gun to drive off any moisture that may be present on the film surface.

2) Resist coating

Resists are mostly radiation-sensitive viscous organic polymers that can be easily dispensed on the film surface. According to the response of a resist to ultraviolet (UV) – radiation, they are mainly classified into positive or negative. In a positive resist, the UV exposure tends to

weaken the polymer, and the exposed resist becomes more soluble in the developing solutions.

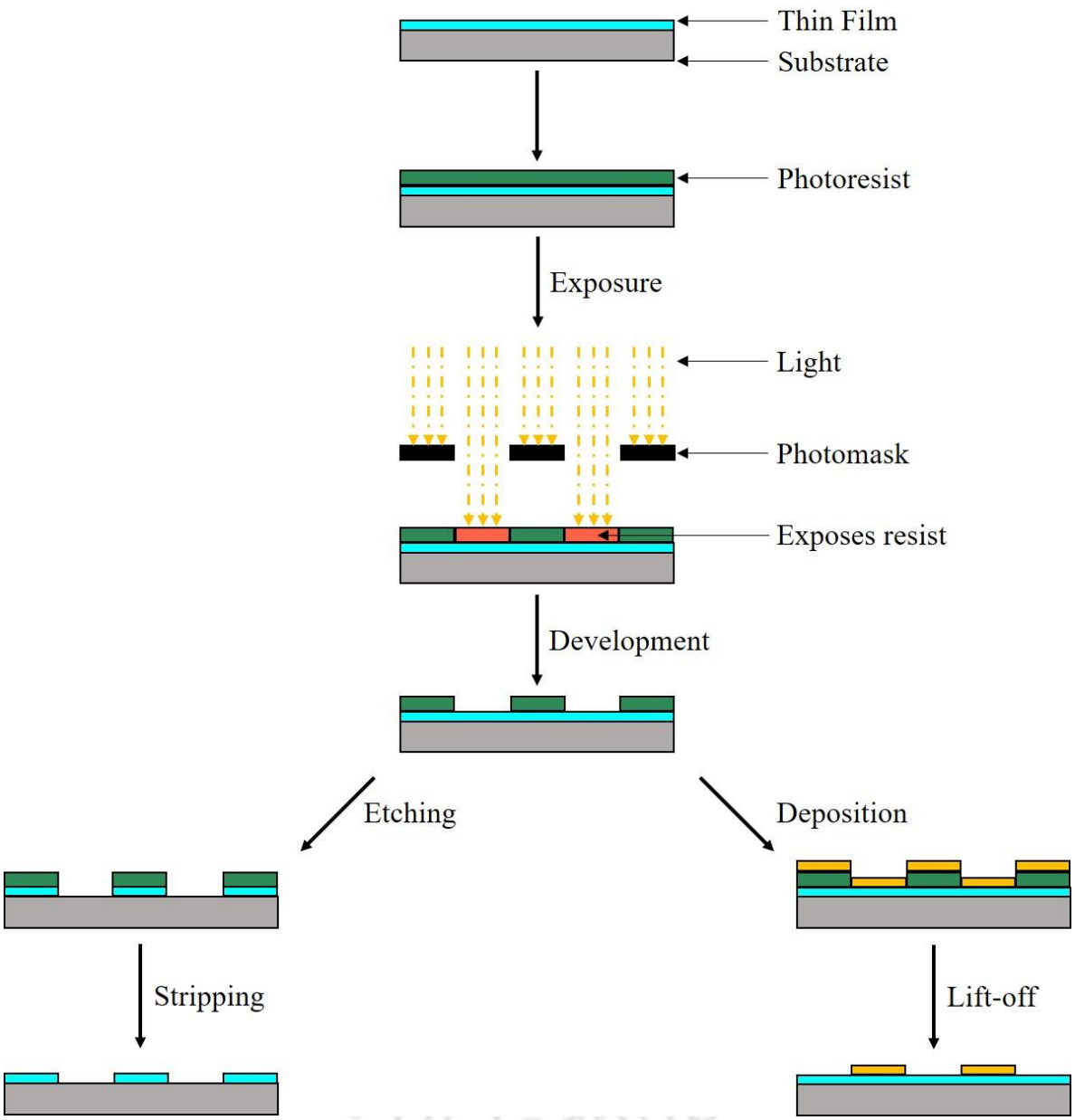

Figure 3.08: Schematic representation of the key steps involved in a typical lithographic process [RASS2011].

The reverse happens in a negative resist, *i.e.*, the reaction strengthens the polymer making it less soluble in the developer. Different types of radiation, determined by choice of resist resulting in wide-ranging lithographic techniques, such as photolithography, electron-beam lithography, ion-beam lithography, X-ray lithography, *etc.*, can be used. In the present thesis,

photolithography has been employed to pattern the films into current-in-plane (CIP)-giant magnetoresistance (GMR) devices.

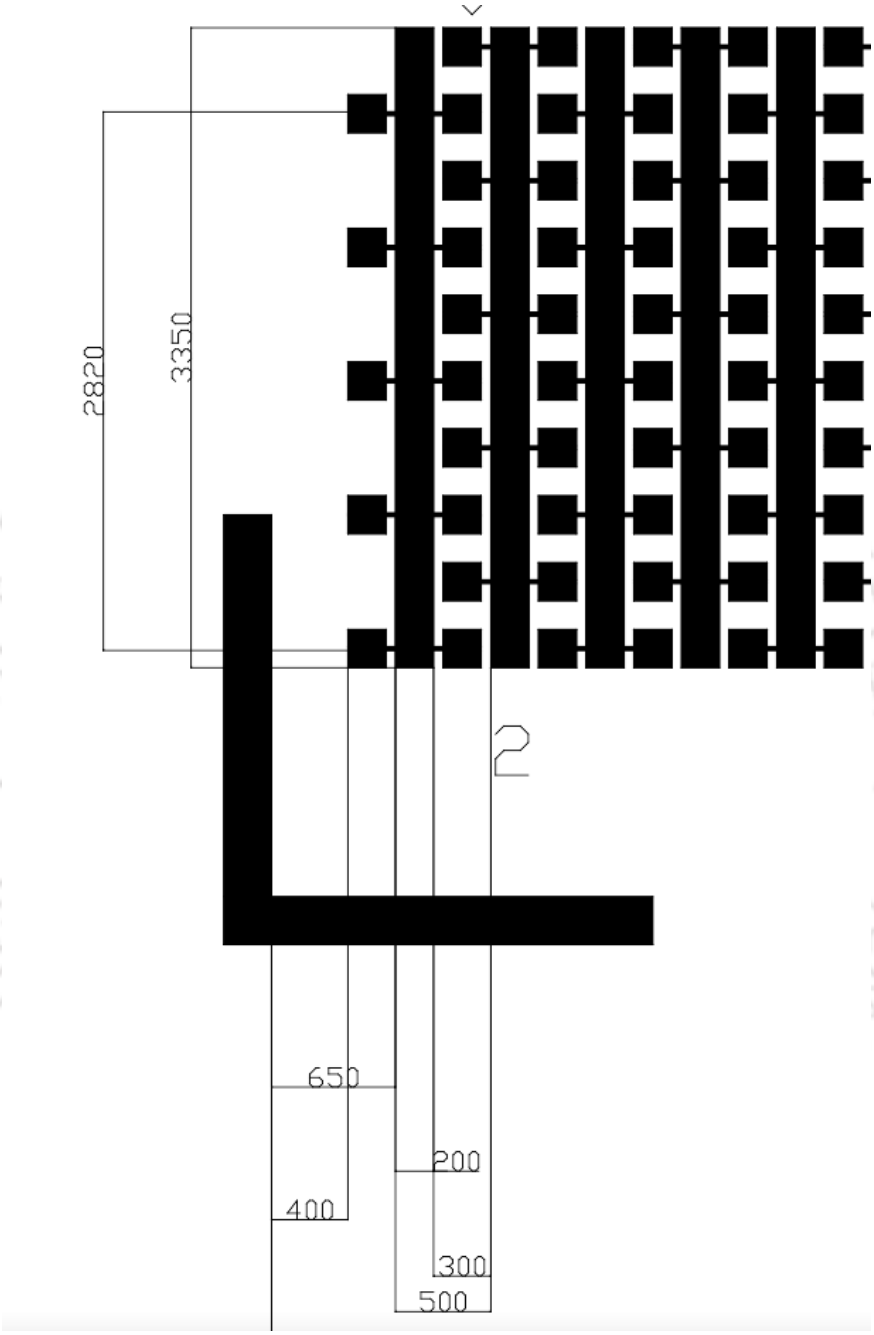

Figure 3.09: A schematic representation of the photomask used in the current study. All lengths are in μm.

A thin uniform layer of the positive photoresist, AZ5214E was spin-coated on the sample surface at 1000 rpm for 5 secs. The photoresist-coated sample was then prebaked to drive off the excess photoresist solvent at 100 °C for 120 seconds on a hotplate. The sample was subsequently kept in a black box to avoid exposure to white light that may interfere with

the ultimate UV exposure. The entire process of patterning has been carried out inside a cleanroom.

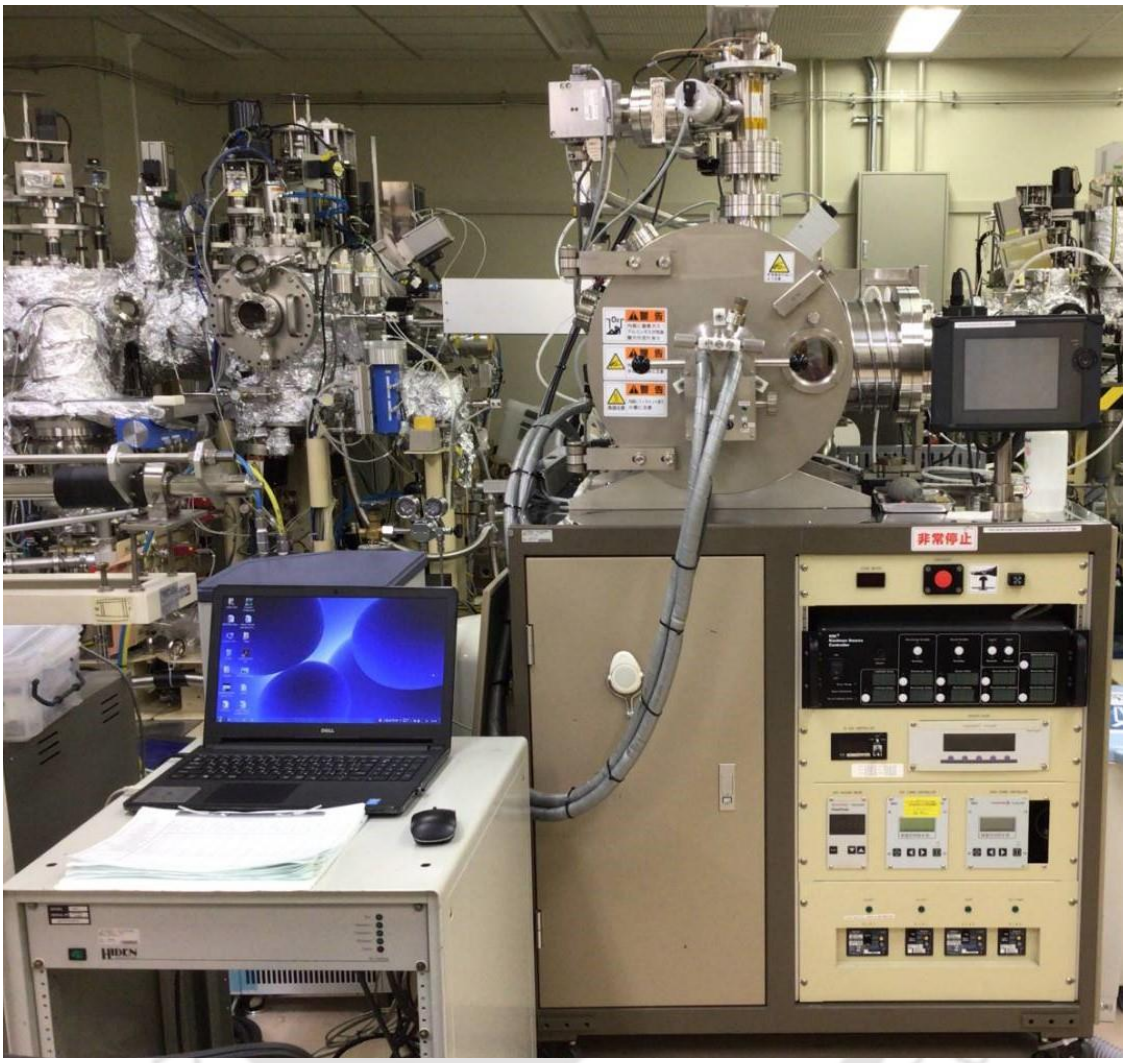

Figure 3.10: Photographic view of the Ar ion milling setup used in the present investigation [NIMS2019].

3) Exposure and development of the pattern

After prebaking, the photoresist is subjected to UV radiation through a master pattern called a photomask. The fundamentals of the operation of a photoresist are the different dissolution rates of the exposed and unexposed resist areas in a special solution, called developer, permitting the realization of a structured photoresist mask. A schematic of the photomask used in the current study is demonstrated in Figure 3.09. After the mask alignment, the photoresist was exposed to UV light for 18 sec. The process of developing the photoresist is essential in controlling the development and uniformity of the device. The patterned photoresist was ultra-sonicated for 90 secs in AZ developer followed by an immediate 30-

sec sonication in distilled water at 25 °C. The sample was then blow-dried by N_2 gas to remove any moisture from the surface. In principle, the standard photolithographic method offers reasonably high resolution down to $\lambda/2$, where λ is the wavelength of the exposure radiation. This explains the prevalence of UV light in photolithography. However, the attainable resolution is often restricted by practical problems, such as photomask damage, properties of the resist, the ability to align subsequent layers to each other, and so on.

4) Etching and removal of the resist

After developing the pattern on the photoresist, the next step is to transfer the pattern to the film surface. It can be achieved using etching, which strips exposed regions of the film, which are no longer covered by photoresists. The UV cured positive photoresist 'resists' the etchant shielding, the coated regions of the film. Etching is carried out either by using chemical and physical methods. The most commonly used physical etching mechanism is the ion-milling technique, achieved by accelerating the ions of an inert gas (typically Ar) onto the surface of the film in a high vacuum chamber to remove the unprotected part of the film to some desired depth necessary to pattern the film. The Ar ion milling setup used in the present investigation is shown in Figure 3.10. After the photoresist is no longer needed, it is removed (or "stripped") from the film surface. For most of the devices, these steps must be iterated multiple times by successively depositing and patterning different layers to construct complex 3D patterns. For electrode deposition in our CIP-GMR devices, a 100 nm layer of gold was deposited on the patterned film surface. Finally, the photoresist pattern is dissolved by ultra-sonicating the film in acetone for 10-15 min. It dissolves that part of the film deposited directly on the resist, leaving behind the part that was deposited on top of the film.

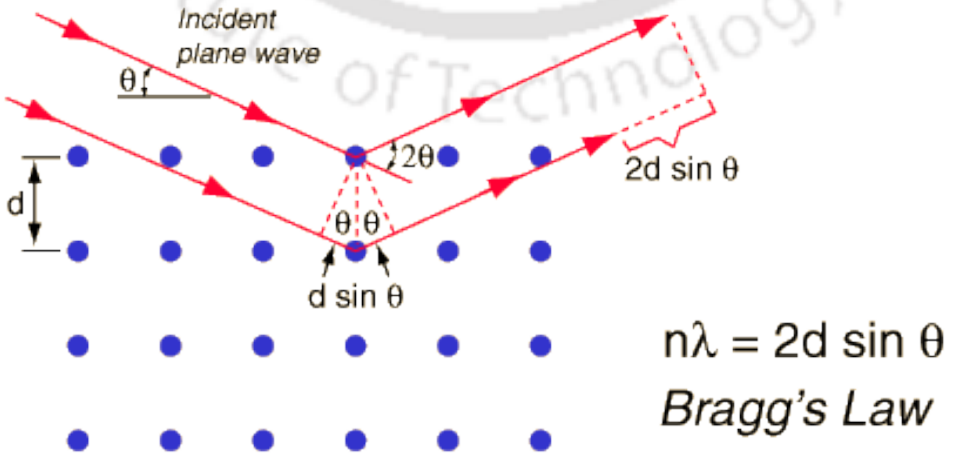

Figure 3.11: Schematic ray diagram of diffraction of X-rays by a crystal.

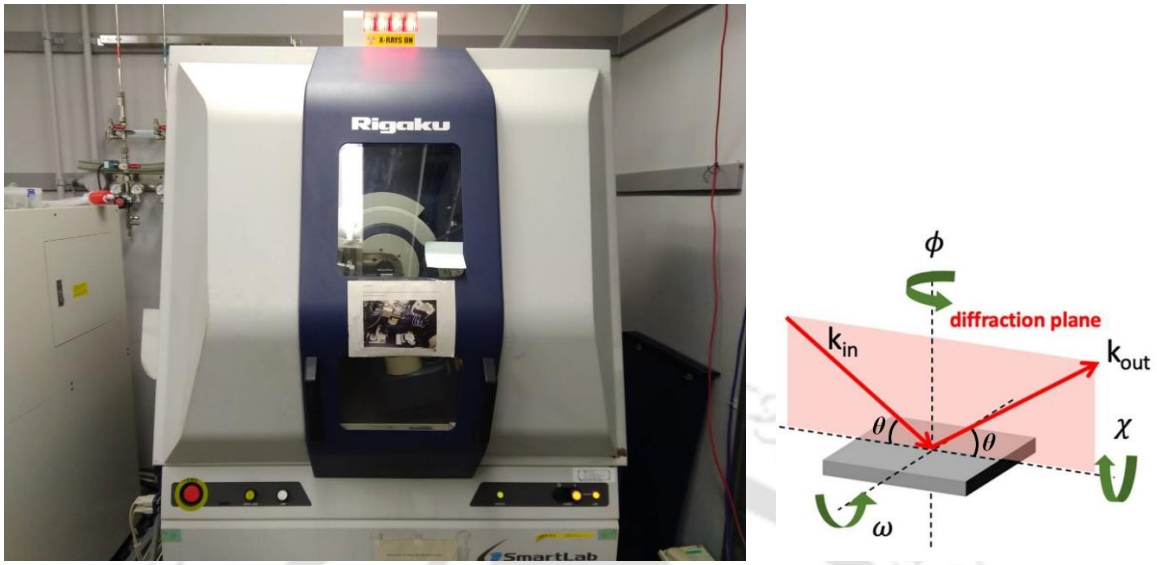

(a) (b)

Figure 3.12: (a) Photographic view of Rigaku, Smartlab X-ray diffractometer used in the present investigation, and (b) Schematics of various geometrical angles related to different scan modes in XRD.

3.4. Structural property characterization

3.4.1. X-ray diffraction

X-ray diffraction (XRD) is a very powerful and nondestructive technique adopted to analyze the presence of various mixed phases, degree of crystalline order, and quantitative analysis of secondary phases present in a crystalline system. A crystallographic structure has a periodic planar arrangement of atoms. The diffraction pattern of X-rays occurs through constructive interference of X-rays reflected from atoms of a set of parallel planes in crystal lattice at specific angular positions of the incident wave known as Bragg angles [CULL2001]. This criterion for obtaining constructive interference of X-rays is well-known as Bragg's law and described by the relation

$$2d_{hkl} \sin\theta = n\lambda \qquad (3.01)$$

where, d_{hkl} is the inter-planer spacing, θ is the glancing angle, λ is the wavelength of incident X-ray (Cu-K_α = 1.541 Å), and n is the order of diffraction. We consider only first-order diffraction, *i.e.*, $n = 1$. A series of these angles can be used to estimate the Miller indices (*hkl*) values of the corresponding crystal lattice planes, and the crystal structure can be recognized from the systematic behavior of these Miller indices. Figure 3.11 displays the diffraction of

X-rays from the crystal lattice planes demonstrating Bragg's law. Various structural parameters, such as the average size of the crystallites, inter-planer distance or *d*-spacing, lattice constants, the strain present inside the crystallites, *etc.*, can be calculated by analyzing the XRD patterns using various models [CULL2001]. In the present work, Rigaku, Smartlab X-ray diffractometer (see Figure 3.12a) was used using various as described in Table 3.01.

Table 3.01: The main scan types available in high-resolution diffractometers. ω refers to the angle between the incident beam (Figure 3.12b) and the sample surface, 2θ refers to the angle between the incident and diffracted beams [MORA2009].

Scan type	Description
2θ - ω	The X-ray source is rotated by ω and the detector by 2θ with an angular ratio of 1:2. When there is no offset and $\omega = \theta$, this results in the symmetric diffraction geometry in parafocusing Bragg-Brentano (BB) arrangement. In this case, both the source and the detector make the same angle θ with the surface of the sample throughout the scan resulting in a double angular speed of the detector arm. The 2θ-θ scan is mainly used to scan powder samples.
2θ	The 2θ scan is one of the most common X-ray diffraction scans for thin film measurement, known as grazing incidence XRD (GI-XRD). Here, only the detector moves, and ω is held fixed at a low angle. This scan can be used to eliminate substrate peaks of thin film samples or align to a substrate peak on an epitaxial thin film sample.
χ - φ	To understand the epitaxy and distribution of crystallite orientations, the sample is rotated along its χ - axis (plane of the sample rotated with respect to the incoming beam (Figure 3.12b)) and φ - axis (in the plane of the sample (Figure 3.12b)) while fixing θ and 2θ corresponding to the Bragg reflection of interest.

3.4.2. Transmission electron microscope

Transmission electron microscopy (TEM) was used to study the microstructure of the films. Figure 3.13 depicts a photo view of the TEM ((S)TEM; FEI Titan G2 80-200) used in the present investigation. Figure 3.14 displays the cut-view of a typical TEM, schematic ray diagrams for imaging (Figure 3.14b), and different diffraction modes (Figure 3.13c). TEM is an optical equivalent to the standard light transmission microscope, which is based on the

fact that electrons not only have an ascribed wavelength but can also interact with magnetic fields as a point charge. Instead of visible light, a beam of electrons is used, and the glass lenses are substituted with magnetic lenses. Since the wavelength of electrons is much smaller than that of light, the magnitude of optical resolution achievable by TEM is multiple orders higher than the light microscope. Thus, the lateral resolution of the best microscopes is down to atomic resolution.

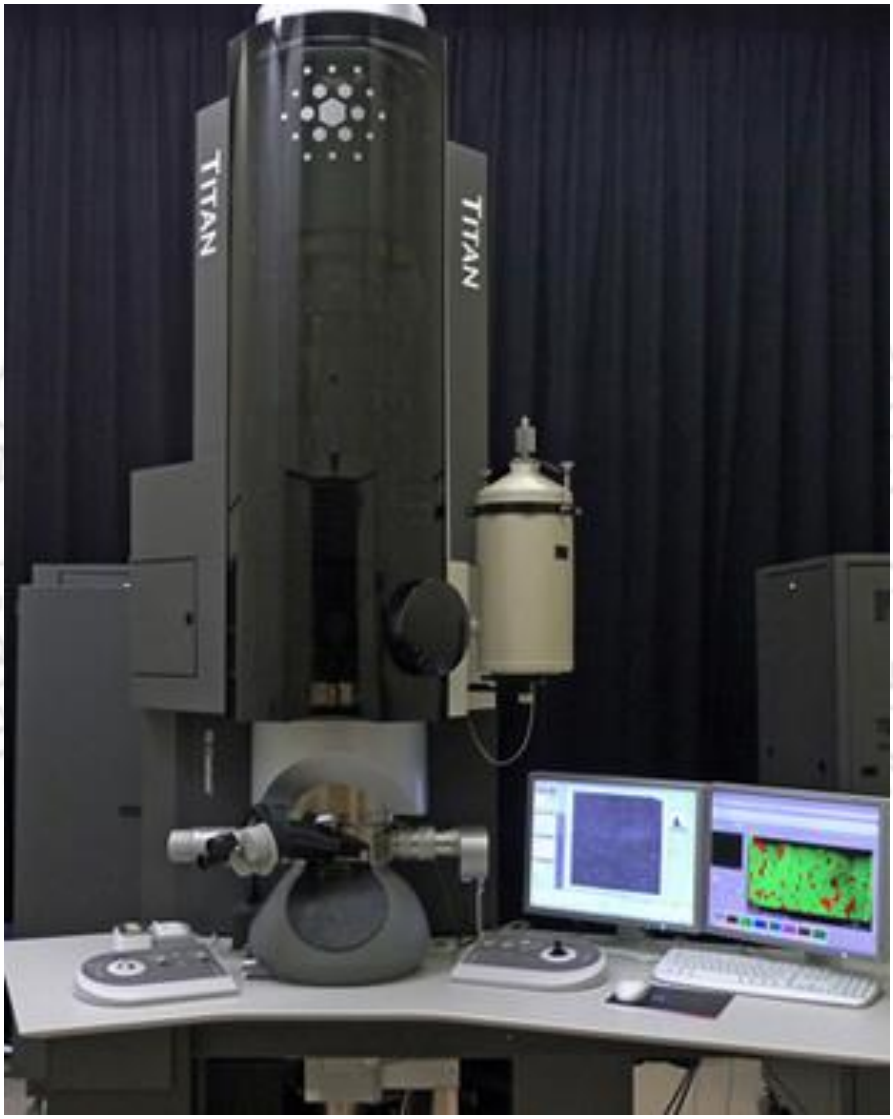

Figure 3.13: Photographic view of the TEM [(S)TEM; FEI Titan G2 80-200] used in the present investigation [NIMS2019].

In TEM, electrons emitted from the gun are rapidly accelerated to 200 keV or higher and first projected onto a thin specimen with the help of an electromagnetic condenser lens system. Scattering processes experienced by the electrons during their passage through the specimen govern the kind of information obtained (see Figure 3.15).

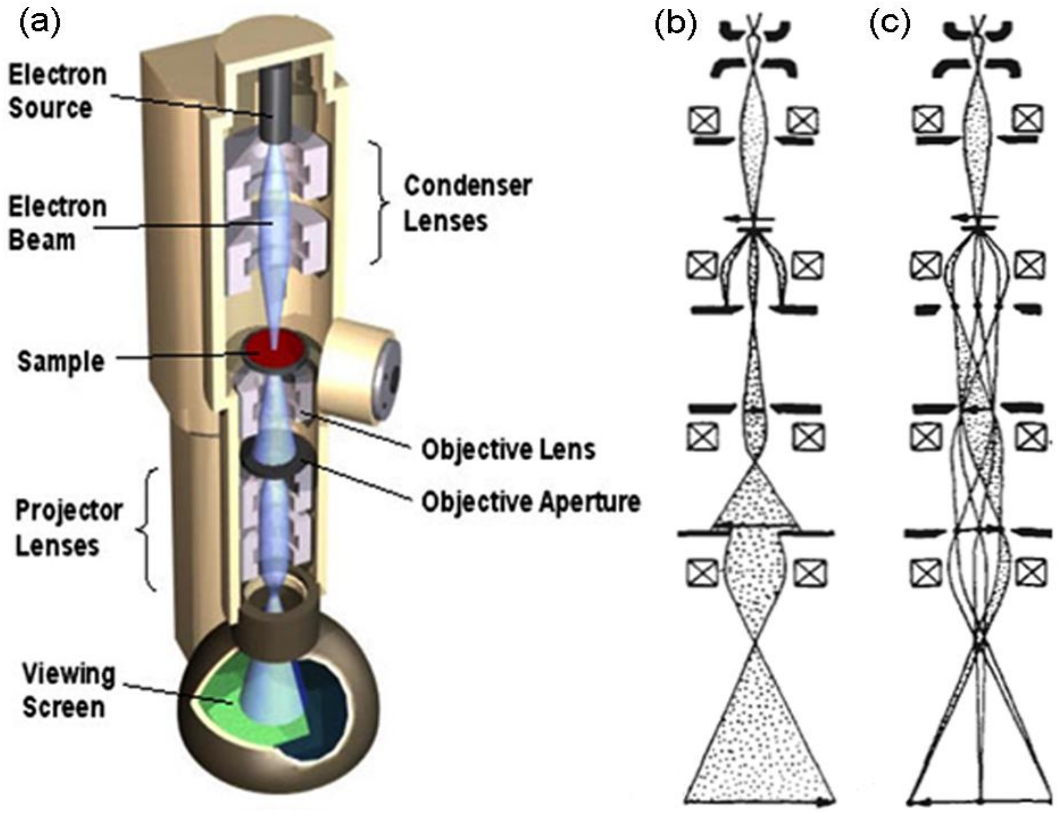

Figure 3.14: (a) Cut-view of the transmission electron microscope, (b) schematic ray diagrams of image mode, and (c) diffraction mode of TEM [PERU2016].

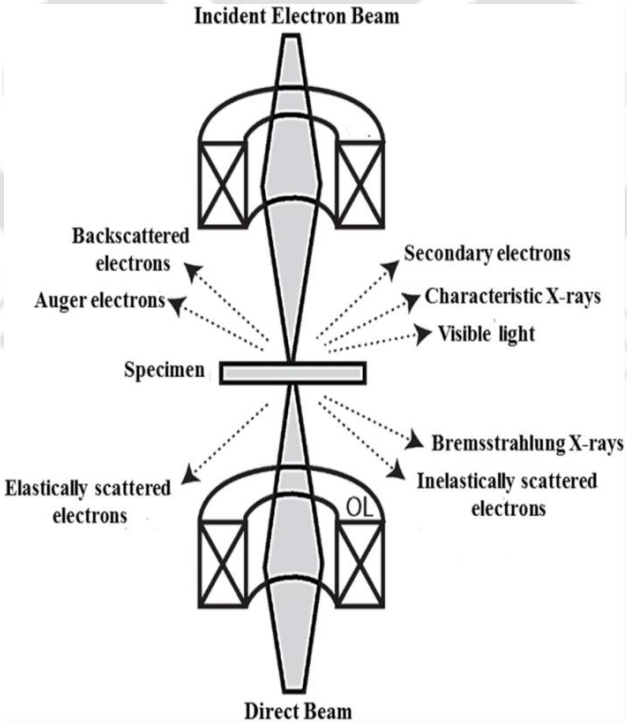

Figure 3.15: Signals generated due to electron beam interaction with a thin solid specimen [PERU2016].

The electrons encounter the following processes: (i) the path of electrons being unobstructed, (ii) elastic scattering, resulting in no energy loss as electrons interact with the potential field of the ion cores, giving rise to diffraction patterns, and (iii) inelastic interaction between the beam electrons and matrix electrons at heterogeneities, in particular grain boundaries, defects, and dislocations, second-phase particles, density variations, *etc*., leading to complex absorption and scattering effects, causing spatial variation in the intensity of the transmitted beam. The transmitted beams are further magnified by a series of intermediate and projector lenses and are finally projected on a fluorescent screen.

Microstructural images can be obtained in several ways. The bright-field TEM image is obtained by intentionally eliminating all the diffracted beams and allowing only the central beam to pass through the specimen. It is accomplished by placing appropriately sized apertures in the back focal plane of the objective lens. Dark-field images are also produced by magnifying one of the diffracted beams with the help of an aperture that blocks the central beam and other diffracted beams. In the third method of imaging, recombination of the primary transmitted and one or more of the diffracted beams is done, thus conserving both their amplitudes and phases. This technique is used in high-resolution lattice imaging, enabling the identification of diffraction planes and arrays of individual atoms. From a high-resolution TEM (HR-TEM) micrograph, average grain size, crystallographic structure, lattice constant, and dislocations can be estimated. On the contrary, the selected area electron diffraction (SAED) is done by completely excluding the central beam using a beam blocker and accumulating all the diffracted beams to produce the diffraction patterns. The composition analysis of the samples can also be performed using X-ray energy dispersive analysis interfaced with TEM. The electrons emitted from the filament (cathode) are accelerated to very high energies colliding with the specimen target (anode). X-rays corresponding to the characteristic of atoms are emitted in the process. The atoms can be identified by examining their energies, and the concentration of atoms in the specimen can be obtained by counting the number of X-rays emitted. In the present study, the microstructures of the samples, especially Rh and Cu spacer interfaces, were analyzed by using an aberration-corrected (scanning) transmission electron microscope [(S)TEM; FEI Titan G2 80-200] as shown in Figure 3.13. The (S)TEM observation specimens were prepared by the lift-out technique using a dual-beam focused-ion-beam/scanning electron microscope (FIB/SEM; FEI Helios G4).

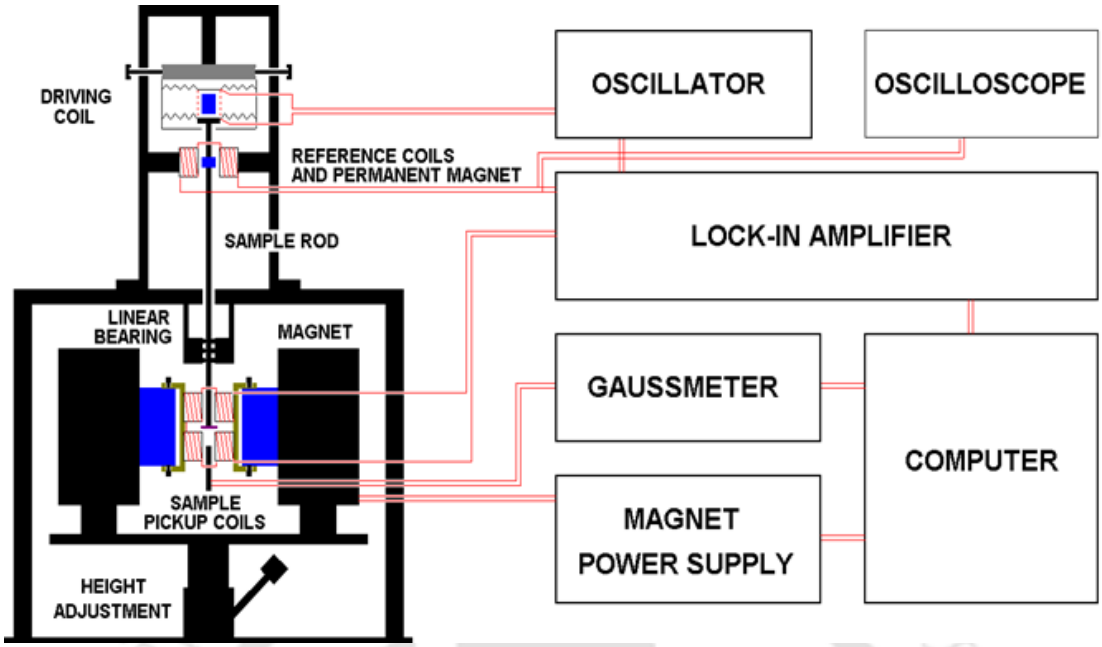

(a)

(b)

Figure 3.16: (a) Schematic diagram [PERU2016] and (b) photograph of vibrating sample magnetometer (VSM, LakeShore Model 7410) used in the present investigation [NIMS2019].

3.5. Magnetic property characterization

Magnetic properties of the magnetic materials can be analyzed with various experimental techniques such as vibrating sample magnetometer (VSM), superconducting quantum interference device (SQUID), physical property measurement system (PPMS), Faraday balance, ac susceptometer, *etc*. In this section, a brief outline of the principle involved in various magnetic measurement techniques used in the present work is described.

3.5.1. Vibrating sample magnetometer

Vibrating sample magnetometer (VSM, Lake Shore Model 7410) was used to characterize the room temperature magnetic properties of our samples. VSM measures the net dipole moment when a magnetic material is exposed to an external magnetic field [CZIC2006, SVOB2004]. The magnetization of the material can be recorded either as a function of the applied magnetic field, known as magnetic hysteresis (*M-H*) loop, to understand the magnetic properties with respect to the applied field or as a function of temperature (*M-T*) to investigate the magnetic phase transition of the material. Figure 3.16 illustrates a schematic diagram of VSM and a photograph of the VSM used in the present study.

VSM comprises of the following main parts: (i) Vibration exciter and specimen holder, (ii) water-cooled electromagnet and power supply, (iii) Hall probe, (iv) pickup coils, (v) amplifier, (vi) control panel, (vii) lock-in amplifier and (viii) computer interface. When a magnetic material is placed in a uniform magnetic field, a dipole moment directly proportional to the product of the material susceptibility, and the applied external field is induced in the material. If the material undergoes periodic motion (vibration driven by a sinusoidal voltage), an electrical signal is induced in the stationary pickup coils based on Faraday's law (see Figure. 3.16). This signal has an amplitude proportional to the magnetization of the sample, the amplitude of vibration, and the vibration frequency. With the help of lock-in-amplifier and feedback techniques, the portion of the signal arising solely from the magnetic moment is precisely picked up and converted into direct read-out in the magnetization unit (*i.e.*, emu) on a digital panel meter.

The thin film sample was fixed at the extreme lower end of the sample holding rod, aligned along either in-plane or out-of-plane direction with respect to the applied field. Prior to the magnetic measurements, a calibration procedure was carried out using a standard Ni sample. The measurement sequence is programmed as per the user's choice by using the software (IDEASVSM) provided with the instrument in a way that the program starts either

from the maximum field or from zero applied field. The sequence is programmed to collect more data points, which helps extracting the magnetic parameters (saturation magnetization, coercivity, remenance magnetization, *etc*.) precisely. The exciter is vibrated at a sinusoidal frequency of 72 Hz (Lakeshore model 7410), and the signal that is received from the Hall probe and the pickup coils is converted into the magnetic moment of the sample. The magnetic field sweeps automatically in user-defined steps for measuring the *M-H* loop.

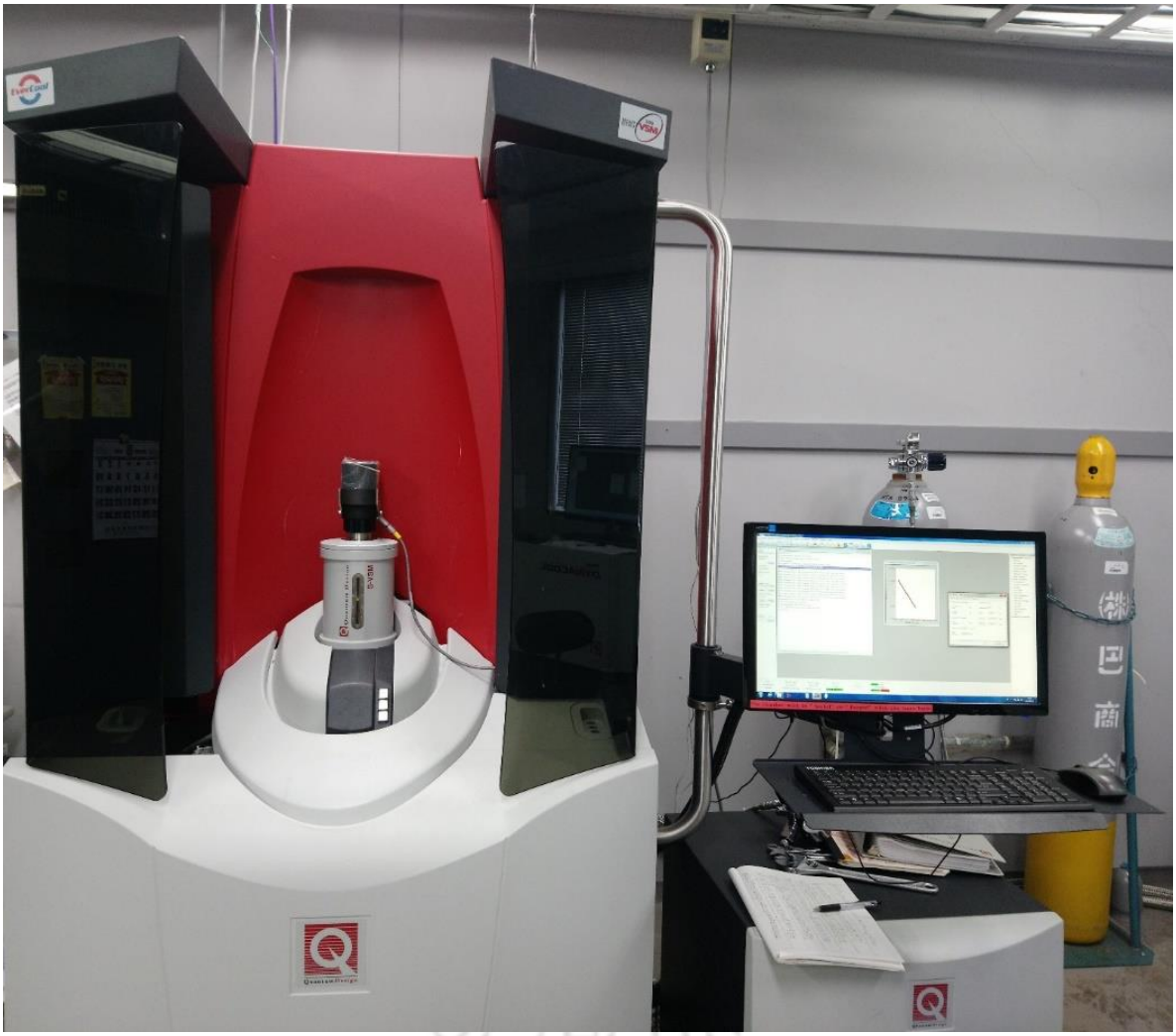

Figure 3.17: Photographic view of a superconducting quantum interference device (SQUID, Quantum Design) used in the present investigation [NIMS2019].

3.5.2. Superconducting quantum interference device magnetometer

The Superconducting Quantum Interference Device (SQUID) magnetometer can be considered as the modern extraction method for magnetic measurement where superconducting material is used for the detection coils instead of the classical ohmic conductors. Figure 3.17 illustrates the photographic view of a SQUID used in the present

investigation. The device works on the principle of tunneling of superconducting electrons across a very narrow insulating gap between two superconductors, known as Josephson junction. The detection coil comprises the loop of superconducting wire, separated by two Josephson's junctions. The effect of magnetic flux on a Josephson junction is used for measuring the magnetic fields or magnetizations. Compared to the classic magnetometers, the SQUID magnetometer provides much higher sensitivity. In principle, the name quantum interference is derived from the fact that signals corresponding to the magnetic flux quantum $\hbar/(2e)$ can be detected using SQUID due to interference effects of the coherent electron-pair wave functions. A typical dc SQUID is built using two Josephson junctions, and a DC is applied to the device. When a changing magnetic flux is applied to the ring, cooper-pair wave packets propagate on each side of the ring, resulting in a phase offset proportional to the penetrating flux but in the opposite sign [COEY2010].

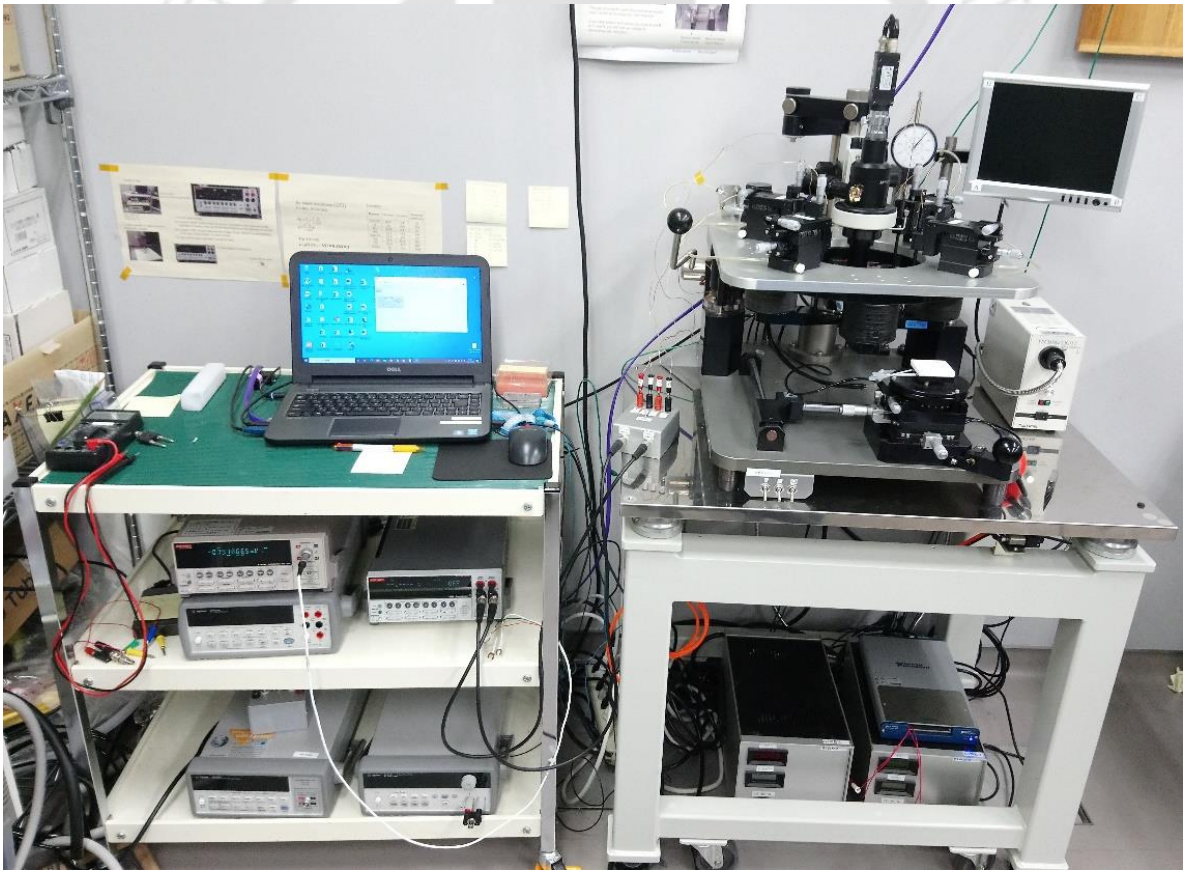

Figure 3.18: Photographic view of a DC four-probe MR prober used in the present investigation [NIMS2019].

The subsequent interference leads to a transmission probability periodic in the flux. The influence of a radio frequency (RF) field on the critical current is employed to detect the

quasi-static flux variations. An RF-SQUID sensor comprises of only one weak link, mostly a metallic point contact with only one Josephson junction. Its high frequency inductance is also periodic in the flux linking the ring. In any case, linearization of the field sensor is realized using a flux-locked loop. A lock-in amplifier is used to detect the resulting variation. A feedback arrangement is put in place to minimize the current flowing through the ring, where the size of the feedback current is a measure of the applied magnetic flux. The detection by means of a SQUID is extremely sensitive with a sensitivity of 10^{-7} emu.

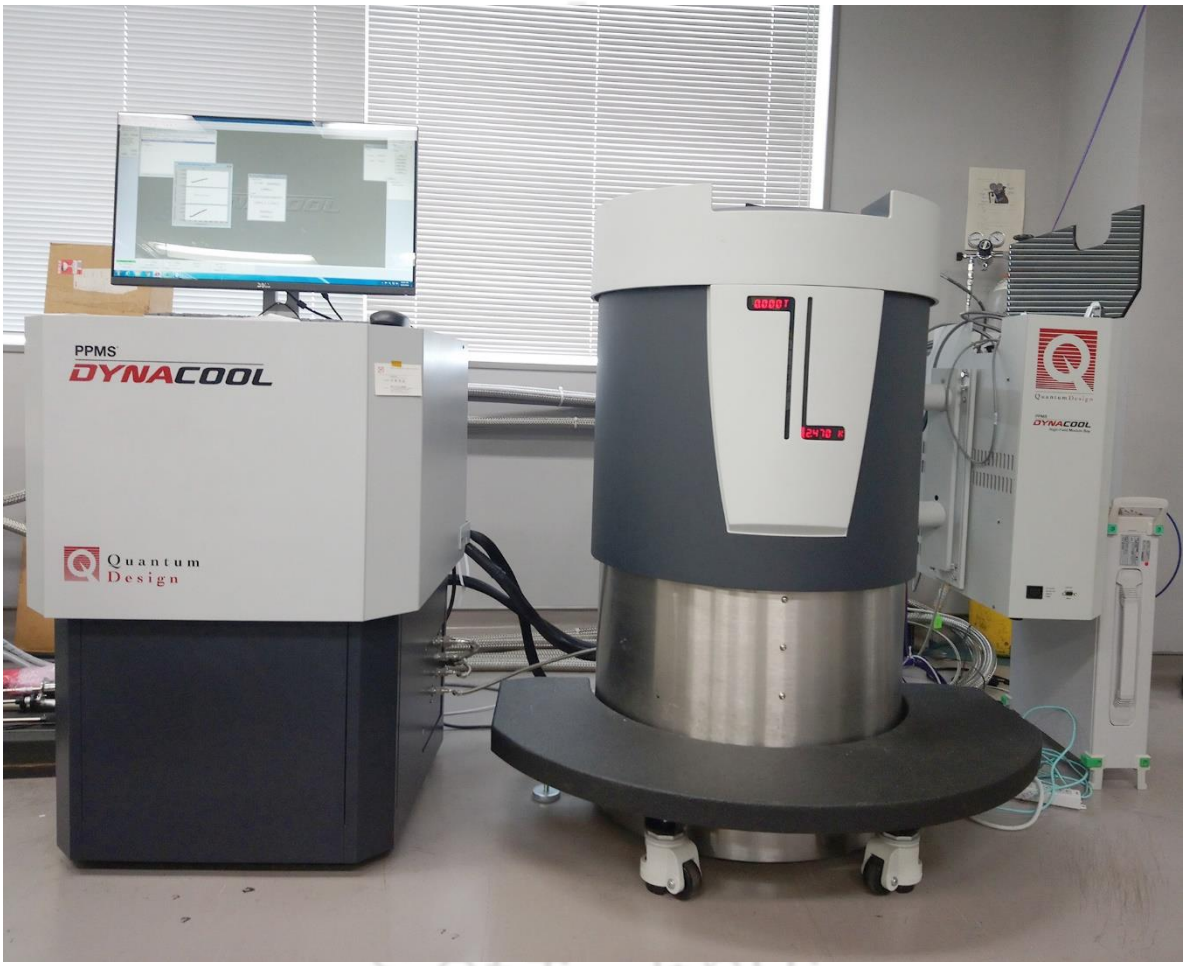

Figure 3.19: Photographic view of a physical property measurement system (PPMS Dynacool, Quantum Design) used in the present investigation [NIMS2019].

3.6. Magnetotransport property characterization

3.6.1. DC four-probe setup

The DC four-probe technique is one of the standard and most commonly used methods for resistivity measurement using separate pairs of current-carrying and voltage-sensing electrodes. The DC four-probe method combined with an externally applied magnetic field

yields the magnetotransport properties of the specimen. Figure 3.18 shows the photographic view of a DC four-probe converted to an MR prober using two perpendicularly arranged pairs of electromagnets surrounding the sample stage. In addition, the sample stage offers 360° rotation for anisotropic measurements. The system comprises four spring-loaded electrodes whose position can be adjusted in the longitudinal, lateral, and transverse directions, allowing the user to perform various experiments, *e.g.*, DC resistivity, Van der Pauw measurement, magnetoresistance (OMR, AMR, GMR, TMR), by this method. The position of the electrodes on the sample surface can be monitored via the LCD panel attached to the system. The pressure contacts offered by the four-probe technique overcomes contact resistance and are especially useful for quick measurements. The electromagnets used in the current investigation have a maximum field range of ±300 mT. The users can design different experiments as per their requirements and interface them with the four-probe set up using software like LabVIEW^{TM}.

3.6.2. Physical property measurement system

Physical property measurement system (PPMS) is a sensitive and versatile instrument for the measurement of a wide variety of physical properties, such as magnetization, Hall Effect, electrical resistivity, thermal conductivity, heat capacity, and thermal transport with a high degree of precision as a function of magnetic field or temperature. Figure 3.19 illustrates the photographic view of PPMS (Dynacool, Quantum Design) equipped with a dewar having a conduction-cooled superconducting switch-less magnet, pump setup for evacuating the sample chamber, lock-in-amplifier, and power source. The chamber integrates a universal 12-pin platform, and each of the measurement options uses its respective insert. The entire system is controlled by sophisticated and user-friendly software named MultiVu, which provides easy control of the operation of Dynacool during the experiment. Most of the measurement options can be operated in a temperature range of 1.8 – 400 K with the applied magnetic fields up to 14 T.

3.6.2.1. Magnetic measurements

For the room temperature magnetization measurements, the VSM mode of the PPMS was used to analyze the magnetic properties. The VSM configuration converts the PPMS into a highly sensitive DC magnetometer for faster and noise-free data acquisition. The VSM option mainly comprises of (i) VSM linear motorhead for vibrating the sample, (ii) detection coil

set puck, (iii) electronics for driving the linear motorhead and detection of response from the pickup coils, and (iv) computer interface. In this technique, by utilizing a suitable pickup coil configuration in the frequency range of 10 – 60 Hz (40 Hz typically) and a relatively large oscillation amplitude (0.1 - 5 mm peak, 2 mm typical), a change in magnetization as small as 10^{-6} emu can be detected with an accuracy of ± 0.5%.

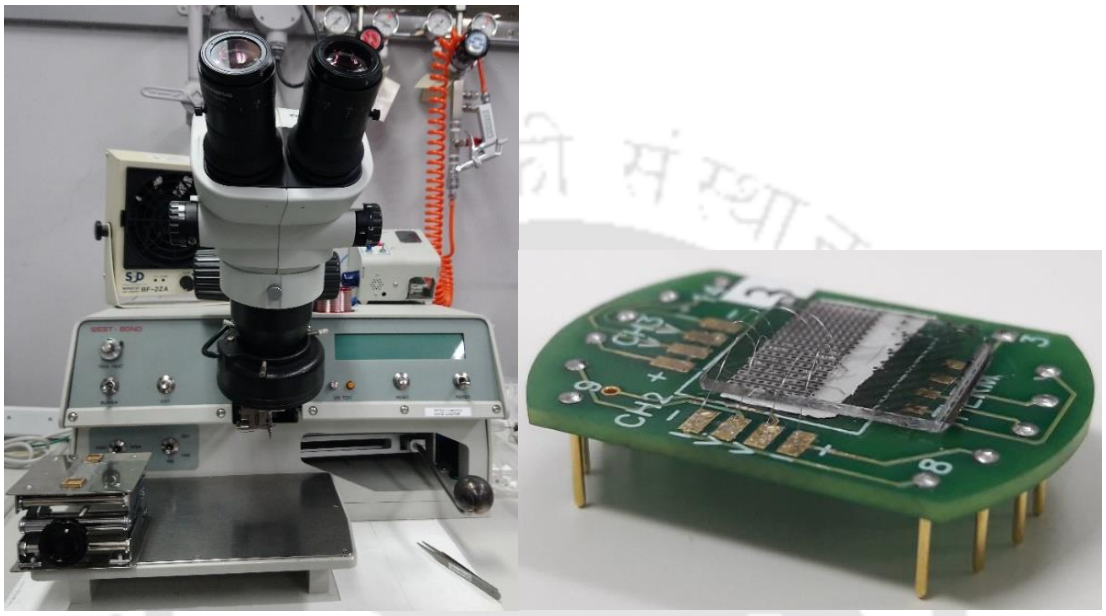

(a) (b)

Figure 3.20: Photographic view of (a) wire bonding (West Bond Model 7700D) setup used in the present investigation and (b) end-to-end point electrical contacts [NIMS2019].

3.6.2.2. Magnetotransport measurements

Transport characterization system incorporates a precise current source having an amplitude range of 2 nA – 8 mA at a frequency of 5 Hz square wave with a typical sensitivity of 15 nV measuring resistance values in the range 10 $\mu\Omega$ – 5 MΩ in the DC excitation mode. The standard four-probe method was used to measure the resistivity of present samples. It is essential to minimize the contact resistance of the attached wires to provide better sensitivity of the measurement, which in turn minimizes the heating of the sample during the experiment. In typical cases, either a colloidal silver paste or a conductive low-temperature epoxy is used to make contact. In this study, Ball – Wedge wire bonding technique, as shown in Figure 3.20(a), has been employed, where wires ranging from 20-50 μm can be used for bonding. Figure 3.20(b) demonstrates the end-to-end electrical contacts made using the wire bonding (West Bond Model 7700D) setup. Bonds are easily made by the ball-to-wedge method using ultrasonic energy and workpiece heat. The user using hand/eye reference to

bond targets and elevations, guides the bonding tool manually. This method of contacting the samples for the transport measurements proved to be extremely helpful for the experiments at low temperatures and, in some cases, for making tiny contacts in samples. The PPMS setup allows the simultaneous measurement of three samples. As a result, both electrical resistivity and Hall voltage can be measured in one experiment, as per user convenience.

Figure 3.21: Photographic view of a VersaLab setup by Quantum Design used in the present investigation [NIMS2019].

3.6.3. Versa lab setup

The PPMS VersaLab is Quantum Design's first portable Physical Property Measurement System. It provides most of the features of the PPMS in a very compact size, without the need for any liquid cryogens and high power infrastructure making them perfect for small laboratories. The system is equipped with a 3 tesla conduction-cooled switch-less superconducting magnet made of NbTi, powered by a hybrid digital/analog magnet controller. A novel thermal switch design in the PPMS VersaLab cryostat enables a temperature range of 50 K to 400 K without any helium gas consumption. The sample chamber is compatible with PPMS sample "pucks" by offering the same 25 mm bore, sample isothermal region, and robust 12-pin sample puck interface. The flexibility of the PPMS VersaLab allows users to create their experiments and easily interface them to the sample chamber using inserts such as the Multi-Function Probe, which provides a fully customizable

sample interface. Meanwhile, the cryostat functions such that the temperature and magnetic field can be controlled from external programs such as LabVIEW or other third-party software.

Chapter 4

Linear magnetoresistance in CIP-GMR magnetic sensor using Rh spacer

4.1. Introduction

Recently, the development of giant magnetoresistance (GMR) based magnetic sensors has received enormous interest, owing to its tunable size, high sensitivity, and low power consumption. These traits make them promising for applications in the air- and space or automotive industry, non-destructive materials testing, and biomedical sensors [BARB2016, ENNE2016, MARC2017, MUSU2020, SAND2017, SHEN2018, VEDM2020, WANG2020, ZHEN2019]. Therefore, extensive research activities have been carried out on tuning the sensing operation range of the magnetic field and enhancing the magnetoresistance (MR) ratio to obtain high sensitivity. One of the critical issues is how to control the linearity of resistance change with respect to the applied magnetic field. In this context, a linear and reversible MR is conceptually attainable by utilizing (i) the competition between magnetic anisotropy and indirect exchange coupling, resulting in a nonorthogonal magnetization when one of the ferromagnetic (FM) layers shows in-plane magnetic anisotropy, whereas the second one prefers to be magnetized out-of-plane [DIJK2005, MANC2000, TAGA2000, YILD20092, YILD20093], and (ii) the biquadratic exchange coupling, originated either intrinsically due to the band properties of the nonmagnetic (NM) spacer or extrinsically due to interface roughness, which favors 90° orientation of the magnetization of the adjacent FM layers [BARN1993, CHAP1999, ERIC1993, RUHR1991, SLON1991, VAVA2001].

For instance, Liu *et al.* [LIU2016] reported on the formation of a linear MR curve in the magnetic tunnel junction (MTJ) type trilayer films of $L1_0$ FePt(15 nm)/ ZnO(5 nm)/ Fe(5 nm). However, they achieved a low sensitivity of 0.0002 %/mT. Alternatively, Mancoff *et al.* [MANC2000] have shown high-field linear MR variation in current-in-plane (CIP)-GMR devices with perpendicular magnetization orientation in the film stack of Pt(0.23 nm)/ Co(0.32 nm)/ Pt(0.23 nm)/ Pd(0.9 nm)]$_{10}$/ Cu(4.5 nm)/ Co(0.5 nm)/ $Ni_{80}Fe_{20}$(6 nm). The Pt/ Co/ Pt/ Pd film stack revealed a large perpendicular magnetic anisotropy, while the Co/NiFe exhibited in-plane anisotropy. They reported the highest sensitivity of 0.014 %/mT at room temperature. It may be noted that the major factors for obtaining large GMR are the lattice and electronic band matching of the majority spin electrons between the FM and NM metal interfaces [ERLE2001, TODO1996, TSYM2001]. In this context, Dijken *et al.* [DIJK2005] in Ta(5 nm)/ Pt(2 nm)/ CoFe(*t* nm)/ Cu(2.9 nm)/ CoFe(2.5 nm)/ Ru(0.7 nm)/ CoFe(2 nm)/ IrMn(10 nm)/ Ta(5 nm) films and Colis *et al.* [COLI2001] in Fe(5 nm)/ Co(0.5 nm)/ Cu(3 nm)/ Co(0.5 nm)/ CoFe(1.5 nm)/ Ir(0.5 nm)/ CoFe(1.5 nm)/ Cu(2 nm)/ Cr(2 nm) films reported the linear and reversible MR sensors, achieving the highest sensitivity of 0.018

%/mT and ~ 0.0015 %/mT, respectively. Recently, Fathoni *et al.* [FATH2019] reported on band match enhanced CIP-GMR in epitaxial $Co_{50}Fe_{50}$/ Cu/ $Co_{50}Fe_{50}$ films with metastable body-centered-cubic (*bcc*) Cu and obtained a very high MR ratio of 40.5 % at room temperature. However, $Co_{50}Fe_{50}$/ Cu/ $Co_{50}Fe_{50}$ based CIP-GMR devices exhibited a nonlinear MR behavior without any linear variation, limiting their application as magnetic field sensors.

Thus, in this study, we focus on the Rh spacer in between CoFe FM layers because (i) it exhibits high electrical conductivity, making it suitable as a spacer in CIP-GMR device, (ii) the structure of the Rh layer changes from stable face-entered-cubic (*fcc*) to metastable body-centered-tetragonal (*bct*) depending on its thickness [TOMA1998], which might give rise to a large MR ratio like the metastable *bcc*-Cu spacer, and (iii) the spin density functional theory calculation has predicted a finite noncollinear interlayer exchange coupling (IEC) in the trilayer films with the Rh spacer [BLIZ2015], which may result in a linear MR response. Accordingly, in this chapter, a systematic investigation on the magnetic coupling and magnetotransport properties in CoFe(3 nm)/ wedge-shaped Rh(t_{Rh} = 0 – 7.3 nm)/ CoFe(1.5 nm) films is presented. Upon optimization of the Rh thickness, the flat samples of CoFe(3 nm)/ Rh(0.84 nm)/ CoFe(1.5 nm)/ MgO(2 nm) CIP-GMR device were fabricated to achieve a linear MR response. To understand the origin of linear MR response, numerical simulation analyses have been carried out for the optimized flat CIP-GMR device. Finally, the sensing parameters of all the devices exhibiting linear MR responses are evaluated to comprehend their usability as magnetic field sensors. The highest sensitivity and nonlinearity are achieved to be 0.001 %/mT and 0.21 %FS, respectively, along with a considerably wider operation field range of 220 mT.

4.2. Experimental details

CIP-GMR films consisting of CoFe(3 nm)/ wedge-shaped Rh(t_{Rh} = 0 – 7.3 nm)/ CoFe(1.5 nm)/ MgO(2 nm) and flat samples of CoFe(3 nm)/ Rh(0.84 nm)/ CoFe(1.5 nm)/ MgO(2 nm) were deposited on single-crystal MgO(001) substrate at room temperature. The deposition was done using an ultra-high vacuum (UHV)-compatible magnetron sputtering system with a base pressure better than 1×10^{-7} Pa. In the sputtering chamber, the surface of the MgO substrate was etched by Argon ion milling before depositing the films to obtain (001)-oriented epitaxial growth. All the CoFe layers in the films had the same composition as $Co_{50}Fe_{50}$. The deposition rates of CoFe and Rh films were pre-calibrated using an *ex-situ*

surface profilometer and found to be 0.67 and 0.11 Å/s, respectively. The wedge-shaped Rh layers with t_{Rh} = 0 - 7.3 nm were fabricated using the linear motion shutter. The sample was prepared on a 20 × 20 mm^2 MgO(001) substrate. Accordingly, the speed of the linear shutter was kept constant at 0.03 mm/s for a time period of 11 min 7 sec. The as-deposited films were post-annealed at 250 °C for 1 hour under a high vacuum for improving the interface roughness. Photolithography and Argon ion etching were used to pattern the film into a four-terminal device structure. The films were patterned into CIP-GMR devices in the shape of wires having dimensions of 2820×200 μm^2 and gold-coated electrodes of 200×200 μm^2 sizes using photolithography.

The crystal structure and the corresponding structural parameters were determined *via* X-ray diffraction (XRD) by employing an X-ray diffractometer (Rigaku, Smartlab) with Cu-K_α radiation (λ = 1.5406 Å). The magnetoresistance (*R-H*) curve was measured at room temperature for each CIP-GMR device using a standard DC four-probe technique in VersaLab and Physical Property Measurement System (PPMS, Quantum Design) setups. The magnetic hysteresis (*M-H*) loop was recorded using Vibrating Sample Magnetometer (VSM, LakeShore Model 7410) at room temperature.

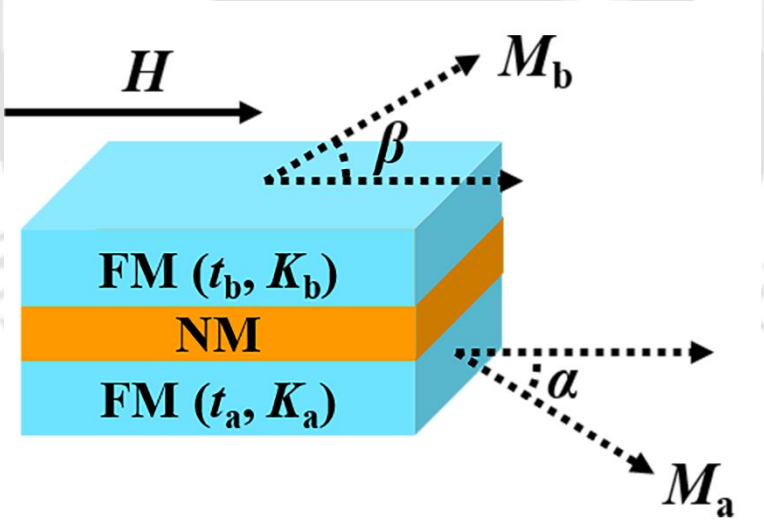

Figure 4.01: Schematic illustration of the numerical simulation parameters in FM/ NM/ FM trilayer structure. All the arrows represent in-plane directions.

4.3. Numerical simulation methods for trilayer structure

The *M-H* loop is simulated using a numerical simulation model to study the nature of magnetic couplings between CoFe layers through Rh and Cu spacers. We consider three

primary energy expressions as illustrated in Eqn. (4.01) [BOSU2010], such as the magnetic anisotropy energy (E_{MA}), the Zeeman energy (E_Z), and the exchange coupling energy (E_{EX}), for the total energy (E_{Total}). *i.e.*,

$$E_{Total} = E_{MA} + E_Z + E_{EX} \tag{4.01}$$

where,

$$\begin{aligned} E_{MA} &= K_a t_a sin^2\alpha\, cos^2\alpha + K_b t_b sin^2\beta\, cos^2\beta \\ E_Z &= -M_a t_a H cos\alpha - M_b t_b H cos\beta \\ E_{EX} &= -J_1 cos(\alpha-\beta) - J_2 cos^2(\alpha-\beta) \end{aligned} \tag{4.02}$$

Here, *M*, *K*, and *t* are the saturation magnetization, the first-order cubic magnetocrystalline anisotropy constant, and the thickness of FM layers, respectively. Subscripts *a* and *b* represent the bottom and top FM layers in FM/ NM/ FM films, as shown in Figure 4.01. The value of *K* is determined from *M-H* loops measured along with the easy and hard axes directions of single-layer FM film. J_1 and J_2 are the bilinear and biquadratic coupling energies, respectively. The positive value of J_1 represents the FM coupling, while the negative values of J_1 and J_2 correspond to 180° and 90° (biquadratic coupling) magnetic configurations, respectively. *H* is the applied magnetic field. The angle α (β) is the angle between the direction of *H* and *M* in the bottom (top) FM layer. Therefore, α-β represents the relative orientation between two magnetization vectors of the bottom and top FM layers.

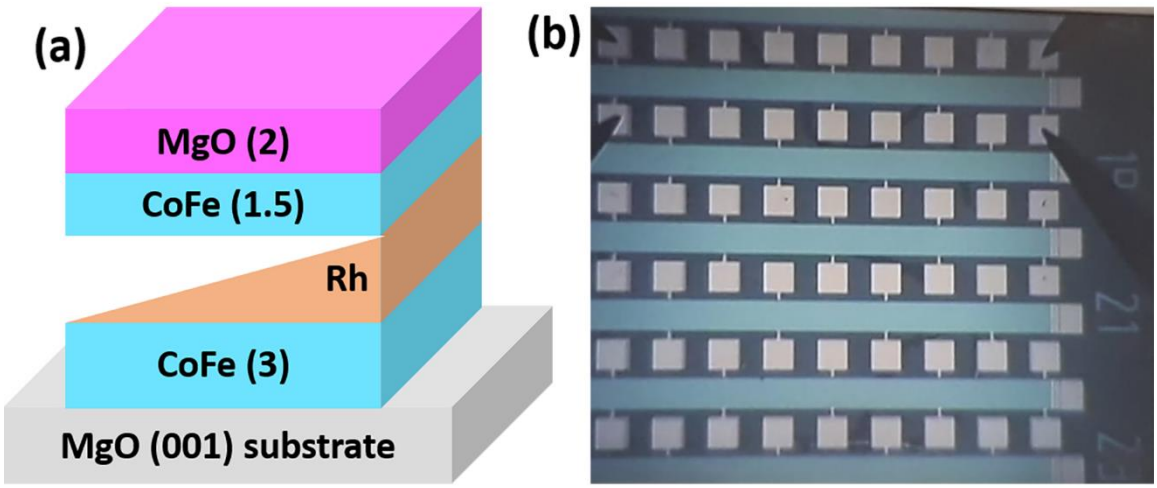

Figure 4.02: (a) The schematic illustration and (b) photograph of the CIP-GMR device (after patterning using photolithography) of the sample structure CoFe(3 nm)/ wedge-shaped Rh(t_{Rh} = 0 - 7.3 nm)/ CoFe(1.5 nm)/ MgO(2 nm) with different t_{Rh} deposited on MgO(001) substrate. All values given in the parenthesis are on the nanometer scale.

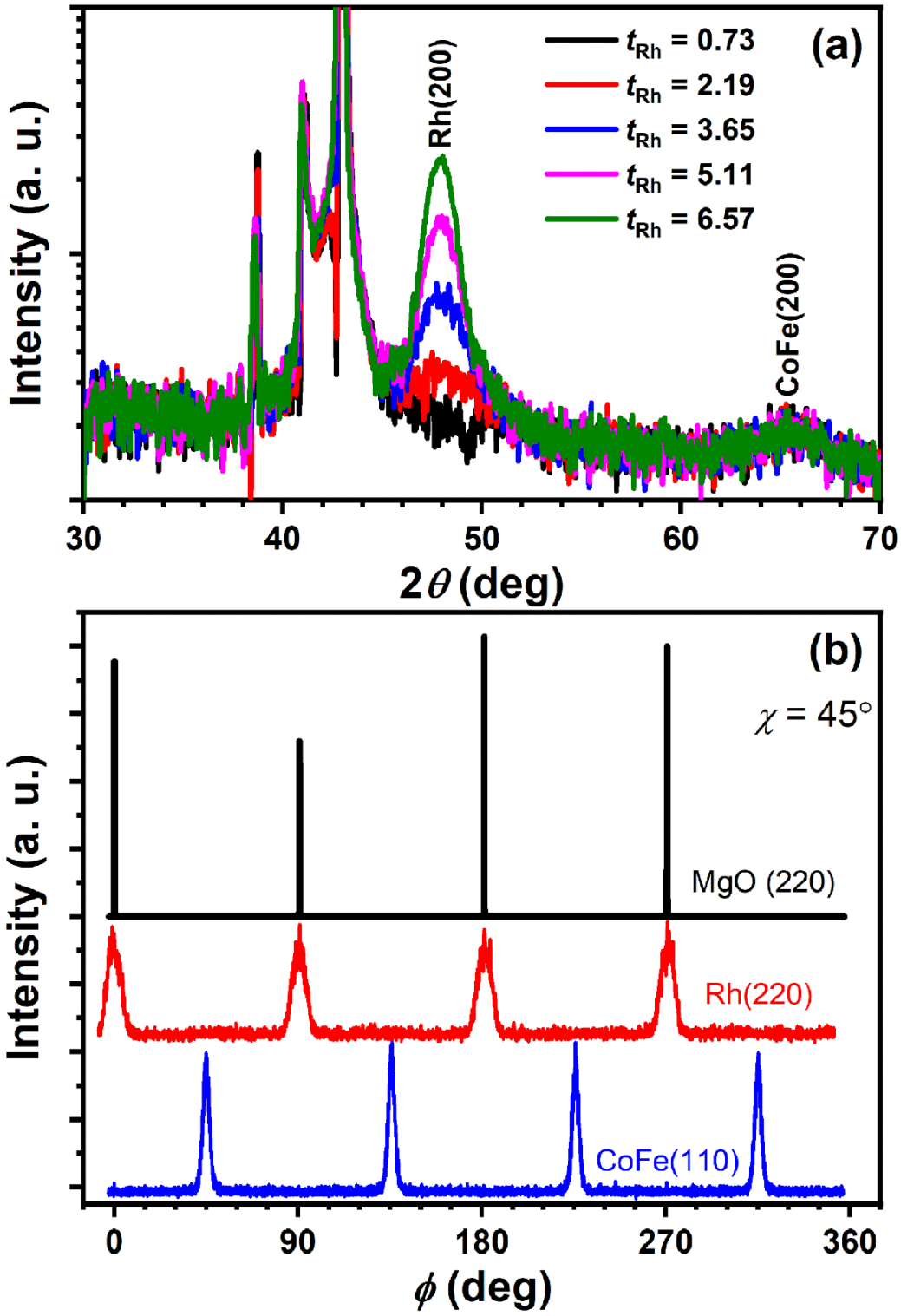

Figure 4.03: (a) Out-of-plane XRD patterns and (b) ϕ-scan of MgO(220), Rh(220) and CoFe(110) reflections for CoFe(3 nm)/ wedge-shaped Rh(t_{Rh} = 0 - 7.3 nm)/ CoFe(1.5 nm)/ MgO(2 nm) film with different t_{Rh} deposited on MgO(001) substrate. The peaks around 2θ =38-44° in Fig.1(a) arise from the MgO substrate.

4.4. Results and discussion

4.4.1. Properties of CoFe(3 nm)/ wedge-shaped Rh(t_{Rh} = 0 – 7.3 nm)/ CoFe(1.5 nm) films

Figure 4.02 displays the schematic illustration and the photograph of the CIP-GMR devices (after patterning using photolithography) of the sample structure CoFe(3 nm)/ wedge-shaped Rh(t_{Rh} = 0 - 7.3 nm)/ CoFe(1.5 nm)/ MgO(2 nm) with different t_{Rh} deposited on MgO(001) substrate.

4.4.1.1. Structural properties

The room temperature out-of-plane XRD patterns of CoFe/ Rh(t_{Rh})/ CoFe films are presented in Figure 4.03. The XRD patterns were obtained for different t_{Rh} positions by narrowing the width of the X-ray beam to 500 μm. In the range of t_{Rh} from 2.2 nm to 6.6 nm, only (200) diffraction peaks from *fcc* Rh and *bcc* CoFe films at 2θ = 47.96° and 65.40° respectively, are observed, indicating the epitaxial growth of the Rh and CoFe films along the (001) orientation. In addition, the XRD peak at 2θ = 43° represents the (200) peaks originating from the MgO substrate. The peak intensity of the Rh film is relatively low at its lower thickness, implying a discontinuous film growth. The ϕ-scan patterns are well-known to verify the epitaxial growth nature of thin films. Hence, to ensure the epitaxial growth nature in the presently investigated thin films, we obtained ϕ-scan patterns of (220) peak of MgO (2θ = 62.17° and χ = 45°) and Rh (2θ = 69.67° and χ = 45°) and (110) peak of CoFe (2θ = 44.31° and χ = 45°) and the same are presented in Figure 4.03(b). It can be seen that MgO substrate, Rh, and CoFe films exhibit four well-defined peaks periodically separated from one another by an angular difference of 90°. These results confirm that *fcc* Rh and *bcc* CoFe thin films grow epitaxially on the MgO substrate. On the other hand, the crystal structure of a thin Rh layer for $t_{Rh} \leq 1.5$ nm could not be identified from the XRD pattern, although the formation of the *bct* Rh was reported for $t_{Rh} < 0.5$ nm [TOMA1998].

4.4.1.2. Rh thickness dependent magnetotransport properties

Figure 4.04 depicts the room temperature in-plane MR curves for the single-layer CoFe and trilayer CoFe/ Rh(t_{Rh})/ CoFe films with different t_{Rh}. In-plane MR curves obtained by applying field along the direction of current in the CIP-GMR devices illustrate that both single-layer CoFe film and trilayer film with $t_{Rh} \leq 0.27$ nm exhibit only ordinary MR curves, which do not saturate even up to 3 T applied field. This indicates that the thin Rh spacer may

not be continuous to separate the top and bottom CoFe layers. Hence, both CoFe layers respond collectively like a single layer film, producing an ordinary MR curve.

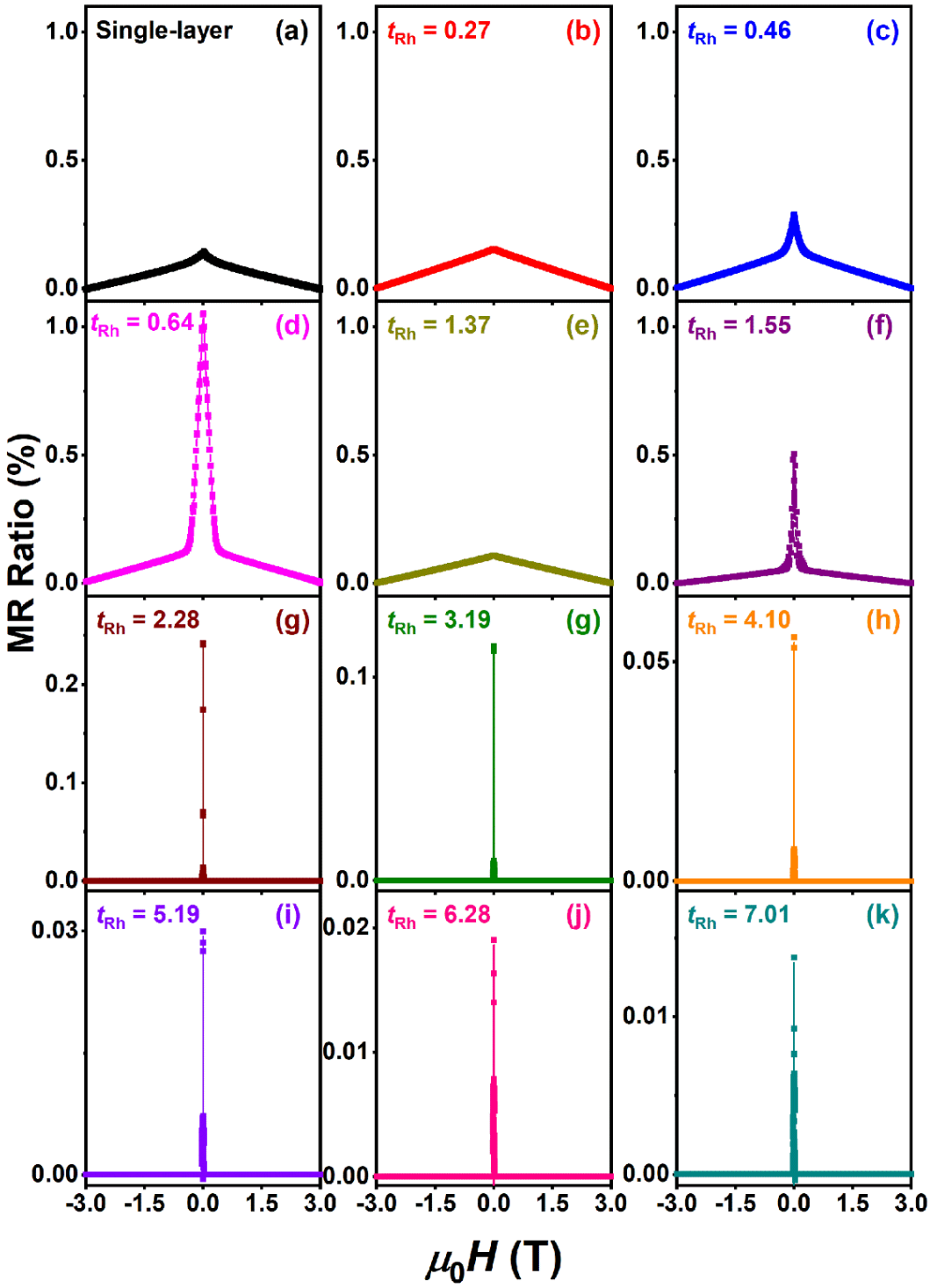

Figure 4.04: Room temperature in-plane MR curves (a) for the single-layer CoFe film, (b)-(k) for CoFe(3 nm)/ Rh(t_{Rh} = 0 - 7.3 nm)/ CoFe(1.5 nm)/ MgO(2 nm) films with different t_{Rh} deposited on MgO(001) substrate.

With increasing Rh thickness to 0.46 and 0.64 nm, the two CoFe layers become well-separated from each other and, the GMR feature can be distinctly observed at the lower field region, along with the ordinary MR, due to the appearance of 180° and/or 90° coupling, as discussed later in this chapter. In order to quantify the actual MR ratio corresponding to the GMR part, we subtract the contribution of ordinary MR from the total MR ratio. Similarly, $\mu_0 H_s$ is also extracted only for the GMR part. Only ordinary MR curves are again seen for the films with t_{Rh} = 1 and 1.37 nm, as the magnetization of two CoFe layers is aligned in the same direction due to ferromagnetic IEC. On further increasing the Rh thickness, the MR curve nature changes from linear variation to nonlinear type (rapid switching at lower applied magnetic field) along with the progressive decrease in the MR ratio.

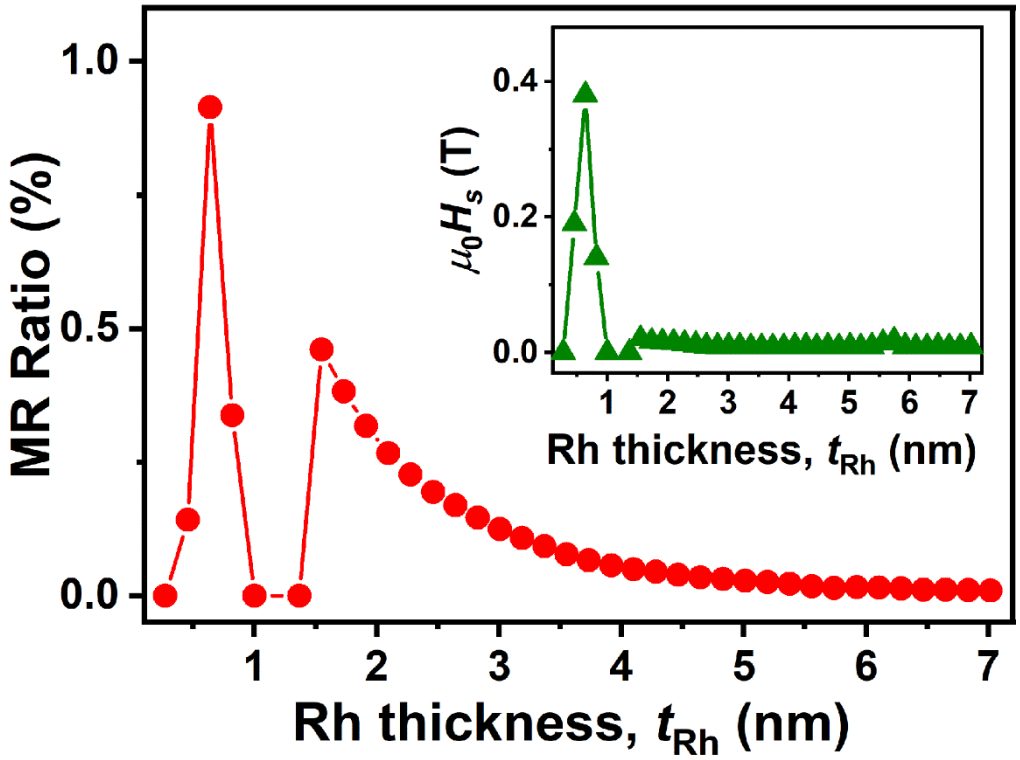

Figure 4.05: Rh thickness dependence of the MR ratio and $\mu_0 H_s$ (in the inset) for CoFe(3 nm)/ wedge-shaped Rh(t_{Rh} = 0 - 7.3 nm)/ CoFe(1.5 nm)/ MgO(2 nm) films with different t_{Rh} deposited on MgO(001) substrate.

Figure 4.05 depicts variations of the MR ratio and saturation magnetic field ($\mu_0 H_s$) (in the inset) for CoFe(3 nm)/ wedge-shaped Rh(t_{Rh} = 0 - 7.3 nm)/ CoFe(1.5 nm)/ MgO(2 nm) films. The MR ratio was calculated using Eqn. (2.38). It can be observed that the MR ratio of the linear GMR curves increases rapidly from zero to about 1 % and then shows a substantial reduction to zero for the films with 0.27 nm $\leq t_{Rh} \leq$ 1 nm. As a result, the variation

of $\mu_0 H_s$ with t_{Rh} also follows a similar trend. For the films with t_{Rh} > 1.37 nm, the MR ratio first increases sharply to 0.48 % and then decreases progressively to 0.01 % at t_{Rh} = 7.3 nm. However, $\mu_0 H_s$ values do not change significantly due to low-field saturating nonlinear MR behaviors for t_{Rh} > 1.37 nm. The decrease of the MR ratio at high t_{Rh} may be attributed to the possible current shunting effect and change in the relative orientation between the magnetization of two CoFe layers.

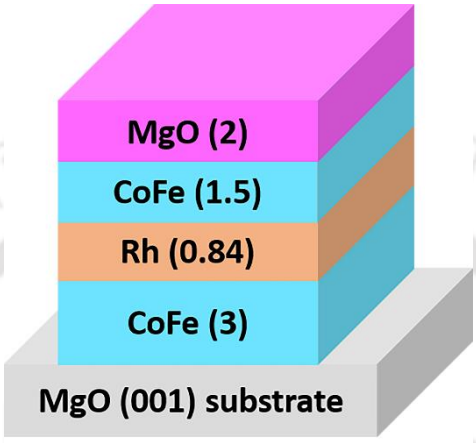

Figure 4.06: The schematic illustration of the flat sample with the structure of CoFe(3 nm)/ Rh(0.84 nm)/ CoFe(1.5 nm)/ MgO(2 nm) deposited on MgO(001) substrate. All values given in the parenthesis are on the nanometer scale.

4.4.2. Properties of flat CoFe(3 nm)/ Rh(0.84 nm)/ CoFe(1.5 nm)/ MgO(2 nm) film

4.4.2.1. Structural properties

To gain more insight into the type of magnetic couplings between CoFe layers through the Rh spacer and correlate with the origin of the linear MR, a few selected samples with completely flat thin films were made to optimize the exact thickness of the Rh spacer layer. After several attempts, it was found that for t_{Rh} = 0.84 nm film, the linear variation of the MR curve with the maximum MR ratio could be successfully obtained. Accordingly, as demonstrated in Figure 4.06, the flat sample of CoFe(3 nm)/ Rh(0.84 nm)/ CoFe(1.5 nm)/ MgO(2 nm) was deposited on a MgO(001) substrate. Figure 4.07 displays the room temperature out-of-plane XRD pattern of the CoFe(3 nm)/ Rh(0.84 nm)/ CoFe(1.5 nm) film and the ϕ-scans of (220) peak of MgO (2θ = 62.17° and χ = 45°) and (110) peak of CoFe (2θ = 44.31° and χ = 45°). The XRD pattern reveals the growth of the (200) peak of CoFe along with the (200) peak from the MgO substrate. However, due to ultra-low Rh thickness (t_{Rh} = 0.84 nm), the (200) peak of the Rh could not be observed. The ϕ-scans shown in Figure

4.08(b) reveal that MgO substrate and CoFe films exhibit four well-defined peaks periodically separated from one another by an angular difference of 90°. This confirms the epitaxial growth of CoFe on the MgO(001) substrate.

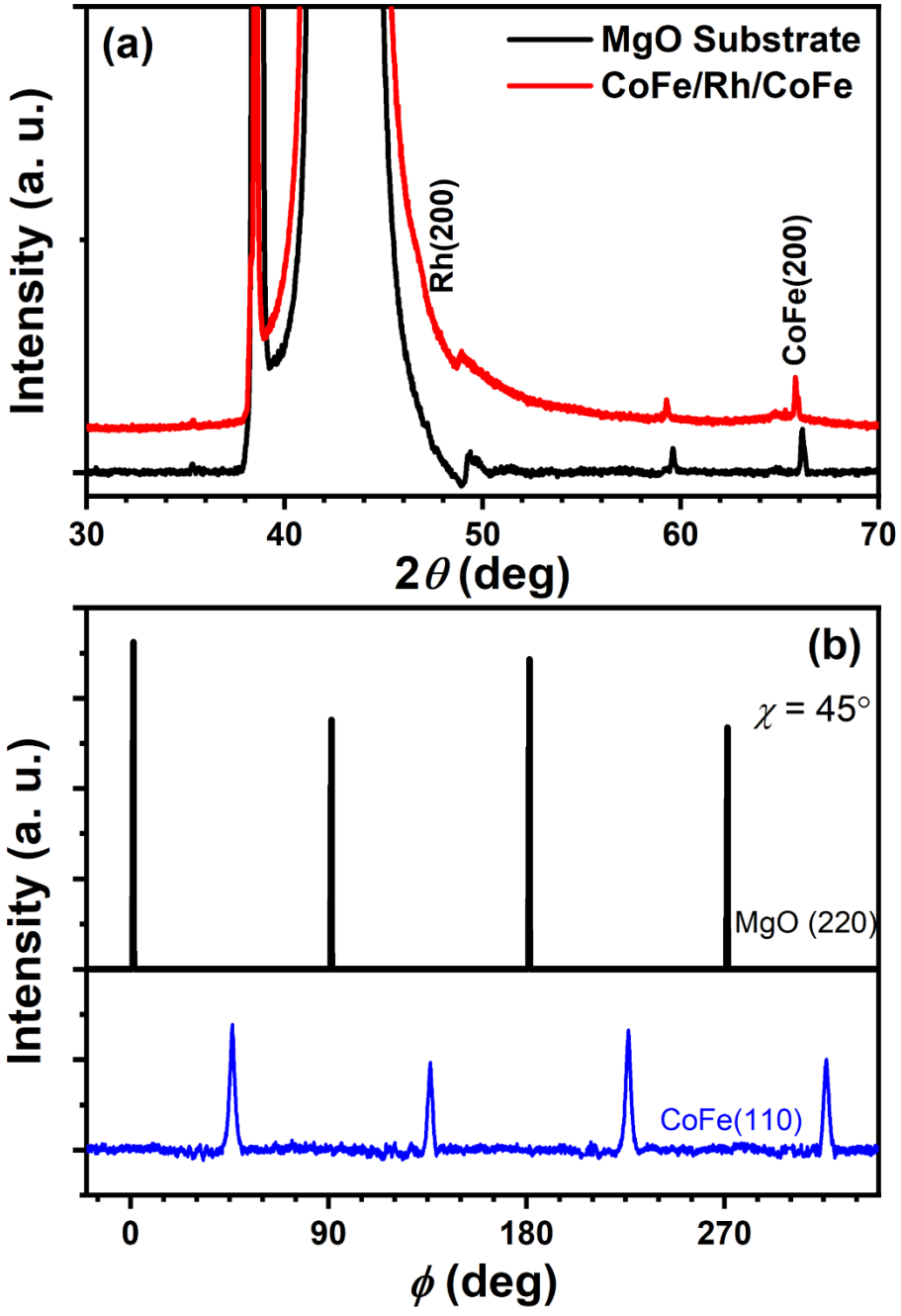

Figure 4.07: (a) Out-of-plane XRD pattern and (b) ϕ-scans of MgO(220) and CoFe (110) reflections for a flat sample of CoFe(3 nm)/ Rh(0.84 nm)/ CoFe(1.5 nm)/ MgO(2 nm) deposited on MgO(001) substrate. Peaks around 2θ = 38-44° in Fig.4.07(a) arise from the MgO substrate.

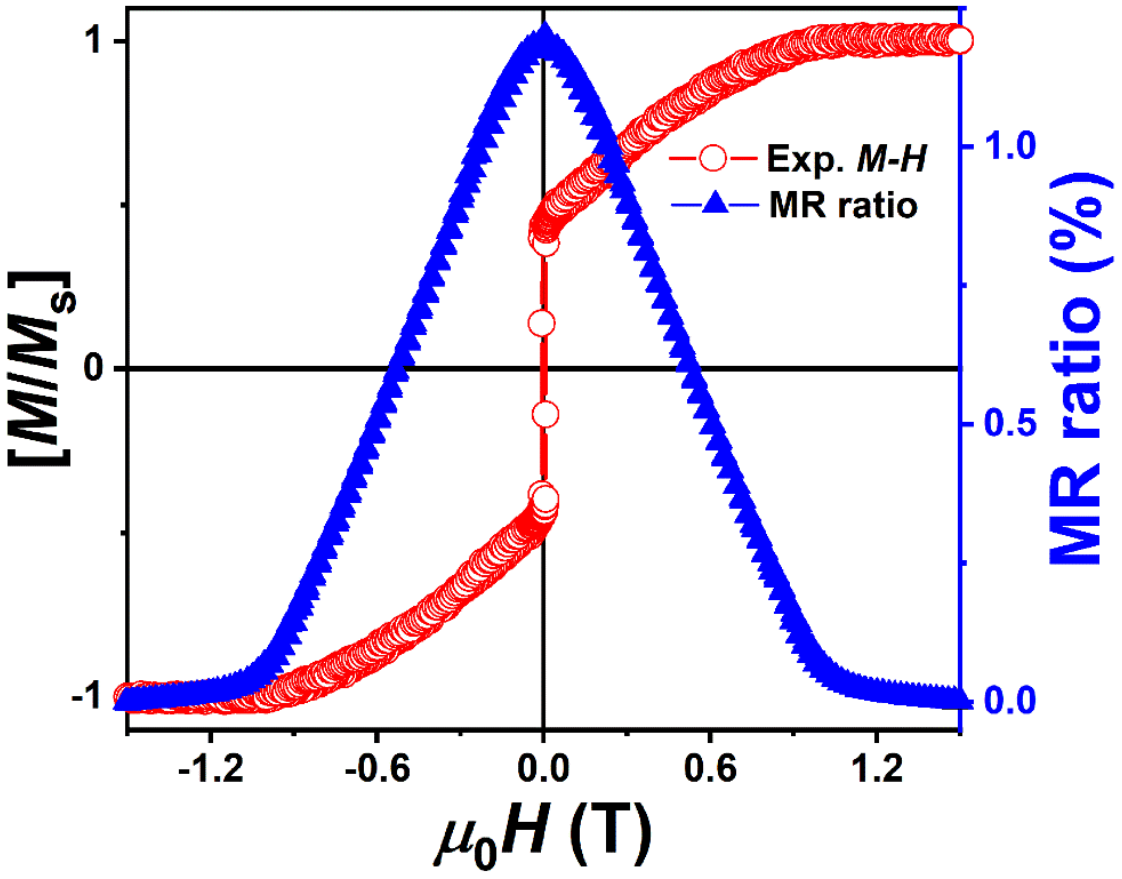

Figure 4.08: Room temperature in-plane *M-H* loop (open circle) and MR curve (solid triangle) for the flat sample of CoFe(3 nm)/ Rh(0.84 nm)/ CoFe(1.5 nm)/ MgO(2 nm) deposited on a MgO(001) substrate.

4.4.2.2. Magnetic and magnetotransport properties: Experiment and numerical simulations

The room temperature in-plane *M-H* loop and MR curve for the optimized flat sample of CoFe(3 nm)/ Rh(0.84 nm)/ CoFe(1.5 nm) are depicted in Figure 4.08. The observation of a linear MR curve with the MR ratio of 1.1 % agrees well with the result obtained for the sample with a similar Rh thickness in the wedge-shaped Rh spacer. Besides, the MR curve reveals a close correlation with the *M-H* loop. Figure 4.09 displays the room temperature in-plane MR curve, the experimental (open circle) and simulated *M-H* loops, and variations of angles between the direction of *H* and *M* in the bottom (α) and top CoFe (β) layers and the relative orientation between α and β (= α-β) at different applied magnetic fields for CoFe/ Rh/ CoFe film.

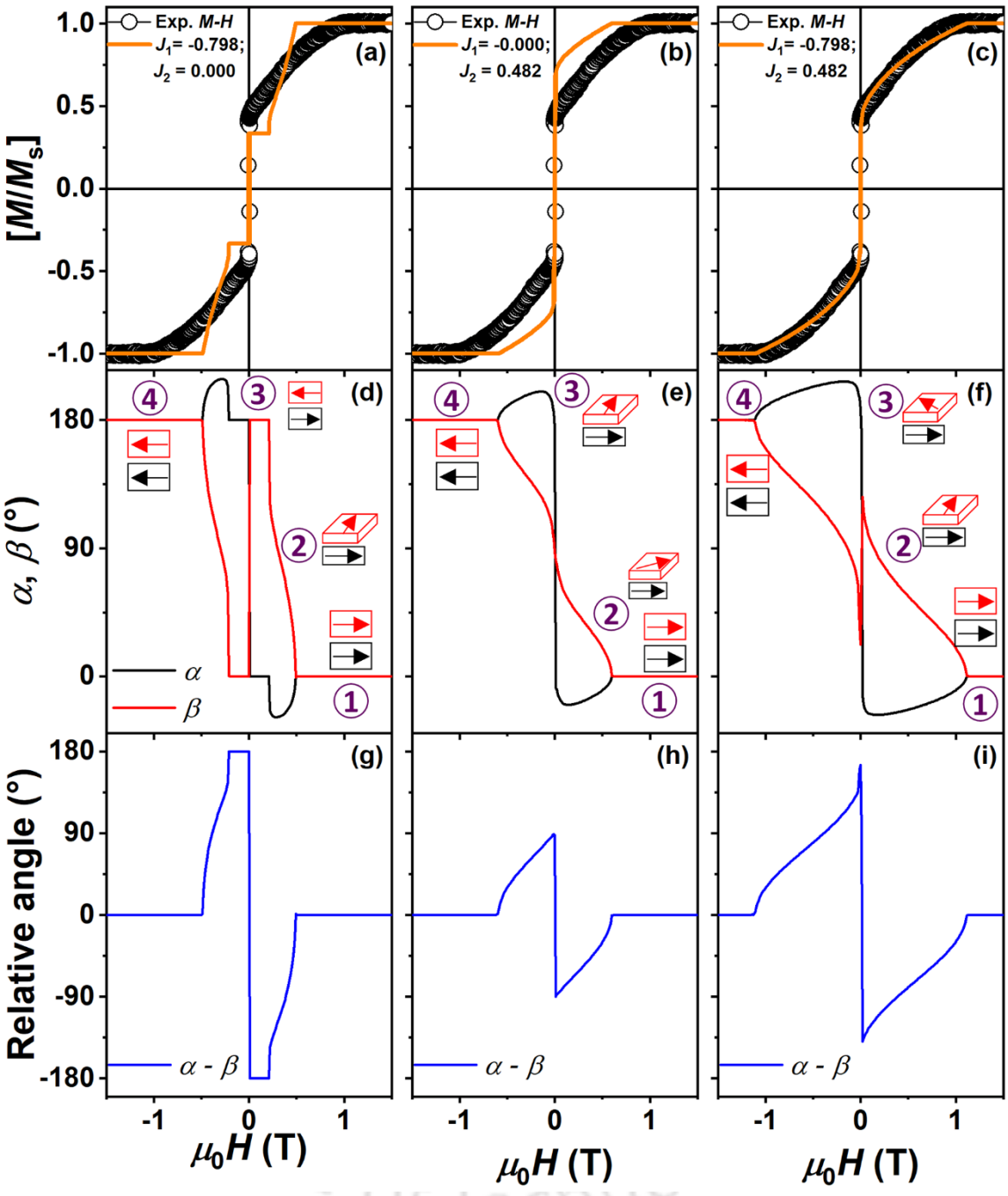

Figure 4.09: Room temperature in-plane experimental (open circle) and numerical simulated (solid line) *M-H* loops (a,b,c) for a flat sample of CoFe(3 nm)/ Rh(0.84 nm)/ CoFe(1.5 nm)/ MgO(2 nm). The variations of the angles [α and β (d,e,f)] and the relative orientation between angles [α-β (g,h,i)] at different magnetic fields for different coupling parameters. The estimated magnetization directions using angles are shown in the insets.

The estimated magnetization directions using angles α and β are shown in the insets. For simulating the *M-H* loop, the minimization of the total energy in Eqn. (4.01) using the terms

given in Eqn. (4.02) is considered. Besides, the values of parameters, $K_a = K_b = 2.13\times10^4$ J/m^3, $\mu_0 M_a = \mu_0 M_b = 1.95$ T, $t_a = 3$ nm and $t_b = 1.5$ nm are fixed. The coupling parameters J_1 and J_2 are left as free fit parameters, and their values are estimated when the simulated *M-H* loop complements the experimental one. To demonstrate the role of different coupling parameters and their influence on the linearity of the MR curves, we simulated *M-H* curves with different coupling parameters as presented in Figure 4.09. It can be evidently seen that the simulated *M-H* loop cannot be complemented to the experimental *M-H* loop when only bilinear or biquadratic coupling is considered [see Figure 4.09(a, b)]. The nature of simulated *M-H* loops changes significantly upon accounting for only one type of magnetic coupling between the CoFe layers. A remanence ratio of 0.33 is observed along with the formation of a stable plateau region [marked as position 3 in Figure 4.09(d)] on considering $J_1 = -0.798$ mJ/m^2 and $J_2 = -0.000$ mJ/m^2. This provides nonlinear variations of α and β. On the other hand, $J_1 = -0.000$ mJ/m^2 and $J_2 = -0.482$ mJ/m^2 results in the formation of a perfect 90° magnetic configuration with $\mu_0 H_s$ of 0.6 T and the remanence ratio of 0.73 [see Figure 4.09(b)].

A close observation of the experimental *M-H* loop shows a remanence ratio, M_R/M_S of 0.45 and $\mu_0 H_s$ of 1.1 T. Note that the M_R/M_S ratio should be 0.67 if magnetizations of the top and bottom CoFe layers align perpendicularly. The deviation between the experimental and predicted M_R/M_S values corroborates different magnetic couplings between CoFe layers. Therefore, both J_1 and J_2 values were fine-tuned in the simulation to complement the experimental *M-H* loop. The simulated *M-H* loop (solid line) provides the best match only when $J_1 = -0.798$ mJ/m^2 and $J_2 = -0.482$ mJ/m^2, supporting the presence of both 180° and 90° magnetic configurations [see Figure 4.09(c)]. This accounts for the large $\mu_0 H_s$ of 1.1 T required to saturate the film along the field direction. Furthermore, the variation of α and β indicates that while the top CoFe layer rotates progressively with decreasing the applied magnetic field from the saturation, the bottom CoFe layer exhibits a rapid switching at lower applied fields [see Figure 4.09(f, i)]. The latter could be attributed to the dominant E_Z contribution that forces the magnetization direction to the applied field direction in thicker bottom CoFe. As a result, the relative orientation between α and β varies nearly a linear fashion due to the existence of biquadratic coupling (90° coupling), which in turn provides the linear MR response.

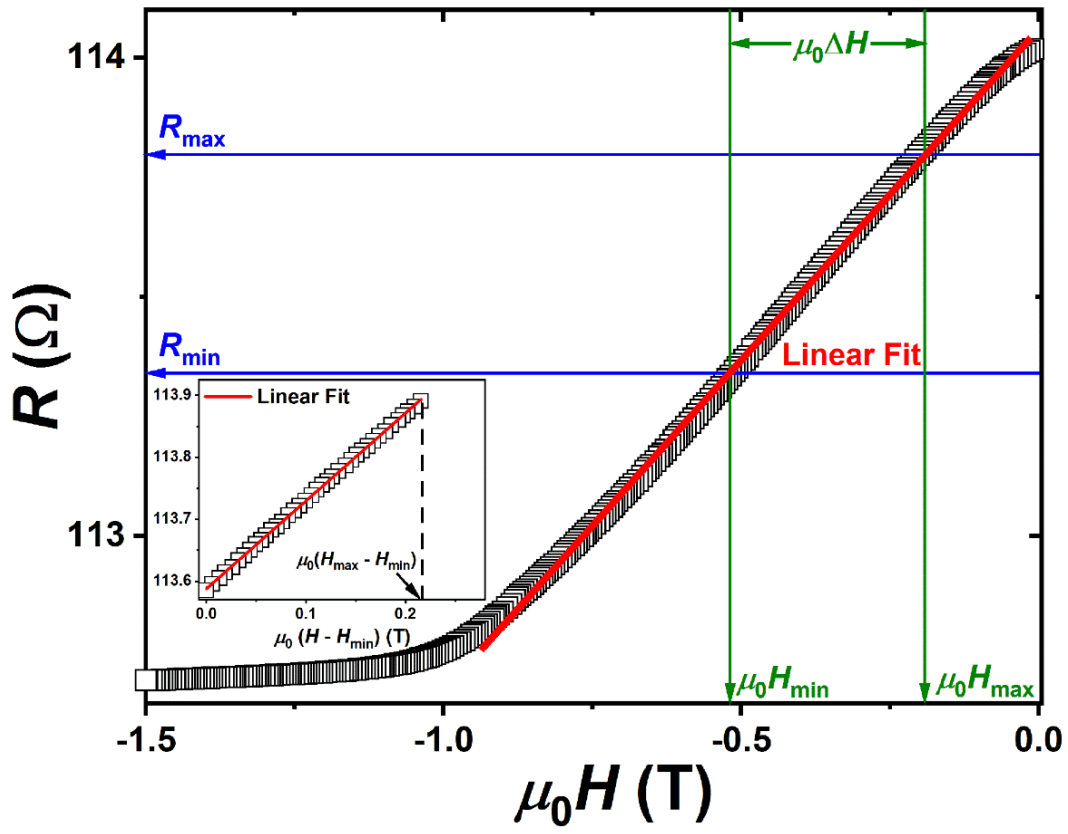

Figure 4.10: Variation of resistance as a function of the normalized effective field and their linear fit for a flat sample of CoFe(3 nm)/ Rh(0.84 nm)/ CoFe(1.5 nm)/ MgO(2 nm) deposited on MgO(001) substrate.

4.4.2.3. Sensing properties as a magnetic field sensor

The magnetic sensor application demands a linear *R-H* response with low nonlinearity and high sensitivity. To study the sensing properties, here, we carried out the linear fitting to the experimental data [SHIR2018] by selecting a magnetic field region of 130 – 350 mT and evaluating the sensitivities and nonlinearities of the CIP-GMR device CoFe(3 nm)/ Rh(0.84 nm)/ CoFe(1.5 nm) and presented in Figure 4.10. The sensitivity is defined as a value of the MR ratio divided by the magnetic field range, *i.e.*, $\Delta MR/\Delta H$. The nonlinearity, represented as %full-scale (FS), is determined as a maximum of the normalized difference between an experimental resistance R_{exp} and its linear fit value R_{fit}, expressed as

$$Nonlinearity\ (\%\text{FS}) = \frac{R_{exp}(H) - R_{fit}(H)}{R_{max} - R_{min}} \times 100 \qquad (4.03)$$

where H is the applied magnetic field, and R_{max} (R_{min}) is the maximum (minimum) of the experimental resistance within the evaluation range of the magnetic field. Most of the

previous studies on trilayer magnetic sensors consist of an out-of-plane magnetized sensing layer demanding perpendicular magnetic anisotropy in one of the FM layers [DIJK2005, LIU2016]. On the other hand, comparable sensing properties are achieved in this study by utilizing the biquadratic coupling energy. For the flat sample of CoFe/ Rh/ CoFe film, the highest sensitivity and nonlinearity are obtained as 0.001 %/mT and 0.21 %FS, respectively. These values are better than the earlier report for $L1_0$ FePt(15 nm)/ ZnO(5 nm)/ Fe(5 nm) based MTJ, where the $L1_0$ FePt reference layer has a perpendicular anisotropy, having a sensitivity of 0.0002 %/mT [LIU2016].

4.5. Summary

A systematic investigation on the effect of thickness of Rh spacer layer on the structural and magnetotransport properties of CoFe(3 nm)/ wedge-shaped Rh(t_{Rh} = 0 - 7.3 nm)/ CoFe(1.5 nm)/ MgO(2 nm) films deposited on MgO(001) substrate and the optimization of Rh layer thickness to obtain the better linearity and sensitivity have been carried out. The salient features of the CoFe(3 nm)/ wedge-shaped Rh(t_{Rh} = 0 - 7.3 nm)/ CoFe(1.5 nm)/ MgO(2 nm) films and a flat sample of CoFe(3 nm)/ Rh(0.84 nm)/ CoFe(1.5 nm)/ MgO(2 nm) film from the current investigations are as follows:

- The out-of-plane XRD patterns and ϕ-scans of CoFe(3 nm)/ wedge-shaped Rh(t_{Rh} = 0 - 7.3 nm)/ CoFe(1.5 nm)/ MgO(2 nm) films confirmed the epitaxial growth of *fcc* Rh and *bcc* CoFe thin films on the MgO(001) substrate.
- The in-plane MR curves illustrate that the single-layer CoFe film and CoFe(3 nm)/ wedge-shaped Rh(t_{Rh} = 0 - 7.3 nm)/ CoFe(1.5 nm)/ MgO(2 nm) films with t_{Rh} = 0.27, 1.00 and 1.37 nm exhibit only ordinary MR curves, which do not saturate up to 3 T applied magnetic field.
- The GMR feature was observed for films with t_{Rh} = 0.46 and 0.64 nm due to the appearance of 180° and/or 90° couplings.
- For the films with t_{Rh} > 1.55 nm, the MR ratio decreased progressively to 0.01 % at t_{Rh} = 7.3 nm. The decrease of the MR ratio at high t_{Rh} was correlated to the possible current shunting effect and change in the relative orientation between the magnetization of two CoFe layers.
- The optimized Rh layer thickness, exhibiting a high MR ratio of 1.1 %, was found to be 0.84 nm in the flat sample of CoFe(3 nm)/ Rh(0.84 nm)/ CoFe(1.5 nm)/ MgO(2 nm).

- The out-of-plane XRD pattern and ϕ-scans in the flat sample revealed the epitaxial growth of *bcc* CoFe thin films on the MgO(001) substrate.
- The numerical simulation analysis demonstrated that the simulated *M-H* loop complements the experimental *M-H* loop only after taking J_1 and J_2 into account. The simulated *M-H* loop provided the best match only when $J_1 = -0.798$ mJ/m^2 and $J_2 = -0.482$ mJ/m^2, supporting the presence of both 180° and 90° magnetic configurations.
- The highest sensitivity and reduced nonlinearity are obtained as 0.001 %/mT and 0.21 %FS in a sensing field range of 220 mT for the flat sample of CoFe(3 nm)/ Rh(0.84 nm)/ CoFe(1.5 nm)/ MgO(2 nm).

Chapter 5

Enhancing linear magnetoresistance in CIP-GMR device with metastable bcc-Cu spacer and auxiliary biquadratic coupling through Rh spacer

5.1. Introduction

The current endeavors for developing high-sensitive magnetic field sensors, using giant magnetoresistance (GMR) concepts, have attracted much interest due to their potential applications in the fields of automotive sensors, biomedical sensors, non-destructive materials testing, non-volatile magnetic memories, read heads in hard disk drives, *etc.* [ENNE2016, HA2021, MUSU2020, PRAS2020, SHEN2018, ZHEN2019]. Recently, substantial research has been reported on enhancing the MR ratio of the GMR devices due to the intrinsically high sensitivity, large-scale fabrication, low signal-to-noise ratio, and GMR ambient working conditions devices [FATH2019, KIM2018, MARC2017, PRAS2020, WANG2020, ZHEN2019]. However, for the advancements in sensor technology, the linear and reversible MR response with respect to the applied magnetic field is one of the crucial factors. In order to tune the linear range of MR based magnetic sensor devices, different approaches have been adopted. Among these, the most straightforward methods are (i) to form perpendicular magnetization orientations between ferromagnetic (FM) layers [COLI2001, DIJK2005, LIU2016, MANC2000, NAKA2017] and (ii) to establish biquadratic coupling between FM layers using a suitable nonmagnetic (NM) spacer layer [CHAP1999].

Recently, Fathoni *et al*. reported that current-in-plane (CIP)-GMR films, consisting of all body-centered cubic (*bcc*) structured $Co_{50}Fe_{50}$/ Cu/ $Co_{50}Fe_{50}$ epitaxial trilayer films, exhibit room temperature MR ratio of 40.5 %, the highest value ever reported for trilayer CIP-GMR devices [FATH2019]. They also showed that nearly perfect lattice matching and large spin-asymmetry of the interfacial electronic band matching at *bcc* $Co_{50}Fe_{50}$ and the metastable *bcc*-Cu spacer contribute to the observed giant MR ratio. Since two $Co_{50}Fe_{50}$ layers are coupled with antiferromagnetic (AFM) interlayer exchange coupling (IEC) and the cubic crystalline magnetic anisotropy in the epitaxial $Co_{50}Fe_{50}$ layer stabilizes the magnetization to the in-plane <110> direction, the resistance versus magnetic field (*R-H*) curve exhibited a strong hysteresis with poor linearity. Hence, the realization of linear *R-H* responses, together with a high MR ratio, is vital. The Rh spacer layer thickness dependent magnetic properties in the CoFe(3 nm)/ Rh(t_{Rh} = 0 – 7.3 nm)/ CoFe(1.5 nm) trilayer films, as discussed in Chapter 4, revealed that IEC between the FM CoFe layers is strongly dependent on Rh thickness, and linear *R-H* response is observed only for low Rh thickness. This is predominantly due to the interfacial roughness, which results in the formation of the biquadratic coupling according to the fluctuation mechanism model proposed by Slonczewski [SLON1991]. This prompted the integration of the Rh spacer layer along with

metastable *bcc* Cu (t = 1.6 nm) [FATH2019] and fine-tuning of the IEC between $Co_{50}Fe_{50}$ layers to obtain the linear *R-H* response with a high MR ratio.

Accordingly, in this chapter, a new CIP-GMR device has been developed with a combination of two spacer materials, *i.e.*, CoFe(3 nm)/ Rh(t_{Rh} = 0 – 2.5 nm)/ CoFe(1.5 nm)/ Cu(1.6 nm)/ CoFe(3 nm)/ MgO(2 nm). To understand the role of Rh on the magnetic interactions in the asymmetric structured CoFe based CIP-GMR devices, a wedge-shaped Rh spacer layer (t_{Rh} = 0 – 2.5 nm) was deposited. Linear *R-H* response could be obtained for 0.79 nm ≤ t_{Rh} ≤ 1.00 nm The Rh spacer thickness was finally optimized to be 0.84 nm by making several flat samples around this thickness range. Subsequently, CoFe(3 nm)/ Rh(0.84 nm)/ CoFe(1.5 nm)/ Cu(1.6 nm)/ CoFe(3 nm)/ MgO(2 nm) CIP-GMR device was fabricated yielding a linear *R-H* response with a MR ratio of 21 % accomplishing a high sensitivity of 0.047 %/mT, reduced nonlinearity of 0.98 % FullScale along with a substantially wider operation field range of 220 mT. Numerical simulation analyses of magnetization curves carried out for the optimized flat samples with two spacer layers established that the middle CoFe sensing layer is well-controlled by IEC through the Rh spacer, giving rise to a linear response without losing the high MR ratio through the *bcc*-Cu spacer.

5.2. Experimental details

CIP-GMR films consisting of CoFe(3 nm)/ wedge-shaped Rh(t_{Rh} = 0 – 2.5 nm)/ CoFe(1.5 nm)/ Cu(1.6 nm)/ CoFe(3 nm)/ MgO(2 nm), and flat sample of CoFe(3 nm)/ Rh(0.84 nm)/ CoFe(1.5 nm)/ Cu(1.6 nm)/ CoFe(3 nm)/ MgO(2 nm) were deposited on single-crystal MgO(001) substrate at room temperature. All films were fabricated using the ultra-high vacuum (UHV) compatible DC magnetron sputtering system. The base pressure of the chamber was better than 1×10^{-7} Pa. Before depositing the films, the MgO substrate's surface was etched using Argon ion milling in the sputtering chamber. The composition of all CoFe layers in different samples is kept as $Co_{50}Fe_{50}$. The deposition rates of CoFe, Rh, and Cu films were pre-calibrated using an *ex-situ* surface profilometer and optimized to be 0.67, 0.11, and 0.39 Å/s, respectively. The wedge-shaped Rh layer was fabricated by utilizing the linear shutter. Post-annealing of the as-deposited films was performed at 250 °C for one hour to stabilize the interfacial roughness under high vacuum conditions. In order to pattern the film into a four-terminal device structure, photolithography and Argon ion etching were used. The films were patterned into CIP-GMR devices in the shape of wires having dimensions of 2820×200 μm^2 and gold-coated electrodes of 200×200 μm^2 sizes using photolithography.

X-ray diffraction (XRD) with Cu-K_α radiation (λ = 1.5406 Å) was employed for the structural characterization of the samples. The microstructures of the samples, especially Rh and Cu spacer interfaces, were analyzed by using an aberration-corrected (scanning) transmission electron microscope [(S)TEM, FEI Titan G2 80-200]. The (S)TEM observation specimens were prepared by the lift-out technique using a dual-beam focused-ion-beam/scanning electron microscope (FIB/SEM, FEI Helios G4). Magnetic properties (*M-H* loops) were measured using a Vibrating Sample Magnetometer (VSM, LakeShore Model 7410) at room temperature. The room temperature resistance versus magnetic field (*R-H*) response of the CIP-GMR devices was investigated by standard DC four-probe technique using VersaLab setup and Physical Property Measurement System (PPMS, Quantum Design).

5.3. Numerical simulation methods for multilayer structure

The *M-H* loop was simulated using a numerical simulation model to study the nature of magnetic couplings between CoFe layers through Rh and Cu spacers. The total energy (E_{Total}) can be expressed in terms of three major energy terms, as shown in Eqn. (5.01) [BOSU2010], such as the magnetic anisotropy energy (E_{MA}), the Zeeman energy (E_Z), and the exchange coupling energy (E_{EX}), *i.e.*,

$$E_{Total} = E_{MA} + E_Z + E_{EX} \tag{5.01}$$

where,

$$\begin{aligned} E_{MA} &= K_a t_a sin^2\alpha\, cos^2\alpha + K_b t_b sin^2\beta\, cos^2\beta + K_c t_c sin^2\gamma\, cos^2\gamma \\ E_Z &= -M_a t_a H cos\alpha - M_b t_b H cos\beta - M_c t_c H cos\gamma \\ E_{EX} &= -J_1' cos(\alpha-\beta) - J_2' cos^2(\alpha-\beta) - J_1'' cos(\beta-\gamma) \\ &\quad - J_2'' cos^2(\beta-\gamma) \end{aligned} \tag{5.02}$$

Here, *M*, *K*, and *t* are the saturation magnetization, the first-order cubic magnetocrystalline anisotropy constant, and FM layers' thickness, respectively. Subscripts *a*, *b*, and *c* represent the bottom, middle, and top FM layers, respectively [FULL1996, GORI2011]. The terms J_1' (J_1'') and J_2' (J_2'') are the bilinear and biquadratic coupling energies, respectively, across the bottom (top) spacer. The positive value of J_1 represents FM coupling, while the negative values of J_1 and J_2 correspond to 180° and 90° magnetic configurations, respectively. α, β, and γ represent angles between *H* and *M* in the bottom, middle, and top FM layers, respectively, as shown in Figure 5.01.

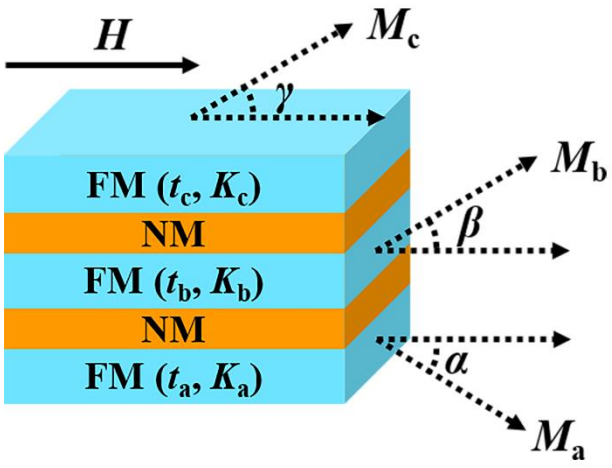

Figure 5.01: Schematic illustration of the numerical simulation parameters in FM/ NM/ FM/ NM/ FM multilayer structure. All the arrows represent in-plane directions.

Therefore, α-β, γ-β and α-γ represents the relative orientation between the magnetization direction of bottom and middle, top and middle, and bottom and top FM layers, respectively. The *M-H* loop is simulated by minimizing the total energy given in Eqn. (5.01).

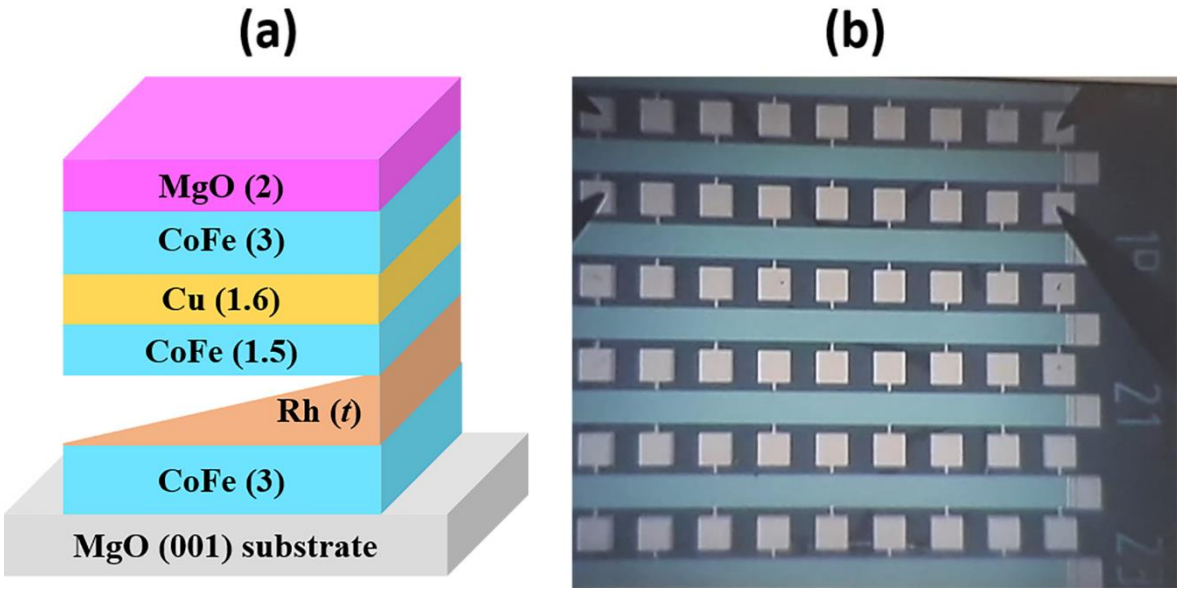

Figure 5.02: (a) The schematic illustration and (b) photo view of the CIP-GMR devices after patterning using photolithography of the sample structure CoFe(3 nm)/ wedge-shaped Rh(t_{Rh} = 0 – 2.5 nm)/ CoFe(1.5 nm)/ Cu(1.6 nm)/ CoFe(3 nm)/ MgO(2 nm) with different t_{Rh} deposited on MgO(001) substrate. All values given in the parenthesis are on the nanometer scale.

5.4. Results and discussion

5.4.1. Properties of CoFe(3 nm)/ wedge-shaped Rh(t_{Rh} = 0 - 2.5 nm)/ CoFe(1.5 nm)/ Cu(1.6 nm)/ CoFe(3 nm)/ MgO(2 nm) films

Figure 5.02(a) and (b) displays the schematic illustration and photo view of the CIP-GMR devices (after patterning using photolithography) of the sample structure CoFe(3 nm)/ wedge-shaped Rh(t_{Rh} = 0 – 2.5 nm)/ CoFe(1.5 nm)/ Cu(1.6 nm)/ CoFe(3 nm)/ MgO(2 nm) with different t_{Rh} deposited on MgO(001) substrate.

5.4.1.1. Rh thickness dependent magnetotransport properties

Figures 5.03 and 5.04 illustrate in-plane MR curves for selected t_{Rh}, and Rh thickness-dependent MR ratio and the saturation magnetic field ($\mu_0 H_s$) for the wedge-shaped samples CoFe(3 nm)/ Rh(t_{Rh} = 0 – 2.5 nm)/ CoFe(1.5 nm)/ Cu(1.6 nm)/ CoFe(3 nm)/ MgO(2 nm). It can be observed that (i) the films with $t_{Rh} \leq 0.72$ nm, marked as zone A in Figure 5.04, exhibit a nonlinear variation of resistance with the applied magnetic field, *i.e.*, the MR curves display rapid variations of the resistance from zero to maximum and then to zero again over a narrow range of applied magnetic field (< ±0.02 T). Although the value of $\mu_0 H_s$ increases slowly with increasing t_{Rh}, the value of $\mu_0 H_s$ is still smaller (< 0.03 T) to saturate the resistance. However, the MR ratio increases first from 15.3 % to 23.1 % with increasing t_{Rh} from 0.24 nm to 0.51 nm and then decreases to 18.4 % for t_{Rh} = 0.72 nm. (ii) As t_{Rh} increases from 0.79 nm to 1.00 nm (marked as zone B), the nature of the MR curve changes from nonlinear behavior to linear type, *i.e.*, the linear variation of resistance in the field range of 0.13 T to 0.65 T, and the MR ratio increases from 11.2 % to 20.6 % with increasing t_{Rh} from 0.79 nm to 1.00 nm. Besides, the value of $\mu_0 H_s$ increases rapidly from 0.03 T to 1.5 T as t_{Rh} increases to 0.86 nm and then decreases to 0.83 T for t_{Rh} = 1.00 nm. (iii) On further increasing t_{Rh} > 1.00 nm, the nature of MR curves again changes from linear behavior to nonlinear type. As a result, the value of $\mu_0 H_s$ decreases rapidly to 0.01 T for t_{Rh} = 1.47 nm and then nearly remains constant between 0.01 T and 0.03 T for 1.47 nm $\leq t_{Rh} \leq$ 2.50 nm. Also, the MR ratio decreases progressively from 19.1 % to 17.1 % by increasing t_{Rh} from 1.13 nm to 1.95 nm (marked as zone C), and then largely drops down to 3.9 % for t_{Rh} = 2.50 nm (marked as zone D). These results reveal the growth nature induced spacer layer thickness dependent magnetic configuration in these films:

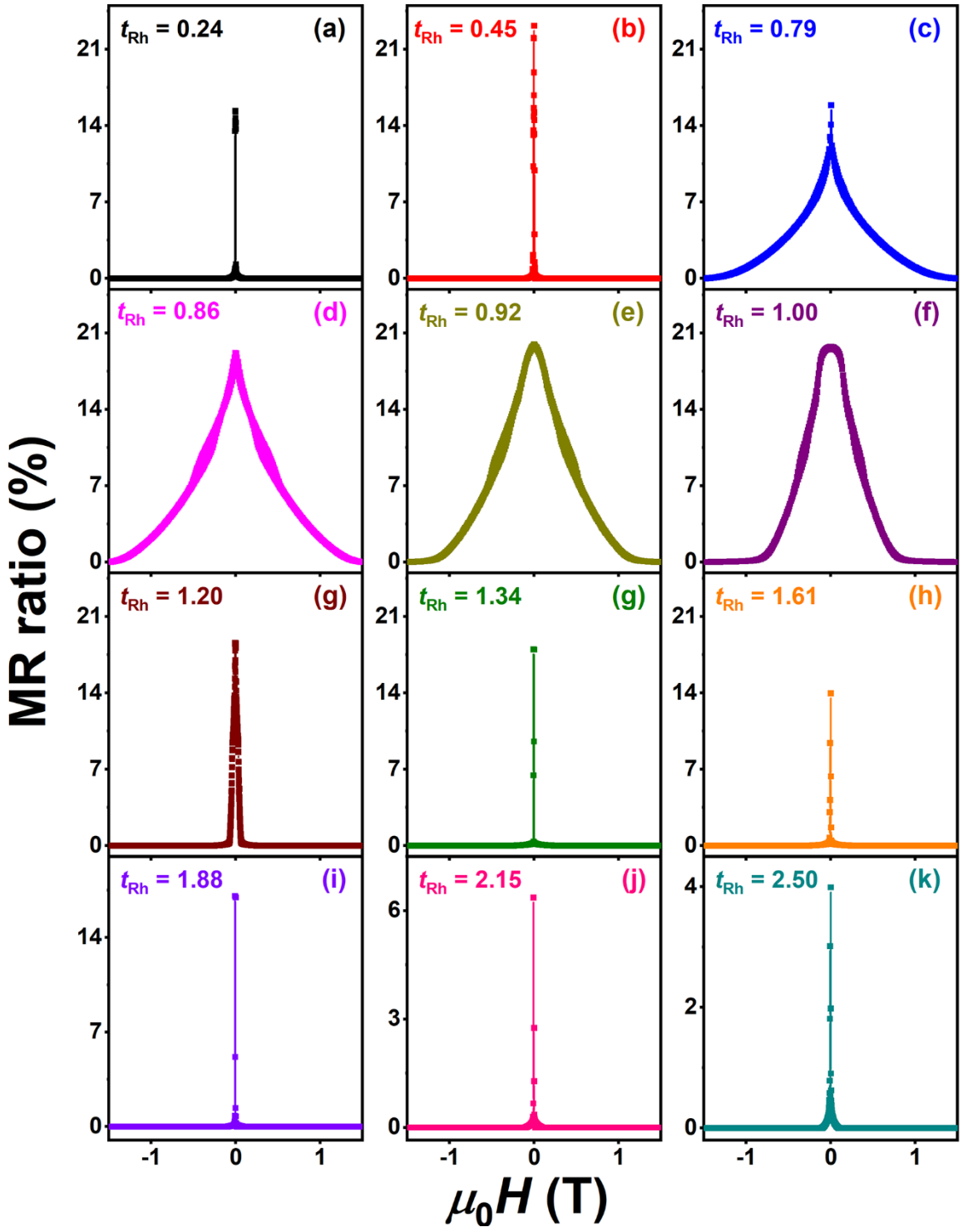

Figure 5.03: Room temperature in-plane MR curves (a)-(k) for wedge-shaped CoFe(3 nm)/ Rh(t_{Rh} = 0 – 2.5 nm)/ CoFe(1.5 nm)/ Cu(1.6 nm)/ CoFe(3 nm)/ MgO(2 nm) films with different t_{Rh} deposited on MgO(001) substrate.

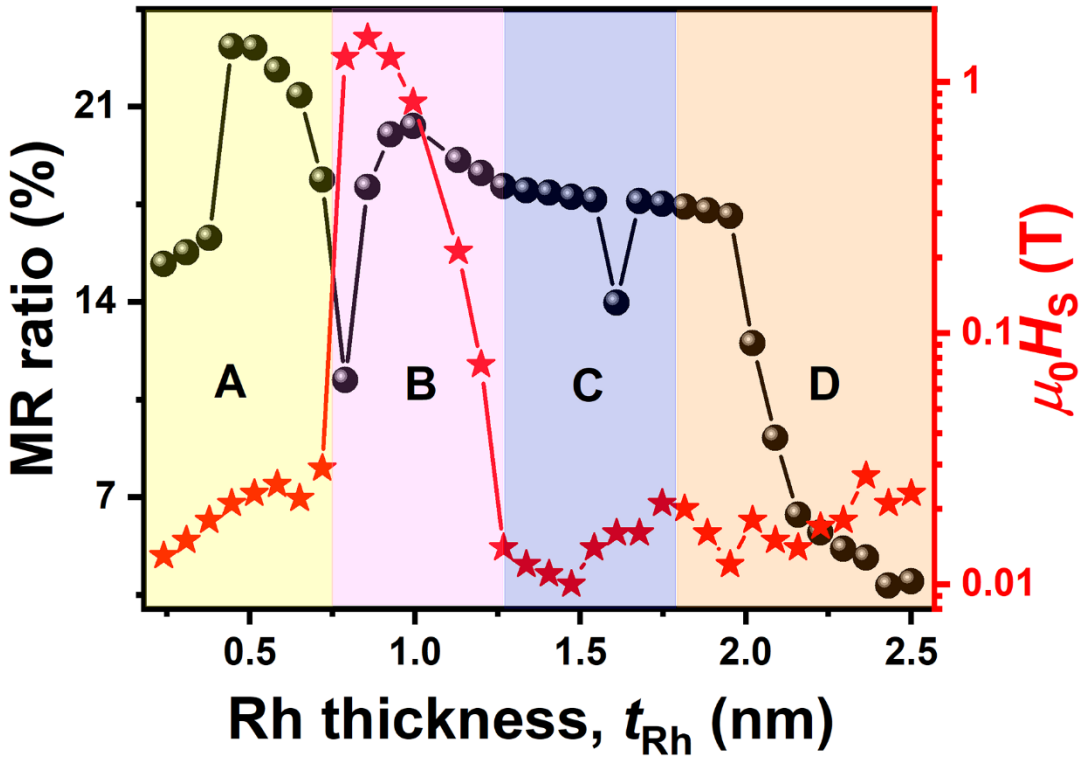

Figure 5.04: Rh thickness-dependent MR ratio and the saturation magnetic field ($\mu_0 H_s$) for CoFe(3 nm)/ Rh(t_{Rh} = 0 – 2.5 nm)/ CoFe(1.5 nm)/ Cu(1.6 nm)/ CoFe(3 nm)/ MgO(2 nm) films with different t_{Rh} deposited on MgO(001) substrate.. The color zones A, B, C, and D represent the different interaction mechanisms described in the text.

(a) in zone A, the nonlinear MR behavior with a large MR ratio is caused by the dominant AFM coupling between the middle and top CoFe layers through the Cu spacer [FATH2019], as the thin Rh spacer does not manipulate the magnetization orientation between the bottom and middle CoFe layers. (b) The change in the MR curves from the nonlinear behavior to linear type with a high MR ratio in zone B is possibly due to the Rh spacer dependent IEC between the bottom and middle CoFe layers. This, in turn, provides the linear MR response [TAPA2021]. (c) For t_{Rh} > 1.25 nm (zone C), the MR curves again transform into nonlinear variation. This could be probably due to ferromagnetic IEC between the bottom and middle CoFe layers. (d) The decrease of the MR ratio at high t_{Rh} in zone D may be due to the current shunting effect through the thick Rh spacer. Besides, the thick Rh spacer layer either changes the structure of the middle CoFe layer or provides substantial strain to the middle layer of CoFe such that the formation of *bcc* Cu remains difficult.

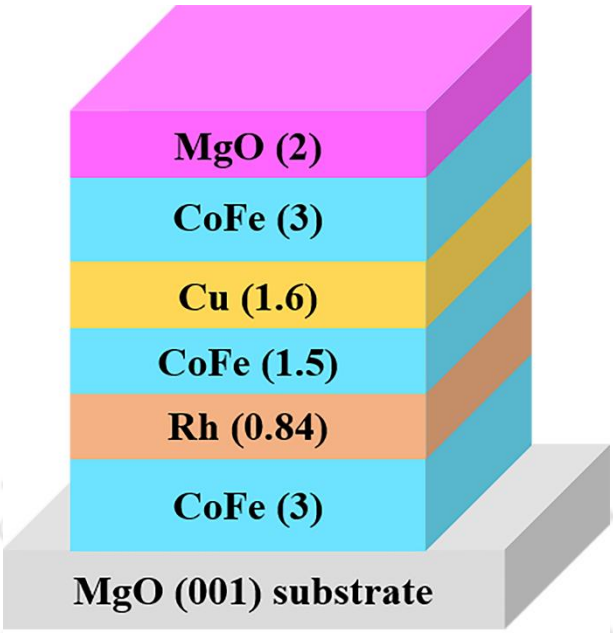

Figure 5.05: The schematic illustration of the flat sample with the structure of CoFe(3 nm)/ Rh(0.84 nm)/ CoFe(1.5 nm)/ Cu(1.6 nm)/ CoFe(3 nm)/ MgO(2 nm) deposited on MgO(001) substrate. All values given in the parenthesis are on the nanometer scale.

5.4.2. Properties of flat CoFe(3 nm)/ Rh(0.84 nm)/ CoFe(1.5 nm)/ Cu(1.6 nm)/ CoFe(3 nm)/ MgO(2 nm) film

5.4.2.1. Structural properties

It should be noted that the magnitudes of IEC and MR ratio are extremely sensitive to t_{Rh} demonstrating linear MR response in the region 0.79 nm $\leq t_{Rh} \leq$ 1.00 nm as shown in Figure 5.04. Therefore, for studying the nature of the IEC between CoFe layers through Rh and Cu spacers, we have fabricated several flat samples having different Rh thickness in the range of 0.79 nm $\leq t_{Rh} \leq$ 1.00 nm, wherein we observed the highest MR ratio for the flat sample with t_{Rh} = 0.84 nm. The discrepancy of the t_{Rh} for obtaining the large MR ratio between wedge-shaped and flat samples should have been caused by the limitation over the control-of the thickness using the linear-motion shutter. Accordingly, the flat sample of CoFe(3 nm)/ Rh(0.84 nm)/ CoFe(1.5 nm)/ Cu(1.6 nm)/ CoFe(3 nm)/ MgO(2 nm) was deposited on a MgO(001) substrate as demonstrated in Figure 5.05. The room temperature out-of-plane XRD patterns and the ϕ-scans of the (220) peak of MgO (2θ = 62.17° and χ = 45°) and the (110) peak of CoFe (2θ = 44.31° and χ = 45°) for flat sample of CoFe/ Rh/ CoFe/ Cu/ CoFe/ MgO are demonstrated in Figure 5.06. The XRD pattern confirmed the growth of the (200) peak of CoFe along with the (200) peaks from the MgO substrate. However, the (200) peak

of Rh could not be observed due to low Rh thickness (t_{Rh} = 0.84 nm). The ϕ-scan patterns elucidate the presence of four-fold symmetry for MgO substrate and CoFe films, confirming the epitaxial growth of *bcc* CoFe on MgO(001) substrate.

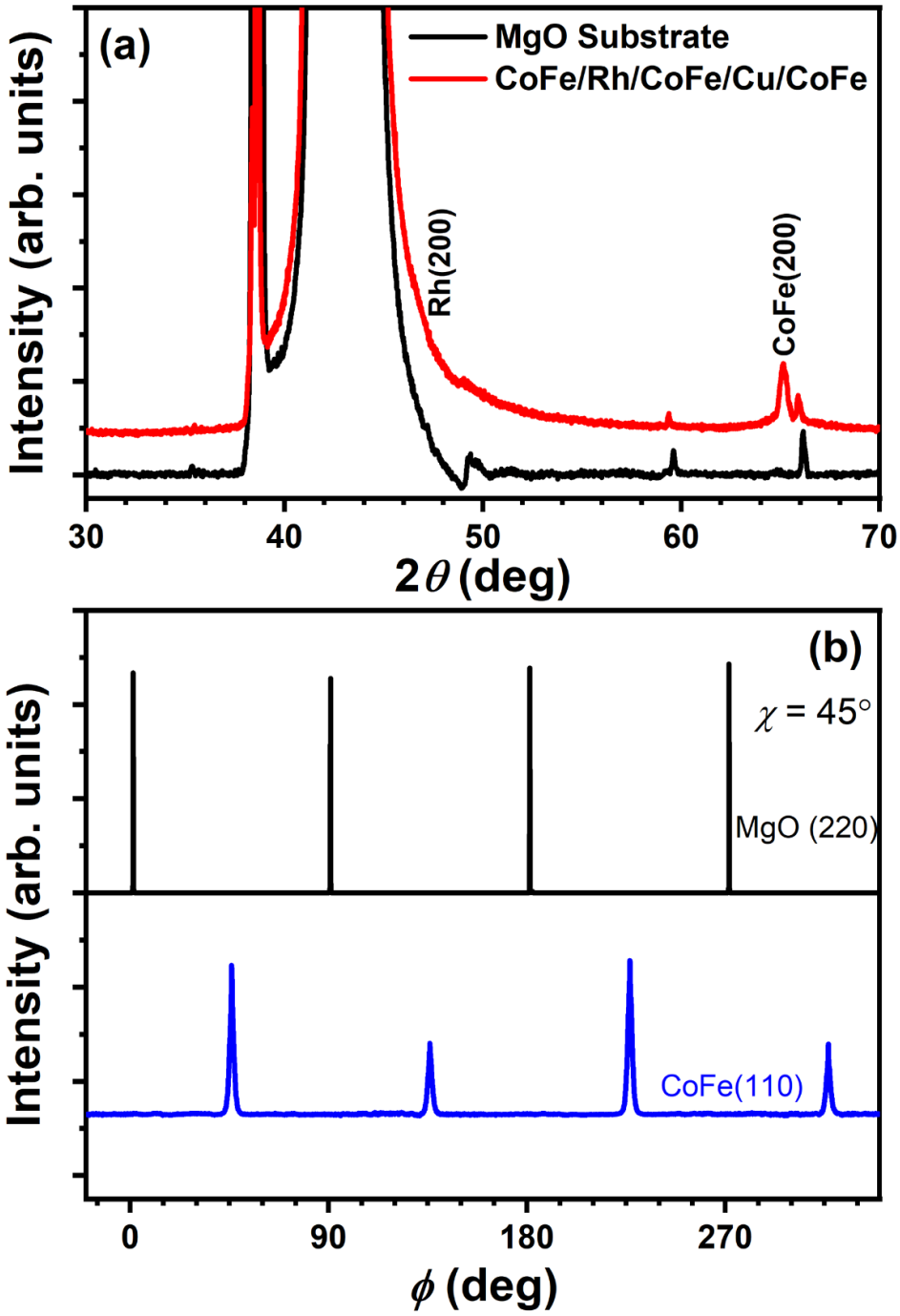

Figure 5.06: (a) Out-of-plane XRD patterns and (b) ϕ-scans of MgO(220) and CoFe (110) reflections for a flat sample of CoFe(3 nm)/ Rh(0.84 nm)/ CoFe(1.5 nm)/ Cu(1.6 nm)/ CoFe(3 nm)/ MgO(2 nm) deposited on MgO(001) substrate.

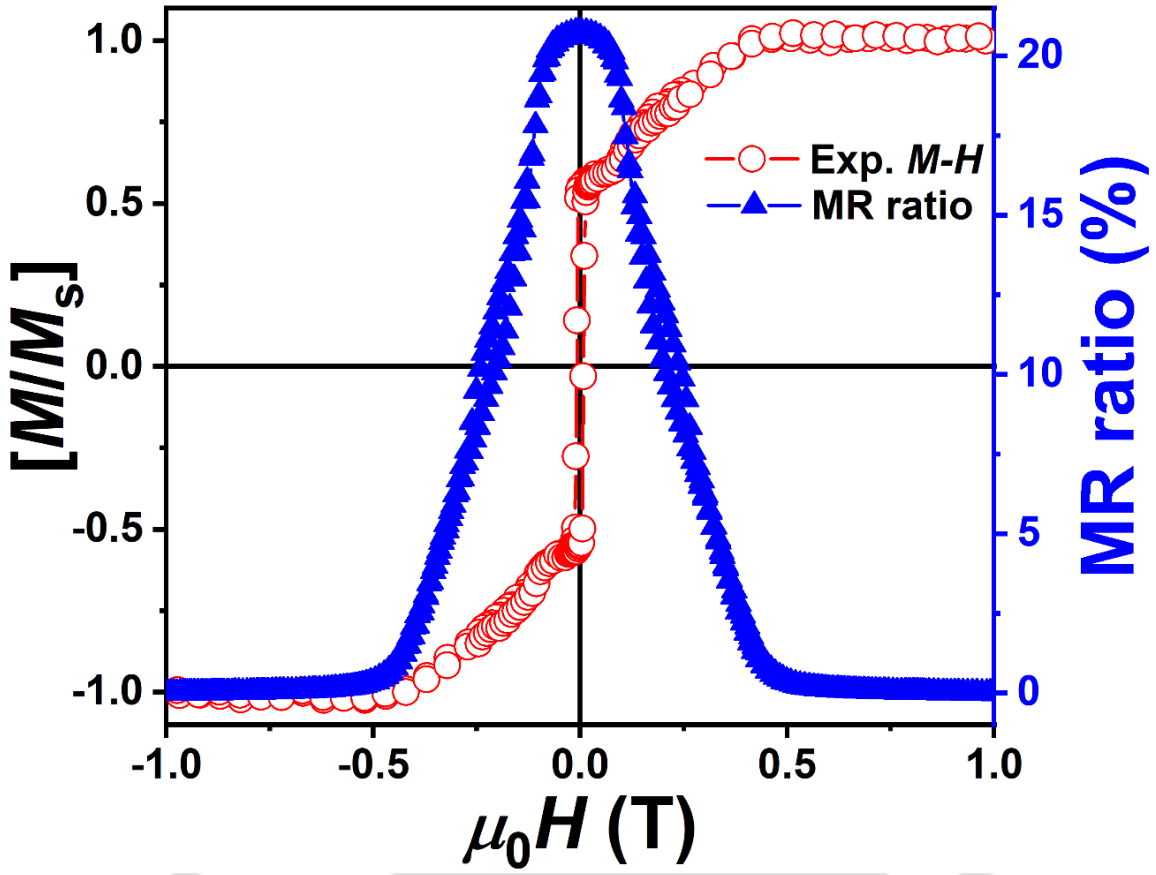

Figure 5.07: Room temperature in-plane *M-H* loop (open circle) and MR curve (solid triangle) for the flat sample of CoFe(3 nm)/ Rh(0.84 nm)/ CoFe(1.5 nm)/ Cu(1.6 nm)/ CoFe(3 nm)/ MgO(2 nm) deposited on a MgO(001) substrate.

5.4.2.2. Magnetic and magnetotransport properties: Experiment and numerical simulations

The room temperature in-plane *M-H* loop and MR curve for the optimized flat sample of CoFe/ Rh/ CoFe/ Cu/ CoFe/ MgO film are depicted in Figure 5.07. The linear MR curve with the large MR ratio of 21 % agrees well with the result obtained for the sample with a similar Rh thickness in the wedge-shaped Rh spacer. It can be clearly seen in Figure 5.07 that both the *M-H* loop and MR curve reveal correlative features between them. For studying the nature of magnetic couplings between CoFe layers through Rh and Cu spacers, we have carried out numerical simulations by minimizing the total energy in Eqn. (5.01) using the terms given in Eqn. (5.02) and considering the following fixed parameters: $K_a = K_b = K_c = 2.13\times10^4$ J/m^3, $\mu_0 M_a = \mu_0 M_b = \mu_0 M_c = 1.95$ T, $t_a = 3$ nm, $t_b = 1.5$ nm, $t_c = 3$ nm, and $J_2'' = 0$. The coupling parameters J_1', J_1'' and J_2' are considered free fit parameters, and their values are estimated when the simulated *M-H* loop complements the experimental one. Following the result by

Fathoni *et al.* [FATH2019] and experiencing the unrealistic fit parameters, no biquadratic coupling is considered through Cu spacer, *i.e.*, $J_2'' = 0$ throughout the simulation.

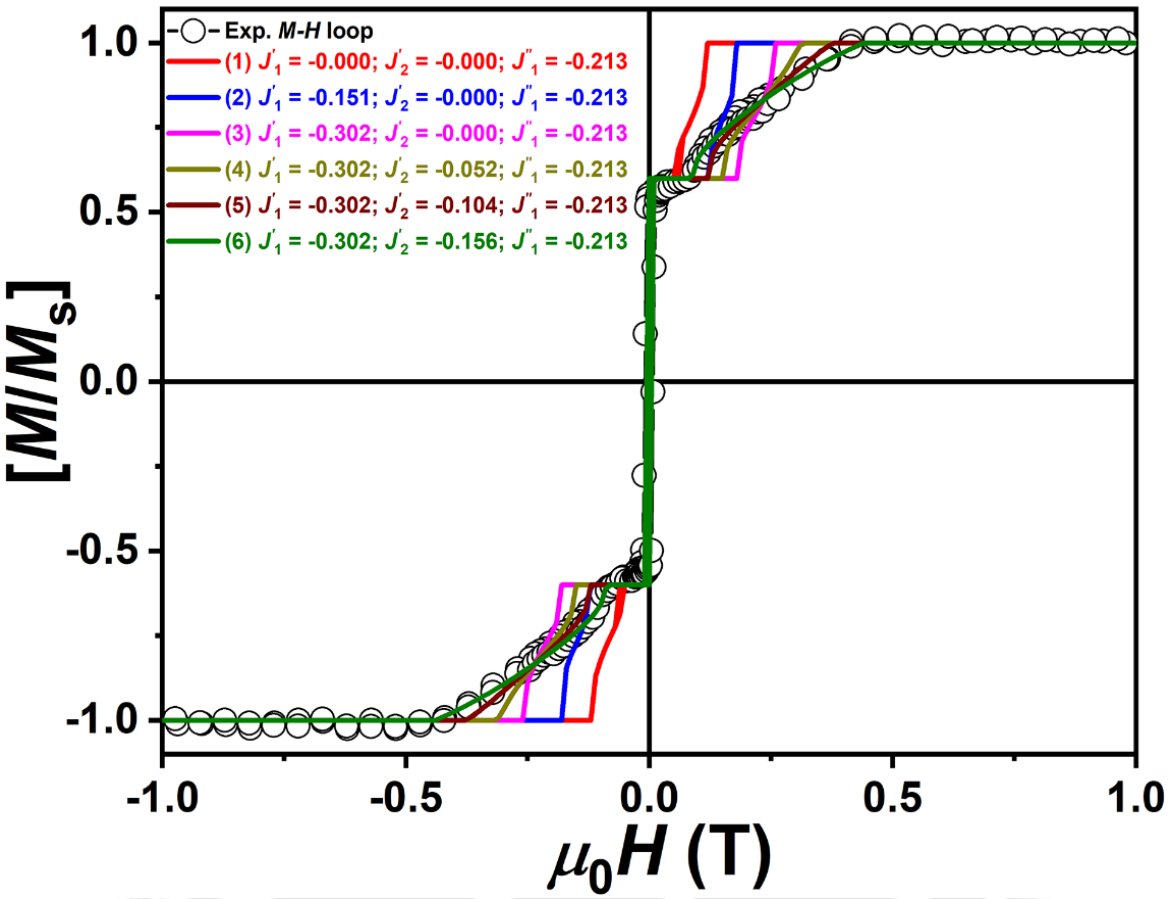

Figure 5.08: Room temperature experimental (open circle) and numerically simulated (solid lines) *M-H* loops with different coupling parameters for the flat sample of CoFe(3 nm)/ Rh(0.84 nm)/ CoFe(1.5 nm)/ Cu(1.6 nm)/ CoFe(3 nm)/ MgO(2 nm) deposited on a MgO(001) substrate.

To demonstrate the role of different coupling parameters and their dependency on linearity, we simulated numerous *M-H* curves with different coupling parameters and presented them in Figure 5.08. It is evident that the obtained simulated *M-H* loop cannot be related with the experimental *M-H* loop when (i) no biquadratic coupling (J_2') is considered and (ii) the ratio between the biquadratic and bilinear couplings, *i.e.*, J_2'/J_1' is below 25% in the simulation.

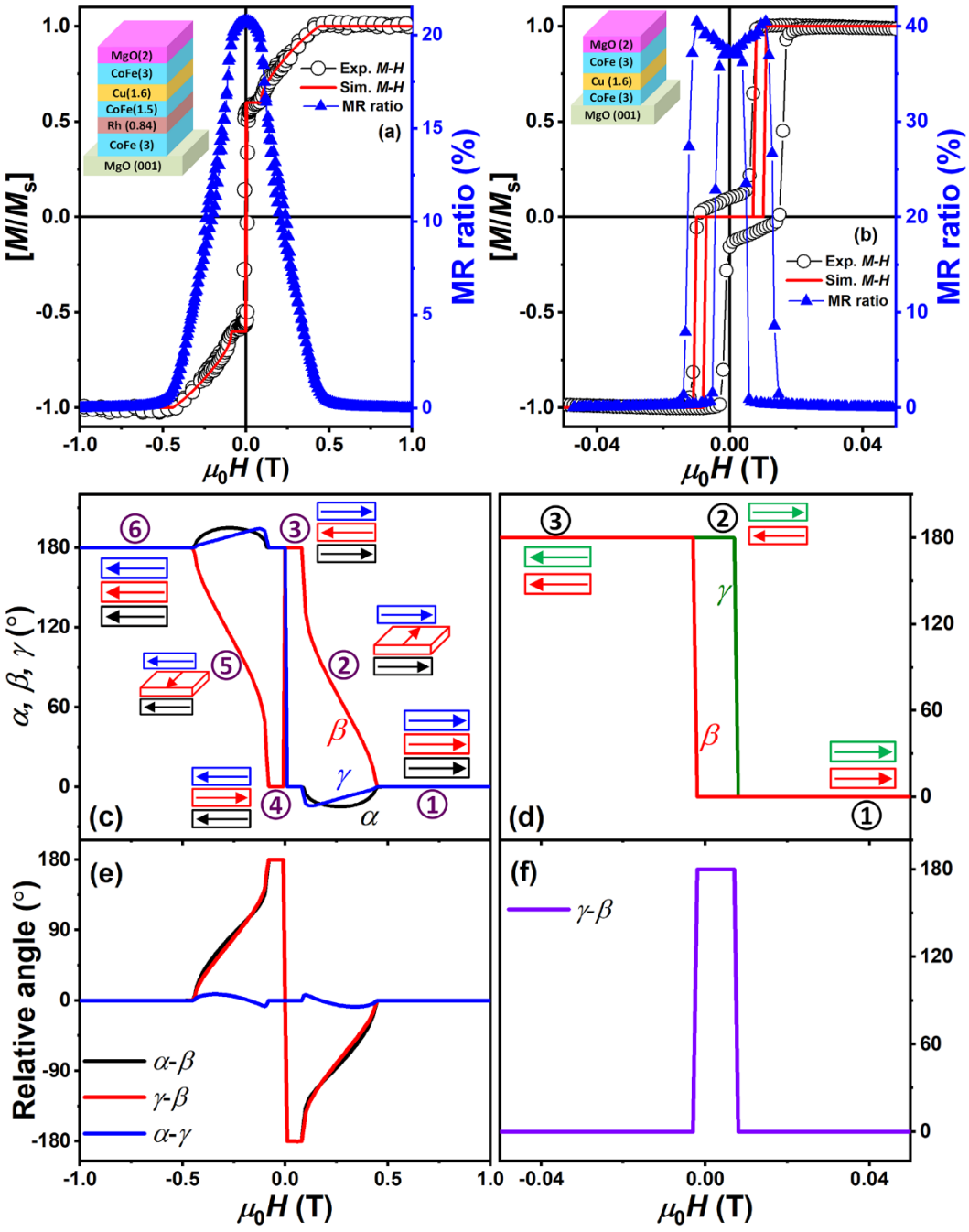

Figure 5.09: Room temperature in-plane experimental (open circle) and numerical simulated (solid line) *M-H* loops and in-plane MR curve (a) for a flat sample of CoFe(3 nm)/ Rh(0.84 nm)/ CoFe(1.5 nm)/ Cu(1.6 nm)/ CoFe(3 nm)/ MgO(2 nm) and (b) for the conventional *bcc* structured CoFe/ Cu/ CoFe films, taken from Ref.[FATH2019]. The variations of the angles [α, β, γ (c) and β, γ (d)] and the relative orientation between angles [α-β,γ-β,α-γ (e) and β-γ (f)] at different magnetic fields for CoFe/ Rh/ CoFe/ Cu/ CoFe and for CoFe/ Cu/ CoFe films, respectively. The schematics of the sample structure and the estimated magnetization directions using the determined angles from simulations are shown in the insets.

These analyses reveal that the ratio between the biquadratic and bilinear couplings should be more than 25% to obtain the simulated *M-H* loop, and the best match within these curves was attained in the simulation with $J_1' = -0.302$ mJ/m^2, $J_2' = -0.156$ mJ/m^2, $J_1'' = -0.213$ mJ/m^2 and $J_2'' = 0$.

Figure 5.09 depicts room temperature experimental (open circle) and simulated (solid line) *M-H* loops, in-plane MR curve and variations of angles (α, β, γ) and the relative orientation between angles (α-β, γ-β, α-γ) at different applied fields in the simulation for the CoFe/ Rh/ CoFe/ Cu/ CoFe film. The schematics of the sample structure and the estimated magnetization directions using angles (α, β, γ) are shown in the insets. For comparison, the *M-H* loop, the MR curve, and detailed analyses of the conventional *bcc* structured $Co_{50}Fe_{50}$/ Cu/ $Co_{50}Fe_{50}$ film are also shown in Figures 5.09(b,d,f). As stated above, the best match of the simulated *M-H* loop (solid line) to the experimental one was attained only when $J_1' = -0.302$ mJ/m^2, $J_2' = -0.156$ mJ/m^2, $J_1'' = -0.213$ mJ/m^2 and $J_2'' = 0$. Note that we obtained significantly different J_1' and J_2' compared to the values we observed for CoFe/ Rh/ CoFe trilayer film as described in Chapter 04. While the exact reason for this variation is not clear, the magnitude of IEC is extremely sensitive to $t_{Rh} < 1$ nm. Thus, it is speculated that the thickness and interfacial microstructure of the Rh spacer possibly gets modified after adding Cu/ CoFe layers and during the post-annealing process.

To correlate the simulation results with the observed MR behavior, the estimated magnetization directions are envisaged based on the extracted values of angles, α, β and γ [see Figure 5.09(c)]. When the applied magnetic field is adequately strong, the magnetizations of all the films align with the direction of the applied magnetic field, *i.e.*, $\alpha = \beta = \gamma = 0$. This exhibits a low resistance state due to the parallel configuration of magnetizations in all three CoFe layers. At a particular magnetic field (~ 0.45 T), β is found to increase gradually with decreasing magnetic field and then reaches quickly to 180° at H = 0.07 T. However, the angles α and γ are observed to be nearly zero for H down to 0.07 T. This behavior can be qualitatively understood by the balance between E_Z and E_{EX} in each CoFe layer, *i.e.*, because of the larger thickness of the top and bottom CoFe layers, E_Z dominantly controls the direction of α and γ, resulting α-γ to be nearly zero. On the other hand, the magnetization of the thinner middle CoFe layer is controlled by the IEC from the top and bottom CoFe layers. Therefore, β gradually changes against the magnetic field due to the contribution of J_2', indicating that the middle CoFe layer acts as a sensing layer of the

magnetic field. These results reveal that with decreasing the magnetic field, the magnetization of the middle CoFe layer starts rotating away from the saturation and eventually forms AFM coupling with both the bottom and top CoFe layers. As a result, α-β and γ-β varies almost linearly and, therefore, giving nearly a linear variation of *R-H* and providing a maximum linear MR ratio of 21 %. When the magnetic field sign changes from positive to negative, the magnetization of the top and bottom CoFe layers switches rapidly to the field direction. Simultaneously, the magnetization of the middle CoFe layer reverses to the opposite with respect to the magnetization of the bottom and top CoFe layers due to IEC. On further increasing the magnetic field negatively, the magnetization of the middle CoFe layer rotates again progressively towards saturation. Thus, the MR ratio decreases linearly to zero when the magnetizations of all the CoFe layers align to the direction of the applied magnetic field.

In order to highlight the significant achievement of linear *R-H* response by adding the CoFe/ Rh layers to the all *bcc* CoFe/ Cu/ CoFe film [FATH2019], the in-plane MR curve, the *M-H* loop, and the detailed analysis of the magnetic coupling for CoFe/ Cu/ CoFe film in Figures 5.09(b,d,f) are presented. The dominant negative J_1 contribution through the Cu spacer and the cubic crystalline magnetic anisotropy, *K* in the CoFe layers provide an abrupt change of the MR due to the magnetization reversal of CoFe layers. This comparison indeed enlightens the role of biquadratic coupling in tuning the shape of the *R-H* response from the nonlinear behavior to the linear one by suitably placing the additional CoFe layer with the Rh spacer. Moreover, this is the first experimental result to demonstrate that a CIP-GMR device, having an asymmetric stacking structure, exhibits a large linear sensitivity through a contribution of biquadratic coupling.

To address the different magnetic couplings between CoFe layers through Rh and Cu spacers, the detailed microstructure analyses covering the cross-sectional annular dark-field STEM (ADF-STEM) and nano-beam electron diffraction patterns are presented in Figure 5.10. The ADF-STEM images taken along the [100] zone axis of the MgO substrate show that CoFe, Rh, and Cu layers grow epitaxially on the MgO substrate [Figure 5.10(a)]. The nano-beam electron diffraction patterns obtained from the MgO substrate and the CoFe layer on the MgO show that there is an orientation relationship described as $(002)_{MgO}//(002)_{CoFe}$, $[020]_{MgO}//[110]_{CoFe}$, indicating the (002)-oriented epitaxial growth of CoFe layer [Figure 5.10(b)].

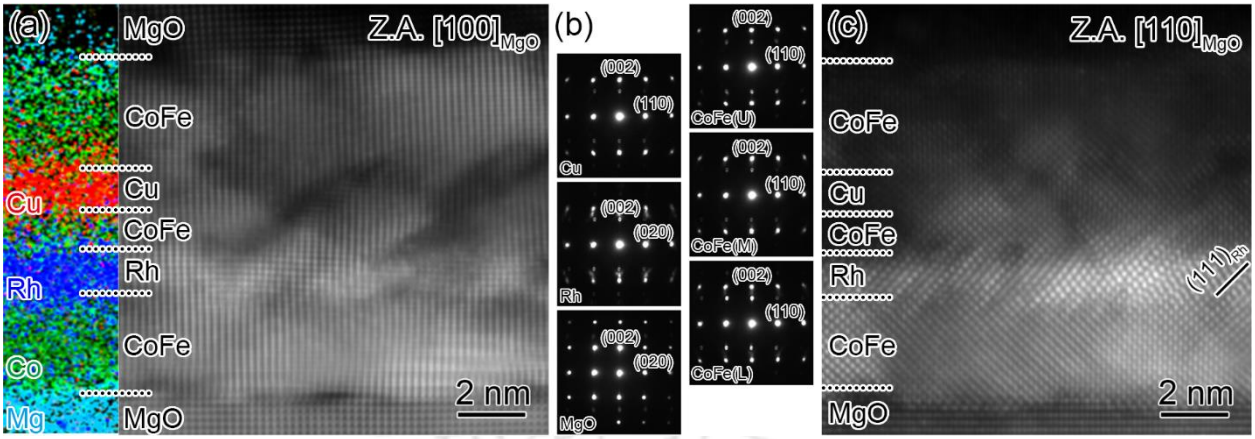

Figure 5.10: (a) EDS elemental map of Mg, Co, Rh and Cu, and ADF-STEM image of the sample taken from the zone axis of $[100]_{MgO}$, (b) Nano-beam electron diffraction patterns obtained from constituent layers, and (c) ADF-STEM image of the sample taken from the zone axis of $[110]_{MgO}$.

The electron diffraction pattern obtained from the Cu spacer is similar to that of CoFe, confirming the metastable *bcc* type structure [Figure 5.10(b)] [FATH2019]. The structure of the Rh spacer is identified as the face-centered cubic (*fcc*) structure from the electron diffraction pattern obtained from the Rh layer [Figure 5.10(b)] and the ADF-STEM image taken from the zone axis of $[110]_{MgO}$ showing a high density of nano-twin with the twinning plane and direction of (112) and <111>, respectively [Figure 5.10(c)]. Such a high density of nano-twin causes an atomically rough and strained CoFe/ Rh interface. This may be one of the possible mechanisms responsible for the biquadratic coupling, in line with the so-called ~~a~~ fluctuation mechanism model proposed by Slonczewski [SLON1991], to yield the linear MR response in the present samples. Note that the formation of *fcc* structure in the 0.84 nm-thick Rh layer agrees with the previous study for Fe/ Rh/ Fe structure, in which body-centered tetragonal Rh forms in the thinner region of less than 0.5 nm [TOMA1998].

5.4.2.3. Sensing properties as a magnetic field sensor

The magnetic sensor application demands a linear *R-H* response with low nonlinearity and high sensitivity. Mancoff *et al.* [MANC2000] and Sebastiaan van Dijken *et al.* [DIJK2005] demonstrated the linear and reversible MR with the magnetic field sensitivity of 0.014 %/mT and 0.018 %/mT, respectively, using a magnetic spin-valve consisting of CoFe FM and thick Cu spacer layers. Thus, to extract the sensitivity and nonlinearity parameters, a linear fitting was carried on the experimental data [SHIR2018] by selecting a magnetic field region of 130

– 350 mT for the CIP-GMR device of CoFe(3 nm)/ Rh(0.84 nm)/ CoFe(1.5 nm)/ Cu(1.6 nm)/ CoFe(3 nm)/ MgO(2 nm) and presented in Figure 5.11.

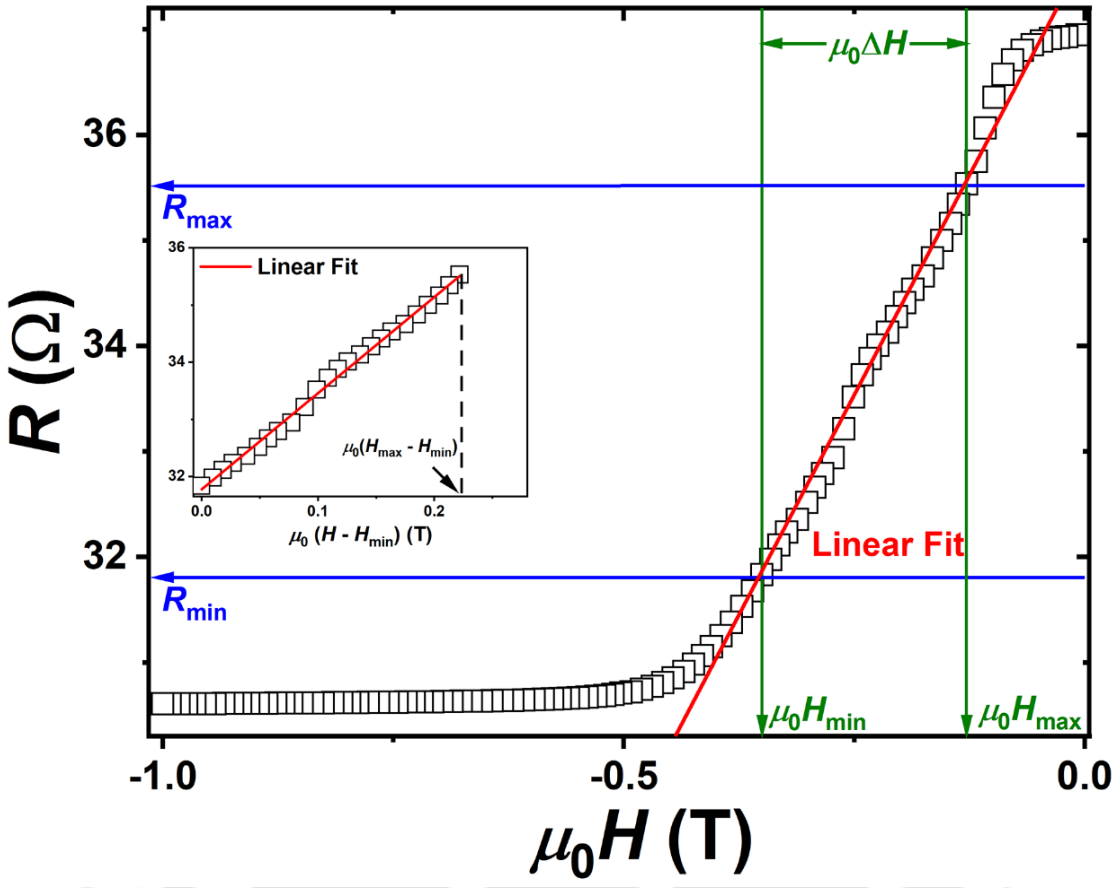

Figure 5.11: *R-H* curve for a flat sample of CoFe(3 nm)/ Rh(0.84 nm)/ CoFe(1.5 nm)/ Cu(1.6 nm)/ CoFe(3 nm)/ MgO(2 nm) deposited on MgO(001) substrate for defining the effective range. The variation of resistance as a function of the normalized effective field is shown in the inset.

The sensitivity is defined as a value of the MR ratio divided by the magnetic field range, *i.e.*, $\Delta MR/\Delta H$. The nonlinearity, represented as %full-scale (FS), is determined as a maximum of the normalized difference between an experimental resistance R_{exp} and its linear fit value R_{fit}, expressed as

$$Nonlinearity\ (\%\text{FS}) = \frac{R_{exp}(H) - R_{fit}(H)}{R_{max} - R_{min}} \times\ 100 \qquad (5.03)$$

where, H is the applied magnetic field, and R_{max} (R_{min}) is the maximum (minimum) of the experimental resistance within the evaluation range of the magnetic field. As discussed in Chapter 04, for the CoFe/ Rh/ CoFe trilayer film, the highest sensitivity and nonlinearity were obtained to be 0.001 %/mT and 0.21 %FS, respectively. Stupendously, the sensitivity

increased to 0.047 %/mT along with a nonlinearity of 0.98 %FS in a sensing magnetic field range of 220 mT for CoFe(3 nm)/ Rh(0.84 nm)/ CoFe(1.5 nm)/ Cu(1.6 nm)/ CoFe(3 nm)/ MgO(2 nm) film. This range of 220 mT was chosen to represent an operating range that is relatively large with a low nonlinearity characteristic. These values are not only found to be enhanced as compared to the earlier report [NAKA2017] on CoFeB/ MgO/ CoFeB based MTJ (sensitivity of 0.053 %/mT and nonlinearity of 3.09 %FS) with a perpendicularly magnetized synthetic AFM reference layer having the film stack of [Co(0.2)/ Pd(0.4)]$_9$ / Co(0.2)/ Ru(0.4)/ Co(0.2)/ [Pd(0.4)/ Co(0.2)]$_7$/ Ta(0.3)/ $Co_{40}Fe_{40}B_{20}$(0.8)/ MgO(2)/ $Co_{40}Fe_{40}B_{20}$(t_{CoFeB})/ Ta(5)/ Ru(8), but also observed to have a wider dynamic range of magnetic fields as compared to the CoFe based magnetic spin-valve [DIJK2005]. It may be noted that one drawback of the present sensor is the requirement of a bias magnetic field of about 200 mT to shift the operation field range. This can be achieved by placing a suitable permanent magnet beside the sensor. In addition, the polarity of the magnetic field can be detected by making a Wheatstone bridge circuit as performed in previous studies [FERR2012]. From the currently obtained results, it can be concluded that the prudent stacking of CoFe layers with *fcc* Rh and the metastable *bcc*-Cu spacers distinctly improves sensor performance metrics in CIP-GMR devices because the contribution of biquadratic coupling through Rh spacer helps in realizing a linear response in the CoFe/ *bcc*-Cu/ CoFe structure giving the high MR ratio. The observed results demonstrate that CIP-GMR devices with a combination of different magnetic couplings between CoFe layers using Rh and metastable *bcc*-Cu spacers are promising candidates for wide dynamic range magnetic sensors. The careful tuning of the thickness of the Rh spacer and CoFe layers in the CIP-GMR device may provide additional pathways for tuning the sensitivity and dynamic range to specific sensor applications in the low and medium magnetic field range, which is discussed in Chapter 6.

5.5. Summary

A novel approach for enhancing linear MR ratio in CIP-GMR magnetic sensors by integrating Cu spacer with the CoFe/ Rh/ CoFe trilayer stacking has been successfully demonstrated in this chapter. Accordingly, CoFe(3 nm)/ wedge-shaped Rh(t_{Rh} = 0 – 2.5 nm)/ CoFe(1.5 nm)/ Cu(1.6 nm)/ CoFe(3 nm)/ MgO(2 nm) and flat sample of CoFe(3 nm)/ Rh(0.84 nm)/ CoFe(1.5 nm)/ Cu(1.6 nm)/ CoFe(3 nm)/ MgO(2 nm) were fabricated on

single-crystal MgO(001) substrate. The salient features of the wedge-shaped multilayer films and the optimized flat sample from the current investigations are as follows:

- The MR ratio and saturating magnetic field were tunable between 3.9 % and 23.5 %, and 0.013 T and 1.5 T for the CoFe(3 nm)/ wedge-shaped Rh(t_{Rh} = 0 – 2.5 nm)/ CoFe(1.5 nm)/ Cu(1.6 nm)/ CoFe(3 nm)/ MgO(2 nm) films.
- Despite obtaining a large MR ratio (> 20 %) over a wide range of Rh spacer thicknesses, the nature of the MR curves (nonlinear/ linear) was found to be sensitive to the Rh spacer.
- The optimized Rh thickness for obtaining a linear *R-H* response with a large MR ratio of 21 % was found to be 0.84 nm.
- The out-of-plane XRD patterns and ϕ-scans of CoFe(3 nm)/ Rh(0.84 nm)/ CoFe(1.5 nm)/ Cu(1.6 nm)/ CoFe(3 nm)/ MgO(2 nm) films confirmed the epitaxial growth of *bcc* CoFe thin films on the MgO(001) substrate.
- The room temperature magnetic properties and numerical simulation analyses confirmed that the middle CoFe sensing layer was well controlled by the interlayer exchange coupling through the Rh spacer and gave the linear response without losing a high MR ratio through the *bcc*-Cu spacer.
- TEM studies confirmed the formation of a fully epitaxial (001)-oriented structure with *fcc* Rh and metastable *bcc* Cu spacer layer replicating the structure of *bcc* CoFe.
- The numerical simulation analysis demonstrated that the simulated *M-H* loop correlates with the experimental *M-H* loop only when J_2'/J_1' is more than 25 %.
- The simulated *M-H* loop provided the best match only when $J_1' = -0.302$ mJ/m^2, $J_2' = -0.156$ mJ/m^2, $J_1'' = -0.213$ mJ/m^2 and $J_2'' = 0$, supporting the presence of both 180° and 90° magnetic configurations through Rh spacer and 180° magnetic configurations through metastable *bcc* Cu spacer
- The CIP-GMR device showed the linear MR curve with the highest MR ratio of 21 %, the enhanced sensitivity of 0.047 %/mT, the reduced nonlinearity of 0.98 %FS and a comprehensive operation field range of 220 mT.

Chapter 6

Effect of CoFe layer thickness on the sensing characteristics of asymmetric structured fully epitaxial CIP-GMR based linear magnetic sensors

6.1. Introduction

Giant magnetoresistance (GMR) devices find widespread applications as magnetic field sensors. They bring aggregative performance improvements in the fabrication process, structure size, anti-noise stability, high sensitivity, low power consumption, *etc*. However, traditional GMR devices face challenges owing to their nonlinear resistance response to the applied magnetic field. The advances in sensor technology demands (i) low cost, (ii) compact size, (iii) simple device structure, (iv) high sensitivity, and (v) low nonlinearity. Taking a cue from the largest MR ratio realized in a current-in-plane (CIP)-GMR device using metastable body-centered-cubic, *bcc*-Cu spacer [FATH2019], a new CIP-GMR device has been developed with a combination of two spacer materials, *i.e.*, CoFe/ Rh/ CoFe(sensing layer)/ *bcc*-Cu/ CoFe asymmetric structure and discussed in Chapter 05. As a result, a large linear sensitivity was achieved due to the enhanced MR ratio of 21 % through a biquadratic coupling resulting in a high sensitivity of 0.047 %/mT, reduced nonlinearity of 0.98 %full-scale, along with a substantially wider operation field range of 220 mT. The detailed Rh spacer thickness-dependent study and numerical simulation analyses confirmed that the middle CoFe sensing layer is well-controlled by interlayer exchange coupling (IEC) through the Rh spacer, giving rise to a linear response without losing the high MR ratio through the metastable *bcc*-Cu spacer [TAPA2021].

One of the technological hurdles in multilayer films is the control of the IEC between the ferromagnetic (FM) layers. It has been reported in the literature that sensing properties can be tuned substantially by controlling various factors such as the FM layer thickness [NAKA2017], the number of multilayers [SHIR2018], and processing conditions in MR devices [YUAN2015]. However, no systematic investigation has been carried out on this type of CIP-GMR structure to manipulate the MR ratio, sensitivity, nonlinearity, and operating field range depending on the requirement of applications. Therefore, in this chapter, the effect of thickness of the top and middle CoFe layers on the IEC, linear MR properties, and sensing parameters is presented. Accordingly, asymmetric structured CIP-GMR device of CoFe(3 nm)/ Rh(0.84 nm)/ CoFe(x = 1.0, 1.5, 2.0 nm)/ Cu(1.6 nm)/ CoFe(y = 0, 2, 3, 4 nm)/ MgO(2 nm) was fabricated on MgO(001) substrate. The MR ratio and saturating magnetic field are tunable between 3.9 % and 23.5 %, and 0.013 T and 1.5 T, respectively. The highest sensitivity (0.047 %/mT), reduced nonlinearity (0.98 %full-scale), and larger operation magnetic field range (220 mT) are achieved for the film with t_{Rh} = 0.84, x = 1.5, and y = 3.0. The numerical simulation analyses confirm biquadratic coupling between the bottom and

middle CoFe layers through Rh and antiferromagnetic (AFM) coupling between the middle and top CoFe layers through a Cu spacer, providing the linear MR. The fine-tuning of thicknesses of the middle and top CoFe layers provides supplementary routes for optimizing the sensitivity and operation field range of the CIP-GMR devices to specific magnetic sensor applications in the low and medium magnetic field range.

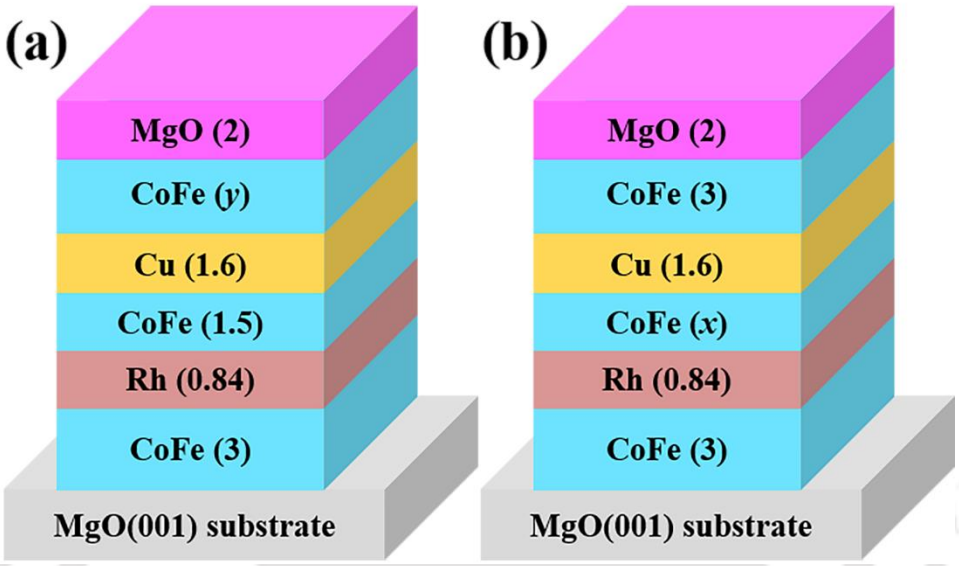

Figure 6.01: The schematic representation of the films' stack for (a) CoFe(3 nm)/ Rh(0.84 nm)/ CoFe(1.5 nm)/ Cu(1.6 nm)/ CoFe(y = 0, 2, 3, 4 nm)/ MgO(2 nm) and (b) CoFe(3 nm)/ Rh(0.84 nm)/ CoFe(x = 1.0, 1.5, 2.0 nm)/ Cu(1.6 nm)/ CoFe(3 nm)/ MgO(2 nm) deposited on MgO(001) substrate. All values given in the parenthesis are on the nanometer scale.

6.2. Experimental details

CIP-GMR films consisting of flat samples of (a) CoFe(3 nm)/ Rh(0.84 nm)/ CoFe(1.5 nm)/ Cu(1.6 nm)/ CoFe(y = 0, 2, 3, 4 nm)/ MgO(2 nm) and (b) CoFe(3 nm)/ Rh(0.84 nm)/ CoFe(x = 1.0, 1.5, 2.0 nm)/ Cu(1.6 nm)/ CoFe(3 nm)/ MgO(2 nm), as shown schematically in Figure 6.01, were directly deposited on MgO(001) substrates at room temperature. All films were fabricated using the UHV compatible DC magnetron sputtering system. The base pressure of the chamber was better than 1×10^{-7} Pa. Before depositing the films, the MgO substrate's surface was etched using Argon ion milling in the sputtering chamber. The composition of all CoFe layers in different samples is kept as $Co_{50}Fe_{50}$. The deposition rate of CoFe, Rh and Cu films was pre-calibrated using an *ex-situ* surface profilometer. The deposition rates of CoFe, Rh, and Cu films were pre-calibrated using an *ex-situ* surface profilometer and optimized to be 0.67, 0.11, and 0.39 Å/s, respectively. Post-annealing of the as-deposited

films was performed at 250 °C for 1 h to stabilize the interfacial roughness under high vacuum conditions. In order to pattern the film into a four-terminal device structure, photolithography and Argon ion etching were used. The films were patterned into CIP-GMR devices in the shape of wires having dimensions of 2820×200 μm^2 and gold-coated electrodes of 200×200 μm^2 sizes using photolithography.

X-ray diffraction (XRD) with Cu-K_α radiation (λ = 1.5406 Å) was employed for the structural characterization of the samples. Magnetic properties (*M-H* loops) were measured using a Vibrating Sample Magnetometer (VSM, LakeShore Model 7410) at room temperature. The room temperature *R-H* response of the CIP-GMR devices was investigated by standard DC four-probe technique using VersaLab setup and Physical Property Measurement System (PPMS, Quantum Design).

6.3. Numerical simulation methods for multilayer structure

For understanding the nature of interlayer couplings between CoFe layers through Rh and Cu spacers, the *M-H* loops are simulated using the numerical simulation model as discussed in Chapter 5 under section 5.3.

6.4. Result and discussion

6.4.1. Properties of flat CoFe(3 nm)/ Rh(0.84 nm)/ CoFe(*x* = 1.0, 1.5, 2.0 nm)/ Cu(1.6 nm)/ CoFe(*y* = 0, 2, 3, 4 nm)/ MgO(2 nm) multilayer films

6.4.1.1. Structural properties

The room temperature out-of-plane XRD patterns and the ϕ-scans of (220) peak of MgO (2θ = 62.17° and χ = 45°) and (110) peak of CoFe (2θ = 44.31° and χ = 45°) for flat samples of CoFe(3 nm)/ Rh(0.84 nm)/ CoFe(1.5 nm)/ Cu(1.6 nm)/ CoFe(*y* = 0, 2, 3, 4 nm)/ MgO(2 nm) and CoFe(3 nm)/ Rh(0.84 nm)/ CoFe(*x* = 1.0, 1.5, 2.0 nm)/ Cu(1.6 nm)/ CoFe(3 nm)/ MgO(2 nm) are presented in Figures 6.02 and 6.03, respectively. The (200) peak of CoFe (2θ = 65.40°) confirmed the formation of *bcc* CoFe in all the multilayer films. However, owing to the critically low thickness of Rh (t_{Rh} = 0.84 nm) the (200) diffraction peaks from face-centered-cubic (*fcc*) Rh could not be observed. In addition, the XRD peak at 2θ = 43° represents the (200) peaks originating from the MgO substrate.

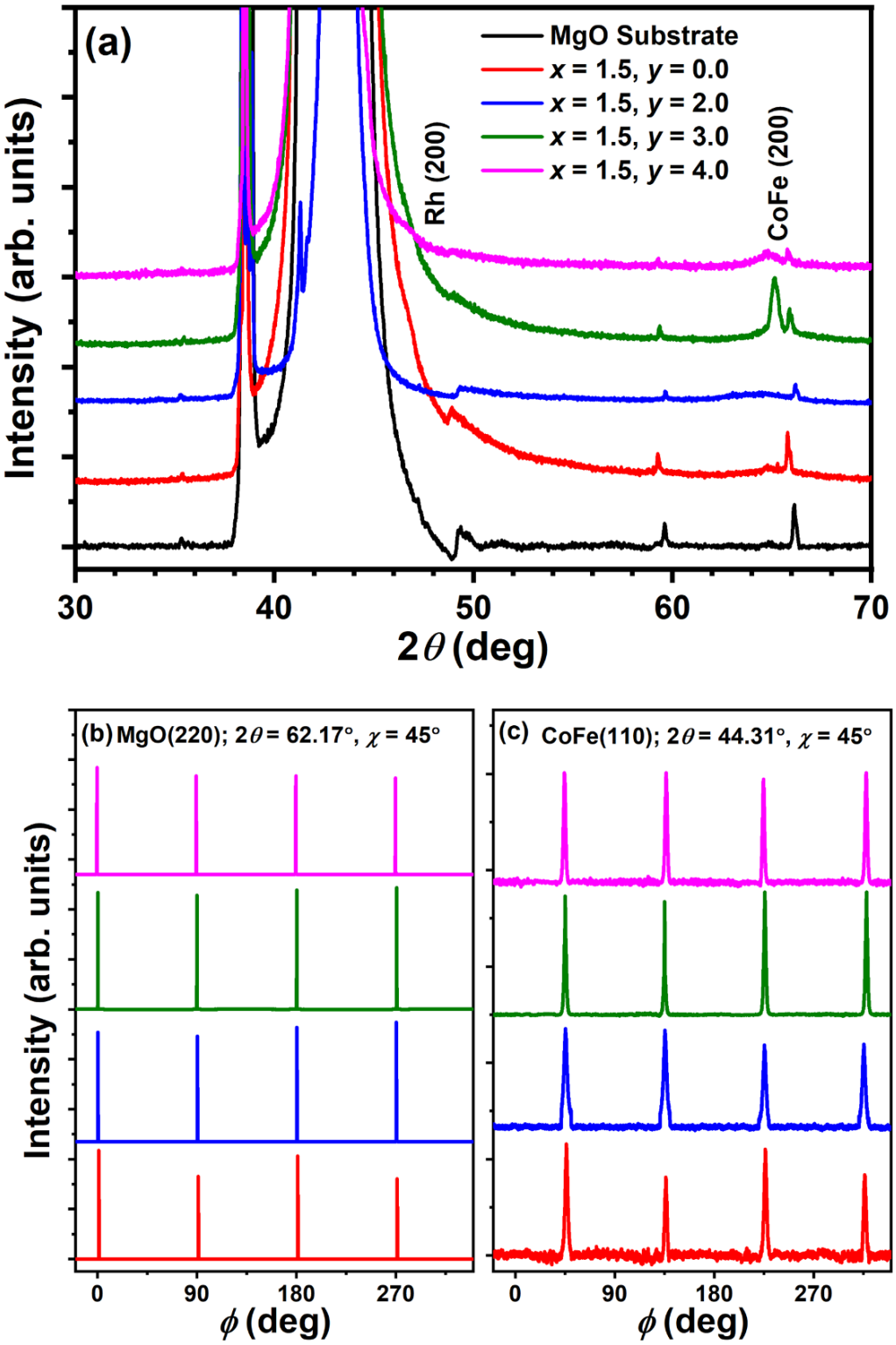

Figure 6.02: (a) Out-of-plane XRD patterns, ϕ-scan of (b) MgO (220), and (c) CoFe (110) reflections for a flat sample of CoFe(3 nm)/ Rh(0.84 nm)/ CoFe(1.5 nm)/ Cu(1.6 nm)/ CoFe(y = 0, 2, 3, 4 nm)/ MgO(2 nm) deposited on MgO(001) substrate.

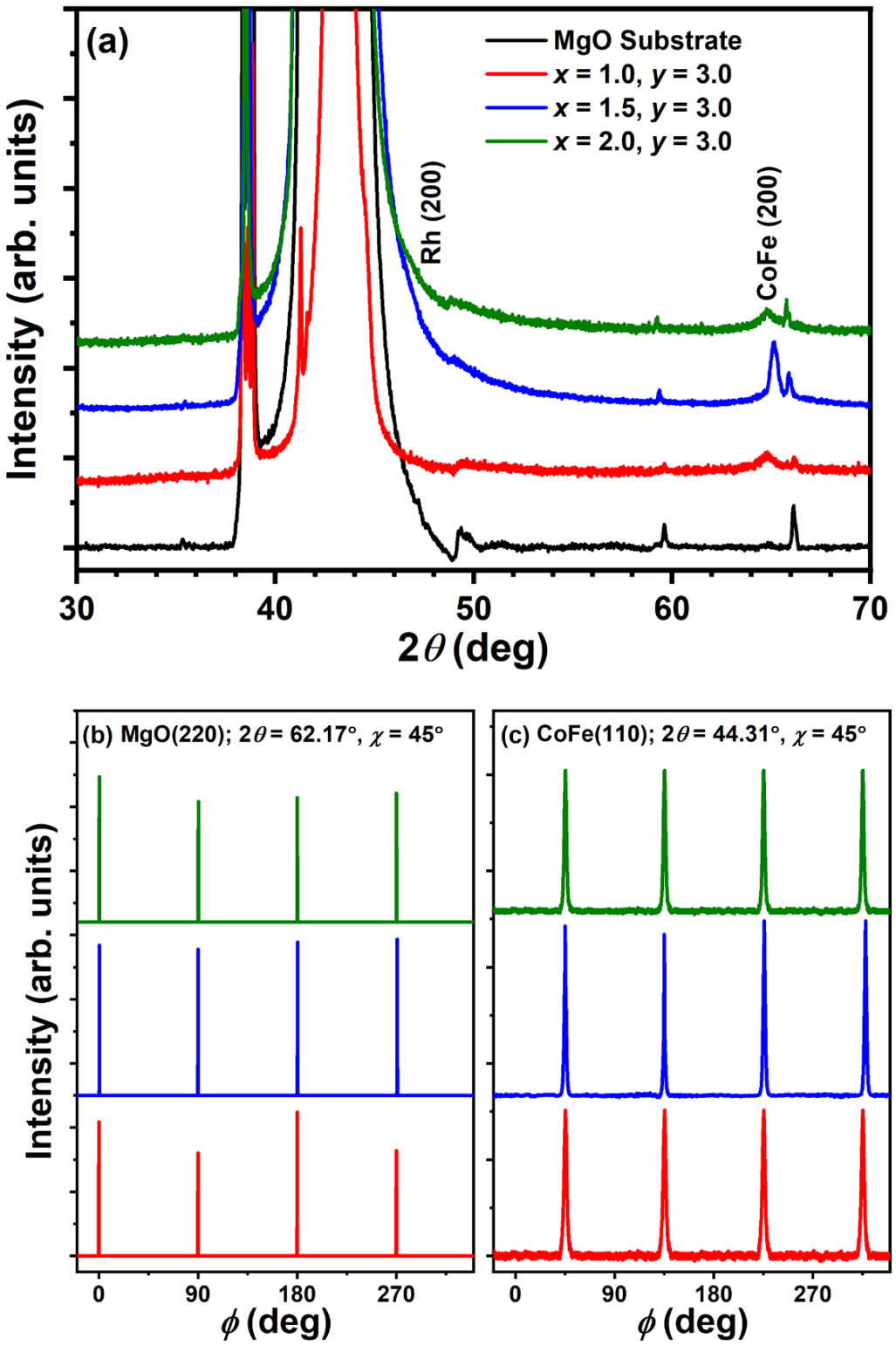

Figure 6.03: (a) Out-of-plane XRD patterns, ϕ-scan of (b) MgO (220), and (c) CoFe (110) reflections for a flat sample of CoFe(3 nm)/ Rh(0.84 nm)/ CoFe(x = 1.0, 1.5, 2.0 nm)/ Cu(1.6 nm)/ CoFe(3 nm)/ MgO(2 nm) deposited on MgO(001) substrate.

The ϕ-scans demonstrated in Figures 6.02(b,c) and 6.03(b,c) reveal that MgO substrate and CoFe films exhibit four well-defined peaks periodically separated from one another by an angular difference of 90°. These results confirm the epitaxial growth of CoFe on the MgO substrate along (001) orientation for all the multilayer films.

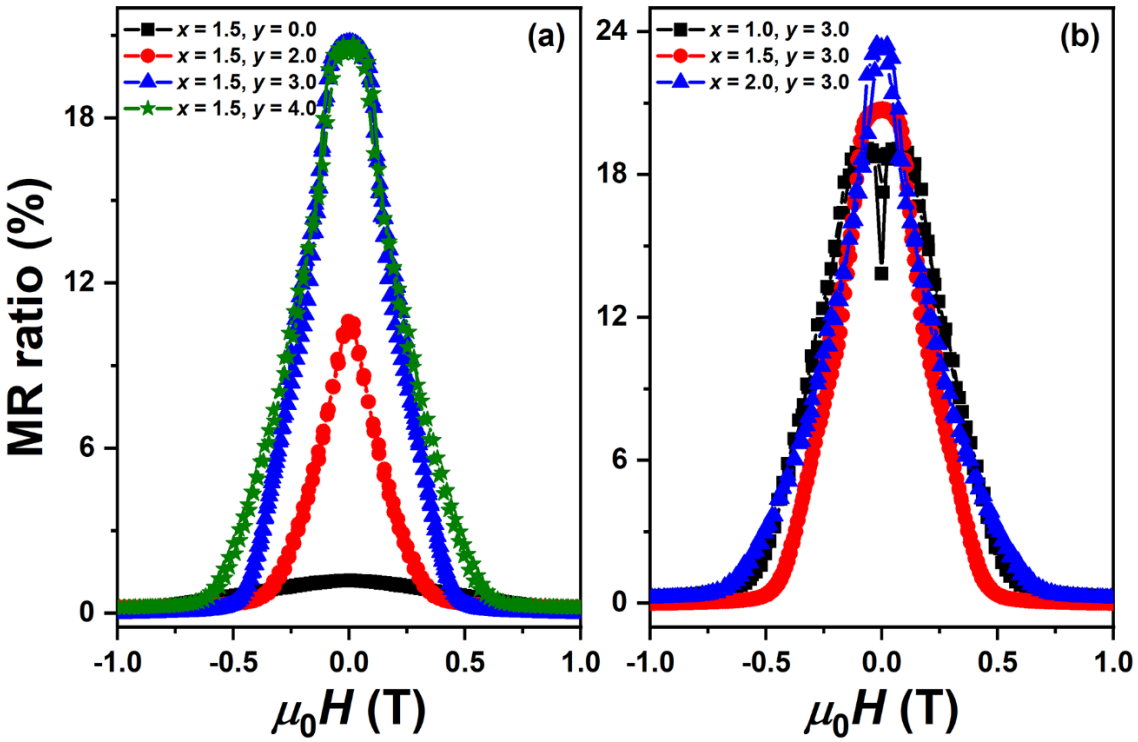

Figure 6.04: Room temperature in-plane MR curve for the flat sample of (a) CoFe(3 nm)/ Rh(0.84 nm)/ CoFe(1.5 nm)/ Cu(1.6 nm)/ CoFe(y = 0, 2, 3, 4 nm)/ MgO(2 nm) and (b) CoFe(3 nm)/ Rh(0.84 nm)/ CoFe(x = 1.0, 1.5, 2.0 nm)/ Cu(1.6 nm)/ CoFe(3 nm)/ MgO(2 nm) deposited on MgO(001) substrate.

6.4.1.2. Magnetic and magnetotransport properties: Experiment and numerical simulations

Figure 6.04 demonstrates the in-plane MR curve for CoFe(3 nm)/ Rh(0.84 nm)/ CoFe(1.5 nm)/ Cu(1.6 nm)/ CoFe(y = 0, 2, 3, 4 nm)/ MgO(2 nm) and CoFe(3 nm)/ Rh(0.84 nm)/ CoFe(x = 1.0, 1.5, 2.0 nm)/ Cu(1.6 nm)/ CoFe(3 nm)/ MgO(2 nm) films deposited on MgO(001) substrate. All the MR curves have a linear response to the applied magnetic field. For top CoFe layer thickness variation [Figure 6.04(a)], the MR ratio is quite low (~1.2 %) for the film with y = 0. As y increases, the MR ratio enhances rapidly to 10.1 % and 20.8 % for y = 2 and 3, respectively, and then remains constant at 20.7 % for y = 4.

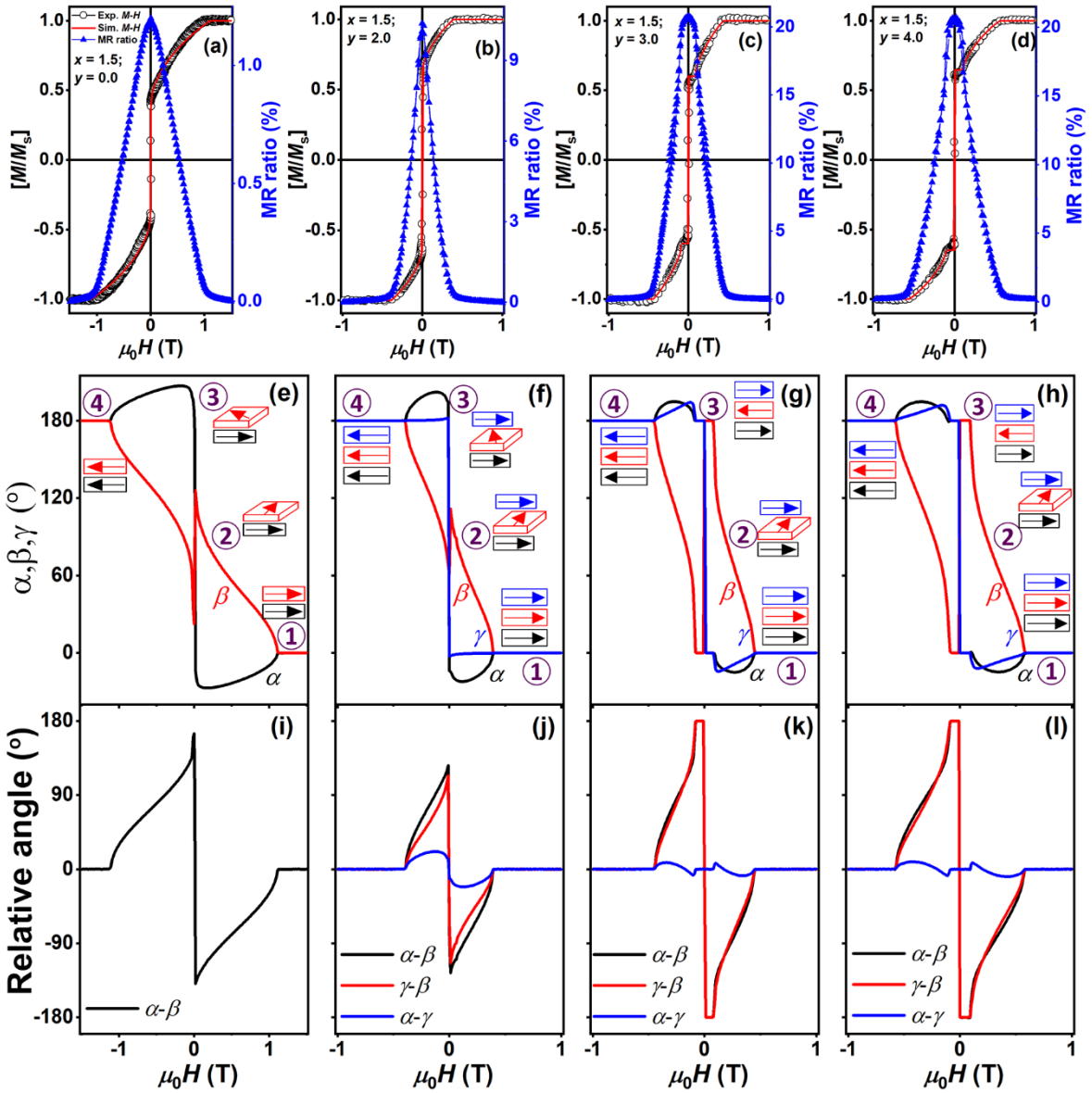

Figure 6.05: Room temperature in-plane experimental (open circle) and numerical simulated (solid line) *M-H* loops and in-plane MR curves for flat samples of CoFe(3 nm)/ Rh(0.84 nm)/ CoFe(1.5 nm)/ Cu(1.6 nm)/ CoFe(*y* nm)/ MgO(2 nm) with *y* = 0 (a), 2 (b), 3 (c), 4 (d). The variations of the angles (*α, β, γ)* (e,f,g,h) and the relative orientation between angles (*α-β,γ-β,α-γ*) (i,j,k,l) at different magnetic fields for the films with *y* = 0, 2, 3, 4. The estimated magnetization directions using the angles are shown in the insets.

These results evidently reveal the importance of the top CoFe layer with a metastable *bcc*-Cu spacer in obtaining the large MR ratio in the CIP-GMR devices. On the other hand, for middle CoFe layer thickness variation [Figure 6.04(b)], the MR ratio increases from 19.1 %

for x = 1 to 20.8 % and 23.5 % for x = 1.5 and 2 nm, respectively. The stable plateau region observed in the *M-H* loop for x = 1 decreases with increasing x and diminishes for x = 2.

Figure 6.05 depicts the room temperature in-plane experimental (open circle) and numerically simulated (solid line) *M-H* loops and in-plane MR curves for flat samples CoFe(3 nm)/ Rh(0.84 nm)/ CoFe(1.5 nm)/ Cu(1.6 nm)/ CoFe(y nm)/ MgO(2 nm) with different y = 0-4 (a-d). The variations of angles (α, β, γ) (e-h) and the relative orientation the between angles (α-β,γ-β,α-γ) (i-l) at different magnetic fields along with the estimated magnetization directions using the angles (as insets) are presented. To study the effect of the top CoFe layer on IEC between CoFe layers through Rh and Cu spacers and the origin of the linear MR, numerical simulations were carried out by minimizing the total energy in Eqn. (5.01). The extracted coupling parameters for the simulated *M-H* loops are summarized in Table 6.01. For the film with y = 0, the simulated and the experimental loops show the best match for $J_1' = -0.798$ mJ/m^2 and $J_2' = -0.482$ mJ/m^2. This reveals the presence of both 180° (bilinear) and 90° (biquadratic) magnetic configurations between two CoFe layers. The ratio between the biquadratic and bilinear couplings is determined to be 60 %. Furthermore, the variation of angles α and β [see Figure 6.05(e)] indicates that the middle CoFe layer rotates gradually with decreasing the magnetic field from the saturation and the bottom CoFe layer shows a rapid switching at lower magnetic fields due to the dominant contribution of E_Z. Thus, the relative orientation between α and β varies almost linearly due to biquadratic coupling [see Figure 6.05(i)], which in turn provides the linear MR response. Similarly, for y = 2, the experimental and the simulated *M-H* loops show the best match for $J_1' = -0.255$ mJ/m^2, $J_2' = -0.195$ mJ/m^2, $J_1'' = -0.005$ mJ/m^2 and $J_2'' = 0$. The ratio between J_1'' and J_1', *i.e.*, J_1''/J_1' (= 2%) confirms the development of weak AFM coupling between the middle and top CoFe layers through the Cu spacer [FATH2019], resulting in a sudden rise in the MR ratio to 10.1 %. On further increasing y, the value of J_1'' increases to -0.213 and -0.291 mJ/m^2, providing the enhanced ratio of J_1''/J_1' to 70.5 % and 80.4 % for y = 3 and 4, respectively. This evidences a strong AFM coupling between the middle and top CoFe layers, leading to the increased MR ratio and the plateau region in the *M-H* loop [marked as position 3 in Figure 6.05(e-h)].

For understanding the linear MR behavior, the magnetization direction of each CoFe layer and the relative magnetization orientation between two CoFe layers are predicted based on the extracted angles from numerical simulations.

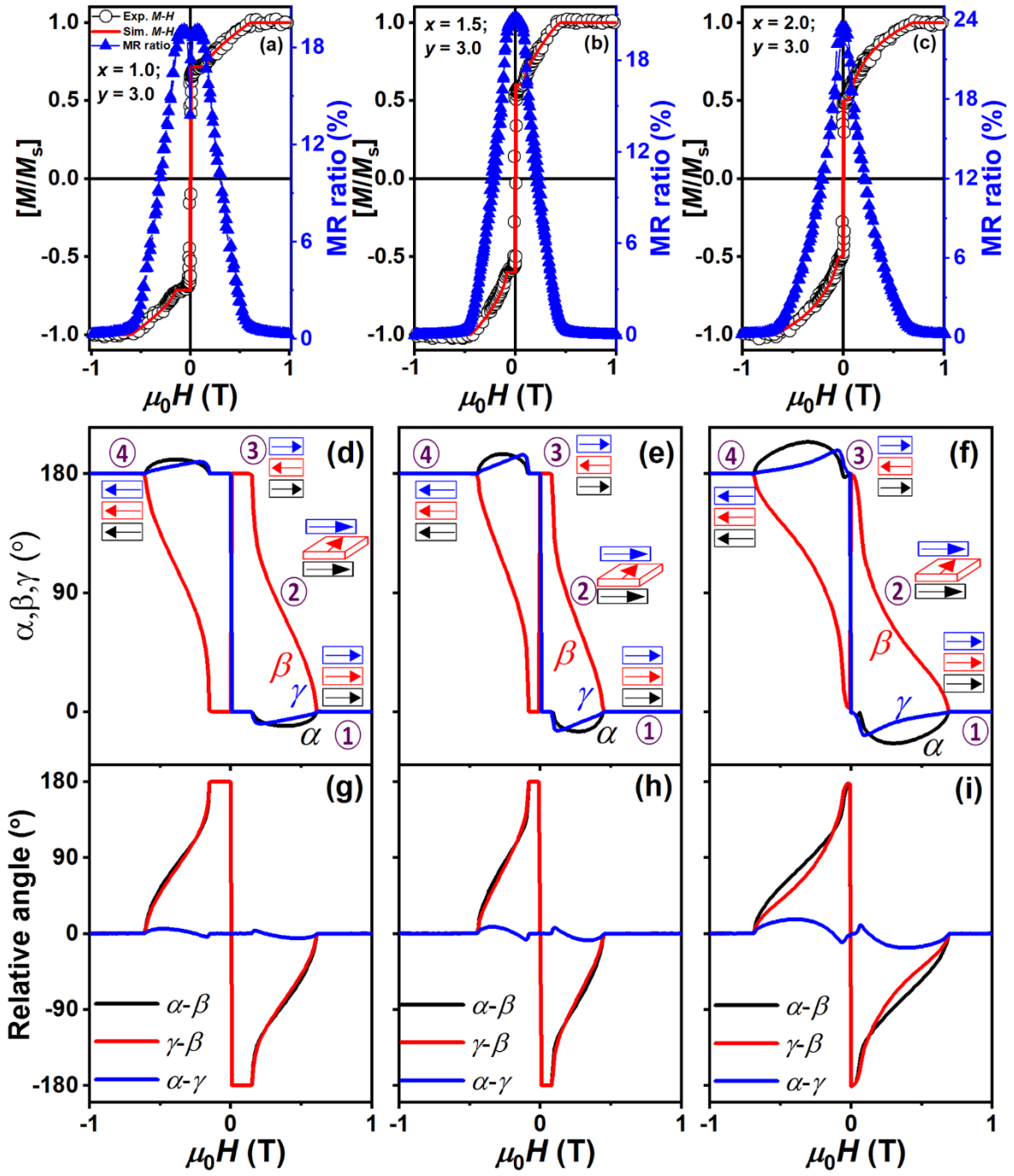

Figure 6.06: Room temperature in-plane experimental (open circle) and numerical simulated (solid line) *M-H* loops and in-plane MR curves for flat samples of CoFe(3 nm)/ Rh(0.84 nm)/ CoFe(*x* nm)/ Cu(1.6 nm)/ CoFe(3 nm)/ MgO(2 nm) with *x* = 1.0 (a), 1.5 (b), 2.0 (c). The variations of the angles (*α, β, γ*) (d,e,f) and the relative orientation between angles (*α-β,γ-β,α-γ*) (g,h,i) at different magnetic fields for the films with *x* = 1.0, 1.5, and 2.0, respectively. The estimated magnetization directions using the angles are shown in the insets.

The magnetizations of all the CoFe layers are aligned to the magnetic field (parallel configuration) at the saturated magnetic field, providing $\alpha = \beta = \gamma = 0$, exhibiting a low resistance state. Upon reducing the magnetic field, the angle β increases progressively to 105° for $y \leq 2$ and then reaches quickly to 180° for $y \geq 3$ [see Figure 6.05(e-h)]. But, angles α and γ are nearly zero as H decreases towards zero. This can be explained by the balance between E_Z and E_{EX} in each CoFe layer. As the thickness of the top and bottom CoFe layers is larger, E_Z mainly controls α and γ, ensuing α-γ is zero. As IEC controls the magnetization of the middle layer from the top and bottom CoFe layers, β changes progressively with the magnetic field due to biquadratic coupling (J_2'), enforcing the middle CoFe layer to act as a sensing layer of the magnetic field. Eventually, the middle CoFe layer forms AFM coupling to both the bottom and top CoFe layers. Therefore, α-β and γ-β varies almost linearly, providing a nearly linear variation of R - H [see Figure 6.05(i-l)]. When the sign of the magnetic field changes from positive to negative, the magnetization of both the top and bottom CoFe layers switches rapidly to the magnetic field direction, resulting in an instantaneous switching of the middle CoFe layer's magnetization to the opposite due to IEC. Subsequently, the magnetization of the middle CoFe layer rotates again progressively towards saturation with increasing the magnetic field, causing the MR ratio to decrease linearly to zero at the saturation magnetic field. The above results confirm that the flat sample CoFe(3 nm)/ Rh(0.84 nm)/ CoFe(1.5 nm)/ Cu(1.6 nm)/ CoFe(3 nm)/ MgO(2 nm) exhibits a large linear MR ratio.

Figure 6.06 shows the room temperature in-plane experimental (open circle) and numerically simulated (solid line) *M-H* loops and in-plane MR curve for flat samples CoFe(3 nm)/ Rh(0.84 nm)/ CoFe(*x* nm)/ Cu(1.6 nm)/ CoFe(3 nm)/ MgO(2 nm) with different *x* =1.0, 1.5, 2.0 (a-c). The variations of angles (α, β, γ) (d-f) and the relative orientation between the angles (α-β,γ-β,α-γ) (g-i) at different magnetic fields along with the estimated magnetization directions (as insets) are presented. To study IEC between CoFe layers, numerical simulation was carried out again and extracted the values of angles as a function of the magnetic field [plotted in Figure 6.06(d-i)] and coupling parameters (listed in Table 6.01). As *x* increases from 1 to 2 nm, both J_1' and J_2' increase largely, while J_1'' exhibits a weak dependence. This suggests that while both 180° and 90° couplings between the bottom and middle CoFe layers enhance substantially, the strength of the AFM coupling between the middle and top CoFe layers remains the same with increasing *x*. Also, the plateau region becomes small and

diminishes due to increased E_Z contribution in the middle CoFe layer with increasing x to 2 nm. On the other hand, the increase in the MR ratio from 19.1 % to 23.5 % is perhaps due to the increasing thickness of the middle CoFe layer from 1 to 2 nm. It is worth mentioning that the IEC parameters (J_1', J_2' and J_1'') are very sensitive to the thickness of each layer and the interfacial roughness, requiring more in-depth microstructural investigations to conclude how the thickness of the middle and top CoFe layers affects the different coupling parameters.

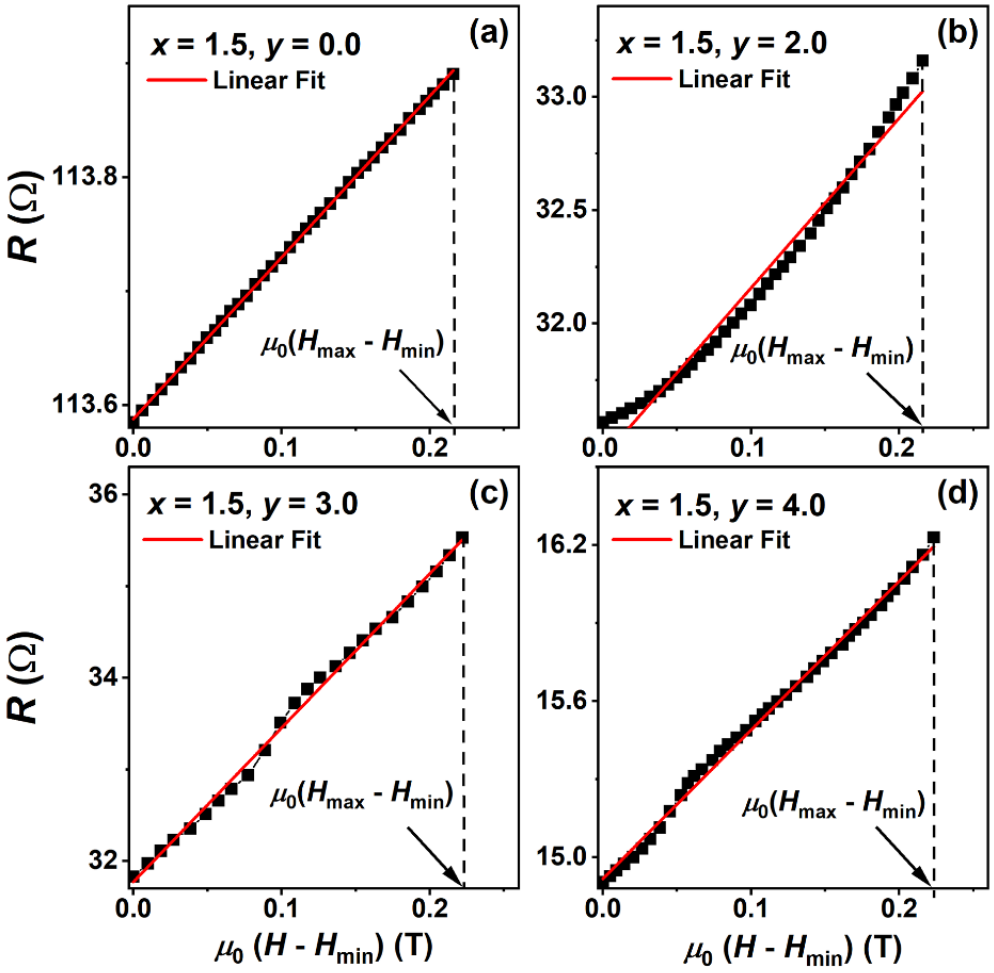

Figure 6.07: The variation of resistance as a function of the normalized effective field and their linear fit for a flat sample of CoFe(3 nm)/ Rh(0.84 nm)/ CoFe(1.5 nm)/ Cu(1.6 nm)/ CoFe(y nm)/ MgO(2 nm) with y = 0 (a), 2 (b), 3 (c), 4 (d) deposited on MgO(001) substrate.

6.4.1.3. Sensing properties as a magnetic field sensor

To understand the effect of the CoFe layer thicknesses on the sensing parameters, sensing properties were evaluated by performing a linear fit of the experimentally observed MR curves, as shown in Figures 6.07 and 6.08. The operation field range defined as ΔH_{sense} =

$\mu_0 H_{max} - \mu_0 H_{min}$ is considered as the maximum field range where the MR curve displays a linear variation of resistance with the magnetic field.

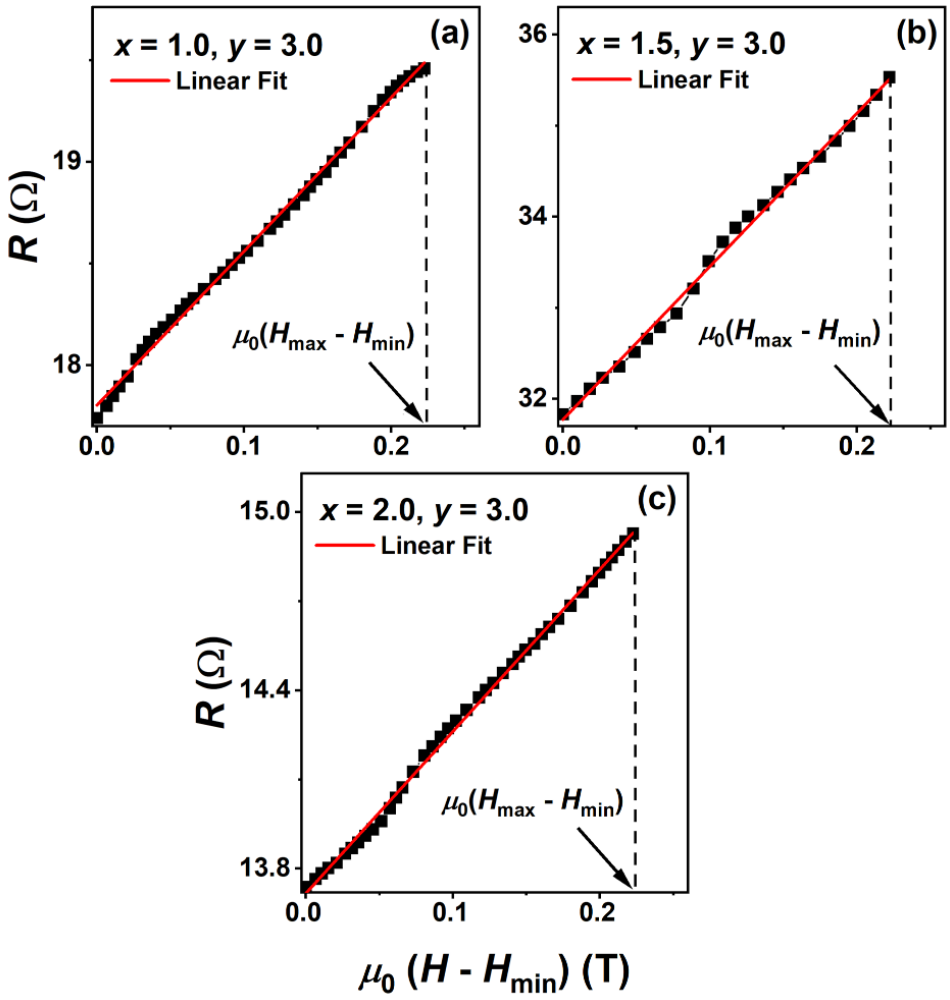

Figure 6.08: The variation of resistance as a function of the normalized effective field and their linear fit for a flat sample of CoFe(3 nm)/ Rh(0.84 nm)/ CoFe(*x* nm)/ Cu(1.6 nm)/ CoFe(3 nm)/ MgO(2 nm) with *x* = 1.0 (a), 1.5 (b), 2.0 (c) deposited on MgO(001) substrate.

As summarized in Table 6.01, the value of ΔH_{sense} can be tuned between 0.37 T and 0.65 T depending on the *x* and *y* values. The sensitivity is defined as a value of the MR ratio divided by the magnetic field range, *i.e.*, $\Delta MR/\Delta H$. The nonlinearity, represented as %full-scale (FS), is determined using Eqn. (5.03). The sensitivity enhances rapidly from 0.001 %/mT for *y* = 0 to a maximum of 0.047 %/mT for *y* = 3. This can be attributed to the corresponding increase in the MR ratio, occurring mainly due to adding the top CoFe layer with the *bcc*-Cu spacer. This reiterates the importance of the top CoFe layer with *bcc*-Cu spacer in obtaining a large MR ratio in the current CIP-GMR devices.

Table 6.01: Extracted parameters for flat samples of CoFe(3 nm)/ Rh(0.84 nm)/ CoFe(x nm)/ Cu(1.6 nm)/ CoFe(y nm)/ MgO(2 nm) deposited on MgO(001) substrate.

Sample	J_1' (mJ/m^2)	J_2' (mJ/m^2)	J_1'' (mJ/m^2)	$\frac{J_1''}{J_1'}$ (%)	$\frac{J_2'}{J_1''}$ (%)	$J_1'+J_2'+J_1''$ (mJ/m^2)	M_R/M_S (%)	$\mu_0 H_S$ (T)	MR (%)	Sen. (%/mT) ΔH =220mT	Nonlinearity (%FS)	ΔH_{sense} (T)
x =1.5, y = 0.0	-0.798	-0.482	---	---	---	-1.28	45	1.10	1.2	0.001	0.21	1.10
x =1.5, y = 2.0	-0.255	-0.195	-0.005	2.0	76.5	-0.46	68	0.37	10.1	0.023	1.56	0.37
x =1.5, y = 3.0	-0.302	-0.156	-0.213	70.5	51.7	-0.67	55	0.46	20.8	0.047	0.98	0.38
x =1.5, y = 4.0	-0.362	-0.207	-0.291	80.4	57.2	-0.86	67	0.57	20.7	0.041	0.69	0.48
x =1.0, y = 3.0	-0.302	-0.142	-0.235	77.8	47.0	-0.68	67	0.61	19.1	0.043	0.78	0.52
x =1.5, y = 3.0	-0.302	-0.156	-0.213	70.5	51.7	-0.67	55	0.46	20.8	0.047	0.98	0.38
x = 2.0, y = 3.0	-0.574	-0.329	-0.232	40.4	57.3	-1.14	49	0.70	23.5	0.036	0.46	0.65

The MR ratio for y = 4 is comparable to y = 3, but the sensitivity decreases significantly. This could be understood by considering the enlargement in ΔH_{sense} due to an increase in the total magnitude of the coupling parameters $(J_1' + J_2' + J_1'')$. Interestingly, the augmented $J_1' + J_2' + J_1''$ also raises $\mu_0 H_s$ and thus expand the operation field range ΔH_{sense}. Similarly, the sensitivity increases gradually from 0.043 to 0.047 %/mT as x increases from 1.0 to 1.5, respectively, and then decreases to 0.036 %/mT for x = 2. While the former change is due to the higher MR ratio (20.8 %) and narrower ΔH_{sense} due to lower $J_1' + J_2' + J_1''$, the latter is caused by the significant increase in ΔH_{sense} due to larger $J_1' + J_2' + J_1''$, despite showing a high MR ratio (23.5 %). The present results are superior to those in the earlier reports, *i.e.*, the sensitivity of 0.014 %/mT [MANC2000], 0.0015 %/mT [DIJK2005], 0.0002 %/mT [LIU2016], 0.053 %/mT, and nonlinearity 1.38 %FS [NAKA2017]. As pointed out earlier, one of the drawbacks of the proposed concept is the requirement of bias magnetic fields to shift the operating magnetic field range, which can be obtained suitably by employing a permanent magnet beside the sensor. Nevertheless, the above results imply that the tuning of thicknesses of the middle and top CoFe layers and the interfacial microstructures of CIP-GMR devices offers additional possibilities for tuning the sensitivity and operation field range to specific magnetic sensor applications in the range of low and medium magnetic fields.

6.5. Summary

A systematic investigation on the effect of thickness of the top and middle CoFe layers on the structural, magnetic and sensing properties of CoFe(3 nm)/ Rh(0.84 nm)/ CoFe(x = 1.0, 1.5, 2.0 nm)/ Cu(1.6 nm)/ CoFe(y = 0, 2, 3, 4 nm)/ MgO(2 nm) multilayer films deposited on MgO(001) substrate has been carried out. The salient features of the multilayer films from the current investigations are as follows -

- The out-of-plane XRD patterns and ϕ-scans of all the flat multilayer films confirmed the epitaxial growth of *bcc* CoFe thin films on the MgO(001) substrate.
- All the room temperature in-plane MR curves illustrated a typical linear *R-H* response to the applied magnetic field.
- The numerical simulation modeling confirmed that the biquadratic coupling between the bottom and middle CoFe layers through Rh and the AFM coupling between the middle and top CoFe layers through a Cu spacer provides the linear MR.

- The IEC parameters (J_1', J_2' and J_1'') are found to be very sensitive to the thickness of each layer and the interfacial roughness.
- The enlargement in ΔH_{sense} is directly proportional to the total magnitude of the coupling parameters ($J_1' + J_2' + J_1''$).
- The addition of the top CoFe layer via *bcc*-Cu spacer enhances the MR ratio and the sensitivity of the CIP-GMR devices significantly from 1.2 % to 20. 8% and 0.001 %/mT to 0.047 %/mT, respectively.
- The MR ratio was increased from 19.1 % to 23.5 % with increasing the middle CoFe layer thickness. Still, the sensitivity was decreased to 0.036 %/mT due to a substantial increase in the total magnitude of coupling parameters.
- Nonlinearity is found to be less than 2 %FS in all the multilayer films.
- The fine-tuning of thicknesses of the middle and top CoFe layers provides supplementary routes for optimizing the sensitivity and operation field range of the CIP-GMR devices to specific magnetic sensor applications in the low and medium magnetic field range.

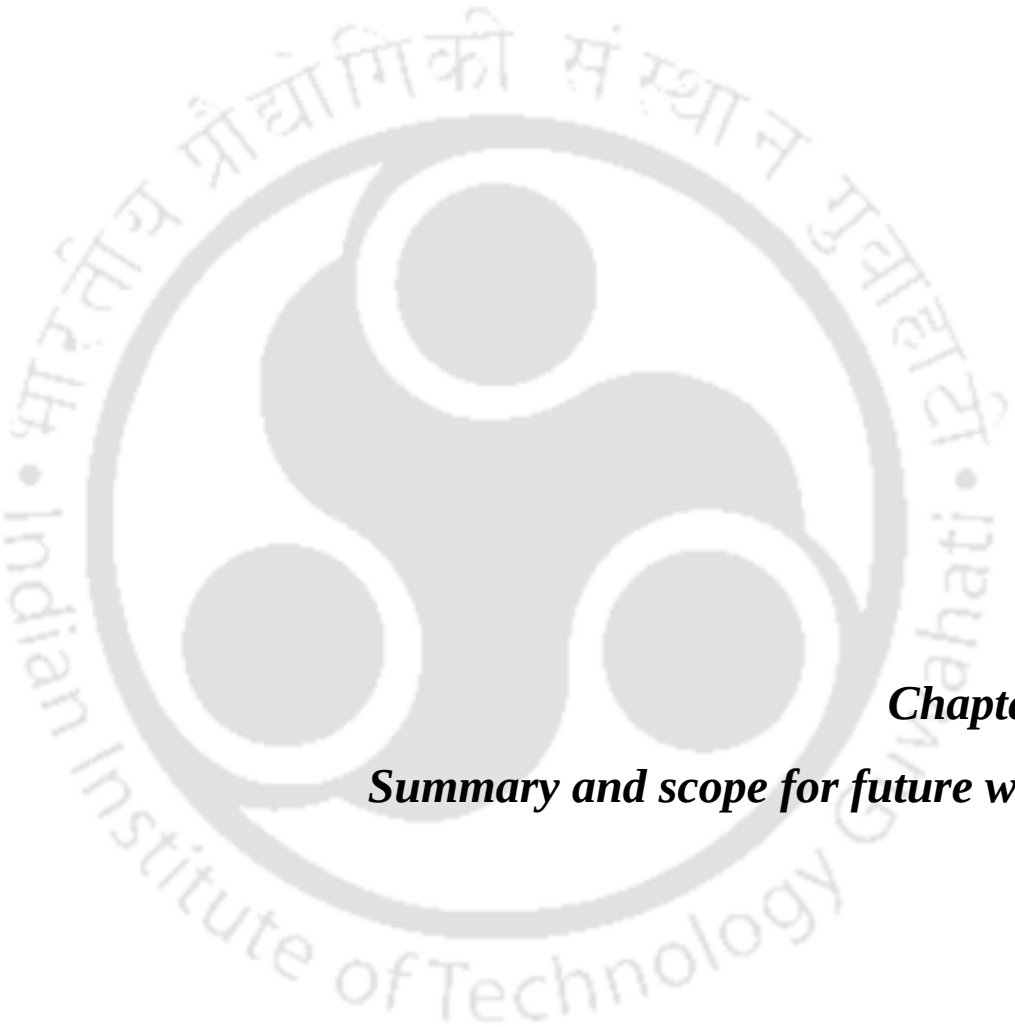

Chapter 7

Summary and scope for future work

This chapter provides an overall summary of the significant results obtained on the structural, magnetic and magnetotransport properties of CoFe(3 nm)/ wedge-shaped Rh(t_{Rh} = 0 – 7.3 nm)/ CoFe(1.5 nm)/ MgO(2 nm) and CoFe(3 nm)/ Rh(0.84 nm)/ CoFe(1.5 nm)/ MgO(2 nm) films with Rh interlayer and, CoFe(3 nm)/ wedge-shaped Rh(t_{Rh} = 0 – 2.5 nm)/ CoFe(1.5 nm)/ Cu(1.6 nm)/ CoFe(3 nm)/ MgO(2 nm) and CoFe(3 nm)/ Rh(0.84 nm)/ CoFe(x = 1.0, 1.5, 2.0 nm)/ Cu(1.6 nm)/ CoFe(y = 0, 2, 3, 4 nm)/ MgO(2 nm) films with two different interlayers, such as Rh and Cu. Highlights of the current investigations and the possibilities for future work are also given below.

7.1. Summary of the results

To study the effect of Rh spacer thickness on the interlayer exchange coupling (IEC) between the ferromagnetic (FM) CoFe layers, CIP-GMR devices consisting of CoFe(3 nm)/ wedge-shaped Rh(t_{Rh} = 0 – 7.3 nm)/ CoFe(1.5 nm)/ MgO(2 nm) and CoFe(3 nm)/ wedge-shaped Rh(t_{Rh} = 0 – 2.5 nm)/ CoFe(1.5 nm)/ Cu(1.6 nm)/ CoFe(3 nm)/ MgO(2 nm) films were deposited on single-crystal MgO(001) substrate using an ultra-high vacuum (UHV)-compatible magnetron sputtering system. Further, flat samples of CoFe(3 nm)/ Rh(0.84 nm)/ CoFe(1.5 nm)/ MgO(2 nm) and CoFe(3 nm)/ Rh(0.84 nm)/ CoFe(x = 1.0, 1.5, 2.0 nm)/ Cu(1.6 nm)/ CoFe(y = 0, 2, 3, 4 nm)/ MgO(2 nm) were fabricated on MgO(001) substrate to optimize the exact Rh thickness for enhanced sensing properties and to understand the effect of middle and top CoFe layer thickness on the IEC parameters.

Room temperature out-of-plane XRD patterns of CoFe(3 nm)/ wedge-shaped Rh(t_{Rh} = 2.2 – 6.6 nm)/ CoFe(1.5 nm)/ MgO(2 nm) revealed the diffraction peaks at 2θ = 47.96° and 65.40° corresponding to the (200) peaks from face-centered-cubic (*fcc*) Rh and body-centered-cubic (*bcc*) CoFe films, respectively, confirming the epitaxial growth nature of the films on the MgO substrate. However, for $t_{Rh} \leq$ 1.5 nm films, the (200) peak from *fcc* Rh could not be identified. The ϕ-scan patterns of (220) peak of Rh (2θ = 69.67° and χ = 45°) and MgO (2θ = 62.17° and χ = 45°) and (110) peak of CoFe (2θ = 44.31° and χ = 45°) revealed that Rh, MgO substrate and CoFe films exhibit four well-defined peaks periodically separated from one another by an angular difference of 90° indicating the epitaxial growth nature of Rh and CoFe films on the MgO(001) substrate. To further examine the growth nature of all the layers, STEM (ADF-STEM) and nano-beam electron diffraction patterns were obtained for the flat sample of CoFe(3 nm)/ Rh(0.84 nm)/ CoFe(1.5 nm)/ Cu(1.6 nm)/ CoFe(3 nm)/ MgO(2 nm). The electron diffraction pattern confirmed the formation of the *fcc*

structure for the Rh spacer layer. The Cu spacer was found to be imitating the structure of the CoFe layer, ensuring the formation of a metastable *bcc* structure.

Magnetotransport properties of the wedge-shaped films revealed a strong dependence of the MR response on the Rh spacer thickness. For CoFe(3 nm)/ wedge-shaped Rh(t_{Rh} = 0 – 7.3 nm)/ CoFe(1.5 nm)/ MgO(2 nm) films, (i) The in-plane MR curves of CoFe(3 nm)/ wedge-shaped Rh(t_{Rh} = 0.27, 1.00, 1.37 nm)/ CoFe(1.5 nm)/ MgO(2 nm) films exhibited only ordinary MR curves, which did not saturate up to 3 T applied magnetic field. (ii) The GMR feature was observed for films with t_{Rh} = 0.46 and 0.64 nm due to the appearance of 180° and 90° couplings. (iii) For the films with t_{Rh} > 1.55 nm, the MR ratio decreased progressively to 0.01 % at t_{Rh} = 7.3 nm. The decrease of the MR ratio at high t_{Rh} was correlated to the possible current shunting effect and change in the relative orientation between the magnetization of two CoFe layers. (iv) The optimized Rh thickness, exhibiting a high MR ratio of 1.1 %, was found to be 0.84 nm in the flat sample of CoFe(3 nm)/ Rh(0.84 nm)/ CoFe(1.5 nm)/ MgO(2 nm). (v) The numerical simulation analysis demonstrated that the simulated *M-H* loop complements the experimental *M-H* loop only after taking J_1 and J_2 into account. Besides, the simulated *M-H* loop provided the best match only when $J_1 = -0.798$ mJ/m^2 and $J_2 = -0.482$ mJ/m^2, supporting the presence of both 180° and 90° magnetic configurations. (vi) The highest sensitivity and reduced nonlinearity were obtained as 0.001 %/mT and 0.21 %FS in a sensing field range of 220 mT for the flat sample of CoFe(3 nm)/ Rh(0.84 nm)/ CoFe(1.5 nm)/ MgO(2 nm).

To enhance the MR ratio and sensitivity, a novel approach was made in CIP-GMR magnetic sensors by integrating Cu spacer with another CoFe to the CoFe/ Rh/ CoFe films. Accordingly, we fabricated CoFe(3 nm)/ wedge-shaped Rh(t_{Rh} = 0 – 2.5 nm)/ CoFe(1.5 nm)/ Cu(1.6 nm)/ CoFe(3 nm)/ MgO(2 nm) and flat sample of CoFe(3 nm)/ Rh(0.84 nm)/ CoFe(1.5 nm)/ Cu(1.6 nm)/ CoFe(3 nm)/ MgO(2 nm) on MgO(001) substrate. The MR ratio and saturating magnetic field were tunable between 3.9 % and 23.5 %, and 0.013 T and 1.5 T for the CoFe(3 nm)/ wedge-shaped Rh(t_{Rh} = 0 – 2.5 nm)/ CoFe(1.5 nm)/ Cu(1.6 nm)/ CoFe(3 nm)/ MgO(2 nm) films. Despite obtaining a large MR ratio (> 20 %) over a wide range of Rh spacer thicknesses, the nature of the MR curves, *i.e.*, linear or nonlinear type, was found to be sensitive to the Rh spacer. The optimized Rh thickness for obtaining a linear *R-H* response with a large MR ratio of 21 % was found to be 0.84 nm. The out-of-plane XRD patterns and ϕ-scans of CoFe(3 nm)/ Rh(0.84 nm)/ CoFe(1.5 nm)/ Cu(1.6 nm)/ CoFe(3 nm)/ MgO(2 nm) films confirmed the epitaxial growth of *bcc* CoFe thin films on the MgO(001)

substrate. Transmission electron microscopy (TEM) analysis confirmed the formation of a fully epitaxial (001)-oriented structure with *fcc* Rh and metastable *bcc* Cu spacer layer replicating the structure of *bcc* CoFe. The room temperature magnetic properties and numerical simulation analyses confirmed that the middle CoFe sensing layer was well controlled by the interlayer exchange coupling through the Rh spacer and gave the linear response without losing a high MR ratio through the *bcc*-Cu spacer. The numerical simulation analysis demonstrated that the simulated *M-H* loop complements the experimental *M-H* loop only when J_2'/J_1' is more than 25 %. The simulated *M-H* loop provided the best match only when $J_1' = -0.302$ mJ/m^2, $J_2' = -0.156$ mJ/m^2, $J_1'' = -0.213$ mJ/m^2 and $J_2'' = 0$, supporting the presence of both 180° and 90° magnetic configurations through Rh spacer and 180° magnetic configurations through metastable *bcc* Cu spacer. The CIP-GMR device showed the linear MR curve with the highest MR ratio of 21 %, the enhanced sensitivity of 0.047 %/mT, the reduced nonlinearity of 0.98 %FS and a comprehensive operation field range of 220 mT.

In order to tune the MR ratio and sensing parameters of the CIP-GMR devices, a systematic investigation on the effect of thickness of the top and middle CoFe layers was carried out in flat samples of CoFe(3 nm)/ Rh(0.84 nm)/ CoFe(x = 1.0, 1.5, 2.0 nm)/ Cu(1.6 nm)/ CoFe(y = 0, 2, 3, 4 nm)/ MgO(2 nm) films deposited on MgO(001) substrate. The out-of-plane XRD patterns and ϕ-scans of all the flat multilayer films confirmed the epitaxial growth of *bcc* CoFe thin films on the MgO(001) substrate. All the room temperature in-plane MR curves illustrated a typical linear *R-H* response to the applied magnetic field. The numerical simulation modeling confirmed that the biquadratic coupling between the bottom and middle CoFe layers through Rh and the antiferromagnetic coupling between the middle and top CoFe layers through a Cu spacer provided the linear MR. The IEC parameters (J_1', J_2' and J_1'') were found to be very sensitive to the thickness of each layer and the interfacial roughness. The enlargement in ΔH_{sense} was directly proportional to the total magnitude of the coupling parameters ($J_1' + J_2' + J_1''$). The addition of the top CoFe layer through *bcc* Cu spacer enhanced the MR ratio and the sensitivity of the CIP-GMR devices significantly from 1.2 % to 20.8 % and 0.001 %/mT to 0.047 %/mT, respectively. The MR ratio was increased from 19.1 % to 23.5 % with increasing the middle CoFe layer thickness. Still, the sensitivity was decreased to 0.036 %/mT due to a substantial increase in the total magnitude of coupling parameters. Nonlinearity was found to be less than 2 %FS in all the multilayer films. The fine-tuning of thicknesses of the middle and top CoFe layers provided supplementary routes

for optimizing the sensitivity and operation field range of the CIP-GMR devices to specific magnetic sensor applications in the low and medium magnetic field range. However, one drawback of the proposed concept was the requirement of bias magnetic fields to shift the operating magnetic field range, which could be obtained suitably by employing a permanent magnet beside the sensor.

7.2. Scope for future work

The current investigations have opened a pathway to achieve linear magnetoresistance response using simple CoFe(3 nm)/ Rh(0.84 nm)/ CoFe(x = 1.0, 1.5, 2.0 nm)/ Cu(1.6 nm)/ CoFe(y = 0, 2, 3, 4 nm)/ MgO(2 nm) film stacks. These observations have not only revealed the potential of CoFe based CIP-GMR devices but also shown directions for future scope of work in the field of information technology, automotive industry, and biosensors. Some of the prospects are briefly discussed below to serve as an appropriate conclusion to the current thesis work.

Since the multilayer thin films exhibited both nonlinear and linear MR response depending on the Rh spacer thickness, it would be appropriate (i) to study the magneto-optic Kerr effect to establish a correlation between the MR response and the change in domain structure, if any, (ii) to measure the temperature-dependent electrical and magnetotransport properties in these films as a function of the applied magnetic field, (iii) to investigate the effect of repetition of the number of multilayers, *i.e.*, [CoFe/ Rh/ CoFe/ Cu/ CoFe/ MgO]$_N$, N = 1, 2, 3, *etc.* on the MR ratio and the sensing parameter (This is because the increase in the number of multilayers changed the nature of nonlinear MR curves into linear MR curves in the case of [CoFe/ Cu/ CoFe]$_n$ films), (iv) to understand the effect of the thickness of the Cu spacer on the MR response of the present CIP-GMR devices. (v) to investigate the effect of the CoFe film's composition on the linear MR response and sensing parameters of the presently investigated structure (As the crystal structure of CoFe films changes with compositions, one can expect changes in the growth nature of the film stack and the magnetic and magnetotransport properties.) (vi) to tune the layer structure such that the linear MR response is observed close to the zero magnetic field. Such linear MR response does not need any bias field to shift the operating range of magnetic fields.

Recently, the ability of GMR-based sensors to detect very low magnetic fields led to the development of bio-magnetic sensors for life science applications, namely magnetocardiography (MCG) and magnetoencephalography (MEG), demanding ultra-

sensitive sub-picoTesla bio-magnetic sensors. On the other hand, the automotive industry requires sensing of much larger magnetic fields for monitoring currents in electric vehicles, position sensors, and magnetic levitating trains. This needs a larger sensing field range, often greater than 1 T. Thus, there is a strong requirement of extreme sensing abilities for different technological aspects. Hence, it will be more attractive to explore further and enhance CIP-GMR based linear magnetic sensors and understand how the sensing parameters can be altered using different types of magnetic interactions between the FM layers.

References

[ALLE1994] Allenspach R, J. Magn. Magn. Mater. 129 (1994) 160.

[ANDE2006] Andersson G, Burkert T, Warnicke P, Björck M, Sanyal B, Chacon C, Zlotea C, Nordström L, Nordblad P, Eriksson O, Phys. Rev. Lett. 96 (2006) 037205.

[ANDE2010] Andersson G, Björck M, J. Nanosci. Nanotechnol. 10 (2010) 6186.

[ANDO2015] Ando Y, Jpn. J. Appl. Phys. 54 (2015) 070101.

[ANGU2000] Anguelouch A, Schrag B.D, Xiao G, Trouilloud Y.L.P.L, Wanner R.A, Gallagher W.J, Parkin S.S.P, Appl. Phys. Lett. 76 (2000) 622.

[ARAK1993] Araki S, J. Appl. Phys. 73 (1993) 3910.

[BAIB1988] Baibich M.N, Broto J.M, Fert A, Nguyen Van Dau F, Petroff F, Eitenne P, Creuzet G, Friederich A, Chazelas J, Phys. Rev. Lett. 61 (1988) 2472.

[BARB2016] Barbieri F, Trauchessec V, Caruso L, Rosillo J. T, Telenczuk B, Paul E, Bal T, Destexhe A, Fermon C, Lecoeur M. P, Ouanounou G, Sci. Rep. 6 (2016) 39330.

[BARN1993] Barnas J, Grünberg P, J. Magn. Magn. Mater. 121 (1993) 326.

[BART1990] Barthélémy A, Fert A, Baibich M.N, Hadjoudj S, Petroff F, Etienne P, Cabanel R, Lequien S, Nguyen Van Dau F, Creuzet G, J. Appl. Phys. 67 (1990) 5908.

[BINA1989] Binash G, Grünberg P, Saurenbach F, Zinn W, Phys. Rev. B 39 (1989) 4828.

[BENN1990] Bennett W. R, Schwarzacher W, Egelhoff Jr. W. F, Phys. Rev. Lett. 65 (1990) 3169.

[BENN1994] Bennett L.H, Watson R.E, Magnetic Multilayers, World Scientific, Singapore (1994).

[BLIZ2015] Blizak S, Bihlmayer G, Blugel S, Abaidia S.E.H, Phys. Rev. B 91 (2015) 014408.

[BLOE19941] Bloemen P.J.H, van Kesteren H.W, Swagten H.J.M, de Jonge W.J.M, Phys. Rev. B 50 (1994) 13505.

[BLOE19942] Bloemen P.J.H, van de Vorst M.T.H, Johnson M.T, Coehoorn R, de Jonge W.J.M, J. Appl. Phys. 76 (1994) 7081.

[BLUN2001] Blundell S, Magnetism in Condensed Matter, Oxford University Press, Chapter 8 (2001).

[BLUN2003] Blundell S, Magnetism in Condensed Matter, Oxford University Press, Chapter 3 (2003).

[BOSU2010] Bosu S, Sakuraba Y, Saito K, Wang H, Mitani S, Takanashi K, Phys. Rev. B 81 (2010) 054426.

[BRAJ2010] Brajpuriya R, J. Appl. Phys. 107 (2010) 083914.

[BRUB1991] Brubaker M.E, Mattson J.E, Sowers C.H, Bader S.D, Appl. Phys. Lett. 58 (1991) 2306.

[BRUK2004] Burkert T, Nordsröm L, Eriksson O, Heinonen O, Phys. Rev. Lett. 93 (2004) 027203.

[BRUN1989] Bruno P, Renard J.P, Appl. Phys. A 49 (1989) 499.

[BRUN1991] Bruno P, Chappert C, Phys. Rev. Lett. 67 (1991) 1602.

[BRUN1992] Bruno P, Chappert C, Phys. Rev. B 46 (1992) 261.

[BRUN1995] Bruno P, Phys. Rev. B 52 (1995) 411.

[CAST1997] Castano F.J, Stobiecki T, Gibbs M.R.J, Czapkiewicz M, Kopcewicz M, Gacem V, Speakman J, Cowlam N, Blythe H.J, J. Phys.: Condens. Matter 9 (1997) 10603.

[CHAP1988] Chappert C, Bruno P, J. Appl. Phys. 64 (1988) 5736.

[CHAP1999] Chapman J.N, Rose J, Aitchison P.R, Holloway H, Kubinski D.J, J. Appl. Phys. 86 (1999) 1611.

[CHOP1985] Chopra K.L, Thin Film Phenomena, McGraw-Hill (1985).

[CHOP2000] Chopra H.D, Yang D.X, Chen P.J, Parks D.C, Egelhoff W.F, Phys. Rev. B 61 (2000) 9642.

[CHOP2005] Chopra H.D, Sullivan M.R, Ludwig A, Quandt E, Phys. Rev. B 72 (2005) 054415.

[COEY1991] Coey J.M.D, Phys. Scr T39 (1991) 21.

[COEY1999] Coey J.M.D, J. Magn. Magn. Mater. 200 (1999) 405.

[COEY2010] Coey J.M.D, Magnetism and Magnetic Materials, Cambridge university press, Cambridge (2010).

[COEY2011] Coey J.M.D, IEEE Trans. Magn. 47 (2011) 4671.

[COLI2001] Colis S, Dinia A, Bouillet C.U, IEEE T. Magn, 37 (2001) 1736.

[CUI2014] Cui J, Choi P, Li G, Polikarpov E, Darsell J, Overman N, Olszta M, Schreiber D, Bowden, M, Droubay T, J. Phys. Condens. Matter 26 (2014) 064212.

[CULL2001] Cullity B.D, Stock S.R, Elements of X-ray diffraction, 3rd edn, Pearson Eduaction, Boston (2001).

[CULL2009] Cullity B.D, Graham C.D, Introduction to Magnetic Materials, 2nd edn, IEEE Press, United States of America (2009).

[CZIC2006] Czichos H, Saito T, Smith L, Handbook of Materials Measurements methods, Springer, Berlin (2006).

[DAVI1966] Davidse P.D, Maissel L.I, J. Appl. Phys. 37 (1966) 574.

[DAVI1967] Davidse P.D, Vacuum 17 (1967) 139.

[DECH2012] Decher G, Schlenoff J.B, Multilayer Thin Films: Sequential Assembly of Nanocomposite Materials, Vol. 1, John Wiley & Sons, Germany (2012).

[DIEN2016] Dieny B, Goldfarb R.B, Lee K.-J, Introduction to Magnetic Random-Access Memory, John Wiley & Sons, New Jersy (2016).

[DIJK2005] Dijken S.V, Coey J.M.D, Appl. Phys. Lett. 87(2005) 022504.

[ERIC1993] Erickson R.P, Hathaway K.B, Cullen J. R, Phys. Rev. B 47 (1993) 2626.

[ENNE2016] Ennen I, Kappe D, Rempel T, Glenske C, Hütten A, Sensors 16 (2016) 904.

[ERLE2001] Erler F, Zahn P, Mertig I, Phys. Rev. B 64 (2001) 094408.

[FATH2019] Fathoni K.B, Sakuraba Y, Sasaki T, Miura Y, Jung J.W, Nakatani T, Hono K, APL Mater. 7 (2019) 111106.

[FELD1971] Feldtkeller E, J. De Physique 32 (1971) 452.

[FERR2012] Ferreira R, Paz E, Freitas P.P, Ribeiro J, Gemano J, Sousa L IEEE Trans. Magn. 48 (2012) 4107.

[FERT1992] Fert A, Barthélémy A, Etienne P, Lequien S, Loloee R, Lottis D.K, Mosca D.H, Petroff F, Pratt W.P, Schroeder P.A, J. Magn. Magn. Mater. 104 (1992) 1712.

[FILI1995] Filipkowski M.E, Krebs J.J, Prinz G.A, Gutierrez C.J, Phys. Rev. Lett. 75 (1995) 1847.

[FREI2016] Freitas P.P, Ferreira R, Cardoso S, Proc. of IEEE 104 (2016) 1894.

[FUSS1992] Fuss A, Demokritov S, Grünberg P, Zinn W, J. Magn. Magn. Mater. 103 (1992) L221.

[FULL1996] Fullerton E.E, Bader S.D, Phys. Rev. B 53 (1996) 5112.

[GARR2005] Garreau G, Hajjar S, Bubendorff J.L, Pirri C, Berling D, Mehdaoui A, Stephan R, Wetzel P, Zabrocki S, Gewinner G, Boukari S, Beaurepaire E, Phys. Rev. B 71 (2005) 094430.

[GORI2011] Goripati H.S, Hayashi M, Furubayashi T, Taniguchi T, Sukegawa H, Takahashi Y.K, Hono K, J. Appl. Phys. 110 (2011) 123914.

[GREE2017] Greene J.E, Review Article: Tracing the recorded history of thin-film sputter deposition: From the 1800s to 2017, J. Vac. Sci. Technol. A 35 (2017) 05C204.

[GRUN1986] Grunberg P, Schreiber R, Pang Y, Brodsky M.B, Sowers H, Phys. Rev. Lett. 57 (1986) 2442.

[GRUN2001] Grünberg P, Bürgler D.E, Demokritov S.O, Johnson M.T, Handbook of Magnetic Materials, Elsevier Science B.V. (2001).

[GUIM1998] Guimaraes A.P, Magnetism and Magnetic Resonance in Solids, Oliveira I.S, John Wiley and Sons, New York (1998).

[HA2021] Ha M, Bermúdez G.S.C, Kosub T, Mönch I, Zabila Y, Mata E.S.O, Illing R, Wang Y, Fassbender J, Makarov D, Adv. Mater. 33 (2021) 2005521.

[HADJ2013] Hadjipanayis G.C, Prinz G.A, Science and Technology of Nanostructured Magnetic Materials, Springer Science & Business Media, New York (2013).

[HART2000] Hartman U, Magnetic Multilayers and Giant Magnetoresistance Fundamentals and Industrial Applications, Springer-Verlag Berlin Heidelberg (2000).

[HEDI2013] Hedin E.R, Joe Y.S, Spintronics in Nanoscale Devices, CRC Press, USA (2013).

[HEIN1990] Heinrich B, Celinski Z, Cochran J.F, Muir W.B, Rudd J, Zhong Q.M, Arrott A.S, Myrtle K, Kirschner J, Phys. Rev. Lett. 64 (1990) 673.

[HEIN1993] Heinrich B, Cochram J.F, Adv. Phys. 42 (1993) 523.

[HEIN1987] Heinrich B, Urquhart K.B, Arott A.S, Cochran J.F, Myrtle K, Purcell S.T, Phys. Rev. Lett. 59 (1987) 1756.

[HEIS1928] Heisenberg V. W, für. Z. Phys. 49 (1928) 619.

[HIND2011] Hindmarch A.T, Rushforth A.W, Campion R.P, Marrows C.H, Gallagher B.L, Phys. Rev. B 83 (2011) 212404.

[HIRO2013] Hirota E, Sakakima H, Inomata K, Giant Magneto-Resistance Devices, Springer Science & Business Media, UK (2013).

[HIRO2015] Hirohata A, Sukegawa H, Yanagihara H, Žutic I, Seki T, Mizukami S, Swaminathan R, IEEE Trans. Magn. 51 (2015) 0800511.

[HYOD2015] Hyodo K, Kota Y, Sakuma A, J. Magn. Soc. Jpn. 39 (2015) 37.

[IANN2014] Iannone E, Labs on Chip: Principles, Design and Technology, CRC Press, Florida (2014).

[IKHT2018] Ikhtiar, Sukegawa H, Xu X, Belmoubarik M, Lee H, Kasai S, Hono K, Appl. Phys. Lett. 112 (2018) 022408.

[INOM1993] Inomata K, Saito Y, J. Magn. Magn. Mater. 126 (1993) 425.

[INOU2014] Inoue J.-I, Nanomagnetism and Spintronics: 2. GMR, TMR, BMR, and Related Phenomena, Elsevier Inc. USA (2014).

[IVES1994] Ives A.J.R, Hicken R.J, Bland J.A.C, Daboo C, Gester M, Gray S.J, J. Appl. Phys. 75 (1994) 6458.

[JILE1997] Jiles D, Introduction to Magnetism and Magnetic Materials, Chapman and Hall, Boca Raton (1997).

[JULL1975] Julliere M, Phys. Lett. 54A (1975) 225.

[KASU1956] Kasuya T, Progress of Theoretical Physics 16 (1956) 45.

[KIM2018] Kim K, Hall D.A, Yao C, Lee J.-R, Ooi C.C, Bechstein D.J.B, Guo Y, Wang S.X, Sci. Reports 8 (2018) 16493.

[KITT2004] Kittel C, Introduction to Solid State Physics, 7th edn Wiley, Singapore (2004).

[KOOL1999] Kools J.C.S, Kula W, Mauri D, Lin T, J. Appl. Phys. 85 (1999) 4466.

[KOON1987] Koon N.C, Jonker B.T, Volkening F.A, Krebs J.J, Prinz G.A, Phys. Rev. Lett. 59 (1987) 2463.

[KOTA2012] Kota Y, Sakuma A, Appl. Phys. Express 5 (2012) 113002.

[KOTA2013] Kota Y, Sakuma A, J. Magn. Soc. Japan 37 (2013) 17.

[KRAM2012] Kramer M.J, McCallum R.W, Anderson I.A, Constantinides S, JOM 64 (2012) 752.

[KRON2003] Kronmuller H, Fahnle M, Micromagnetism and the Microstructure of Ferromagnetic Solids, Cambridge University Press, United Kingdom (2003).

[KURI2017] Kurinec S.K, Iniewski K, Nanoscale Semiconductor Memories: Technology and Applications, CRC Press, Florida (2017).

[LEON2014] Castillo-León J, Svendsen W.E, Lab-on-a-Chip Devices and Micro-Total Analysis Systems: A Practical Guide, Springer, UK (2014).

[LIU2011] Liu X, Kanda H, Morisako A, J. Phys. Conf. Ser. 266 (2011) 012037.

[LIU2016] Liu X, Song Z.L, Wang R, Quan Z.Y, Adv. Cond. Matter Phys. 2016 (2016) 8528617.

[LIUT2012] Liu T, Cai J.W, Sun L, AIP Adv 2 (2012) 032151.

[LUO2007] Luo F, Fu X.L, Winkelmann A, Przybylski M, Appl. Phys. Lett. 91 (2007) 262512.

[MACK2007] Mack C, Fundamental Principles of Optical Lithography: The Science of Microfabrication, John Wiley & Sons Ltd, England (2007).

[MAED1994] Maeda A, Kume M, Oikawa S, Kuroki K, J. Appl. Phys. 76 (1994) 6793.

[MALK1999] Małkiński L.M, Wang J.-Q, Seip C.T, Wiemann J, Wiley J.B, J. Appl. Phys. 85 (1999) 4471.

[MALL2012] Mallinson J.C, The Foundations of Magnetic Recording, Elsevier, Academic Press, UK (2012).

[MANC2000] Mancoff F.B, Dunn J.H, Clemens B.M, White R.L, Appl. Phys. Lett. 77 (2000) 1879.

[MAND2018] Mandal R, Jung J.W, Masuda K, Takahashi Y.K, Sakuraba Y, Kasai S, Miura Y, Ohkubo T, Hono K, Appl. Phys. Lett. 113 (2018) 232406.

[MARC2017] Marcellis A.D, Reig C, Beltrán M.-D.C, Madrenas J, Santos J.D, Cardoso S, Freitas P. P, Solid State Electron. 135 (2017) 100.

[MELE2015] Mele P, Endo T, Arisawa S, Li C, Tsuchiya T, Oxide Thin Films, Multilayers, and Nanocomposites, Springer, Switzerland (2015).

[MILT2002] Milton O, Materials Science of Thin Films: Deposition and Structure, Academic Press (2002).

[MITC2012] Mitchell I.V, Coey J.M, Givord D, Harris I. R, Hanitsch R, Concerted European Action on Magnets, Springer (2012).

[MORA2009] Moram M.A, Vickers M.E, Rep. Prog. Phys. 72 (2009) 036502.

[MORA2013] Morán-López J.L., Sánchez J.M, New Trends in Magnetism, Magnetic Materials, and Their Applications, Springer Science & Business Media, New York (2013).

[MUSU2020] Musuroi C, Oproiu M, Volmer M, Firastrau I, Sensors 20 (2020) 323.

[NAIK2012] Naik V.B, Meng H, Sbiaa R, AIP Adv. 2 (2012) 042182.

[NAKA2017] Nakano T, Oogane M, Furuichi T, Ando Y, Appl. Phys. Lett. 110 (2017) 012401.

[NALW2002] Nalwa H.S, Handbook of Thin Film Materials: Characterization and spectroscopy of thin films. Vol. 2, Academic Press, Florida (2002).

[NAOE1996] Naoe M, Nakagawa S, J. Appl. Phys. 79 (1996) 5015.

[NAVA2014] Navas D, Redondo C, Confalonieri G.A.B, Batallan F, Devishvilli A, Iglesias-Freire O, Asenjo A, Ross C.A, Toperverg B.P, Phys. Rev. B 90 (2014) 54425.

[NEAL1994] Neal H.B, Theory of Magnetic Recording, Cambridge University Press, New York (1994).

[NEEL1954] Néel L, J. Phys. Rad. 15 (1954) 225.

[NIMS2019] Facilities used in Research Center for Magnetic and Spintronic Materials, National Institute for Materials Science (NIMS), Tsukuba, 305-0047, Japan.

[NOBE2007] https://www.nobelprize.org/prizes/physics/2007/summary/

[OEPE1990] Oepen H.P, Benning M, Ibach H, Schneider C.M, Kirschner J, J. Magn. Magn. Matt. 86 (1990) L137.

[OHAN2000] O'Handley R.C, Modern Magnetic Materials Principles and Applications, Wiley, New York (2000).

[OHRI1992] Ohring M, Materials Science of Thin Films, Academic Press, London (1992).

[OLIV1999] De Oliveira A.J.A, Ortiz W.A, Mosca D.H, Mattoso N, Mazzaro I, Schreiner W.H, J. Phys.: Condens. Matter. 11 (1999) 47.

[OOMI2015] Oomiya H, Wang B, Yoshida S, Kataguchi T, Takahashi K, Kanatani S, Zhang L, Liu L, Hasegawa T, Hayasaka K, Saito S, Inami N, Ueno T, Ono K, Ishio S, J. Phys. D: Appl. Phys. 50 (2015) 475003.

[OUNA1992] Ounadjela K, Muller D, Dinia A, Arbaoui A, Panissod P, Phys. Rev. B 45 (1992) 7768.

[PAND2016] Pandey H, Perumal A, Wang J, Takahasi Y.K, Hono K, IEEE Trans. Magn. 52 (2016) 3201004.

[PARK1990] Parkin S.S.P, More N, Roche K.P, Phys. Rev. Lett. 64 (1990) 2304.

[PARK19911] Parkin S.S.P, Bhadra R, Roche K.P, Phys. Rev. Lett. 66 (1991) 2152.

[PARK19912] Park S.S.P, Li Z.G, Smith D.J, Appl. Phys. Lett. 58 (1991) 2710.

[PARK1992] Parkin S.S.P, Appl. Phys. Lett. 60 (1992) 512.

[PARK2008] Park J.-H, Park C, Jeong T, Moneck M.T, Nufer N.T, Zhu J.-G, J. Appl. Phys. 103 (2008) 07A917.

[PERU20131] Perumal A, Srinivasan A, Physics of Magnetic Recording and Recording Media, NPTEL Courses (2013).

[PERU20132] Perumal A, Spintronics: Physics and Technology, NPTEL Courses (2013).

[PERU2016] Perumal A, Characterization of Materials, NPTEL Courses (2016).

[PESC1987] Pescia D, Stampanoni M, Bona G.L, Vaterlaus A, Willis R.F, Meier F, Phys. Rev. Lett. 58 (1987) 2126.

[PETR1991] Petroff F, Barthélemy A, Mosca D.H, Lottis D.K, Fert A, Schroeder P.A, Pratt Jr. W.P, Loloee R, Lequien S, Phys. Rev. B 44 (1991) 5355.

[PIRA2007] Piramanayagam S.N, J. Appl. Phys. 102 (2007) 11301.

[PIRA2011] Piramanayagam S.N, Chong T.C, Developments in Data Storage: Materials Perspective, John Wiley & Sons, New Jersy (2011).

[PONG2008] Pong P.W.T, Dennis C.L, Castillo A, J. Appl. Phys. 103 (2008) 07A902.

[PRAS2020] Prasad B, Huang Y.-L, Chopdekar R.V, Chen Z, Steffes J, Das S, Li Q, Yang M, Lin C.-C, Gosavi T, Nikonov D.E, Qiu Z.Q, Martin L.W, Huey B.D, Young I, Íñiguez J, Manipatruni S, Ramesh R, Adv. Mater. 32 (2020) 2001943.

[PURC1992] Purcell S.T, Johnson M.T, McGee N.W.E, Coehoorn R, Hoving W, Phys. Rev. B 45 (1992) 13064.

[QIU1993] Qiu Z.Q, Pearson J, Bader S.D, J. Appl. Phys. 73 (1993) 5765.

[RASS2011] Rassaei L, Singh P.S, Lemay S.G, Anal. Chem. 83 (2011) 3974.

[REIG2013] Reig C, Cardoso S, Mukhopadhyay S.C, Giant Magnetoresistance (GMR) Sensors: From Basis to State-of-the-Art Applications, Springer Science & Business Media, Berlin (2013).

[RIJK1994] Rijks T.G.S.M, de Jonge W.J.M, Folkerts W, Kools J.C.S, Coehoorn R, Appl. Phys. Lett. 65 (1994) 916.

[RUDE1954] Ruderman M.A, Kittel C, Phys. Rev. 96 (1954) 99.

[RUHR1991] Rührig M, Schäfer R, Hubert A, Mosler R, Wolf J.A, Demokritov S, Grünberg P, Phys. Stat. Sol. (a) 125 (1991) 635.

[SAIT2002] Saitoh E, Matumoto H, Nakamura T, Miyajima H, J. Appl. Phys. 91 (2002) 7215.

[SAND2017] Sander D, Valenzuela S.O, Makarov D, Marrows C.H, Fullerton E.E, Fischer P, McCord J, Vavassori P, Mangin S, Pirro P, Hillebrands B, Kent A.D, Jungwirth T, Gutfleisch O, Kim C.G, Berger, J. Phys. D: Appl. Phys. 50 363001.

[SANG1995] Sang H, Jiang Z.S., Guo G, Ji J.T, Zhang S.Y, Du Y.W, J. Magn. Magn. Mater. 140 (1995) 589.

[SATO2015] Sato K, Saitoh E, Spintronics for next generation innovative devices, Wiley Series in materials for electronic & optoelectronic applications, Willoughby A, Capper P, Kasap S (Edts). Wiley, UK (2015).

[SCHA1994] Schad R, Potter C.D, Beliën P, Verbanck G, Moshchalkov V.V, Bruynseraede Y, Appl. Phys.Lett. 64 (1994) 3500.

[SCHA1995] Schad R, Potter C.D, Beliën P, Verbanck G, Dekoster J, Langouche G, Moshchalkov V.V, Bruynseraede Y, J.Magn.Magn.Mater. 148 (1995) 331.

[SCHR2000] Schrag B.D, Anguelouch A, Ingvarsson S, Xiao G, Trouilloud Y.L.P.L, Gupta A, Wanner R.A, Gallagher W.J, Rice P.M, Parkin S.S.P, Appl. Phys. Lett. 77 (2000) 2373.

[SESH2002] Seshan K, Handbook of Thin-film Deposition Processes and Techniques: Principles, Methods, Equipment, and Applications, Noyes publication, New York (2002).

[SHEN2018] Shen H.-M, Hu L, Fu X, Sensors 18 (2018) 148.

[SHIK2009] Shikada K, Ohtake M, Kirino F, Futamoto M, J. Appl. Phys. 105 (2009) 07C303.

[SHIR1987] Shiroishi Y, Sellers C, Hilliard J.E, Ketterson J.B, J. Appl. Phys. 62 (1987) 3694.

[SHIR2018] Shiroyama T, Sakuraba Y, Nakatani T, Sepehri-Amin H, Jung J. W, Hono K, J. Appl. Phys. 124 (2018) 163910.

[SLON1991] Slonczewski J.C, Phys. Rev. Lett. 67 (1991) 3172.

[SLON1993] Slonczewski J.C, J. Appl. Phys. 73 (1993) 5957.

[SING2013] Singh A.K, Mallik S, Bedanta S, Perumal A, J. Phys. D: Appl. Phys. 46 (2013) 445005.

[SING2015] Singh A.K, PhD Thesis, Indian Institute of Technology Guwahati, Guwahati, India (2015).

[STIL2002] Stiles M.D, Zangwill A, J. Appl. Phys. 91 (2002) 6812.

[STIL2005] Stiles M.D, Interlayer Exchange Coupling in Ultrathin Magnetic Structures III: Fundamentals of Nanomagnetism ed. Bland J.A.C, Heinrich B, Springer, New York (2005).

[SONG2018] Song T, Cai X, Tu M.W.-Y, Zhang X, Huang B, Wilson N.P, Seyler K.L, Zhu L, Taniguchi T, Watanabe K, McGuire M.A, Cobden D.H, Xiao D, Yao W, Xu X, Science 360 (2018) 1214.

[SPAL2010] Spaldin N.A, Anisotropy, In Magnetic Materials: Fundamentals and Applications, Cambridge: Cambridge University Press (2010) 135-144.

[SVOB2004] Svoboda J, Magnetic Technique for the Treatment of Materials, Kluwer Academic Publishers, Dordrecht (2004).

[TAGA2000] Taga A, Nordstrom L, James P, Johansson B, Eriksson O, Nature (London) 406 (2000) 280.

[TAKA2010] Takanashi K, Jpn. Appl. Phys. 49 (2010) 11001.

[TANG2010] Tang D.D, Lee Y.-J, Magnetic Memory: Fundamentals and Technology, Cambridge University Press, UK (2010).

[TAPA2021] Taparia D, Fathoni K.B, Kulkarni P.D, Srinivasan A, Alagarsamy P, Sakuraba Y, Sasaki T, Hono K, J. Phys. D: Appl. Phys. 54 (2021) 255004.

[THIR2017] Thirumalai J, Introductory Chapter: The Prominence of Thin Film Science in Technological Scale, IntechOpen (2017).

[THOM1857] Thomson W, Proc. Royal Soc. Lond. 8 (1857) 546.

[TODO1996] Todorov T, Tsymbal E.V, Pettifor D, Phys. Rev. B 54 (1996) R12685.

[TOMA1998] Tomaz M.A, Harp G.R, Mayo E, Lederman D, Wu R, O'Brien W.L, J. Vac. Sci. Technol. A 16 (1998) 1336.

[TSYM2001] Tsymbal E.Y, Pettifor D.G, Solid State Phys. 56 (2001) 113.

[TSYM2016] Tsymbal E.Y, Zutic I, Handbook of Spin Transport and Magnetism, CRC Press, Tayler & Francis Group, Florida (2016).

[TURE2012] Turek I, Kudrnovský J, Carva K, Phys. Rev. B 86 (2012) 174430.

[TUMA2001] Tumanski S, Thin Film Magnetoresistive Sensors, Institute of Physics Publishing, Bristol (2001).

[VAVA2001] Vavassori P, Grimsditch M, Fullerton E, J. Magn. Magn. Mater. 223 (2001) 284.

[VEDM2020] Vedmedenko E.Y, Kawakami R.K, Sheka D.D, Gambardella P, Kirilyuk A, Hirohata A, Binek C, Chubykalo-Fesenko O, Sanvito S, Kirby B.J, Grollier J, Everschor-Sitte K, Kampfrath T, You C.-Y, Berger A, J. Phys. D: Appl. Phys. 53 (2020) 453001.

[VILL2010] Villard P, Ebels U, Houssameddine D, Katine J, Mauri D, Delaet B, Vincent P, Cyrille M.-C, Viala B, Michel J.-P, Prouvee J, Badets F, IEEE J. Solid-State Circuits 45 (2010) 214.

[WAGE1994] Wagendristel A, Wang Y, An Introduction to Physics and Technology of Thin Films, World Scientific, Singapore, (1994).

[WANG2017] Wang X, Metallic Spintronic Devices, CRC Press, Florida (2017).

[WANG2020] Wang L, Hu Z, Zhu Y, Xian D, Cai J, Guan M, Wang C, Duan J, Wu J, Wang Z, Zhou Z, Jiang Z.-D, Zeng Z, Liu M, ACS Appl. Mater. Interfaces 12 (2020) 8855.

[WEHN1955] Wehner G.K, Advance in Electronics and Electron Physics, 7 (1955) 239.

[WEIS2013] Weisbuch C, Physics, Fabrication, and Applications of Multilayered Structures, Springer Science & Business Media, New York (2013).

[WINK2006] Winkelmann A, Przybylski M, Luo F, Barthel J Phys. Rev. Lett. 96 (2006) 257205.

[WOLF2001] Wolf S.A, Awschalom D.D, Buhrman R.A, Daughton J.M, Von Molnar S, Roukes M.L, Chtchelkanova A.Y, Treger D.M, Science 294 (2001) 1488.

[YILD20091] Yildiz F, Przybylski M, Kirschner J, J. Appl. Phys. 105 (2009) 07E129.

[YILD20092] Yildiz F, Przybylski M, Ma X.D, Kirschner J, Phys. Rev. B 80 (2009) 064415.

[YILD20093] Yildiz F, Przybylski M, Kirschner J, Phys. Rev. Lett. 103 (2009) 147203.

[YOSI1957] Yosida K, Phys. Rev. 106 (1957) 893.

[YOUC2017] You C.-Y, Kim H, IEEE Trans. Magn. 53 (2017) 1400504.

[YUAN2015] Yuan Z.H, Huang L, Feng J.F, Wen Z.C, Li D.L, Han X.F, Nakano T, Yu T, Naganuma H, J. Appl. Phys. 118 (2015) 053904.

[ZHAN19961]Zhang J, White R.M, J. Appl. Phys. 79 (1996) 5113.

[ZHAN19962]Zhang J, White R.M, IEEE Trans. Magn. 32 (1996) 4630.

[ZHEN2019] Zheng C, Zhu K, de Freitas S.C, Chang J.-Y, Davies J.E, Eames P, Freitas P.P, Kazakova O, Kim C, Leung C.-W, Liou S.-H, Ognev A, Piramanayagam S.N, Ripka P, Samardak A, Shin K.-H, Tong S.-Y, Tung M.-J, Wang S.X, Xue S, Yin X, Pong P.W.T, IEEE Trans. Magn. 55 (2019) 0800130.

[ZHOU2017] Zhou J, Zhao W, Peng S, Qiao J, Klein J.-O, Lin X, Zhang Y, Bournel A, IEEE Trans. Magn. 53 (2017) 1300504.

Publications

Publication in Journals / Conference Proceedings:

[1]	Systematic investigation of the effect of layer thickness on the linear sensing characteristics of asymmetric structured fully epitaxial CIP-GMR based linear magnetic sensors, Dolly Taparia, Kresna Bondan Fathoni, Prabhanjan Dilip Kulkarni, Ananthakrishnan Srinivasan, Perumal Alagarsamy, Yuya Sakuraba, Tomoya Nakatani and Kazuhiro Hono, *Journal of Magnetism and Magnetic Materials* (Accepted, 19 July 2021)
[2]	Large linear sensitivity of asymmetric structured giant magnetoresistive device with metastable bcc Cu spacer and auxiliary biquadratic coupling through Rh spacer, Dolly Taparia, Kresna Bondan Fathoni, Prabhanjan Dilip Kulkarni, Ananthakrishnan Srinivasan, Perumal Alagarsamy, Yuya Sakuraba, Tomoya Nakatani, Taisuke Sasaki and Kazuhiro Hono, *Journal of Physics D: Applied Physics* 54 (2021) 255004.
[3]	Tuning magnetic anisotropy in $Fe_{1-x}Ni_x$ thin films: The effects of composition and substrate temperature, D. Taparia, J. Arout Chelvane, A. Srinivasan and Perumal Alagarsamy, *AIP Conference Proceedings* 2269 (2020) 030050.
[4]	Thickness-dependent thermal oxidation of Ni into NiO thin films, Patta Ravikumar, Dolly Taparia and Perumal Alagarsamy, *Journal of Superconductivity and Novel Magnetism* 31 (2018) 3761.

Presentation in Conferences:

[1]	Tunable sensing characteristics of fully epitaxial CIP-GMR magnetic sensors using bcc Cu and Rh spacers, D. Taparia, A. Srinivasan, A. Perumal, K. B. Fathoni, T. Sasaki, Y. Sakuraba and K. Hono, Contributed Talk at The 2020 Around-the-Clock Around-the-Globe Magnetics Conference (AtC-AtG-2020), 27 August, Virtual Conference by the IEEE Magnetics Society.

[2]	Large linear sensitivity of CIP-GMR magnetic sensor using metastable bcc Cu and Rh spacers, D. Taparia, A. Srinivasan, A. Perumal, K. B. Fathoni, Y. Sakuraba, and K. Hono Digest accepted for presentation at The International Magnetics Conference (INTERMAG-2020), 4 - 8 May, Montréal, Canada.
[3]	Tuning magnetic anisotropy in $Fe_{1-x}Ni_x$ thin films: The effects of composition and substrate temperature, D. Taparia, J. Arout Chelvane, A. Srinivasan, and Perumal Alagarsamy, Oral presentation at International Conference on Multifunctional Materials (ICMM-2019), Geethanjali College of Engineering and Technology, 19-21 December, Telangana, India.
[4]	$L1_0$ ordering in FeNi thin films: effect of substrate temperature, Dolly Taparia, J. Arout Chelvane, and Perumal Alagarsamy, Poster presented at International conference on magnetic materials and application (ICMAGMA-2018), NISER, 9-13 December, Bhubaneswar, India.
[5]	Preparation and characterization of $L1_0$ ordered FeNi thin films, Dolly Taparia and Perumal Alagarsamy, Poster presented at Research Conclave, 2018, IIT Guwahati, 8-11 March, Assam, India.
[6]	Effect of oxidation on structural, magnetic, and vibrational properties of sputtered iron thin films, Dolly Taparia, A. Nande, and Perumal Alagarsamy, Poster presented at Condensed Matter Days (CMDAYS-2017), Tezpur University, 29-31 August, Assam, India.